Magnetic Nanoparticles for Biomedical Applications

A Dissertation
SUBMITTED TO THE FACULTY OF
UNIVERSITY OF MINNESOTA
BY

YING JING

IN PARTIAL FULFILLMENT OF THE REQUIREMENTS
FOR THE DEGREE OF
DOCTOR OF PHILOSOPHY

JIAN-PING WANG, ADVISOR

December, 2012

Acknowledgements

I'm very happy to have this opportunity to thank all the people who have helped me during the past years. I was grateful to receive the admission of University of Minnesota, and to be able to spend my time in Prof. Jian-Ping Wang's group. I would like to thank my advisor, Prof. Wang, for his sharing of passion on science, novel ideas, and confidence. I really appreciate his constant encouragement and mentoring, as well as support.

I have received a lot of help from former and current members in Prof. Wang's group. I appreciate help on the development of nanoparticle deposition techniques from Jiaoming Qiu, Yunhao Xu, Xiaoqi Liu and Shihai He. I really enjoyed the time working together with all the group members: Timothy Kline, Xiaofeng Yao, Haibao Zhao, Yuanpeng Li, Yisong Zhang, Nian Ji, Hao Wang, Liang Tu, Hui Zhao, Xuan Li, Yi Wang, Yinglong Feng, Xiaowei Zhang, Todd Kline, Andy Lyle, John Harms, Postdocs Torfizur Raman, Yanfeng Jiang, and visiting scholars and students Jingzhi Han, Bin Ma, Qi Zhang, Meiyin Yang and Shaoqian Yin.

I'd like to thank all other faculty members in the Center of Micromagnetic Information Technology here in University of Minnesota, especially Prof. Randall Victora and Prof. Beth Stadler. I've harvested knowledge and inspiration on magnetism and magnetic materials from their courses and talks. Also I want to thank their group members, especially Hweerin Sohn, Yan Dong, K. Sai Madhukar Reddy and Xiaobo Huang. I'd like to thank Prof. Chris Leighton and his group members, Manish Sharmar, Mike Manno and Chunyong He for MPMS measurements.

During my graduate research, many collaborators provided significant help on the projects. Their input brings in valuable interdisciplinary part to the work. Special acknowledgments are for Prof. Chun Wang, Weihang Ji, Xiaoze Jiang of Biomedical Engineering (UMN); Prof. Shaohorn Yang and Wenchao Sheng of Mechanical Engineering (MIT); Prof. Chengguo Xing and Dr. Balasubramanian Srinivasan of Medicinal Chemistry (UMN); Prof. Timothy Widemann, Pengyun Zeng and Tanmoy Sadhukha of Pharmaceutics (UMN); Prof. Debabrata Mukhopadhyay, Prof. Priyabrata Mukherjee and Prof. Stephen Ekker of Mayo Clinic; Prof. Andrew Taton, Ying Chen of Chemistry (UMN); Prof. Wei Chen, Dr. Xiao-Hong Zhu, Prof. Mike Garwood, Dr. Djaudat Idiyatullin of the Center of Magnetic Resonance Research (CMRR, UMN); Prof. John Bischof and Michael Etheridge, Prof. Steven Girshick and Pingyan Lei of Mechanical Engineering (UMN).

I'd like to thank Dr. Ozan Ugurlu and Dr. Jason Meyer of Charfac Charaterization facilities (UMN) for tutoring and help on TEM; Dr. Mike Jackson, Dr. Julie Bowles and Dr. Peter Solheid of Institute of Rock Magnetism (UMN) for help on VSM and MPMS; Prof. David Norris previously of Materials Science (UMN), Prof. Sang-Hyun Oh and Xiaoshu Chen of Electrical Engineering (UMN) for optical measurements.

I really appreciate the mentoring and help from Dr. Bin Lu, Dr. John Westwood, Dr. Tim Klemmer of Seagate Technology, and Dr. Daniel Bai, Dr. Carl Elliott, Dr. Yunfei Ding of Western Digital during my internships.

I thank all the generous funding supports: NSF BME 0730825, UMN IEM, UMN CNA, OTC GMR Innovation Grant.

Dedication

To My Families

Abstract

Nanotechnology is revolutionizing human's life. Synthesis and application of magnetic nanoparticles is a fast burgeoning field which has potential to bring significant advance in many fields, for example diagnosis and treatment in biomedical area. Novel nanoparticles to function efficiently and intelligently are in desire to improve the current technology. We used a magnetron-sputtering-based nanocluster deposition technique to synthesize magnetic nanoparticles in gas phase, and specifically engineered nanoparticles for different applications.

Alternating magnetic field heating is emerging as a technique to assist cancer treatment or drug delivery. We proposed high-magnetic-moment Fe_3Si particles with relatively large magnetic anisotropy energy should in principle provide superior performance. Such nanoparticles were experimentally synthesized and characterized. Their promising magnetic properties can contribute to heating performance under suitable alternating magnetic field conditions.

When thermal energy is used for medical treatment, it is ideal to work in a designed temperature range. Biocompatible and "smart" magnetic nanoparticles with temperature self-regulation were designed from both materials science and biomedicine aspects. We chose Fe-Si material system to demonstrate the concept. Temperature dependent physical property was adjusted by tuning of exchange coupling between Fe atoms through incorporation of various amount of Si. The magnetic moment can still be kept in a promising range. The two elements are both biocompatible, which is favored by in-vivo

medical applications. A combination of "smart" magnetic particles and thermo-sensitive polymer were demonstrated to potentially function as a platform for drug delivery.

Highly sensitive diagnosis for point-of-care is in desire nowadays. We developed composition- and phase-controlled Fe-Co nanoparticles for bio-molecule detection. It has been demonstrated that $Fe_{70}Co_{30}$ nanoparticles and giant magnetoresistance sensor make a successful integrated system for bio-molecule detection. In addition, we proposed the concept of "magnetic coloring": magnetic nanoparticles with different M-H loop form an archive of labels for detection of multiple molecules in the same sample. The composition- and phase- controlled Fe-Co particles are candidate to serve this application.

Magnetic nanoparticles can also play a role in "green" catalysis. We synthesized core-shell structured nanoparticle with core rich in Fe, and shell rich in FeSiO, which have capability for phtocatalysis and magnetic recycling. The magnetic core enables recycling of catalysts by applying an external magnetic field. The shell shows good optical absorption which indicates the possibility of phtocatalysis.

A big challenge for nanoparticles synthesized in gas phase is to transfer them into aqueous environment, especially in biomedical field. We experimented different approaches to modify the surface of magnetic nanoparticles. A direct way was developed to introduce functional molecule onto the surface of nanoparticles in vacuum. A new design of nanoparticle collection was implemented to assist surface modification in vacuum and to enable large quantity of manufacturing.

Table of Contents

List of Tables

List of Figures

CHAPTER 1

Overview of Magnetic Nanoparticles: Synthesis and Applications

1.1 Introduction

The ever advancing nanotechnology has brought revolutionary changes to human's life. If we take a peer look into daily life, there are numerous examples of it, from personal computers of high processing speed to portable drive of high storage volume. The essence of state of art technology is nanoscale materials and devices. Magnetic nanoparticles make up an influential part of the edgy technology. They are nanometer scale in size and have unique magnetic properties. There is potential to use them for future high density information storage. Because of their comparable size with DNA and protein, magnetic nanoparticles play a significant role in biomedical area for healthcare. This topic is in leading position of research about magnetic nanoparticles. Nanoparticles are also found useful in environmental redemption, energy storage and catalysis, etc.

The great potential of using magnetic nanoparticles to solve some of today's most

important problems drives the innovations in the synthesis of particles with novel design and functionality. It is crucial to produce particles with good control, understand properties of them and apply them to achieve a progress in scientific applications.

1.2 Outline of the Thesis

The thesis will focus on designing, synthesizing and applying magnetic nanoparticles for particular biomedical use. In our lab, a gas phase synthesis method was developed and it is employed for the synthesis of different nanoparticles in this thesis. We will start with an overview of synthesis and applications of magnetic nanoparticles in Chapter 1. The overview covers popular synthesis methods with an emphasis on gas phase synthesis. Their pros and cons will be discussed. Applications of magnetic nanoparticles are then introduced. A major portion of the applications is for biomedical field, whereas magnetic particles are also useful for catalysis, information storage and so on. Chapter 2 presents the investigation of high-magnetic-moment particles for the purpose of heat generation. A very important use of the thermal energy is to assist local cancer therapy although its application is not limited in biomedicine. The study reveals the relationship between the heating performance and the magnetic properties at high frequency. In Chapter 3, we will show a design of "smart" nanoparticles for self-regulated heat generation. The self-regulation relies on temperature dependent magnetic properties. The basic working principle is analyzed first based on calculations in different heating domains. To obtain a proper candidate material, exchange coupling strength between atoms is tuned to yield a desirable magnetic property with intrinsic temperature regulation. The approach realizes

engineering of nanoparticles on both material science aspect and biocompatibility aspect. Chapter 4 is a study of high-magnetic-moment nanoparticles for disease diagnosis. A design to accomplish "magnetic coloring" is explored for biomarker detection. Nanoparticles of varying composition are synthesized and their magnetic properties are characterized. The study gives insight view of magnetism of the nanoparticles. With such an archive of particles, biomarkers can be distinguished by the unique "magnetic color" associated with them. Chapter 5 devotes to another important application field of magnetic nanoparticles, catalysis. The magnetic moment of particles provides a green and efficient solution of catalyst recycle. It is in desire to have nano-catalysts which can easily recover and catalyze well. Unique optical and magnetic property of a core-shell structured nanoparticle provides possibility for that. Nanoparticles are suitable photocatalysts and possess promising magnetic moment for recycle. Chapter 6 is an outlook of different schemes for direct functionalization of gas phase synthesized nanoparticles. A large number of applications require nanoparticles to have functional group on the surface for next step use. To avoid tedious process and loss of yield, we propose to bind functional group onto nanoparticle surface in vacuum chamber in the following of synthesis. Initial attempts to realize it will also be presented.

1.3 Synthesis of Magnetic Nanoparticles

Different methods have been used to synthesize magnetic nanoparticles. In this session, some commonly used methods will be introduced. Their features, advantages and disadvantages will be analyzed. The overview will have a major focus on physical

method because it is relevant with our way to synthesize particles.

1.3.1 Top-down

One way to make nanoparticles is to start from a bulk material and bring it down to nanoscale. The method is called top-down. It can include milling, grinding, electron beam lithography and nano-imprinting lithography. They are used not only to make nanoparticles, but also nanowires, other nanostructrures and devices. Semiconductor quantum dots are one typical example that has been made by lithography. Fe-Mg alloy particles have been obtained by mechanical grinding, which are difficult to get by other synthesis methods[1]. Top-down method has advantages in creating unique structures to achieve special property. For example, magnetic disks of multilayer structure have been made as multiplex magnetic labels for biodetection[2]. The disadvantage of top-down method is the limitation of reducing size down to really small range. Although electron beam lithography can possibly give 10nm-20nm feature size, it is time and cost consuming.

In comparison, bottom-up methods offer chances to make very small size of particles in a relatively easy way. In the following, several important bottom-up methods will be discussed.

1.3.2 Wet Chemistry

Wet chemistry method is very popular for making magnetic nanoparticles. It is mainly due to the simple set-up and the capability to produce nanoparticles of high quality.

There are different kinds of chemical synthesis, such as co-precipitation, thermal decomposition, metal reduction, reverse micelles, microemulsion to name a few[3]. Thermal decomposition of metal carbonyl is one routinely applied method nowadays. It has good control of size and morphology. But it has difficulty in generating a large yield of particles and organmetallic precursors are unstable. Metal reduction is another widely adopted method. Compared to thermal decomposition, this method uses metal salts which are stable and easy to access. When thermal decomposition and metal reduction are combined, metallic alloy particles can be made, for example, FePt nanoparticles[4]. Wet chemistry methods are very successful in making ferrite oxide particles[5,6,7]. It is essentially because the nature of high temperature and aqueous conditions involved in the process. Heterostructured magnetic nanoparticles have also been synthesized, which demonstrates the great capability of chemical synthesis[8-10]. There are nevertheless shortcomings of wet chemistry approach. The intermediate reaction complexes and phase segregation bring challenges to synthesis of bi-metallic alloy particles in a well-controlled manner. Generation of waste chemicals is also a disadvantage of the method.

1.3.3 Inert Gas Condensation

Inert gas condensation is to evaporate a solid target by heat into a background gas, and then mix it with a cold gas to condense the vapor into particles. The method is suitable for most of metals because of their moderate evaporation temperature. It can make oxide or compound particles by including reactive gas in the cold gas stream. The method has been studied both theoretically and experimentally[11]. It is possible to control the size

distribution by controlling the flow field and the mixing of the cold gas with the gas carrying evaporated metals. The control of morphology is also demonstrated through the controlled sintering of single particles after their formation[12]. Nevertheless, for a lot of applications where dispersed and uniform particles are preferred, inert gas condensation has limitations in providing satisfactory particles.

1.3.4 Laser Ablation

In laser ablation, a high power laser beam shoots onto a solid target at atmosphere pressure. Materials evaporate from the target under the high energy bombardment. A typical experimental set-up is shown in Figure 1.1. Particles will condense from the evaporated fume and can be collected or sent to other analyzer through the outlet. The technique doesn't have restriction on the type of material to fabricate. As long as it vaporizes the solid material, particles can be generated through the condensation of vapor. High melting point element or compound has been made through laser ablation, such as Si and W. The yield is high and can easily reach ~10nm/min. A big disadvantage of the technique is large size distribution. It doesn't provide good control of either morphology, or crystallinity.

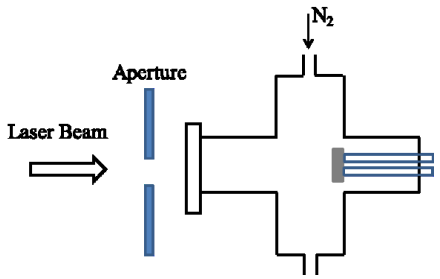

Figure 1.1 Schematic view of experimental set-up of laser ablation

1.3.5 Arc Discharge

Another way to vaporize materials is through arc discharge. In this method, electrodes made of metals are charged and vaporized in the presence of inert gas. When the breakdown voltage is reached, the arc forms across the electrode and vaporizes the electrodes. It produces small particles made of the electrode materials. Instead of having a constant inert gas in presence, it is also possible to pulse the gas between the electrodes. The method gives flexibility to study behavior of particles in the absence of any supporting substrate. For example, it was used to study catalytic property of Ni particles in gas phase. Additionally, it allows reaction with different background gas such as O_2 to prepare metal oxides or other compounds. Similar with laser ablation, the arc discharge doesn't provide good control of size and morphology of particles.

1.3.6 Chemical Vapor Synthesis

In this approach, chemical gas precursors are used as the source to generate a supersaturation state for nucleation to happen[13]. Vapor phase precursors are brought into a hot-wall reactor. Suitable condition will be applied to initiate nucleation of particles in the vapor phase rather than deposition of a film on the wall. Therefore, chemical vapor synthesis is in analogy with the chemical vapor deposition that is commonly used to grow solid thin films. Chemical vapor synthesis is usually performed at higher process temperature, higher partial pressure and longer residence time than chemical vapor deposition. The method is applicable to a wide range of materials and can take advantage of the developed precursor chemistries in chemical vapor deposition. By carefully

adjusting the partial pressure of reactive precursors, non-agglomerated, single crystalline particles are able to be formed[14]. The type of precursor used in the process can also have effect on particle size. For example, organometallic precursor has been found to lead to smaller particles than ionic precursor[15]. The former has higher vapor pressure and lower decomposition temperature than the latter, which gives rise to initially very small particles. By introducing multiple precursors, composite and doped nanoparticles can be made with ease[16].

1.3.7 Flame Aerosol

Another means of inducing reaction of precursor and particle nucleation is to carry out the synthesis in a flame. The energy needed is produced by combustion reactions. It is the most widely used method to manufacture nanoparticles in industry[13]. Carbon black, fume silica, iron oxide and catalysts are synthesized by flame aerosol in large quantity[17]. A typical flame aerosol reactor consists of an evaporator to provide precursor, a burner accompanied by a gas delivery system and a filter to collect particles. There are a few ways to control the particle size and morphology. Reactant mixing, additives and electric fields are important gadgets when gaseous precursors are used[17]. Reactant mixing mainly determines the flame temperature field. The temperature and the time particles experience in the flame determine their size and morphology greatly. Additives are additional precursors added to control the physical property of particles through material composition. Electric field charges the newly formed particles to reduce coagulation through charge repulsion[18]. The method is simple one-step process and has no need for

moving machinery parts. However, it is a complex process which gives difficulty to control. Agglomeration of particles is one big disadvantage for this method particularly, although agglomeration exists for most of gas phase synthesis. In addition, the method is mainly for synthesis of oxide materials because of the high oxidizing environment in the flame.

1.3.8 Sputtering

Sputtering a solid target by a beam of inert gas ions is another way to vaporize the solid. The vapor reaches supersaturation when temperature and pressure are at suitable value. Compared with fabrication of thin films using sputtering, formation of particles is usually conducted under high pressure. A reduction of mean free path of atoms leads to nucleation and growth of particles. There are different types of sputtering systems, for example, RF diode sputtering, ion beam sputtering and magnetron sputtering. Sputtering produces particles in high purity with little contamination. It is also applicable to various materials and is easy to adjust composition of the synthesized particles. In this thesis, we use DC magnetron sputtering to synthesize magnetic nanoparticles in a way with good control of the particles generated. The basic configuration of the equipment and the working principle will be briefly introduced here first. More details on the system and fabrication technique can be found Ph.D dissertation of J. M. Qiu[19], Y. H. Xu[20] and X. Liu[21].

Figure 1.2 is a schematic view of the nanocluster synthesis system used for the work in this thesis. In the set-up, a piece of planer target locates at the cathode. Permanent

magnets locate at the back of the target as part of the magnetron sputtering gun. During the synthesis process, sputtering gas is fed onto the surface of the target through a shielding cap. A voltage is applied to the cathode and the anode. The chamber wall functions as the anode, which is at the same potential with the ground. The shielding cap possibly works as a pseudo anode. In sputtering, sputtering gas molecules are continuously ionized through their collisions with electrons. The voltage between the anode and the cathode accelerates ionized ions towards cathode. Atoms of the target material are bombarded out while secondary electrons are generated at the same time. The presence of magnetic field modifies the travel path of secondary electrons leading to more ionization process. A glow discharge is thus formed between the anode and the cathode, which consists of different particles, such as ions, electrons and neutral molecules.

There are several different regions within glow discharge where physical property and main species are distinct. Detailed construction of DC glow discharge is displayed in Figure 1.3. Just above the cathode, a region called Crookes dark space exists. This region is close to the cathode with large electric potential fall in the direction pointing towards the cathode. Major specie in Crookes dark space is ions with high velocity. Density of electrons is low due to the force exerted by the electric field. Following the dark space is a negative glow which comes from the excitation of the gas molecules. Next to that there is a Faraday dark space with high density of electrons. The dark space is filled with accelerated electrons of high velocity. A large number of collisions take place in this region between electrons and gas molecules. Positive column is a region with equal

number of ions and electrons. Anode dark space has high density of electrons and low density of ions due to the high potential of the anode.

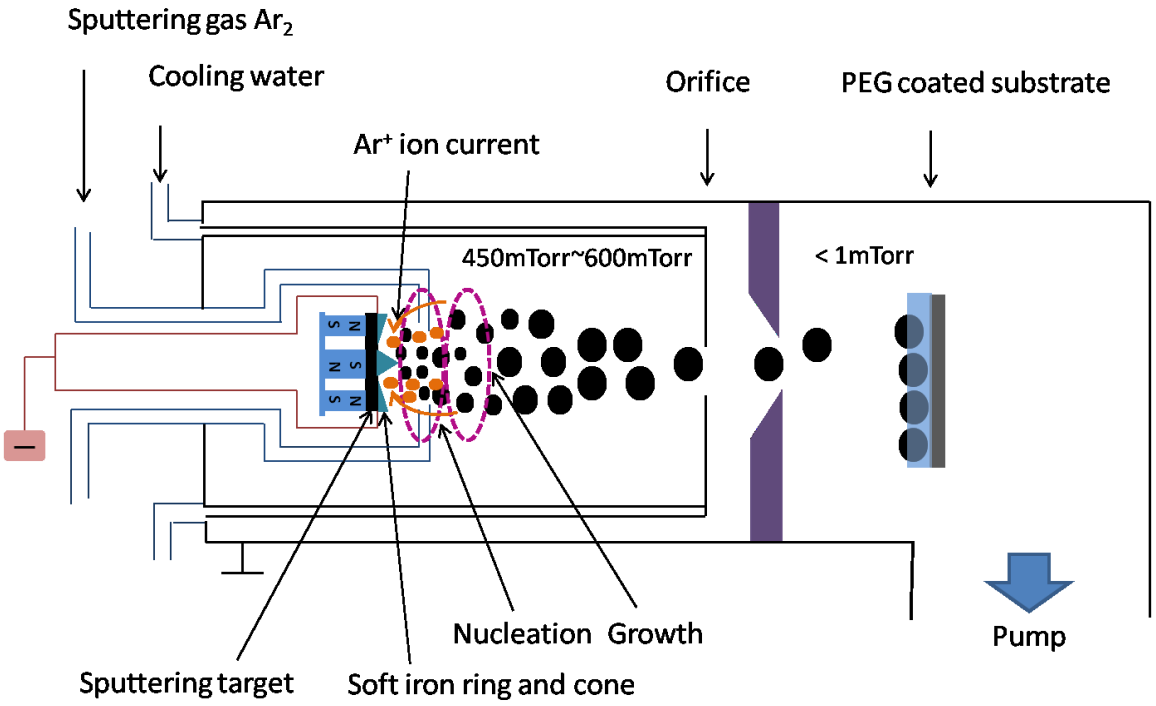

Figure 1.2 Schematic drawing of gas condensation nanoparticle deposition system

The cathode dark space which has most potential fall is an important region for the formation of nanoparticles. The Ar ions are accelerated by the potential fall and gain much kinetic energy. Ar ions transfer the kinetic energy to atoms of target material through collisions. Atoms come off the target by breaking bonds in sacrifice of the kinetic energy. A vapor is formed by atoms, Ar gas molecules, electrons and Ar ions. When supersaturation is reached, atoms nucleate to small clusters and continue with growth. Supersaturation is a function of the total amount of species in the space,

temperature and pressure. Consecutive collisions with Ar ions provide kinetic energy to atoms to maintain an energy path for crystal growth. It is important to remember that atoms and small clusters travel in the space carried by the gas flow, therefore we have both spatial and time control of the thermal history.

There are a few important parameters to realize a control of synthesis process. One is discharge current density, which has a unit of A/m^2. It is proportional to the sputtering current and inversely proportional to the effective sputtering area. It describes how many Ar ions bombard onto the unit sputtering area per second. Because Ar ions are the main source of kinetic energy, the discharge current density suggests how energetic the atoms can be.

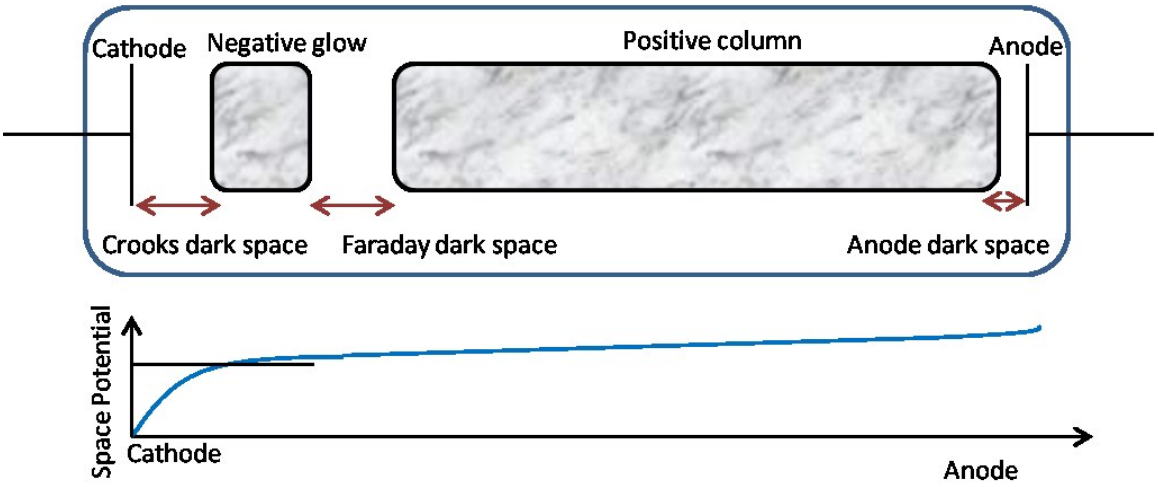

Figure 1.3 A schematic illustration of the structure of glow discharge (up) and a qualitative showing of space potential between the cathode and the anode

The important role of magnetic field B is related with its influence on the cathode dark space. When B is superimposed with electrical field E orthogonally, movement of

electrons will be influenced by the two combined and follows a spiral behavior. Their motion is governed by equations

$$m\frac{d^2x}{dt^2} = qE - Bq\frac{dy}{dt} \quad \text{(Equation 1.1)}$$

$$m\frac{d^2y}{dt^2} = Bq\frac{dx}{dt} \quad \text{(Equation 1.2)}$$

The spiral circular radius can be found to be R=$\frac{2V^2/d}{\frac{V^2}{d^2}+\frac{B^2q}{m}}$, where d is the conventional Crookes dark space width for DC sputtering without magnetic field, V is the cathode potential drop [22]. Usually, R will be smaller than d, which means that superposition of the magnetic field reduces the dark space width. For DC sputtering without magnetron, the width of dark space is inversely proportional to gas pressure. Because reduced gas pressure increases mean free path of electrons, which then extends the width of cathode dark space. In this sense, addition of a magnetic field has the same effect with increasing the gas pressure as for conventional DC sputtering. As the magnetic field confines electrons by reinforcing them travel spirally, loss of electrons is greatly reduced and the magnetic field helps to increase discharge current density when the same voltage is applied.

When magnetron sputtering is applied for synthesis of particles, it's critical to manipulate the magnetic field for synthesis control. The addition of a strong magnetic field increases the sputtering efficiency by confining secondary electrons, but it reduces the width of the cathode dark space especially for highly magnetic targets. Because of the

important relationship between cathode dark space and crystal growth, there is a need to adjust its width and its distribution in practice. A soft magnetic ring and a magnetic cone of specific dimensional parameters can be added onto the surface of the target to adjust the distribution of the magnetic field, as well as the cathode dark space. (Figure 1.2) They tend to re-define how magnetic flux distributes on the surface of the target. A major benefit by using them is to extend the cathode dark space and generates a more evenly distributed energetic regime in the transverse direction across the erosion track. Current density is increased by reducing the effective sputtering area. The strength of the magnetic field and the geometry of the target can have effect on the primary environment under which particles form. According to the type of particles to synthesis, those conditions can be correspondingly adjusted. Detailed demonstration of that will be shown in the following chapter 2 and Chapter 3.

1.4 Applications in Life Science

Nanoparticles are popularly studied for life science because they can offer new opportunities for the challenges and problems.[23] A specified term for the subject emerges in recent years, namely biomedicine or nanomedicine. The research focuses on development of nanoparticles with specific property for a technological application related with medical and biological field. Magnetic nanoparticles are an important type among a variety of particles. Major application fields using magnetic nanoparticles include magnetic resonance imaging (MRI) contrast agents, magnetic hyperthermia, drug delivery, biomarker labeling, magnetic sorting and separation, cellular activity control

and gene transfer. The small size of particles makes them suitable for bonding process with biological subjects. When particles are used in the human body, they can be easily manipulated because penetration of a magnetic field through tissues is very efficient. It is an important advantage when we compare magnetic nanoparticles with ones by optical control, such as laser, whose penetration through tissues usually suffers great loss. The magnetic manipulation gives feasibility to physically move particles, which is desirable for targeted delivery of drugs, DNA or RNA to a specific region. In addition, there is negligible magnetic background from biological substance, which contributes to high signal to noise ratio and low interference.

The most widely used particles for bio-nanotechnology are magnetite or maghemite nanoparticles. Their synthesis procedure is relatively mature particularly by wet chemistry. They have good biocompatibility and magnetic property. However, lately attention has been paid to nanoparticles made of highly magnetic materials in pursuit of better performance than oxide particles. In the following, we will give an overview of some important applications of magnetic nanoparticles. Design consideration and examples of novel magnetic nanoparticles are included.

1.4.1MRI Contrast Agents

MRI is a powerful diagnostic tool for disease detection. The imaging relies on magnetic moment of protons in the region of body. When a large static magnetic field (1.5T-7T) is applied to the protons, nuclear spins are aligned either parallel or anti-parallel to the field direction. A net moment is resulted from all the nuclear spins in the region. The net

moment undergoes processional movement with respect to the magnetic field direction. The procession frequency is defined as Lamor frequency which is determined by external magnetic field strength B_0 and gyro-magnetic ratio γ, an intrinsic parameter of the material (Equation 1.3)

$$\varpi_0 = \gamma B_0 \qquad \text{(Equation 1.3)}$$

If the static magnetic field is constantly applied, an equilibrium status will be reached with the net moment processing around the field. In MRI, RF pulses are introduced into the system to interrupt the equilibrium state. After application of an RF pulse, some nuclear spins will flip their direction from parallel to anti-parallel or vice versa as illustrated in Figure 1.4. At this time, the moment can be decomposed into transverse component and longitudinal component with respect to the external magnetic field. It takes certain time for nuclear spins to come back to the equilibrium status, which is called relaxation time. There are two types of relaxation time, T1 relaxation time and T2 relaxation time. T1 relaxation time is a measure of time cost for longitudinal component to relax back. T2 relaxation time is a measure of time cost of transverse component to relax back to original state. Relaxation time is characteristic for biological matters due to their different content of water or hydrogen atoms. By coding different relaxation time length, contrasted images can be formed which makes the technique capable to examine a particular biological part of interest.

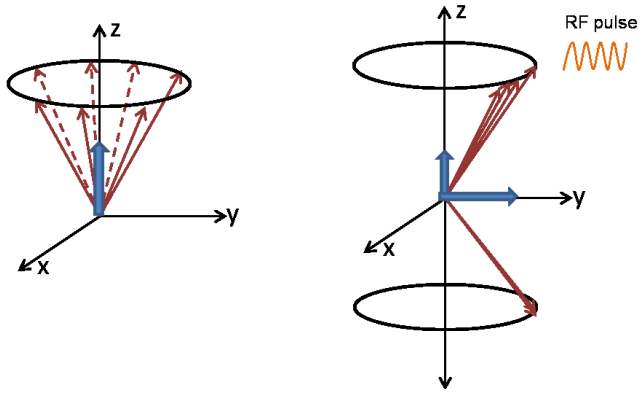

Figure 1.4 Illustration of alignment of magnetic moment of protons in magnetic resonance imaging without and with RF pulse input

Magnetic nanoparticles are used as T2 contrast agents in MRI. Dipolar field from magnetic moment of particles poses an inhomogeneous field surrounding the protons nearby. The field accelerates de-phasing of protons and shortens the time for spins relax back to the state of zero net transverse moment. Figure 1.5 illustrates the acceleration effect on incoherence of transverse nuclear magnetic moment by magnetic contrast agents. Magnetite particles have been mostly studied and are available for clinical use. However, they are not necessarily the optimal candidate for MRI contrast agents. According to the principle, strength of the dipolar field affects how well the particles enhance the contrast. Dipolar field of a nanoparticle is expressed as:

$$H = \sum_{ij} \frac{3\vec{n}(\vec{m}_j \bullet \vec{n}) - \vec{m}_i}{\left|r_{ij}\right|^3} \qquad \text{(Equation 1.4)}$$

where m_j and m_i are moment of the i_{th} and j_{th} atom, n is the field direction, and r_{ij} is the distance between i_{th} and j_{th} atom. To increase the magnetic moment of nanoparticles is the direction based on Equation 1.4. The spatial distribution of dipolar field also affects the effectiveness of increasing contrast. Therefore, high-magnetic-moment particles of

different morphology are new candidates with strong dipolar field of variable spatial distribution.

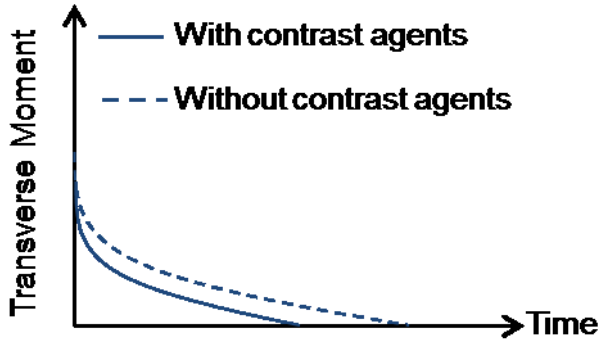

Figure 1.5 Change of transverse magnetic moment versus time

We have performed simulation to design how high-magnetic-moment particles can be used for MRI imaging of cells. The model considers cells taking up many liposomes loaded with magnetic particles. The magnetic flux density distribution around a 200nm-liposome-particle array is simulated using Comsol Multiphysics 3.5 (http://www.comsol.com/). In Figure 1.6(a), there are 11 of 200nm-liposome-particle with 100nm interspacing in each column and row. Each liposome particle is consisted of a 20nm FeCo nanoparticle array (6 of 20nm-FeCo nanoparticle with 20nm interspacing in each column and row). The external applied field in the simulation is 7 T and the relative permeability of FeCo nanoparticle is 5000. Spatial resolution of MRI is 0.00025T distortion of magnetic flux density. By plotting out the magnetic flux density distribution as a function of distance, it is shown that there'll be 0.00025T distortion at 0.14mm away from liposome particle array center (Figure 1.6(b)). Therefore, the 200nm-liposome-particle array is at MRI detection level. A cell that uptakes such amount of liposome magnetic particles can be imaged by MRI. Compared with same configuration liposome

particle array in which each liposome particle consisted of 20nm-iron oxide-particle array, the array with high-moment particle gives resolution boundary at a distance 1.7 times of that of iron oxide particles. It shows the advantage of using high-magnetic-moment nanoparticles.

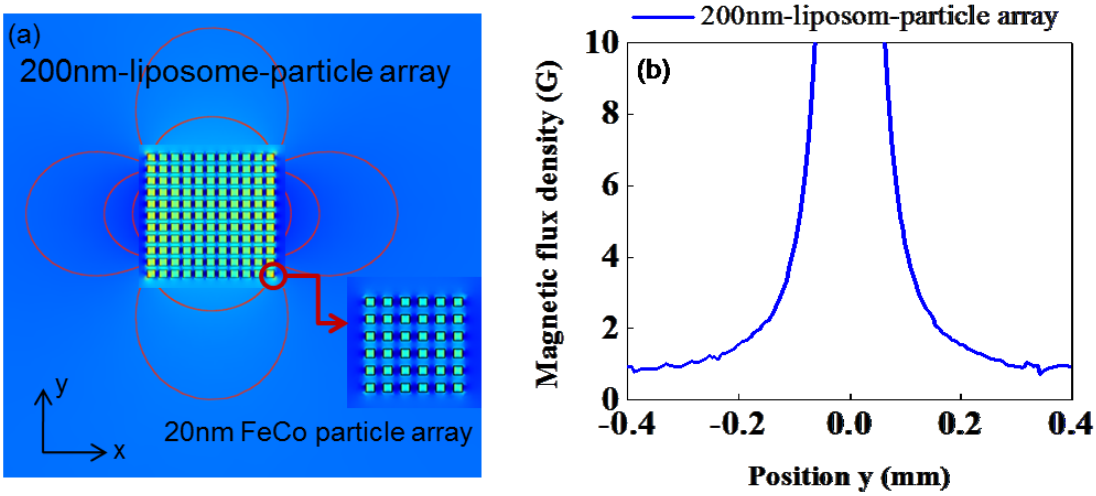

Figure 1.6 (a)A liposome-particle-array configuration and contour plot of magnetic flux density (b)Magnetic flux density distribution of a liposome-particle-array as a function of position along y direction through array center

1.4.2 Magnetic Hyperthermia

The growing number of cancerous disease cases calls for great research attention to develop advanced cancer therapy. Hyperthermia, which cures disease by elevating the temperature of the corresponding region, has long been used in the history. In the early days, different ways to increase temperature were employed: hot water bath, heating stainless steel needle, metal thermal seeds[24] and so on. Tumor cells usually undergo endogeogenesis growth where blood vessels self-develop branches in a fast pace. The vascular structure of malignant cells is thus quite different from the normal cells. Tumor

vasculature is more immature, composed of single-layered endothelium and devoid of basement memberane and neural junction[25]. Increased temperature can cause increase of blood flow around tumor as observed in many animal studies. The increase of blood flow could come from mechanical or passive dilation of the vessels. It then imposes stress to the immature vessels and therefore leads to breakdown of vessels till final death of malignant cells[26,27]. Magnetic hyperthermia uses magnetic nanoparticles as the heat source and an alternating magnetic field to accomplish the therapeutic treatment.

Besides magnetic hyperthermia, there is other technology which uses thermal energy to treat cancerous disease, such as Laser induced photo-thermal effect, radio frequency ablation, ultrasound thermal therapy and microwave thermal therapy. Compared to them, magnetic hyperthermia has its advantages. First, penetration depth of the magnetic field is not a concern because 150kHz-900kHz frequency range of field can reach deep in the tissue. Second, the magnetic field itself at such frequency range won't cause injury of normal tissue. Third, nanoparticles can be targeted to the cancerous region and function locally without affecting non-cancerous region.

Magnetic particles have also been used to destroy cancer cells through mechanical method. Ferromagnetic microdiscs were excited to physically rotate under an AC magnetic field and lead to stress induced damage of cancer cells attached to them[28]. The discs have 1um diameter which is large enough to experience quick renal clearance by the body. Although engineering efforts can possibly bring down the size, to maintain the votex domain structure limits the room for size reduction. The method is not as promising as thermal therapy.

1.4.3 Drug Targeting Delivery

Drug targeting has emerged as one of the most important modern technologies. Besides drugs, genes and radionuclides are also studied for targeting delivery. It is a challenge to deliver them to the desired position inside body because of the circulation system and renal clearance system of body. By combining magnetic nanoparticles and a magnetic field, it allows to deliver drugs to the desired location and fix them there during medical procedure. Therefore, small dosage can be used and the systematic effect of drugs can be minimized. To successfully target and deliver, magnetic nanoparticles need to move together with drugs all the time. A gradient magnetic field needs to be engineered in terms of direction and strength. Particles will move under the force imposed by the field together with the drugs. The force felt by a nanoparticle is given by

$$F = (m \bullet \nabla)B \qquad \text{(Equation 1.5)}$$

where B is the applied field and m is the magnetic moment of the particle. The force is thus proportional to the moment of the particle as well as the gradient of the field. To obtain an efficient magnetic delivery, it is critical to increase the gradient of the field and the moment of the particle. A common structure of magnetic carriers consists of a magnetic core, together with drugs inside a shell of copolymer or mesoporous silica. Recently, carbon nanotubes loaded with magnetic particles have also been demonstrated as a good carrier for drug delivery[29].While most of the study focuses on the development of magnetic carriers based on iron oxide particles[30,31], some attempts on high-magnetic-moment metallic particles have been made[32,33]. From a design point of view, there are a

few aspects to consider. First, magnetic particles should have as high as possible magnetic moment. Second, the shell layer or the cargo needs to secure the particles and drugs inside without leaking. Third, the carriers should not aggregate in the presence of the field. Proper surface modification is important for this.

1.4.4 Biomarker Sensing

Biosensors or biochips are assay analytes which detect bio-molecules immobilized on a solid surface. Extensive research and development have been devoted to biosensors because they provide quick and accurate detection of biomarkers in body fluid. It has potential for diagnosis of particular disease associated with the biomarker at an early stage conveniently. The detection relies on immunoassay and the output signal can be chemical, mechanical, optical or magnetic[34-37]. Magnetic biosensors consist of arrays of giant magnetoresistance (GMR) sensors or magneto tunneling junction (MTJ) sensors, and magnetic nanoparticle tags. When magnetic nanoparticles conjugate onto the sensor surface through antibody-antigen coupling, the dipolar field from nanoparticles under a detection field causes a resistance change of GMR or MTJ. Change of resistance is related with the strength of dipolar field, thus the number of particles on the sensor surface. Quantification of biomarkers is feasible based on the relationship between magnetic particles and bio-molecules. Most commercial biosensing systems use optical signal such as fluorescent tags. They come across sensitivity problem due to complex interference of optical signals from the background. Magnetic biosensing has low noise and is able to be miniaturized. Ever since the first demonstration by Naval Research

Lab[38], many groups worldwide contribute to the progress of realizing a portable, low cost, highly sensitive point-of-care device[39-43].

In addition to critical requirements for GMR or MTJ design, special attention to magnetic nanoparticles is needed for improvement on the overall sensing performance. First of all, magnetic nanoparticles should possess high magnetization. The detection signal is proportional to the strength of dipolar field, and according to Equation 1.4 high magnetization can give strong dipolar field. Second, particles should not agglomerate. Agglomeration will cause difficulty in correct quantification as it affects conjugation process as well as the final signal. Superparamagnetism and surface coating are two important factors that help prevent particles from agglomeration. Third, interparticle interaction has to be considered for interpretation of detection signal. In reality, dipolar interaction is a primary type that exists among the particles. Even though it doesn't cause agglomeration with proper surface treatment, its presence changes the magnetic response of particles under the detection field. From a practical point of view, the detection signal is a reflection of dipolar field imposed on the GMR or MTJ sensor by an ensemble of randomly distributed anisotropic particles with certain degree of interaction. Furthermore, particles can also have interaction with magnetic domains of sensors. Last, there could be noise from particles due to thermal fluctuation, distribution of anisotropy and size. Therefore, uniform particles are desired for the reduction of system noise.

1.5 Other Applications

1.5.1 Catalyst

Magnetic nanoparticles can be used as a catalyst or catalyst supports. Catalysts participate in chemical reactions and change the rate of reaction by providing a path of low activation energy. The catalyst is not consumed by the reaction. A catalyst support is material with high surface area to which catalysts attach to. When magnetic nanoparticles are used, not only do they provide necessary functions a catalyst or a catalyst support should have, but also they enable easy recycle by a magnetic field. This feature makes them more and more appealing in catalysis. Metallic particles such as Fe have been used as catalyst for synthesis of carbon nanotube[44]. Ferrite particles have been used as catalyst supports which carry catalytic particles made of Pt, Pd or Ru on the surface[45]. It is also possible to engineer a composite structure including magnetic particles and the catalytic particles in the supports[46]. Because magnetic particles add motion capability to catalysts, enhanced catalytic efficiency is possible through excitation of Brownian motion of magnetic catalysts by an alternating magnetic field[47].

A good candidate for recyclable catalysis is magnetic nanoparticles with superior magnetic property: High saturation magnetization and zero remanence in the absence of a field. Superparamagnetic particles of high-magnetic-moment are ideal candidates. However, it is also important that the particles are stable in the chemical reactions involved. Therefore, it is often required that particles have a special coating of either surfactant or inert inorganic materials.

1.5.2 Information Storage

Magnetic nanoparticles were used for information storage back since the date when tape recording media was predominant. Particulate tape recording media of iron oxide particles was used at that time. Nowadays in a hard disk drive, recording media is typically textured thin film with grain size less than 10nm. A recording bit "1" or "0" consists of a few grains of the same magnetization orientation. To further increase the recording density, it is proposed to have a recording bit consisting of only one grain or one particle[48]. Magnetic nanoparticles can be applied for such single bit recording media. High anisotropic FePt, CoPt and $SmCo_5$ nanoparticles are promising for future high density recording media.

A few challenges remain to apply magnetic nanoparticles for information storage. First, in order to use particles of small size, high crystalline anisotropy must be retained to ensure thermal stability. Chemical ordering of the particles is thus critical and it should be controllable through processing conditions. Second, how to assemble nanoparticles into aligned, regular pattern is an important aspect for their application on recording. So far, most attempts were made through chemical self-assembly[49]. Third, the particles need to be highly uniform and the requirement for uniformity becomes even stringent compared to traditional recording media. The uniformity is not only size or morphology wise, but also chemical, magnetic wise.

1.5.3 Permanent Magnet

An ideal permanent magnet should emanate a large magnetic field and should not be easily demagnetized. Therefore, a high magnetic remnance magnetization and a large

magnetic coercivity are required. Magnetic materials with high magnetization usually are magnetically soft whereas magnetically hard materials don't have high magnetization. To make the ideal permanent magnet, a possible solution is a composite magnet with exchange-coupled soft and hard phase[50].

Magnetic nanoparticles are good candidates to make such composite permanent magnet. Theoretical study suggests the soft phase should have a dimension smaller than the twice of domain wall thickness of the hard phase, which is typically 3nm-15nm[4]. The dimensional requirement is on the similar scale of magnetic nanoparticles. It is possible to optimize the exchange interaction between the hard phase and soft phase on the nanoscale. The composite density, grain size, as well as intermixing of soft and hard phase is also changeable through adjustment of synthesis conditions. Special care is needed to control microscopic structure, the physical and chemical properties of both hard phase and soft phase. While some efforts have been made to synthesize the composite structure[51,52], further optimization of a highly ordered phase and magnetic property of the nanocomposites are needed to produce ultra-high energy product.

References

1 A. Hightower, B. Fultz, and R. C. Bowman Jr, Journal of Alloys and Compounds **252,** 238 (1997).

2 W. Hu, R. J. Wilson, A. Koh, A. Fu, A. Z. Faranesh, C. M. Earhart, S. J. Osterfeld, S.-J. Han, L. Xu, S. Guccione, R. Sinclair, and S. X. Wang, Advanced Materials **20,** 1479 (2008).

3 T. Hyeon, Chemical Communications**,** 927 (2003).

4 N. A. Frey, S. Peng, K. Cheng, and S. Sun, Chemical Society Reviews **38,** 2532 (2009).

5 S. Sun and H. Zeng, Journal of the American Chemical Society **124,** 8204 (2002).

[6] J. Rockenberger, E. C. Scher, and A. P. Alivisatos, Journal of the American Chemical Society **121,** 11595 (1999).
[7] T. Hyeon, S. S. Lee, J. Park, Y. Chung, and H. B. Na, Journal of the American Chemical Society **123,** 12798 (2001).
[8] H. Yu, M. Chen, P. M. Rice, S. X. Wang, R. L. White, and S. Sun, Nano Letters **5,** 379 (2005).
[9] W. S. Seo, J. H. Lee, X. Sun, Y. Suzuki, D. Mann, Z. Liu, M. Terashima, P. C. Yang, M. V. McConnell, D. G. Nishimura, and H. Dai, Nat Mater **5,** 971 (2006).
[10] W. Zhao, J. Gu, L. Zhang, H. Chen, and J. Shi, Journal of the American Chemical Society **127,** 8916 (2005).
[11] K. Wegner, B. Walker, S. Tsantilis, and S. E. Pratsinis, Chemical Engineering Science **57,** 1753 (2002).
[12] K. Nakaso, M. Shimada, K. Okuyama, and K. Deppert, Journal of Aerosol Science **33,** 1061 (2002).
[13] M. T. Swihart, Current Opinion in Colloid & Interface Science **8,** 127 (2003).
[14] M. L. Ostraat, J. W. De Blauwe, M. L. Green, L. D. Bell, H. A. Atwater, and R. C. Flagan, Journal of The Electrochemical Society **148,** G265 (2001).
[15] S. Polarz, A. Roy, M. Merz, S. Halm, D. Schröder, L. Schneider, G. Bacher, F. E. Kruis, and M. Driess, Small **1,** 540 (2005).
[16] R. Schmechel, M. Kennedy, H. von Seggern, H. Winkler, M. Kolbe, R. A. Fischer, L. Xaomao, A. Benker, M. Winterer, and H. Hahn, Journal of Applied Physics **89,** 1679 (2001).
[17] H. K. Kammler, L. Mädler, and S. E. Pratsinis, Chemical Engineering & Technology **24,** 583 (2001).
[18] H. K. Kammler, S. E. Pratsinis, P. W. Morrison Jr, and B. Hemmerling, Combustion and Flame **128,** 369 (2002).
[19] J.-M. Qiu, Thesis, University of Minnesota.
[20] Y.-H. Xu, Thesis, University of Minnesota, 2007.
[21] X.-Q. Liu, Thesis, University of Minnesota, 2009.
[22] K. W. a. S. Hayakawa, *Handbook of Sputtering Deposition Technology: Princinples, Technology and Applications* (Noyes Publications).
[23] J. C. Q A Pankhurst, S K Jones and J Dobson, J. Phys. D: Appl. Phys. **36** (2003).
[24] J. A. Paulus, G. R. Parida, R. D. Tucker, and J. B. Park, Biomaterials **18,** 1609 (1997).
[25] J.-C. Bolomey, *Thermoradiotherapy and Thermochemotherapy*, Vol. 2 (Springer, 1995).
[26] C. W. Song, Cancer Research **44,** 4721s (1984).
[27] R. K. Jain and K. Ward-Hartley, Sonics and Ultrasonics, IEEE Transactions on **31,** 504 (1984).
[28] D.-H. Kim, E. A. Rozhkova, I. V. Ulasov, S. D. Bader, T. Rajh, M. S. Lesniak, and V. Novosad, Nat Mater **9,** 165 (2010).
[29] D. Cai, J. M. Mataraza, Z.-H. Qin, Z. Huang, J. Huang, T. C. Chiles, D. Carnahan, K. Kempa, and Z. Ren, Nat Meth **2,** 449 (2005).

[30] M. Liong, J. Lu, M. Kovochich, T. Xia, S. G. Ruehm, A. E. Nel, F. Tamanoi, and J. I. Zink, ACS Nano **2,** 889 (2008).
[31] N. Nasongkla, E. Bey, J. Ren, H. Ai, C. Khemtong, J. S. Guthi, S.-F. Chin, A. D. Sherry, D. A. Boothman, and J. Gao, Nano Letters **6,** 2427 (2006).
[32] M. Arruebo, M. Galán, N. Navascués, C. Téllez, C. Marquina, M. R. Ibarra, and J. Santamaría, Chemistry of Materials **18,** 1911 (2006).
[33] A. A. Kuznetsov, V. I. Filippov, O. A. Kuznetsov, V. G. Gerlivanov, E. K. Dobrinsky, and S. I. Malashin, Journal of Magnetism and Magnetic Materials **194,** 22 (1999).
[34] J. L. Arlett, E. B. Myers, and M. L. Roukes, Nat Nano **6,** 203 (2011).
[35] M. A. Cooper, Nat Rev Drug Discov **1,** 515 (2002).
[36] P. I. Nikitin, P. M. Vetoshko, and T. I. Ksenevich, Journal of Magnetism and Magnetic Materials **311,** 445 (2007).
[37] P. Knight, Nat Biotech **7,** 175 (1989).
[38] D. R. Baselt, G. U. Lee, M. Natesan, S. W. Metzger, P. E. Sheehan, and R. J. Colton, Biosensors and Bioelectronics **13,** 731 (1998).
[39] D. L. Graham, H. Ferreira, J. Bernardo, P. P. Freitas, and J. M. S. Cabral, Journal of Applied Physics **91,** 7786 (2002).
[40] G. Li, V. Joshi, R. L. White, S. X. Wang, J. T. Kemp, C. Webb, R. W. Davis, and S. Sun, Journal of Applied Physics **93,** 7557 (2003).
[41] J. Schotter, P. B. Kamp, A. Becker, A. Pühler, G. Reiss, and H. Brückl, Biosensors and Bioelectronics **19,** 1149 (2004).
[42] B. Srinivasan, Y. Li, Y. Jing, Y. Xu, X. Yao, C. Xing, and J.-P. Wang, Angewandte Chemie International Edition **48,** 2764 (2009).
[43] W. Shen, X. Liu, D. Mazumdar, and G. Xiao, Applied Physics Letters **86,** 253901 (2005).
[44] C. Emmenegger, J. M. Bonard, P. Mauron, P. Sudan, A. Lepora, B. Grobety, A. Züttel, and L. Schlapbach, Carbon **41,** 539 (2003).
[45] A. Schätz, O. Reiser, and W. J. Stark, Chemistry – A European Journal **16,** 8950 (2010).
[46] A.-H. Lu, W. Schmidt, N. Matoussevitch, H. Bönnemann, B. Spliethoff, B. Tesche, E. Bill, W. Kiefer, and F. Schüth, Angewandte Chemie International Edition **43,** 4303 (2004).
[47] Kostedt, J. Drwiega, D. W. Mazyck, S.-W. Lee, W. Sigmund, C.-Y. Wu, and P. Chadik, Environmental Science & Technology **39,** 8052 (2005).
[48] C. Ross, Annual Review of Materials Research **31,** 203 (2001).
[49] N. A. Frey and S. Sun, in *Inorganic Nanoparticles: Synthesis, Applications, and Perspectives* (CRC Press, 2010), p. 33.
[50] E. F. Kneller and R. Hawig, Magnetics, IEEE Transactions on **27,** 3588 (1991).
[51] J.-H. Lee, J.-t. Jang, J.-s. Choi, S. H. Moon, S.-h. Noh, J.-w. Kim, J.-G. Kim, I.-S. Kim, K. I. Park, and J. Cheon, Nat Nano **6,** 418 (2011).
[52] Y. Hou, S. Sun, C. Rong, and J. P. Liu, Applied Physics Letters **91,** 153117 (2007).

Chapter 2 High-Magnetic-Moment Nanoparticles for Alternating Magnetic Field Heating

2.1 Introduction

Thermal energy is highly demanded in various application fields, such as chemical engineering, biomedical treatment, industrial engineering and so on. There has been extensive study on the heat generation by magnetic nanoparticles under a high-frequency alternating magnetic field. In this technique, the conversion of thermal energy is through the magnetic work done on nanoparticles by the alternating magnetic field. This thermal energy can fulfill the demand in different fields. For example, the heat can be used for healing polymeric materials [1]. It can also assist the release of drugs from a thermal-sensitive matrix for cancer therapy [2-3]. Another intensively investigated application is to use the thermal energy directly and locally to treat cancer or other diseases [4-6]. All cells within the proximity to nanoparticles will be heated up while malignant cells cannot endure temperature as high as normal cells do. The viability of them will be greatly reduced, leaving normal cells hardly affected [7]. Because there is a large scope of potential applications for this technique, much attention has been paid to the development of magnetic nanoparticles and optimization of their heating performance [8-11]. The history starts from using mircrometer size magnetic materials under an alternating magnetic field. Nowadays, most researchers use nanoparticles whose size is below 100nm. To use magnetic particles of very small size enables the possibility to provide localized heating

under the excitation of an alternating magnetic field. Successful demonstration of generation of thermal energy by magnetic nanoparticles encourages a burst of research work. Most intensively investigated nanoparticles are oxides and ferrites[12,13]. Some work has been done on FePt[14,15] and Fe[10,16], FeCo(-Au)[17,18] nanoparticles. However, so far there are still only limited choices of available magnetic nanoparticles. Also, it hasn't been clarified yet the criteria of searching for proper magnetic nanoparticles.

This chapter will present investigation of Fe_3Si magnetic nanoparticles for magnetic field heating. Fe_3Si nanoparticles were synthesized with narrow size distribution in gas phase. Magnetic characterization was carried out in combination with an analytical calculation. Our results show that these nanoparticles have both features of high-magnetic-moment and a large dynamic coercivity under an AC magnetic field. Furthermore, we found that the fulfillment of above criteria doesn't guarantee an expected large heat generation. Field dependent magnetic characterization unravels the fact that sufficient switching of magnetic nanoparticles is critical for heat generation. It is highly important to find a match between available AC magnetic field and high-frequency magnetic properties of nanoparticles in order to achieve a large hysteresis loop area.

2.2 Mechanism of High Frequency Magnetic Field induced Heating

Magnetic properties of nanoparticles determine if they are suitable for magnetic field heating. The rate of heat generation is reflected by the area of the hysteresis loop of nanoparticles under the alternating magnetic field. The larger the hysteresis loop area, the

more heat is generated in a conserved system. Hysteresis loops of magnetic particles can be governed by different magnetization reversal mechanisms[19].

Magnetization reversal can take place through physical rotation of particles, namely Brownian motion, when particles are in a low viscous environment. A schematic drawing to illustrate the process can be found in Figure 2.1(a). The time interval for magnetization to switch to the field direction is called relaxation time and is given by

$$\tau_B = \frac{3V\eta}{kT} \quad \text{(Equation 2.1)}$$

where V is the hydrodynamic volume of magnetic nanoparticles. η is viscosity of the solvent, k is Boltzman constant and T is temperature. The Brownian relaxation is not of high interests for heat generation because heat release is very sensitive to the viscosity of surrounding media in this case. The viscosity or relative viscosity is not well-controlled when nanoparticles are used in-vivo. In addition, for a lot of other thermal energy related applications such as polymer healing and drug release, nanoparticles are usually embedded in a matrix where their physical rotation is greatly restricted. It poses difficulty on taking advantage of Brownian motion for heat generation. Therefore, such mechanism is not a main focus here.

Magnetization reversal can also be realized through thermally assisted switching of magnetization across magnetic anisotropy energy barrier E_a (E_a=anisotropy constant K × volume of a particle V). This mechanism is of main interests since it is considered to play a major role for sufficient heat generation practically[19]. Many studies employ superparamagnetic iron oxide nanoparticles. There was some confusion on the heat generation from nanoparticles in superparamagnetic regime. Superparamagnetic

nanoparticles are commonly defined under room temperature in an infinite time window, namely zero frequency. They have zero hysteresis and follow Langevin's law in approach to saturation. Heat release of these particles was not categorized as "hysteresis loss" sometimes. In reality, magnetic heating effect comes from the area of hysteresis loops. A detailed explanation of how superparamagnetic nanoparticles produce hysteresis is given below.

The illustration uses a uniaxial magnetic nanoparticle as the example, which is often true for small particles. Two potential wells corresponding to the free energy minimum defines the direction that magnetic moment will align to. For instance, if we define a magnetic nanoparticle with anisotropy constant K and magnetization M_s oriented at φ=45° with respect to easy axis. The angle between the easy axis and an applied magnetic field is θ. The free energy can be expressed as:

$$E = KV\sin^2\theta - M_s HV\cos(\theta - \varphi) \quad \text{(Equation 2.2)}$$

Two energy minima can be found by taking derivative of Equation 2.2. The energy minima is represented by (θ_1, E_1) and (θ_2, E_2) in Figure 2.1(b). Magnetization switches between the two states as the magnetic field sweeps. In real life there is influence or assistance from thermal agitation. The time needed to cross the anisotropy energy barrier is:

$$\tau_1 = \tau_{01}\exp(\frac{E_3 - E_1}{kT}) \quad \text{(Equation 2.3)}$$

$$\tau_2 = \tau_{02}\exp(\frac{E_3 - E_2}{kT}) \quad \text{(Equation 2.4)}$$

The expressions are valid for coherent rotation and anisotropy energy barrier E_3-E_1, E_3-E_2 larger than thermal energy kT. The probability to find magnetization taking energy state E_1 and E_2 is p_1 and $(1-p_1)$. When there is no magnetic field or a very small magnetic field applied, the two anisotropy energy barriers are equal. The probability changes along with time following:

$$dp_1 = \frac{1-p_1}{\tau}dt - \frac{p_1}{\tau}dt \quad \text{(Equation 2.5)}$$

where τ is the relaxation time that magnetization takes to cross the anisotropy energy barrier. The magnetization at each time point is:

$$M = M_r S_0 \exp(-\frac{t}{\tau}) \quad \text{(Equation 2.6)}$$

When a magnetic field is present and non-negligible, the probability as a function of time becomes:

$$dp_1 = \frac{1-p_1}{\tau_2}dt - \frac{p_1}{\tau_1}dt \quad \text{(Equation 2.7)}$$

where the τ_1 is time for magnetization jumps from the lowest energy minimum to the upper minimum and and τ_2 is time for the revere process.

The magnetization is expressed with respect to time as:

$$M = M_r(\frac{\tau_1-\tau_2}{\tau_1+\tau_2} - (S_0 - \frac{\tau_1-\tau_2}{\tau_1+\tau_2})\exp(-\frac{t}{\tau})),\ \frac{1}{\tau} = \frac{1}{\tau_1} + \frac{1}{\tau_2} \quad \text{(Equation 2.8)}$$

When the magnetic field sweeps slow enough, the time needed to cross the energy barrier is so short that the magnetic moment relaxes to the thermal equilibrium state and aligns with the field at every step. At zero field, we will have $\tau_1 = \tau_2 = \tau$ and $t >> \tau$. There won't be any remanent magnetic moment or hysteresis as a consequence. Superparamagnetism is

observed. However, when the magnetic field sweeps very fast comparable to the time needed to cross the anisotropy energy barrier, hysteresis develops due to the inability to reach thermal equilibrium state. At zero field, a remanent magnetic moment will be observed with $\tau_1=\tau_2=\tau$. Therefore, superparamagnetic nanoparticles can develop hysteresis and generate heat when the magnetic field sweeps fast enough. The relaxation time can be calculated within the scope of a simplified form of Néel model when the magnetic field is so small that Zeeman energy is magnitude of orders smaller than the magnetic anisotropy energy barrier. The expression has a form given by Equation 2.9 where τ_0 is attempt frequency, K is anisotropy constant, V is physical volume of magnetic nanoparticles, k is Boltzman constant and T is temperature.

$$\tau_N = \tau_0 \exp(\frac{KV}{kT}) \quad \text{(Equation 2.9)}$$

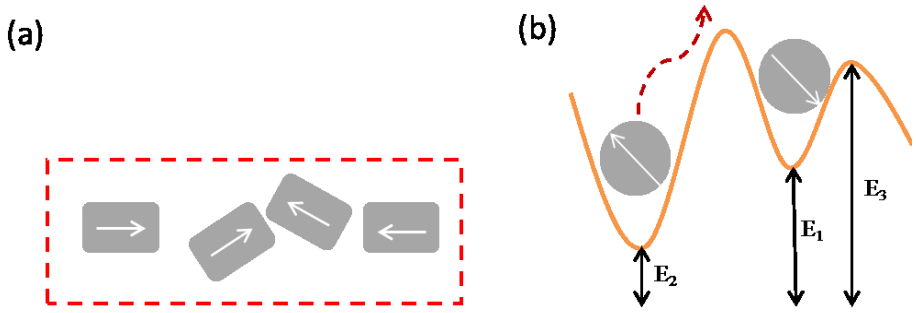

Figure 2.1 Schematic illustration of magnetization reversal through (a) physical motion (b) across magnetic anisotropy barrier

In order to enhance the heat generation, it is essential to increase the area of the loop. On one hand, remanent magnetic moment should be kept high. High-magnetic-moment nanoparticles are therefore preferable. On the other hand, the area of the loop is also related with coercivity. Appealing heating performance has been found on single-domain

magnetic nanoparticles with a relatively large magnetic anisotropy energy barrier recently[17,20-22], which is a result of hysteresis loops with large coercivity under the alternating field. The coercivity is typically larger than that of commonly seen superparamagnetic iron oxide nanoparticles. The magnetic anisotropy energy barrier of these nanoparticles is large and they may not be superparamagnetic. Magnetization reversal under an alternating magnetic field still governs the hysteresis under thermal effects. However, magnetic relaxation time does not satisfy the simplified Néel model. Overall, it is desirable to have nanoparticles with both high magnetic moment and a relatively large magnetic anisotropy energy barrier for a great amount of heat generation.

2.3 Fe_3Si Nanoparticles

2.3.1 Unique Aspects of Fe_3Si

The combination of Fe and Si makes up a material system with near zero environmental impact, low cost, good biocomapitility and great potential in several technological areas. Iron and silicon are two of the most abundant materials on the earth. They are green materials that don't have negative impact on environment. Their wide accessibility makes them easy for industrial commercialization with low cost. What's more, the two elements are low toxic.

According to Fe-Si phase diagram[23], iron silicides have various properties, which have drawn attention in different technological areas. For instance, $FeSi_2$ is semiconductor and is compatible with current IC technology. Ferromagnetic metallic materials like Fe_5Si_3

has interesting effects on enhancing giant magnetoresistance in nanogranular structures[24,25]. One of the most interesting materials in Fe-Si system is Fe_3Si, which has a $D0_3$ ordered crystal structure and is ferromagnetic below 803K[26]. The interest in Fe_3Si initially comes from its similar crystallography structure with Heuslar alloy[27,28]. Usually the Heuslar alloy XY_2Z has $L2_1$ structure with X at (½ , ½, ½) site and Y at (±¼, ±¼, ± ¼) site. If X is replaced by Y, a crystallographically equivalent $D0_3$ structure is derived, which means the possibility to have half-metallic property like the Heuslar alloy XY_2Z [29]. In Figure 2.2, lattice of Fe_3Si with $D0_3$ structure is shown. A unit cell of Fe_3Si is presented as the shaded area. Two different Fe sites are marked out as Fe(1) and Fe(2).

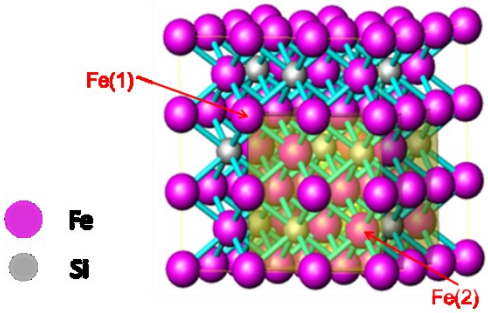

Figure 2.2 Crystal structure of Fe_3Si nanoparticles in ordered $D0_3$ structure. Shaded region is a unit cell of Fe_3Si. Fe(1) and Fe(2) represent two different Fe site, respectively

The possible half-metallic property of Fe_3Si has technical significance. Half metallic materials have a band structure with high density of states for one spin direction near Fermi level while low density of states for the other spin direction. Such band structure indicates a high spin polarization, which is highly desirable for spintronics. Calculations on band structure have been conducted for Fe_3Si and are still under research[30,31]. A small lattice mismatch of Fe_3Si with GaAs and Si provides an advantage for the integration of hybrid structure, where high interface quality can be maintained [32]. Additionally the high

Curie temperature of Fe_3Si makes it applicable in real devices. Spin injection has already been studied based on Fe_3Si/GaAs thin film. Selective substitution of other transitional elements has also been conducted to provide a control of band structure of the material.

Besides the major interests in the physical property of Fe_3Si, the material has potential in magnetic field heating, especially as heating mediators for thermal therapy in biomedicine. The saturation magnetization of Fe_3Si is 800 emu/cm^3 [33,34], higher than that of iron oxide which is commonly used today for biomedicine. The high saturation magnetization means only a small dose of particles is needed to give equal amount of heat. Fe_3Si is magnetically soft with small magnetocrystalline anisotropy. Anisotropy constant has been reported to be $(3.1\pm0.6)*10^4$ ergs/cm^3 for thin films. This is comparable to iron oxide. Overall, Fe_3Si is a promising material for biomedical applications. We will focus on its use as magnetic heating media for generation of thermal energy.

2.3.2 Fabrication of Fe_3Si Nanoparticles in Gas Phase

Fabrication of Fe_3Si has been studied mainly in thin film form by several research groups around the world. Masahiro Miyazaki et al. grew $D0_3$ structure in Fe-Si thin films using RF magnetron sputtering technique[35]. As-sputtered thin films required post annealing to transform into ordered $D0_3$ structure. Jens Herfort et al. used molecular-beam epitaxy (MBE) method to get a Fe_3Si layer on (001) GaAs substrate[36]. However

MBE method is unattractive to industry because of the complex equipment, slow growth process and requirement of special substrates.

In our lab, we are able to fabricate Fe_3Si nanoparticles using a gas condensation method. The method doesn't have limitation on what type of substrate to use and is feasible to control thermal environment directly, as introduced in section 1.2.6. Composite iron-silicon target with atomic composition ratio 3:2 was used. Purities of iron and silicon targets were 99.9% and 99.999%, respectively. A negative voltage was applied to the target, working as the cathode while the chamber was grounded as the anode. The base pressure of the sputtering chamber was about 1×10^{-7} Torr. Ar gas was used as both sputtering gas and carrier gas. In the deposition process, an adjustment of the magnetic field was made to modify the thermal environment for the formation of nanoparticles by placing a soft iron ring and a cone on the surface of the target [37]. The optimal result was given by tuning the strength of the magnetic field and the magnitude of the sputtering current between the anode and cathode.

Both the strength of the magnetic field on the surface of the target and the magnitude of sputtering current has to reach a certain threshold value in order to form the $D0_3$ structure. Phase diagram shows that Fe_3Si phase can exist in a wide composition range at relatively high temperature. The $D0_3$ structure however needs sufficient energy and time for ordering as indicated by the annealing process in thin film fabrication. In other words, sufficient energy supply for relatively long period of time is needed because the ordered structure calls for breaking bonds, redistribution of atoms through diffusion and crystallization. The magnitude of sputtering current determines how much energy can be

provided for ordering. As discussed in section 1.2.6, a high sputtering current indicates that discharge current density is high for a particular sputtering area, thereby Ar ions density is increased. Energetic Ar ions sustain high energy supply through energy transfer by collisions. The magnetic field adjusts the time particles experience with high energy supply. A strong magnetic field confines a large number of electrons by magnetic flux lines in space. The electrons determine how Ar ions, the energy source distribute in space. When the flow speed is not varied much, the strong magnetic field maintains the energy supply over the surface of the target and equivalently for relatively long time.

Electron diffraction was used to characterize whether the formation of $D0_3$ structure takes place by a transmission electron microscope (TEM). Nanoparticles were prepared under different strength of surface magnetic field and sputtering current while the pressure was kept around 450mTorr. Appearance of (111) diffraction ring from stabilized space group $Fm\bar{3}m$ was used to judge whether there is existence of $D0_3$ structure[31], which provides qualitative evidence instead of quantification of the ordering parameter. It has been found that a correlation exists between the appearance of (111) diffraction ring and strength of surface magnetic field as well as sputtering current. The strength of magnetic field was tuned by manipulating the distance between target surface and permanent magnets. When the magnetic field was smaller than 1000 Oe on the surface of the target, we didn't observe any (111) diffraction no matter what current was used (Figure 2.3 (a)(b)). This means that the formation of $D0_3$ structure cannot be promoted with only high current but insufficient time. When the magnetic field was increased to 1200 Oe, the (111) diffraction ring started to appear under 0.5A-0.6A sputtering current

condition (Figure 2.3(d)). Low sputtering current such as 0.3A didn't initiate ordering (Figure 2.3(c)). Therefore, both magnetic field and sputtering current have to meet certain criteria for the $D0_3$ structure to form.

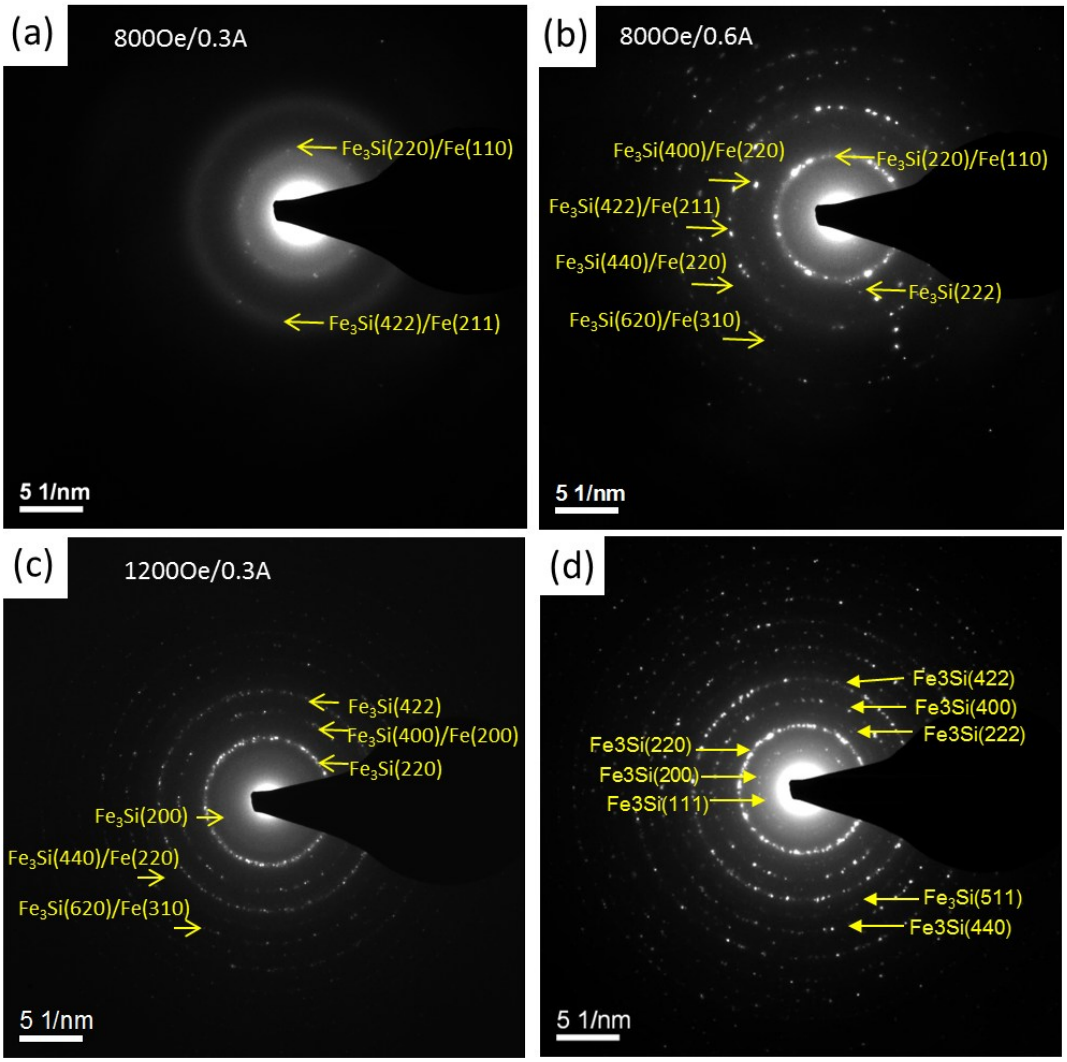

Figure 2.3 Selected area diffraction of Fe_3Si nanoparticles under 800Oe magnetic field and sputtering current of (a) 0.3A (b) 0.5A ; Selected area diffraction under 1200Oe magnetic field and sputtering current of (a)0.3A (b) 0.5A

2.3.3 Characterization of Fe_3Si nanoparticles

Further characterization was performed on nanoparticles fabricated under suitable conditions which led to the formation of $D0_3$ structure. A scheme to transfer nanoparticles into distilled water was employed for preparation of characterization and magnetic field heating experiments. The process is illustrated in Figure 2.4. An aliquot of 400 μL of polyethylene glycol (PEG) solution (15wt% in 3:1 ethanol/H_2O, Mn = 2,000 g/mol) was placed on a glass slide, and spin coated at 3500 rpm for 30s. The coated slides were placed in the deposition chamber as substrates. After deposition, the slides with nanoparticles on were treated with distilled water, and aliquots of water and nanoparticles were collected in glass vials. Sonication was applied to make an evenly dispersed solution.

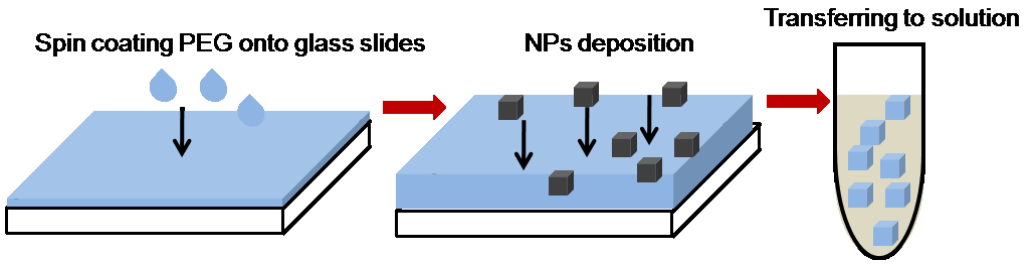

Figure2.4 Scheme of transferring gas-phase-synthesized nanoparticles into water

Drops of Fe_3Si nanoparticle solution were dried on amorphous carbon coated Cu grid. The morphology and crystallinity of Fe_3Si nanoparticles were then characterized by a TEM (FEI, FEG 300keV). Si wafer substrate was used for magnetic measurements. The

temperature dependence of magnetization was measured by a vibrating sample magnetometer (VSM) (Princeton Measurements).

TEM examination was done on both a collection of nanoparticles and a single nanoparticle level. Figure 2.5(a) shows the bright field TEM image of Fe_3Si nanoparticles. Nanoparticles show faceted shape indicating their crystalline state. The contrast between the particle surface and the core part is mainly due to oxidation because the particles are kept in ambient air after deposition. Figure 2.5(b) is the selected area diffraction pattern for an ensemble of Fe_3Si nanoparticles. Good crystallinity was indicated by the discrete diffraction spots originated from the electron beam reflected by certain crystal planes. The diffraction pattern was consistent with that of Fe_3Si phase. The diffraction ring corresponding to (111) plane of Fe_3Si shows up as expected. The mean diameter of the nanoparticles was analyzed by software (DigitalMicrograh, Gatan) and was used to represent the size in later study. Figure 2.5(c) depicts the histogram of the size of nanoparticles. The mean size is about 17.0 nm with 13% standard deviation. High resolution TEM (HRTEM) was conducted to explore the structural information of Fe_3Si nanoparticles. As shown in Figure 2.5(d), d spacing of 2.8 Å corresponding to Fe_3Si (200) was found through the HRTEM characterization. Energy dispersive X-ray spectroscopy (EDX) analysis was done on TEM equipped with an EDX detector. Composition analysis was taken from a large area in which hundreds of particles were included. Atomic composition ratio is approximately 3:1 which agrees with the phase of Fe_3Si. X-ray diffraction scan was also performed on a selective sample directly deposited on a substrate. A small peak corresponding to Fe_3Si (111) was observed. It further

confirms the emergence of $D0_3$ crystal structure. Diffraction peaks from Fe_2O_3 were also observed, a sign of imperfection caused by oxidation. Above characterizations provide the proof of the formation of well-crystallized Fe_3Si particles with uniform size.

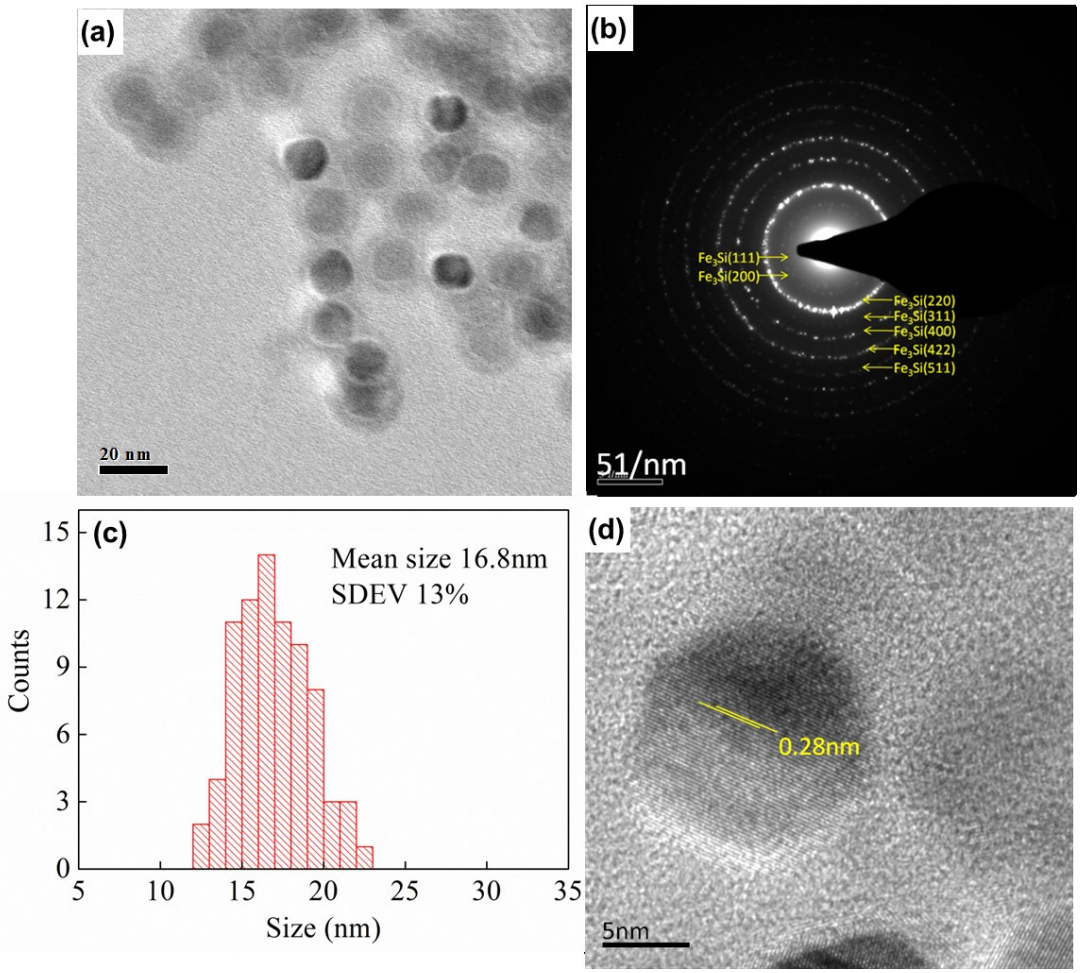

Figure 2.5 (a) Bright field TEM image of Fe_3Si nanoparticles (b) High resolution TEM image of a single Fe_3Si nanoparticle

Curie temperature provides another evidence of the phase of the sample. The measurement was conducted using VSM with 1 T constant applied field. The sample was

kept in saturation status. It is shown in Figure 2.6 that the magnetic moment decreases with the increase of temperature. At approximately 800K, a transition point could be observed as indicated by the curvature change. This point corresponds to the Curie temperature (803K) of Fe_3Si[38].The other transition point possibly comes from the residual magnetic moment of oxidized surface of the nanoparticles.

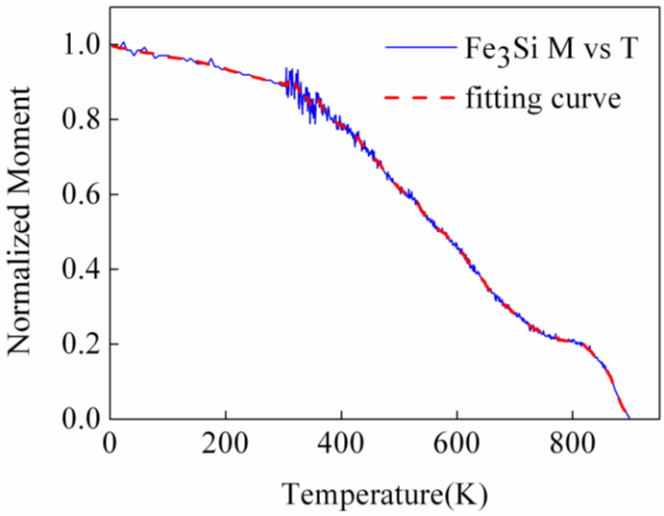

Figure 2.6 Normalized magnetic moment versus temperature of Fe_3Si NPs

2.4 AC Magnetic Field Heating of Fe_3Si Nanoparticles

2.4.1 Analysis of Heating Performance

Subsequently magnetic properties were analyzed to evaluate the performance of Fe_3Si nanoparticles for alternating magnetic field heating. Specifically, interests were on saturation magnetization and coercivity of Fe_3Si nanoparticles under the magnetic field, namely dynamic coercivity. In principle, the dynamic coercivity is affected by either the temperature at which a magnetic field is applied, or the frequency of the magnetic field. The investigation method used here incorporates a temperature dependent magnetic

measurement and an analytical calculation of dynamic coercivity as a function of frequency. The method is convenient to use in reality and provides an indication of the heating performance of nanoparticles under high frequency.

Magnetic parameters of Fe_3Si nanoparticles were obtained through hysteresis loops and promising saturation magnetization was found. A SQUID magnetometer (Quantum Design) was used to investigate the temperature dependence of hysteresis loops within 5K-300K range. Hysteresis loops were measured with maximum applied field of 1T at different temperatures, from which coercivity values were determined at each temperature. For randomly distributed nanoparticles, its coercivity (H_c) decreases linearly with $T^{2/3}$ as described by Equation 2.10 [39].

$$H_c(t) = H_0\{1-[\frac{kT}{KV}\ln(\frac{f_0 t}{0.693})]^{0.67}\} \qquad \text{(Equation 2.10)}$$

where k is Boltzman constant, f_0 is $1.0*10^9$ Hz and t is experimental time. The ratio of remanent magnetic moment to total moment is around 0.42 at 5K, which is slightly lower than 0.5 of an ideal non-interacting case. This indicates that some of the nanoparticles might be magnetically coupled. However, it has been shown by Lacroix et. al that this coercivity-temperature relationship could still be valid to estimate magnetic parameters of weakly coupled nanoparticles for a simplified situation [17]. Here it is also reasonably assumed that there is no temperature dependence of magnetic anisotropy energy barrier E_a=KV. Because the magnetic property has temperature dependence in general, the obtained value of magnetization and anisotropy constant could have small discrepancy

from the exact value in practice. Figure 2.7(a) presents both the experimental data and the fitting curve of the coercivity with respect to temperature based on Equation 2.10. Coercivity at absolute zero Kelvin was first extrapolated from the data: H_0 = 222.7Oe. Second, from the slope of the curve, the magnetic anisotropy energy barrier E_a was found to be 0.635eV for Fe_3Si nanoparticles. The saturation magnetization was found to be 961emu/cm^3 (133.5emu/g), which is close to the reported value of Fe_3Si thin film [33,34]. A comparison is made between Fe_3Si and other common magnetic materials in terms of saturation magnetization in Table 2.1. As listed Fe_3Si has higher saturation magnetization than that of magnetite and other kind of ferrite oxides. This means that Fe_3Si nanoparticles have high-magnetic-moment and their loops can have high remanent magnetic moment under an alternating magnetic field.

Table 2.1 Saturation magnetization of selected magnetic materials

Materials	Fe_3O_4[40]	γFe_2O_3[13]	Fe_2CoO_4[41]	Fe_2MnO_4[41]	$Fe_2Mn_{0.5}Zn_{0.5}O_4$[42]	Fe[40]	Fe_3Si
Ms(emu/g)	84	57	60.4	32-52	47	220	133.5

Dynamic coercivity was calculated to examine whether large hysteresis can be generated under an alternating magnetic field. The analytical calculation was performed with different sweep rates of the field based on Equation 2.10. Experimentally obtained H_0 and E_a values were used. The alternating magnetic field was assumed to be a sinusoidal function and time t was considered to be the inverse of the sweep rate of the field. Figure 2.7(b) shows the dynamic coercivity value under the magnetic field of different frequencies. Coercivity increases exponentially along with the increase of

frequency initially. The increase of coercivity gradually slows down and finally the coercivity value saturates to the maximum value H_0 when approaching to the infinitely high frequency. In kHz frequency range (100kHz-400kHz), a relatively large dynamic coercivity value (140Oe-180Oe) is observed from the calculated curve if the nanoparticles can be saturated by the magnetic field. Recently, rigorous models have been proposed for the magnetic behavior of nanoparticles under an AC magnetic field [19,43]. An expression given by J. Carrey et al. incorporates real AC magnetic field parameters for the calculation of the dynamic coercivity for randomly distributed nanoparticles[19]. The dynamic coercivity of Fe_3Si nanoparticles was also calculated by using the model proposed by J. Carrey and applying the same parameters above. Figure 3.8 displays the calculated curve with the equation and parameters listed. The calculation showed similar trend of the change of the dynamic coercivity with respect to the field frequency. The dynamic coercivity was 151Oe-165Oe in 100kHz-400kHz range. With only 10Oe-15Oe discrepancy between the two approaches, it is safe to assume that the dynamic coercivity of Fe_3Si nanoparticles is close to 150 Oe at the frequency range. Thus Fe_3Si nanoparticles are able to generate appreciable area of hysteresis loops based on the indication of their dynamic coercivity. It can be concluded from the analysis above that Fe_3Si nanoparticles have high-magnetic-moment and relatively large dynamic coercivity. Their magnetic properties are proper to generate a desirable amount of heat in the kHz frequency range.

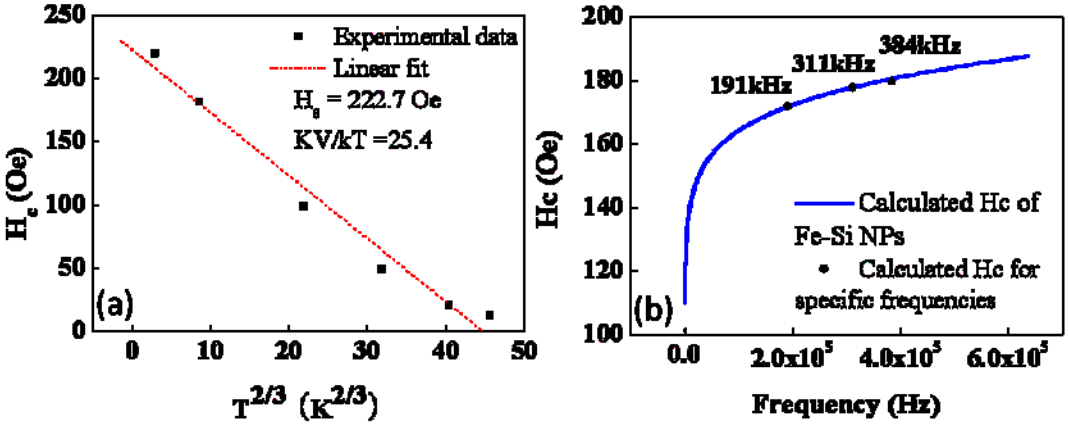

Figure 2.7 (a) Temperature dependence of H_c of Fe_3Si nanoparticles; (b) Calculated H_c versus frequency of Fe_3Si nanoparticles

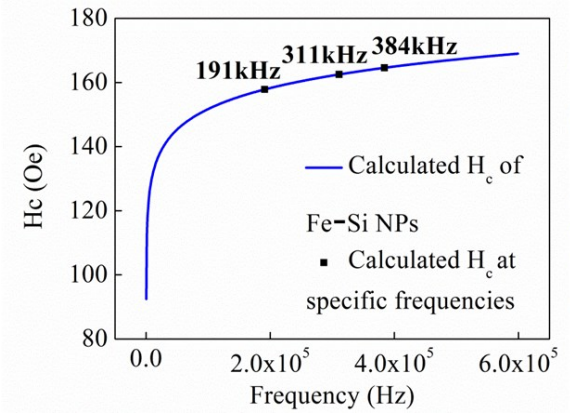

$$H_c = 0.48\mu_0 H_K\left(1-\left(\frac{kT}{KV}\ln\left(\frac{kT}{4\mu_0 H_{max} M_s V f \tau_0}\right)\right)^{0.8}\right)$$

$$0.48\mu_0 H_K = 2.227\times10^{-2} T$$

$$\frac{kT}{KV} = \frac{1}{25.4}$$

$$\mu_0 H_{max} = 0.005T$$

$$M_s = 961000\ A/m$$

$$K = 2.14\times10^4\ J/m^3$$

Figure 2.8 Calculated H_c versus frequency of Fe_3Si nanoparticles based on model by J. Carrey et al

A reference sample of commercial Fe_3O_4 nanoparticles was also analyzed in the same way that was applied for Fe_3Si. Figure 2.9(a) presents temperature dependence of coercivity. The fitting based on Equation 2.10 gave H_0 = 161.2Oe and E_a=0.15eV for Fe_3O_4. Calculated dynamic coercivity shows that Fe_3O_4 nanoparticles possess small coercivity (40Oe-95Oe) below 400kHz frequency range (Figure 2.9(b)). Compared to

Fe_3Si, Fe_3O_4 nanoparticles have low magnetic moment and relatively small dynamic coercivity.

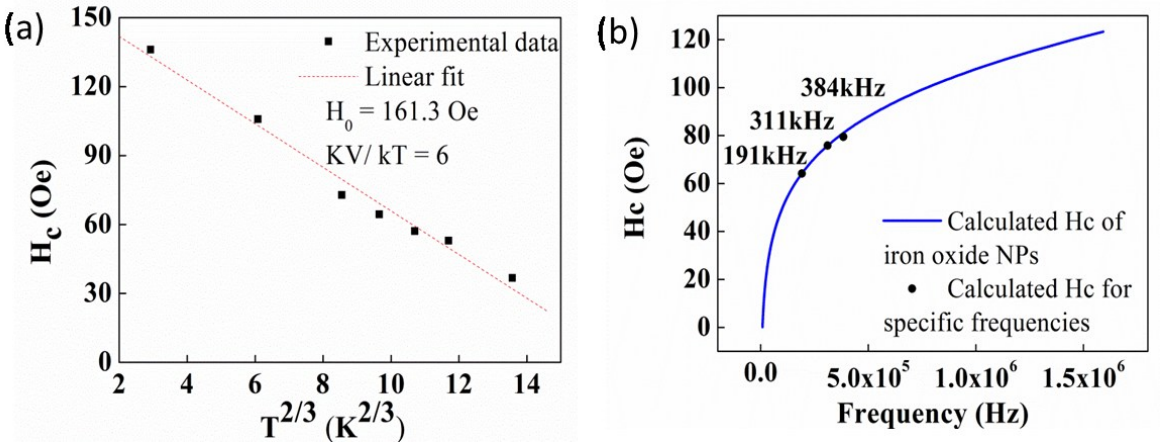

Figure 2.9 Temperature dependence of H_c of (a) Fe_3O_4 nanoparticles; (b) Calculated H_c versus frequency of Fe_3Si nanoparticles

2.4.2 Heating Experiments

Magnetic field heating was performed with an induction coil system which has about 40 Oe-50 Oe maximum field strength at frequencies: 191kHz, 311kHz and 384kHz. The strength of the magnetic field was determined by a pick-up coil. Different capacitors were applied to change the frequency of the magnetic field. Temperature of water solution of Fe_3Si nanoparticles was monitored by a fluoroptic thermometry system (Luxtron 3100, Lumasense Technologies) connected to a computer.

Fe_3Si nanoparticles suspended in distilled water (0.038g/ml) were subjected to the alternating magnetic field. Figure 2.10(a) displays the temperature rise with respect to time at different frequencies after deduction of room temperature background. Specific loss power (SLP) per cycle was calculated using the equation below

$$P = \frac{m_{fluid}}{m_{particle}} \frac{dT}{dt} c \text{, (Equation 2.11)}$$

where m represents either the mass of the fluid or the mass of nanoparticles, $\frac{dT}{dt}$ is the initial slope of the curve of temperature rise, c is the heat capacity of water (4.187 J/g/K) and f is the field frequency. The SLP per magnetic field cycle is shown in Figure 2.10(b) as well as the total SLP at three different frequency conditions, which were all obtained according to the data in Figure 2.10(a). The small amount of heat is not consistent with the magnetic properties of Fe_3Si nanoparticles we already probed at the first glance. Especially if we compare it with total SLP of commercial Fe_3O_4 (30g/ml) obtained in the same way and depicted in Figure 2.10(d). SLP of Fe_3O_4 nanoparticles is 2-3 times of that of Fe_3Si nanoparticles. This again cannot be explained simply viewing the dynamic coercivity and magnetic moment values. The observation actually reflects an important aspect of nanoparticles with high-magnetic-moment and relatively large dynamic coercivity to be used as future magnetic heating media.

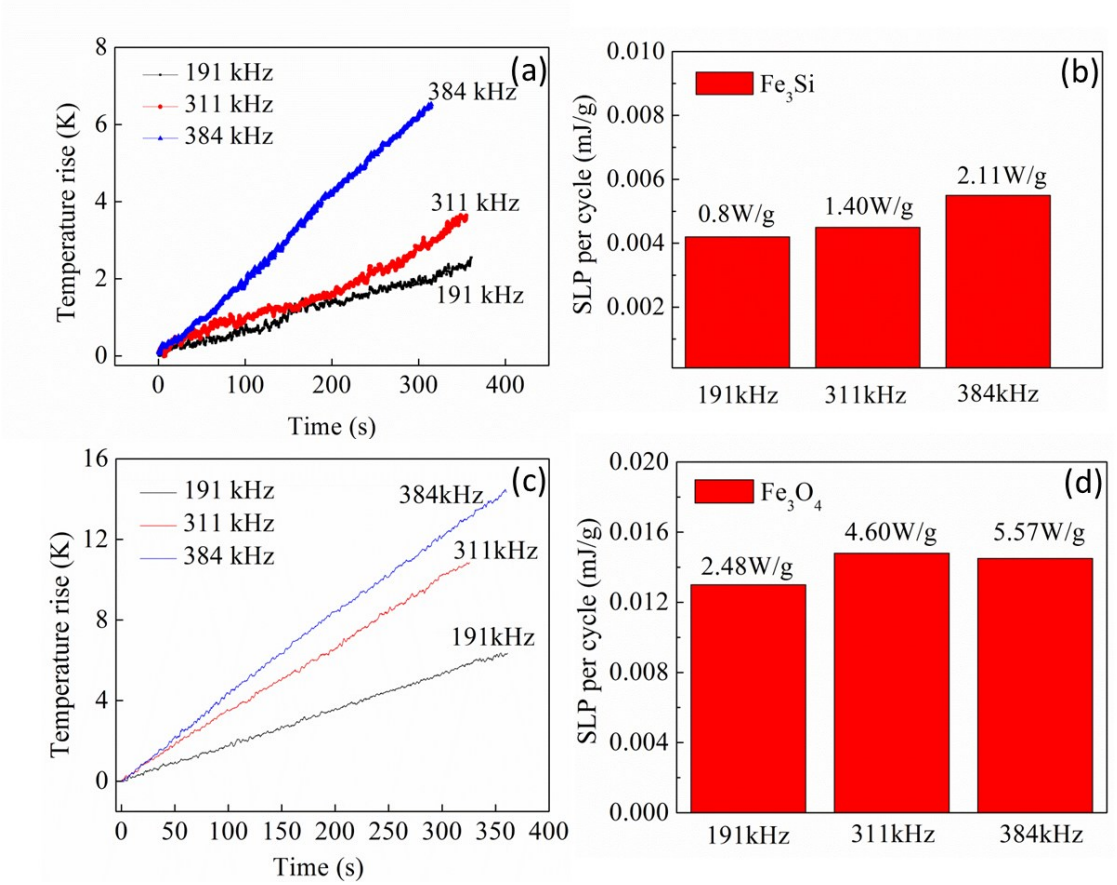

Figure 2.10 (a) Temperature rise with respect to time of Fe_3Si under AC magnetic field (b) SLP per cycle of Fe_3Si obtained from AC magnetic field heating (c) Temperature rise with respect to time of Fe_3O_4 under AC magnetic field (d) SLP per cycle of Fe_3O_4 obtained from AC magnetic field heating

2.4.3 Optimization of Heat Generation

To explain the observation, minor hysteresis loops were measured by SQUID under different maximum magnetic fields at 80K. At this low temperature, the saturated hysteresis loop has a coercivity value of about 130Oe for Fe_3Si nanoparticles and 75Oe for Fe_3O_4. Nanoparticles develop similarly large dynamic coercivity under high frequency magnetic field at room temperature. The area of minor hysteresis loop is very

small under the 50Oe maximum field as seen in Figure 2.11(a) for Fe_3Si. The area was expressed in terms of energy density as marked in the figure. Minor hysteresis loops were also measured at an increased temperature under which saturated loops have smaller coercivity than 130Oe. However, as long as the maximum field amplitude is not approaching the coercivity, there is only little hysteresis loop area. When the maximum magnetic field increases to a high value, for example 300Oe, a large growth of minor hysteresis loop area can be seen. Fe_3O_4 nanoparticles shows similar behavior except that they have larger area of minor hysteresis loop at small field and much smaller area at large field than that of Fe_3Si. Because Fe_3O_4 has a small dynamic coercivity, there is a high possibility for the particles to switch and generate heat compared to Fe_3Si under a small applied field. It is why larger SLP was observed for Fe_3O_4 than Fe_3Si even though the latter has better magnetic properties.

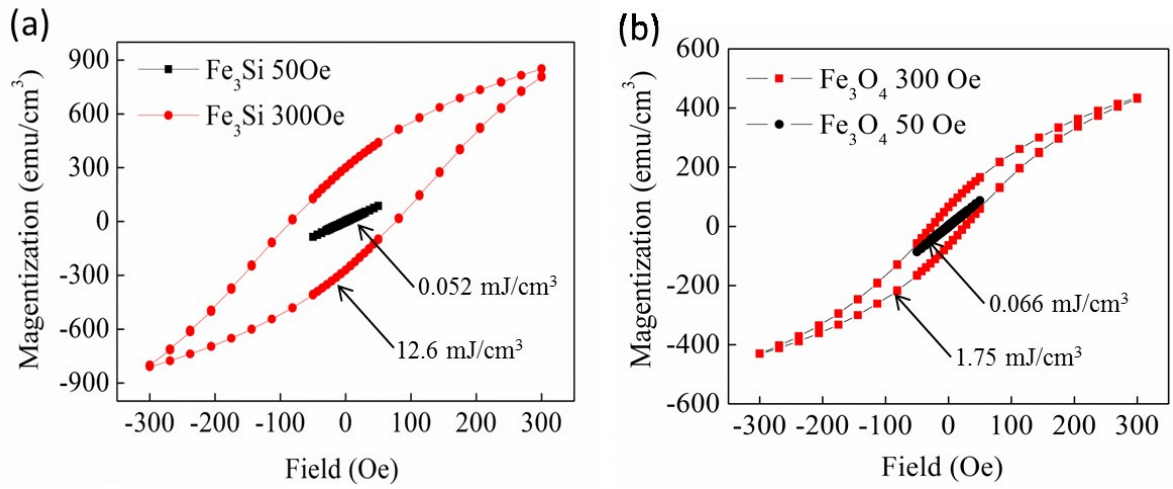

Figure 2.11 Minor hysteresis loops of (a) Fe_3Si and (b) Fe_3O_4 at 50Oe and 300Oe maximum field amplitude

A summary of integrated area of hysteresis loop is shown in Figure 2.12 for both Fe_3Si and Fe_3O_4. A substantial growth is suggested when the maximum magnetic field is larger than the coercivity of Fe_3Si. The field dependence clarifies the result of much less heat generated from Fe_3Si nanoparticles than expected. It is mainly due to an insufficient magnetization reversal of nanoparticles caused by the situation that maximum magnetic field generated by the coil is much smaller than their dynamic coercivity. Under such circumstance, neither high-magnetic-moment nor large magnetic anisotropy energy barrier can bring in significant contribution to the hysteresis area even though these properties are expected to be beneficial. It is clear that the heat generation depends not only on the magnetic properties of the high-magnetic-moment nanoparticles, but also on how efficiently the magnetic field can switch the nanoparticles.

By looking at the shape of minor hysteresis loops under a large magnetic field in Figure 2.11, it can be found that profound non-linearity develops when magnetic field amplitude and dynamic coercivity are comparable. It indicates that when the magnetic field is far smaller than dynamic coercivity, particles work in a linear heating regime. Change of magnetic moment with respect to the field can be approximated by a collinear relationship. When magnetic field is approaching the dynamic coercivity, the increase of nonlinearity can induce the increase of the area of hysteresis loops. It is thus desirable to work in the non-linear regime for an efficient generation of heat. The comparison between Fe_3Si and Fe_3O_4 reveal different field dependence of hysteresis in Figure 2.12. A steep rise of hysteresis area can be seen for Fe_3Si when they start to work in non-linear regime under a magnetic field larger than the dynamic coercivity. Hysteresis area of

Fe_3O_4 follows a power law where it continues to grow in an almost constant rate. The difference indicates that for nanoparticles with relatively large magnetic anisotropy energy barrier, heating performance is more sensitive to the amplitude of magnetic field. The sensitivity arises from the low probability to switch through thermal agitation. In conclusion, it requires a careful choice of the magnetic field parameters to avoid any great suppression of the anticipated heating performance and bring nanoparticles to non-linear regime. This is especially true for nanoparticles with relatively large magnetic anisotropy energy barrier. High-magnetic-moment nanoaprticles with relatively large magnetic energy barrier is a good candidate to work with due to the capability to provide large hysteresis area in the non-linear regime.

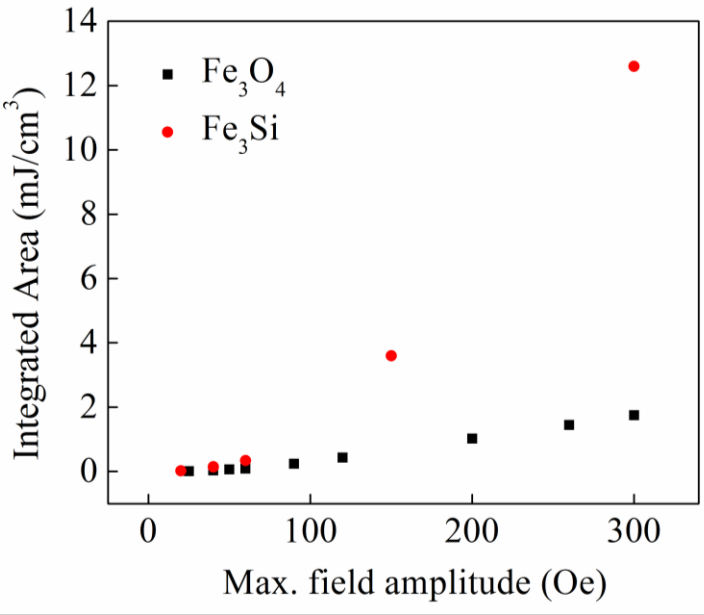

Figure 2.12 Integrated loop area determined from minor loops under different maximum magnetic field

Combined with all the information above, there should be an optimal design point for the alternating magnetic field. For these Fe_3Si nanoparticles, a proper working condition

should be an alternating magnetic field with amplitude over 150Oe and frequency over 100kHz. Such a condition can bring nanoparticles to non-linear heating regime. Magnetic field heating was not conducted under these conditions because of limitations of our instrument. Fulfillment of suitable magnetic field conditions is possibly the main reason for reported successful demonstration of high-magnetic-moment nanoparticles with relatively large magnetic barrier energy[10,17].

2.5 Conclusions

We discussed generation of heat using magnetic nanoparticles. Magnetization reversal across magnetic anisotropy barrier is the practical process to use for the production of thermal energy. Suitable nanoparticles should be able to generate sufficient hysteresis area. Fe_3Si nanoparticless were synthesized by a physical gas condensation method. It was found that these nanoparticles have high saturation magnetization and relatively large magnetic anisotropy energy barrier. The intrinsic magnetic properties of Fe_3Si nanoparticles fall into the potential range for high frequency magnetic field heating. However, it's not necessary to realize the promising heat generation even though the magnetic properties show advantages. This was explained by looking into the minor loops under different field amplitude. Successful application of this type of nanoparticles requires them to work under a magnetic field condition capable of sufficient excitation to switch nanoparticles, namely magnetic field strength larger than dynamic coercivity of nanoparticles. Suitable working condition was predicted to be over 150Oe magnetic field amplitude and 100kHz frequency for the Fe_3Si nanoparticles.

References

[1] C. C. Corten and M. W. Urban, Advanced Materials **21,** 5011 (2009).

[2] C. Sun, J. S. H. Lee, and M. Zhang, Advanced Drug Delivery Reviews **60,** 1252 (2008).

[3] S.-H. Huang and R.-S. Juang, Journal of Nanoparticle Research **13,** 4411 (2011).

[4] R. M. R. K. Gilchrist, W.D. Shorey, R.C. Hanselman, J.C. Parrot and C.B. Taylor, Ann Surg. **161,** 890 (1957).

[5] R. Sharma and C. Chen, Journal of Nanoparticle Research **11,** 671 (2009).

[6] R. Hergt, S. Dutz, R. Müller, and M. Zeisberger, Journal of Physics: Condensed Matter **18,** S2919 (2006).

[7] W. A. a. H. Nowak, *Magnetism in Medicine* (Wiley-VCH, Weinheim, 2007).

[8] C. G. Hadjipanayis, M. J. Bonder, S. Balakrishnan, X. Wang, H. Mao, and G. C. Hadjipanayis, Small **4,** 1925 (2008).

[9] J.-H. Lee, J.-t. Jang, J.-s. Choi, S. H. Moon, S.-h. Noh, J.-w. Kim, J.-G. Kim, I.-S. Kim, K. I. Park, and J. Cheon, Nat Nano **6,** 418 (2011).

[10] B. Mehdaoui, A. Meffre, J. Carrey, S. Lachaize, L.-M. Lacroix, M. Gougeon, B. Chaudret, and M. Respaud, Advanced Functional Materials **21,** 4573 (2011).

[11] T.-Y. Liu, S.-H. Hu, D.-M. Liu, S.-Y. Chen, and I. W. Chen, Nano Today **4,** 52 (2009).

[12] P. Guardia, R. Di Corato, L. Lartigue, C. Wilhelm, A. Espinosa, M. Garcia-Hernandez, F. Gazeau, L. Manna, and T. Pellegrino, ACS Nano **6,** 3080 (2012).

[13] J.-P. Fortin, C. Wilhelm, J. Servais, C. Ménager, J.-C. Bacri, and F. Gazeau, Journal of the American Chemical Society **129,** 2628 (2007).

[14] M. S. S. a. V. S. a. P. D. a. S. N. a. Y. Y. C. a. C. L. C. a. S. W. C. a. C. C. Chen, Journal of Physics D: Applied Physics **43,** 145002 (2010).

[15] S. Maenosono and S. Saita, Magnetics, IEEE Transactions on **42,** 1638 (2006).

[16] C. Martinez-Boubeta, K. Simeonidis, D. Serantes, I. Conde-Leborán, I. Kazakis, G. Stefanou, L. Peña, R. Galceran, L. Balcells, C. Monty, D. Baldomir, M. Mitrakas, and M. Angelakeris, Advanced Functional Materials**,** n/a (2012).

[17] L. M. Lacroix, R. B. Malaki, J. Carrey, S. Lachaize, M. Respaud, G. F. Goya, and B. Chaudret, Journal of Applied Physics **105,** 023911 (2009).

[18] T. L. Kline, Y.-H. Xu, Y. Jing, and J.-P. Wang, Journal of Magnetism and Magnetic Materials **321,** 1525 (2009).

[19] J. Carrey, B. Mehdaoui, and M. Respaud, Journal of Applied Physics **109,** 083921 (2011).

[20] R. Hergt, R. Hiergeist, M. Zeisberger, D. Schüler, U. Heyen, I. Hilger, and W. A. Kaiser, Journal of Magnetism and Magnetic Materials **293,** 80 (2005).

[21] Y. Jing, H. Sohn, T. Kline, R. H. Victora, and J.-P. Wang, Journal of Applied Physics **105,** 07B305 (2009).

[22] E. Kita, T. Oda, T. Kayano, S. Sato, M. Minagawa, H. Yanagihara, M. Kishimoto, C. Mitsumata, S. Hashimoto, K. Yamada, and N. Ohkohchi, Journal of Physics D: Applied Physics **43,** 474011 (2010).
[23] O. Kubaschewski, ASM Handbooks Online (2004).
[24] J. H. a. D. Spišák, Phys. Rev. B **75** (2007).
[25] Y. P. L. Y. V. Kudryavtsey, J. Dubowik, J. Y. Rhee, Phys. Rev. B **68** (2003).
[26] M. R. A. Kawaharazuka, J. Herfort, H. –P. Schönherr, H. Kostial and K. H. Ploog, Appl. Phys. Lett. **85** (2004).
[27] D. N. T. Yoshitake, T. Ogawa, M. Itakura, N. Kuwano, Y. Tomokiyo, T. Kajiwara, K. Nagayama, Appl. Phys. Lett. **86** (2005).
[28] M. T. Ryosho Nakane, and Satoshi Sugahara, Appl. Phys. Lett. **89** (2006).
[29] F. Gazeau, M. Lévy, and C. Wilhelm, Nanomedicine **3,** 831 (2008).
[30] D. F. N. I. Kulikov, J. Hugel and A. V. Postnikov, Phys. Rev. B **66** (2002).
[31] S. K. A. Bansil, P. E. Mijnarends and J. Tobola, Phys. Rev. B **60** (1999).
[32] B. Daniel Kmiec, Marcel Sladecek, Marcus Rennhofer, Svetoslav Stankov, Gero Vogl, Bart Laenens, Johan Meersschaut, Tomasz Ślęzak and Marcin Zając, Phys. Rev. B **75** (2007).
[33] T. Y. D. Nakagauchi, K. Nagayama, Vaccum **74,** 653 (2004).
[34] S. K. Kensuke Akiyama, Teiko Kadowaki, Yasuo Hirabayashi and Hiroshi Funakubo, Jap. J. Appl. Phys **47** (2008).
[35] M. I. Masahiro Miyazaki, Takayuki Komatsu, and Kazumasa Matusita, J. Appl. Phys **71** (1992).
[36] P. K. M. J. Herfort, K. –J. Friedland, H. –P. Schönherr, K. H. Ploog, J. Magn. Magn. Mater. **310** (2007).
[37] J.-M. Qiu and J.-P. Wang, Applied Physics Letters **88,** 192505 (2006).
[38] A. Ionescu, C. A. F. Vaz, T. Trypiniotis, C. M. Gürtler, H. García-Miquel, J. A. C. Bland, M. E. Vickers, R. M. Dalgliesh, S. Langridge, Y. Bugoslavsky, Y. Miyoshi, L. F. Cohen, and K. R. A. Ziebeck, Physical Review B **71,** 094401 (2005).
[39] M. P. Sharrock, Journal of Applied Physics **76,** 6413 (1994).
[40] R. C. O'Handley, *Modern Magnetic Materials - Principles and Applications* (JOHN WILEY AND SONS LTD 1999).
[41] K. Dong-Hyun, Y. T. Thai, D. E. Nikles, and C. S. Brazel, Magnetics, IEEE Transactions on **45,** 64 (2009).
[42] M. Jeun, S. J. Moon, H. Kobayashi, H. Y. Shin, A. Tomitaka, Y. J. Kim, Y. Takemura, S. H. Paek, K. H. Park, K.-W. Chung, and S. Bae, Applied Physics Letters **96,** 202511 (2010).
[43] N. A. Usov, Journal of Applied Physics **107,** 123909 (2010).

Chapter 3 Biocompatible Nanoparticles with Adjustable Self-Regulation of Temperature for Medical Applications

3.1 Introduction

The advancing nanotechnology is in the hope to bring revolutions on medical diagnosis and treatment, such as for cancerous diseases. While diagnosis technology provides quick response with high sensitivity, advanced therapies have been investigated to assist or replace conventional ones, in order to reduce severe side effects due to the non-localized nature. Thermal energy has been realized as an important tool for medical treatment[1]. On one hand, the thermal energy can directly destroy malignant cells which have weak endurance to high temperature[2]. On the other hand, it can assist the release of drug from temperature-sensitive carriers. The latter one is considered to be a more practical and efficient therapy than the prior one[3]. Delivering thermal energy locally overcomes the drawbacks of conventional therapies by exposing only the disease region to drugs for instance. Magnetic nanoparticles enable such delivery of thermal energy when they are triggered by an alternating magnetic field[4]. Magnetic work can convert to heat and gives rise to an increase of local temperature. Deep penetration of the magnetic field into tissues gives advantages of the magnetic way compared to delivery of heat using optical laser.

Ideally it is expected to work in a designed temperature range which won't cause a significant influence on normal cells. Nevertheless, it was found that nanoparticles can induce more than 15°C increase in a short time on cell surface[5]. Traditional thermal sensors face difficulty to adapt with small space deep in the body and map temperature profile. Huang et. al. showed that fluorophore tags on the surface of magnetite nanoparticles can probe local temperature cleverly[5]. However, the method involves additional labeling procedure and complicated photophysical process. The lack of an effective way to monitor the change of temperature puts challenges on controllable operation. It is neither convenient nor safe to rely on manual manipulation of external electrical power. To address the inconvenience and the risk, it is desirable to use "smart" nanoparticles that can regulate generation of heat by themselves. Due to the temperature dependent magnetic properties, magnetic materials are not able to generate heat when ferromagnetism disappears at the critical temperature, Curie temperature (T_c). In other words, the heating automatically slows down when approaching T_c and will totally cease once T_c is reached. Magnetic nanoparticles with T_c close to the safe temperature range are therefore candidates that people are chasing for.

In this chapter, we will present how we approach the functional material with intrinsic temperature regulation in Fe-Si material system. Analytical calculations are to be shown to illustrate how temperature dependent magnetic properties affect generation of heat. Experimentally, Fe-Si nanoparticles were synthesized and characterized in consideration of both the physical engineering and biomaterial engineering aspects.

3.2 Analytical Calculation of Heat Generation with Temperature Dependent Magnetic Properties

It is essential to have an idea of how temperature dependent magnetic properties of nanoparticles play a role in heat generation under an alternating magnetic field. The low T_c materials have been discussed mainly in the context of vanishing of magnetic moment. Another important aspect that has rarely been paid attention to is that magnetic anisotropy of nanoparticles is also a function of temperature and can be even more sensitive to temperature than that of magnetization. It has great influence on the self-regulated heat generation because the heating efficiency is closely related to anisotropy. Considering the sensitivity of anisotropy to temperature, a decay of heat generation could happen before the temperature reaches T_c. That is to say nanoparticles with low T_c provide self-regulated thermal therapies owing to the combined contribution of magnetization and anisotropy. It is thus of importance to pay attention to both temperature dependence of magnetization and anisotropy. Analytical calculations of heat generation were performed to explore their influences. Both linear working regime and non-linear working regime have been investigated for heat generation.

3.2.1 Mean Field Analytical M-T/K-T

Before performing calculation of heat generation, temperature dependence of magnetic properties was first established analytically in known systems. Change of saturation magnetization can be analytically expressed by Equation 3.1:

$$M(T) = M_0 \left[\frac{\left(\frac{M(T)}{M_0} + \frac{H}{NM_0} \right)}{\frac{T}{T_c}} \right] \quad \text{(Equation 3.1)}$$

where M_0 is the magnetization at zero Kelvin, and N is the molecular field constant (10^7), H is the external applied field (1T). This equation is a phenomenological mean-field expression. It cannot be used to predict transition temperature, but it has been applied for extrapolation and fitting of materials with known property with ease to handle practically [6]. The trend of magnetization change given by this equation is also applicable for most of metal materials. Therefore, we can perform analytical calculation of temperature dependence of magnetization on materials with high and low T_c.

Table 3.1 Material parameters used in calculations

	Parameters
T_c	385K
Saturation Magnetization	597 emu/cm^3
Anisotropy Constant	1.5e^5 ergs/cm^3
Mass Density	6.7 g/cm^3

Temperature dependence of anisotropy can be described by a function of change of magnetization[7]. We can estimate the change of anisotropy based on the calculated magnetization–temperature curves. Since we are mostly interested in the high temperature range, here we only take part of the magnetization-temperature curve starting from room temperature 298K. All curves were normalized to the room temperature value.

Anisotropy constant was calculated according to the power law for uniaxial anisotropic materials:

$$\frac{K(T)}{K(0)} = \left(\frac{M(T)}{M(0)}\right)^3 \quad \text{(Equation 3.2)}$$

Figure 3.1 shows both magnetization and the corresponding anisotropy as a function of temperature. As expected, there is a quicker decay of anisotropy than that of magnetization as the temperature approaches to T_c.

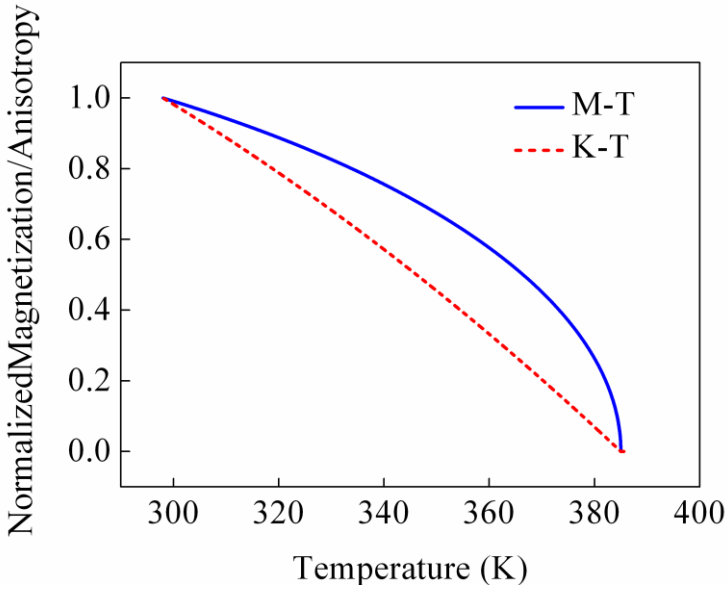

Figure 3.1 Analytically calculated temperature dependence of magnetization and anisotropy

3.2.2 Linear Theory Regime

With the information of temperature dependence of magnetization and anisotropy, hysteresis loss can be calculated by taking into account temperature dependent magnetic properties. The calculation was first conducted using the linear theory, in which magnetic

field is much smaller than dynamic coercivity of nanoparticles under particular frequency and the response of nanoparticles is in the linear regime.

The relationship of magnetization and magnetic field can be expressed through a co-linear function in this regime. Complex susceptibility χ' connects magnetization and magnetic field together as in Equation 3.3:

$$M = \chi' H = \chi_0 \frac{1}{1 + i\varpi\tau} H \quad \text{(Equation 3.3)}$$

where ω and τ are radius frequency of the magnetic field and the relaxation time of magnetic nanoparticles, respectively. Static susceptibility χ_0 is the initial susceptibility in the form of $\chi_0 = \frac{\mu_0 M_s{}^2 V}{3kT}$ (Equation 3.4)

Equation 3.3 tells us that the difference between magnetization and magnetic field can be mathematically expressed by amplitude and phase. If a magnetic field is a cosine function of time as expressed in Equation 3.5, magnetization then has a phase angle with respect to the field and possesses different amplitude as described by Equation 3.6.

$$H = H_0 \cos(\varpi t) \quad \text{(Equation 3.5)}$$

$$M = |\chi| H_0 \cos(\varpi t + \phi) \quad \text{(Equation 3.6)}$$

The above two equations are in fact the mathematical description of an ellipse in two dimensional plane. The enclosed geometrical area therefore represents hysteresis of magnetic nanoparticles. The geometrical area or hysteresis can be calculated through integration of magnetization over magnetic field. The geometrical area of an ellipse has a formula of $S = \pi ab$, where a and b are one-half of the ellipse's major and minor axes

respectively. Based on Equation 3.3, magnitude of χ and angle φ as a function of ω and τ are shown by Equation 3.7.

$$|\chi| = \frac{\chi_0}{\sqrt{1+\varpi^2\tau^2}} \qquad \tan\phi = -\varpi\tau \quad \text{(Equation 3.7)}$$

Hysteresis loss after integration is in the form of

$$S = \oint MdH$$
$$= \pi H_0{}^2 \chi_0 \frac{\varpi\tau}{1+\varpi^2\tau^2} \qquad \text{(Equation 3.8)}$$

The effective relaxation time τ can be given as

$$\frac{1}{\tau} = \frac{1}{\tau_N} + \frac{1}{\tau_B} \qquad \text{(Equation 3.9)}$$

The Brownian relaxation time τ_B and Néel relaxation time τ_N have the same definition in section 2.2. Their expressions were given in Equation 2.1 and Equation 2.9. A few requirements have to be met when the linear theory is applied. First, Néel-Brown model for the relaxation type of switching is usually suitable for small field amplitude. The relaxation time is thus independent on field strength[8]. Second, a general initial susceptibility should be nearly independent of field strength to meet the linear theory regime [9]. Third, magnetic anisotropy energy barrier should be relatively small in order to promote dominant relaxation type of reversal. It is because nanoparticles with a small magnetic anisotropy barrier can have linear correlation between magnetization and the magnetic field in a large range of field strength. However, if they possess a certain magnitude of magnetic anisotropy energy barrier, nonlinearity can easily take place and the behavior of nanoparticles will deviate from the linear regime. For nanoparticles with

even large magnetic anisotropy energy barrier such as ferromagnetic single domain nanoparticles, they are always viewed in the context of a non-linear theory regime.

Calculations of heat generation were conducted including the effects of temperature dependent magnetic properties. Results of anisotropy constant and magnetization calculated in section 3.2.1 were used. Generation of heat per cycle was calculated at temperature step of 1K. In each step, corresponding magnetization and anisotropy values were substituted into Equation 3.7 together with other parameters listed in Table 3.1. A variation of diameter of nanoparticles was performed to explore how size influences the heating process. Any contribution of size and surface effects to magnetic properties was neglected in the calculation. In the whole size range explored, nanoparticles share the same temperature dependence of magnetization and anisotropy. A parameter $\xi = M_s V H_0 / kT$ was monitored all the time at different temperature for various size of nanoparticle. ξ is the reduced term of Zeeman energy by thermal energy. Numerical results revealed that the linear regime model (Equation 3.7) fit very well to real hysteresis loss when ξ was smaller than 0.7 and was acceptable when ξ is between 0.7 and 1 [10]. In our calculations, ξ was kept below 0.7 for most cases and fell into the range 0.7-1 in some circumstances. Figure 3.2 shows calculated results for nanoparticles of T_c at 385K. 400kHz and 15Oe sinusoidal magnetic field was applied for the calculations. Hysteresis area as a representative of heat generation is displayed in Figure 3.2(a) in the temperature range of 310K to 350K. It was assumed that nanoparticles started to heat from the in-vivo body temperature. Nanoparticles of 11nm size give relatively small hysteresis loss probably due to their small magnetic anisotropy energy barrier. Nanoparticles start to

show appreciable amount of hysteresis loss from 12nm. As temperature increases, heat generation slows down due to a decrease of magnetization and anisotropy. A similar decay trend can be observed for 11nm-13nm particles. However, there is a peak of heat generation for 14nm and 15nm nanoparticles which locates at a certain temperature between 310K and 350K. It is an effect of thermal fluctuation modulated magnetization reversal. Hysteresis loop develops due to dominant thermal switching at a small field as discussed in Chapter 2. The hysteresis loop has the largest enclosed area at a certain anisotropy value under a fixed alternating magnetic field in the linear theory regime. At the optimal condition, thermal fluctuation and the magnetic field together gives the high probability of irreversible switching. Similarly, the change of anisotropy along with temperature leads to a moment where the anisotropy becomes favorable for high probability of irreversible switching to happen and a peak of heat generation is resulted. When temperature is lower than the favorable temperature which gives a suitable anisotropy, magnetic field is not big enough to realize the switching. When temperature is higher, magnetic anisotropy energy barrier is small and so is the hysteresis area.

For self-regulated heat generation, it's proper to generate as much as possible heat before reaching the desired limit of working temperature range. Percentage drop of heating power at 318K compared to that at 310K is displayed in Figure 3.2(b) from 11nm to 14nm particles. Nanoparticles of 13nm size are better than others at the applied field condition because it has high heating efficiency at 310K and a prominent drop of the power at 330K-350K range. Overall, it proves the possibility to take advantage of

temperature dependent magnetic properties. It is also found that the size of nanoparticles has influence on heating power and its decay with temperature.

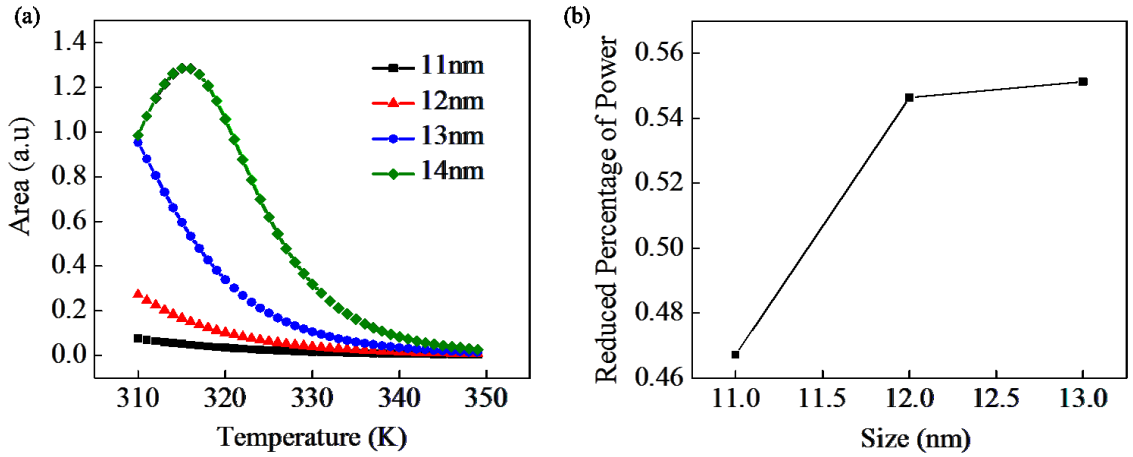

Figure 3.2 (a) Calculated area representing hysteresis loss as a function of temperature for different size of nanoparticles (b) Reduced percentage of heating power at 330K compared to that at 310K based on results in (a)

different T_c in a hypothetical condition. Nanoparticles were set to have the same material parameters at room temperature as in Table 3.1 with only difference in T_c. Size of nanoparticles was chosen to be 13nm. The same magnetic field condition as before was used for the calculation. Heating power is plotted as a function of temperature for the three types of nanoparticles (Figure 3.3(a)). A decrease of the heating power with increasing temperature is mainly due to the change of magnetization and anisotropy. More heat can be generated at 310K (37°C), the human body temperature, than at 318K (45°C), which is a sign of regulation behavior. Reduced percentage of the heating power at 318K compared to that at 310K is shown in Figure 3.3(b). Nanoparticles with low T_c such as 333K can produce almost ideal heat regulation although particles with T_c of 385K already show appreciable regulation effect. The analysis indicates that a change of

anisotropy brings in additional contribution to the temperature regulation performance of nanoparticles. Temperature regulation starts to take effect before T_c which relaxes strict requirements on the development of very low T_c materials.

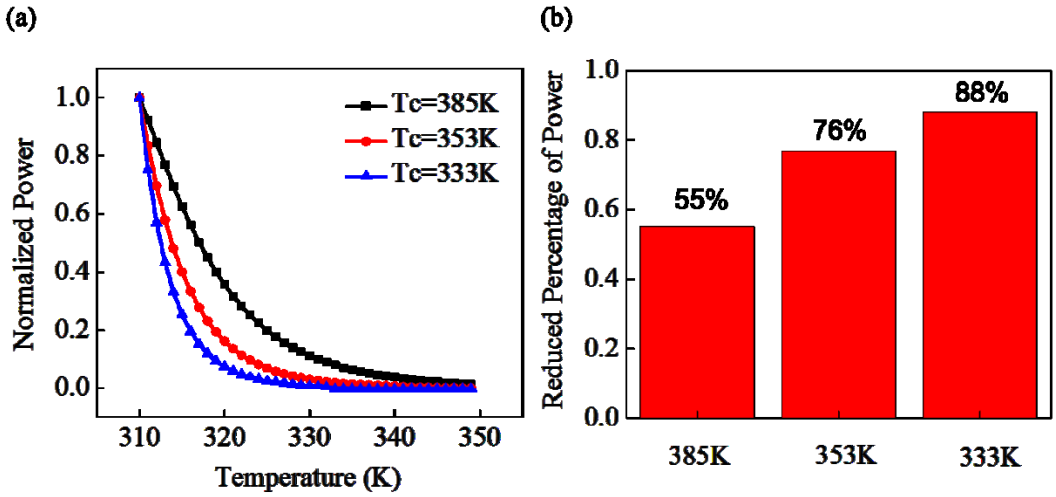

Figure 3.3 (a) Calculated hysteresis loss as a function of temperature for nanoparticles of different T_c (b) Reduced percentage of heating power at 318K compared to that at 310K based on results in (a)

3.2.3Nonlinear Theory Regime

Hysteresis loss under a relatively large magnetic field was also calculated with consideration of the temperature effect. When the magnetic field is large, large nonlinearity develops and the linear theory is no longer suitable. It is possible to calculate the loss based on dynamic coercivity under an extreme condition, where particles are almost saturated. The hysteresis loss per cycle is

$S = 2H_c \bullet M$ (Equation 3.10)

where dynamic coercivity H_c was calculated using Equation 2.10. The same material parameter and temperature dependent properties were used as in previous linear regime.

Calculation was first performed for particles of different size and the results are shown in Figure 3.4. Parameter $\zeta = \frac{kT}{KV}\ln(\frac{kT}{4\mu_0 H_{\max} M_s V f \tau_0})$ was kept below 1 to ensure the calculation was in a valid range for various size condition (Figure 3.4(a)). The dynamic coercivity shows a general decrease along with the increase of temperature. It is attributed to temperature dependent magnetic properties. The particles of a small size have quicker decrease of dynamic coercivity than the large ones because they are easily influenced by the thermal agitation when temperature increases. The hysteresis loss in Figure 3.4(c), represented by the area, has a similar tendency of change as the dynamic coercivity. It indicates the important role of dynamic coercivity in self-regulated heating behavior. Significant reduction of hysteresis loss takes place in 330K-350K range before reaching T_c. The percentage change of hysteresis loss at 318K was compared to that at 310K in Figure 3.5(d). Nanoparticles with large size show less decay of hysteresis loss than small ones. Overall, the self-regulation performance is not as significant as that in the linear theory regime.

A comparison between results in the linear and nonlinear regime reveals that there is different temperature sensitivity of hysteresis loss although temperature dependent magnetic properties are the same. The difference originates from how much thermally agitated switching of nanoparticles contributes to the generation of hysteresis. When the magnetic field and the anisotropy energy barrier of particles are small, as in the linear theory regime, switching relies on the thermally activated relaxation mostly. A little change of magnetic anisotropy energy barrier due to the increasing temperature will give rise to a large impact on the hysteresis process. Whereas in the non-linear regime,

especially for the extreme situation we investigated, switching is accomplished by the magnetic field mainly. Thermal effect still exists but it is no longer as important as it is for particles with small anisotropy energy barrier. Therefore, in order to take advantage of the temperature sensitive behavior for self-regulated heating, it's proper to work in the range where thermally agitated switching plays a dominant role.

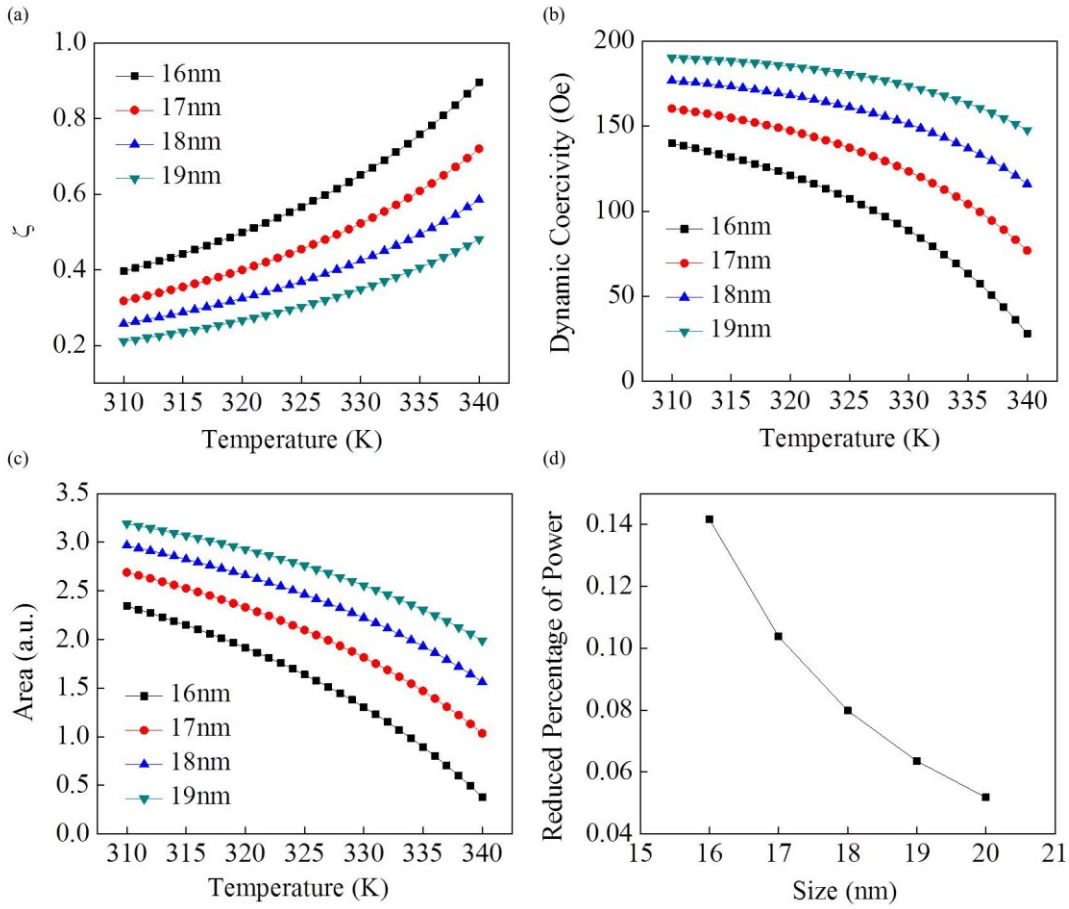

Figure 3.4 (a) Parameter ζ of nanoparticles of various sizes (b) Dynamic coercivity of nanoparticles of various sizes with respect to temperature (c) Hysteresis area of nanoparticles of various sizes with respect to temperature (d) Reduced percentage of power at 318K compared to 310K

The power generation by particles with different T_c under a hypothetical condition was also calculated using the same parameters in section 3.2.2. 16nm size of nanoparticle was

used for the calculation. The power decays as temperature increases and becomes very small before reaching T_c as shown in Figure 3.5(a). It suggests that temperature dependent magnetic properties have great influence on the heating process. At 318K, the reduced percentage of power compared to 310K is generally smaller than what's obtained in linear regime. T_c below 343K could provide a reasonably safe operation if we work mainly in this regime.

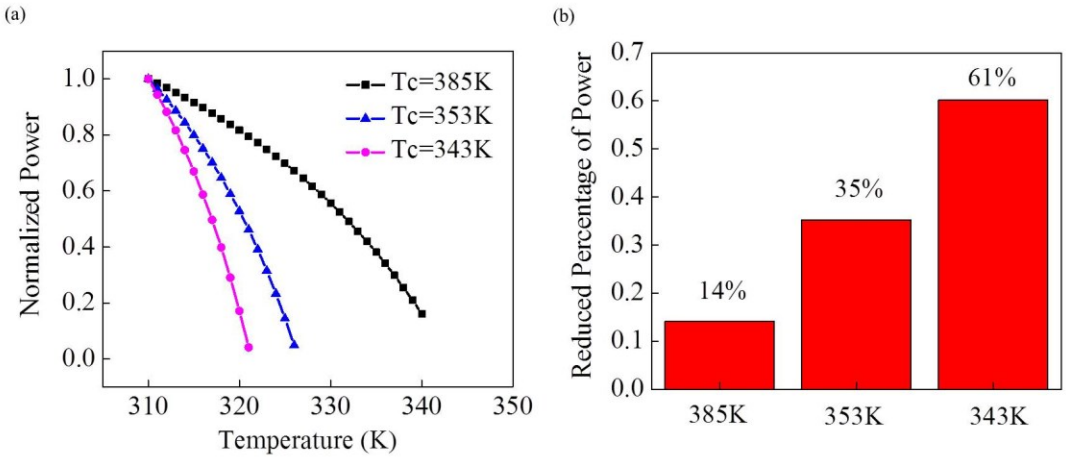

Figure 3.5 (a) Calculated hysteresis loss as a function of temperature for nanoparticles of different T_c (b) Reduced percentage of heating power at 318K compared to that at 310K based on results in (a)

3.3 Fe-Si Nanoparticles with Adjustable Self-Regulation of Temperature

It has been illustrated that how temperature dependent magnetic properties provide the possibility for self-regulation. What can be the candidate materials for "smart" nanoparticles? There have been some proposals of low T_c materials previously. $La_{1-x}Sr_xMnO_3$ [11] [12] [13], and Zn ferrite[14] are examples of ferrite materials which suffer from low magnetization value. The desire to find nanoparticles with as high as possible magnetic

moment arises from the fact that fewer nanoparticles will be required to be injected into the body for an equal amount of heat generation. Although it is possible to increase the magnetic moment by doping with rare earth elements [15], it is not economically efficient, needless to say the potential toxic effects[16]. Ni-Cu[17,18], Fe-Ni[19], FeNiZrB [20], FeCoCr [21] and Ni-Cr[22] possess good magnetic property but contain toxic elements. A composite structure, such as a core-shell structure, could be employed to enhance biocompatibility of such particles[13]. But it involves further coating steps and requires careful treatment to ensure a complete coverage of the toxic material. The challenges lie in reducing T_c while maintaining reasonable magnetization value, and without the use of toxic elements and excessive heavy metals. The issue posed here requires engineering of the materials from a fundamental physics level to biomedical implementation.

Table 3.2 Candidate materials with low T_c

Material	Composition	Magnetization	Curie Temperature
Ni-Cu	Ni 70wt% Cu 30wt%	150emu/g (300K)	370K
LaSrMnO	La 25at% Sr 75at%	40emu/g (300K)	352K
Fe-Co-Cr	$(Fe_{65}Co_{35})_{71}Cr_{18}Zr_7B_4$	104 emu/g (4K)	335K
Fe-Zn-Gd	$Zn_{0.02}Gd_{0.98}FeO$	$8.3e^{-17}$ emu/NP 9.61emu/g	315.6K
	$Mn_{0.54}Zn_{0.46}[Fe_{1.9}Gd_{0.1}]O_4$	$1.85e^{-16}$emu/NP 21.4 emu/g	383.5K
Fe-Zn-Mn	$Mn_{0.5}Zn_{0.5}FeO$	$1.21e^{-16}$ emu/NP 14emu/g	320.8K
FeNi	Fe 75at% Ni 25at%	66 emu/g	355
FeNiMn	$(Fe_{75}Ni_{25})$ 99wt% Mn 1wt%		351

3.3.1 Temperature Dependence of Magnetization

The physical picture of temperature dependence of magnetization can be a guide for engineering materials to obtain self-regulated nanoparticles. There has been a history on the progress of understanding the origin of temperature dependence of magnetization, which is also related with the understanding of ferromagnetism.

Historically, Pierre Weiss first found out that some materials had spontaneous magnetization, which responses to a magnetic field strongly such as Fe. A molecular field theory was then developed as a classical theory to explain that. It has been proposed that a huge internal magnetic field H_w called molecular field exists and is proportional to magnetization. The molecular field has an expression of $H_w=\beta M$, where β is the molecular field constant. Magnetization of ferromagnetic materials is expressed according to Brillouin function by including the molecular field term [7].

$$M = N_v \mu_m g J B_j(x) = N_v \mu_m g J [\frac{2j+1}{2j}\coth(\frac{2j+1}{2j}x) - \frac{1}{2j}\coth(\frac{x}{2j})]$$
$$x = \frac{\mu_m \mu_0 (H + H_w)}{kT} \quad \text{(Equation 3.11)}$$

where j is the quantum value of orbital momentum L, J is the total angular momentum J=L+S, in the form of $[j(j+1)]^{1/2}$. The molecular field is responsible for the long range inter-atomic interaction against thermal fluctuation. Therefore, the expression is able to show how magnetization changes with respect to temperature. T_c given by Weiss theory is [23]

$$Tc = \frac{\mu_m g J(J+1)}{3k} H_w \quad \text{(Equation 3.12)}$$

Because the pure phenomenological nature of Weiss' molecular field theory, it could predict neither the exact value of M_s nor of T_c. It is nevertheless possible to present the trend of magnetization change for particular materials [23].

Heisenberg came up with a new effective Hamiltonion to address the microscopic origin of molecular field, which is critical for fundamental understanding of the temperature dependence. The Hamiltonion is the energy to keep spins parallel or antiparallel depending on the sign of the exchange integral. The effective Heisenberg Hamiltonian for N-electron system is

$$H_{eff} = -\sum_{i \neq j}^{N} J_{ij} s_i s_j \quad \text{(Equation 3.13)}$$

where s is the quantum value of spin momentum for the i_{th} and j_{th} electron. J_{ij} is the exchange integral which has an expression of

$$J_{ij} = \iint \psi_i(r_1)\psi_j(r_2)\frac{e^2}{4\pi\varepsilon_0 r_{12}}\psi_i^*(r_2)\psi_j^*(r_1)dr_1 dr_2 \quad \text{(Equation 3.14)}$$

In Equation 3.14, ψ_i and ψ_j are wavefunction of i_{th} and j_{th} electron. $\frac{e^2}{4\pi\varepsilon_0 r_{12}}$ is the term to describe electron-electron interaction. The expression shows that exchange integral reflects the energy associated with a change of quantum states between two electrons. When spins of electrons are parallel, wavefunction of electrons are symmetric and the electrons tend to be close to each other. When spins of electrons are antiparallel, wavefunction of electrons are antisymmetric and the electrons tend to avoid each other. Therefore, exchange interaction arises from the Coulomb interaction $\frac{e^2}{4\pi\varepsilon_0 r_{12}}$ between

two electrons as well as the symmetry of wavefunction. In Heisenberg's effective Hamiltonian, when J_{ij} is positive, parallel spins $s_i * s_j > 0$ gives minimal expectation value of H_{eff}, indicating ferromagnetic coupling. The temperature dependence of magnetization under Heisenberg's model can be analyzed by employing the mean field concept. Consider the energy of an atomic moment s and place it under the influence of the mean value of all other atomic moment, the energy of a given magnetic moment is then

$$E_i = -2s_i \sum_j J_{ij} s_j = -m_i H_w \quad \text{(Equation 3.15)}$$

By using the mean field approximation, for a material consisting of identical atomic spins s with exchange constant J_{ij} per pair, the total energy E_i can be expressed by Equation 4.16 where product of spin vector is replaced by its expectation value.

$$E_i = -2s \bullet s \sum_j J_{ij} = -2s(s+1) \sum_j J_j \quad \text{(Equation 3.16)}$$

In analogy to Equation 3.12, T_c in Heisenberg mean field approximation is

$$T_c = \frac{2(s+1)sJ}{3k}, J = \sum_j J_{ij} \text{ (Equation 3.17)}$$

According to above principles, inter-atomic exchange against thermal energy defines how well ferromagnetism sustains. When temperature increases, electron spins experience more thermal excitation and fluctuates randomly to overcome spin-orbital coupling and spin-spin coupling. T_c is proportional to the exchange energy E_i which is a function of spin moment and the exchange constant. The theory indicates that engineering T_c of the material requires tuning of exchange energy E_i.

Stoner developed a rigid band model which addresses non-localized feature of 3d electrons for understanding ferromagneitsm of Fe, Ni, Co and their alloys. Because atoms

in crystal lattice pose periodic potential well, energy state of electrons is in the form of band with some forbidden states, unlike the total free electron. It's typical for metallic ferromagnetic materials to have a narrow 3d electron band and a broad 4s electron band. Fermi energy level lies below the energy up to which 3d band can be occupied. Exchange coupling among electrons results in different energy states of spin-up electrons (majority) and spin-down electrons (minority). It leads to a shift of two subbands and redistribution of electrons in energy states as required by Pauli exclusion and potential energy conservation. The splitting gives difference in density of states at Fermi level, which is the origin of spontaneous magnetization. According to Stoner's criteria, the stronger exchange coupling and the larger density of states is beneficial for the formation of ferromagnetism. The band theory model explains non-integer magnetic moment per atom based on overlapping electron clouds. The temperature dependence is determined by the change of density of state at Fermi level. Fermi distribution function is employed where μ is chemical potential (Equation 3.18). With increasing temperature, the convolution of density of state D(E) with function $\frac{\partial f(T_c)}{\partial E}$ gives a decrease of density of state at Fermi level. At T_c, multiplication of exchange splitting I and total density of states becomes 1 (Equation 3.19). Typically, exchange splitting I from band structure calculation is on the order of 0.1eV. It then leads to unrealistic T_c on the order of 10000K. In summary, although band theory explains non-integer magnetic moment per atom of metallic materials well, it doesn't provide good explanation of T_c [23].

Fermi distribution function $f(T) = \frac{1}{e^{(E-\mu)/kT} + 1}$ (Equation 3.18)

Temperature dependent Stoner criterion: $I\int_0^\infty D(E)\left|\frac{\partial f(T_c)}{\partial E}\right|dE = 1$ (Equation 3.19)

Rigid band model however paves the way for modern band theory. Heisenberg's Halmitonian is integrated with the modern band theory to provide improved calculation of temperature dependence of magnetization and T_c. Therefore, it is the Heisenberg's exchange model that is the critical part for temperature dependent magnetization.

3.3.2Temperature Dependence of Magnetization at Low Temperature

A spin wave theory was developed to explain the magnetization change at low temperature. Fast decrease rate of magnetization was observed compared to that given by Brillouin function at low temperature. Spin wave theory takes into consideration of the collective behavior of neighboring atomic moments under the influence of temperature. A chain of spins produces spin wave where adjacent spins precess with defined phase shift. The wavelength is the distance between spin sites over which 360 degree precession occurs. The equation called Bloch $T^{3/2}$ law acts well in describing the magnetization decay at low temperature range.

$M(T)=M(0)(1-A*T^{3/2})$ (Equation 3.20)

The theory is also consistent with the quantum level explanation of ferromagnetism: exchange coupling from spin momentum adds another Hamiltonian into the total energy system. Because the theory is in the frame of Heisenberg's exchange coupling, it has been used to study exchange coupling in the material as an indirect way. It provides an estimation of the strength of exchange coupling.

3.3.3 Temperature Dependence of Anisotropy

It is also important to understand the origin of temperature dependence of anisotropy. Anisotropy in magnetic materials is the consequence of coupling between spin momentum and orbital momentum. The distribution of electron cloud around an atom has to be anisotropic instead of isotropic in order to minimize total energy of the atom. The preferred direction of orbital momentum possesses minimal energy. Spin momentum also has preference which leads spins to align parallel or antiparallel to the direction of orbital momentum, called spin-orbital coupling. The temperature dependence of anisotropy is related with the spin-orbital coupling and the spin-spin interaction. Callen interpreted the temperature dependence based on solid state quantum physics. In a highly symmetric crystal field, temperature dependence of anisotropy is strong. In a less symmetric field, temperature dependence is weak. Relative angle change of neighboring spins due to thermal agitation leads to a much greater influence on the coupling when a highly symmetric crystal field is present. It is a reflection of mutual interaction between spin momentum and orbital momentum. Anisotropy therefore exhibits higher temperature sensitivity compared with magnetization. Decay of anisotropy is to the power of decay of magnetization as shown in Table 3.3 for uniaxial and cubic materials.

Table 3.3 Temperature dependence of anisotropy

Temperature	Function	l=2 (Uniaxial)	l=4 (Cubic)
Low	$m^{l(l+2)}$	m^3	m^{10}
High	m^l	m^2	m^4

3.4 Curie Temperature in Fe-Si

To acquire the functional material with intrinsic temperature regulation, we approach the issue through incorporation of Si into Fe. From the aspect of materials science, T_c is determined by the strength of exchange interactions between Fe atoms. Investigations on Fe-Si alloy bulk samples have revealed that possible hybridization between Fe and Si has influence on the magnetic property. Study suggests there is an underlying physical basis for Si to reduce T_c [24]. Tuning T_c has been demonstrated to be feasible in our Fe-Si particles through the control of exchange. From a viewpoint of biomaterial engineering, Fe and Si provide a biologically friendly combination without using toxic metals, and it avoids extra processing to form composites by direct formation of a biocompatible material system. The high magnetization of Fe has attracted much attention in biomedical area [25] [26] [27]. Fe has been applied for implantable stents and can be well endured by the body[28,29]. Si is a semiconducting material with inherently low toxicity [30]. It has been extensively studied for applications such as cell labeling, drug delivery and implanted devices [31-34]. Good biocompatibility of Si nanocrystals has been established through in-vitro and in-vivo experiments [35-37]. Additionally, the two elements are widely available at low cost.

We purposely synthesized Fe-Si nanoparticles of different composition in pursuit of particles with adjustable temperature sensitive magnetic property. The gas phase synthesis method as introduced in section 1.2.6 was employed to make the particles. It was demonstrated that the method enabled thermal environment for crystal growth[38], diffusion and segregation on nanoscale [39], which facilitates fabrication of a wide range of nanoparticles. Such flexibility in a variety of aspects is not all fulfilled in wet chemistry. Although it is possible to produce Fe-Si particles by chemical methods[40 41], it is not in an optimally controlled manner. Our synthesis method provides inherently easy adjustment of composition and established capability of phase control. In our synthesis, we used Fe-Si composite targets of different ratio of Fe to Si. Sputtering current and gas pressure were varied in the range of 0.3A-0.6A and 300mTorr-500mTorr, respectively. Figure 4.6 displays transmission electron microscope (TEM) bright field images of typical Fe-Si nanoparticles. The particles mostly crystalize to faceted shape. Nanoparticles are of good crystallinity and relatively high uniformity. To examine whether Si brings in any effect on the reduction of T_c, temperature dependence of saturation magnetization was measured by a vibrating sample magnetometer (VSM). T_c was determined through the tangential slope of the curve around where ferromagnetism transition happened. By plotting T_c as a function of atomic percentage of Si, It can be clearly seen that a decrease of T_c takes place with the increase of Si from Figure 3.7(a). Low T_c of 393K -373K is found for nanoparticles of about 38 at%-42at% Si. Observation of similar trend in nano-particulate samples done here is for the first time and the feature is not sensitive to size

effect but more to Fe-Si chemical environment. The results reflect effective reduction of T_c by Si. It proves that tuning T_c can be achieved by incorporating Si into Fe.

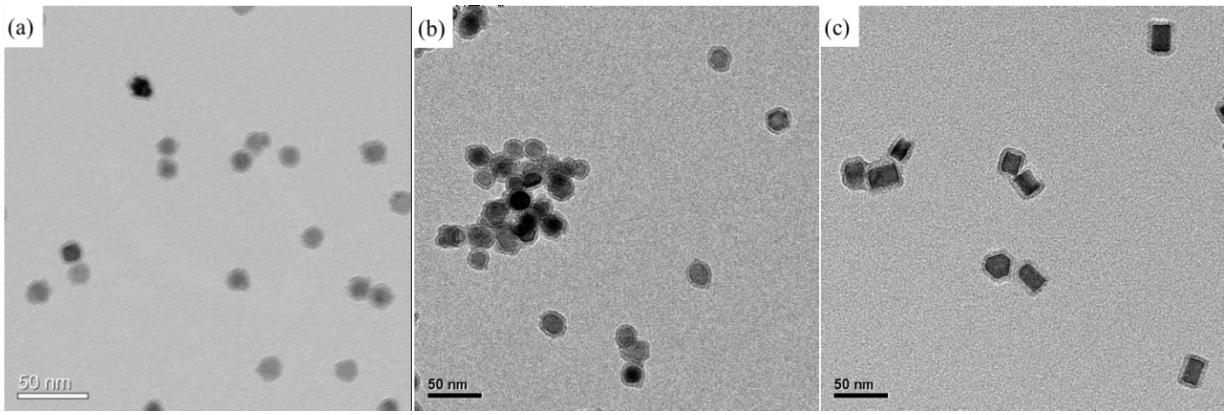

Figure 3.6 Bright field TEM images of Fe-Si nanoparticles with (a) 17at% Si (b) 25at% Si (c) 42at% Si

To investigate how Si modulates the T_c, spinwave stiffness coefficient was explored based on measurements of magnetization as a function of temperature in 5K-300K range. It has been observed in several material systems that spinwave stiffness can be used as a measure of exchange interactions[42,43]. The temperature dependence of magnetization at low temperature follows Equation 4.20. Figure 3.7(b) shows the change of magnetization versus temperature for different Si content from 5K to 300K. The curves were fitted to $T^{3/2}$ law in the range of 5K-150K with above 90% confidence as displayed in Figure 3.7(c). To be noted, the best fitting didn't occur with intercept of 1, but close to 1 even though exponent was varied. Spinwave stiffness D from the spinwave dispersion relationship $h\omega=Dq^2$ can be calculated based on the slope A using $A=2.612(V/S)(k/4\pi D)^{3/2}$, where V is the atomic volume of a magnetic atom and S is the spin[44,45]. The calculated D is presented in Figure 3.7(d). A general trend shows a decline

of D with an increasing atomic percentage of Si. It indicates that a weakening of exchange interactions among Fe atoms is realized by incorporation of Si and thus T_c is correspondingly tuned. A strong exchange coupling can resist thermal randomness of spins when temperature increases, and vice versa. We can conclude here that Fe-Si nanoparticles are engineered from intrinsic physical property aspect for intrinsic temperature regulation.

The dependence of exchange strength on the concentration of Si is associated with the microscopic intimacy between Fe and Si. Multiple Fe and Si bonding was found mostly covalent [46]. The covalence between Fe and Si can affect the overlapping or distribution of electron cloud of Fe atoms. As the concentration of Si increases, there is an increasing near neighbors of Si around the Fe atom. It increases the probability for 3d electrons to participate in forming bonds with p electrons [47]. In consequence, it could lead to a decrease of exchange coupling between Fe atoms. When the Si concentration reaches 38at%-42at%, particles form a hexagonal crystal structure. The arrangement of Fe and Si indicates a large coordination number of Si around Fe according to reference [45]. That is the driving force for the weakening of exchange, and lowering of T_c. It is therefore important to have the suitable chemical composition and chemical environment of Fe in order to obtain the low T_c.

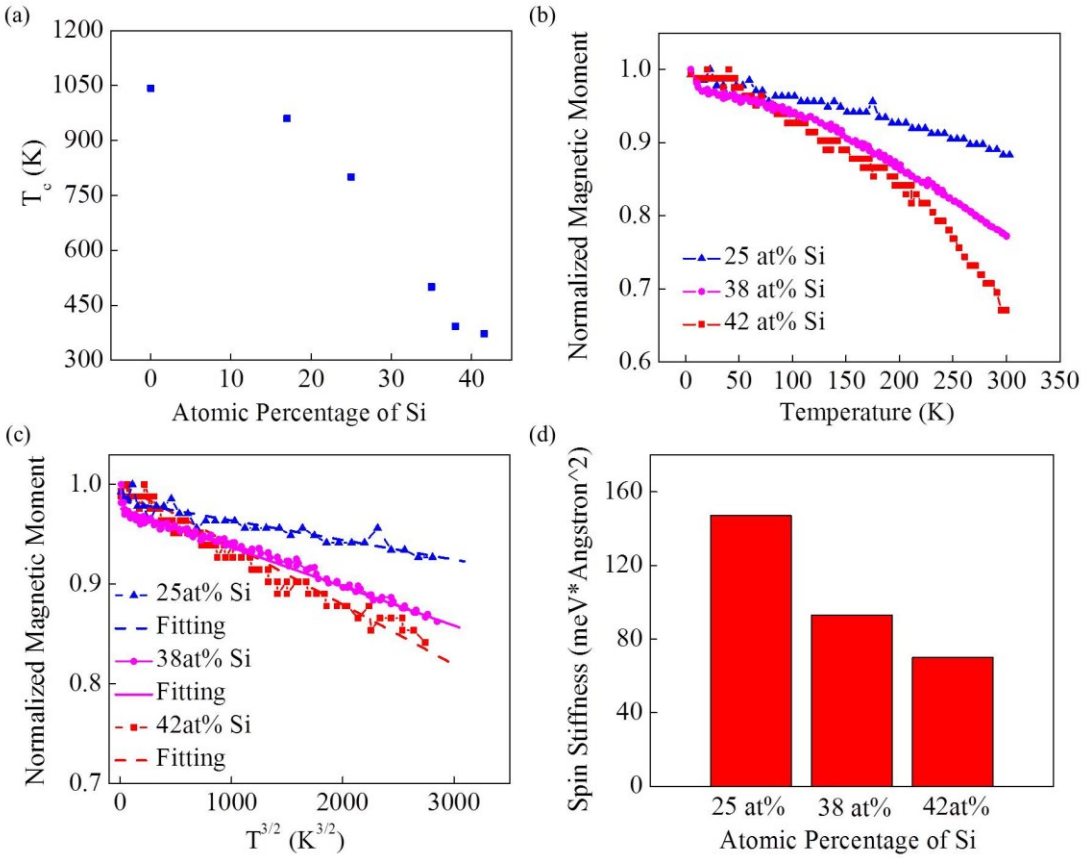

Figure 3.7 (a) T_c of Fe-Si nanoparticles as a function of atomic percentage of Si (T_c of Fe was taken from Reference [19]) (b) Temperature dependence of magnetization from 5K to 300K (c) Fitting of curves in (b) based on Bloch's law (d) Spin stiffness extrapolated from experimental fitting for Fe-Si particles of different composition

3.5 Fe-Si Nanoparticles of Low T_c

3.5.1 Characterization of Low T_c Nanoparticles in Fe_5Si_3 Phase

With the established capability of tuning T_c through a modulation of exchange interactions in Fe-Si, we now turn to nanoparticles of low T_c which can be candidates for self-regulated cancer therapy. Figure 3.8(a) is a TEM bright field image of nanoparticles with 38 at% Si. The fabrication condition was 400mTorr of sputtering pressure and 0.6A of sputtering current. The particles were collected onto a carbon coated Cu grid in-situ.

The particles mostly possess cuboidal shape. Figure 3.8(b) shows the selected area diffraction (SAD) pattern of nanoparticles in Figure 3.8(a). The Fe-Si nanoparticles are well crystalized as indicated by the discrete spots arising from the diffraction of the electron beam by the crystal planes. The SAD pattern reveals that the Fe-Si nanoparticles form Fe_5Si_3 phase of hexagonal structure, which is supported by the strong diffraction from crystal planes of (00.2) and (21.0) particularly (Figure 3.8(c)).

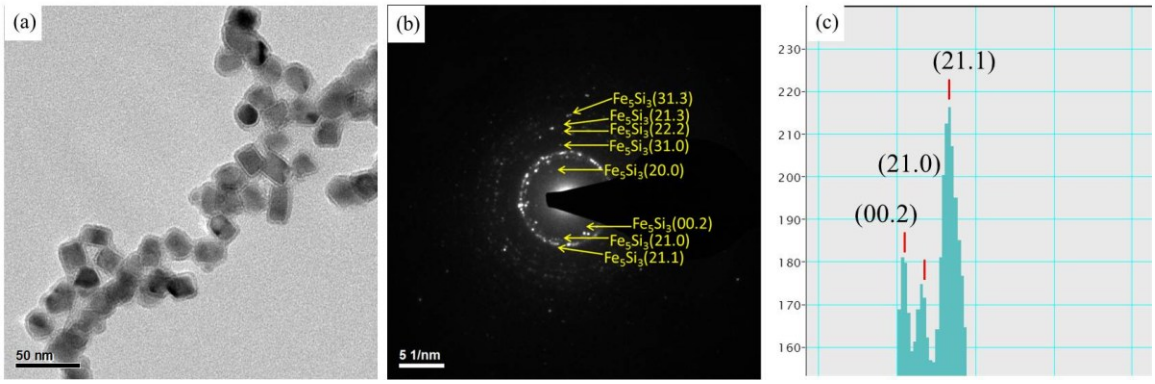

Figure 3.8(a) Bright field TEM image of Fe-Si nanoparticles with 38at% Si (b) SAD pattern of the nanoparticles (c) Integrated strength of diffraction from (00.2), (21.0) and (21.1) planes based on the pattern in (b)

Further characterization on crystal structure was carried out on a single particle level. High resolution imaging was conducted on nanoparticles of different projection view. Figure 3.9 shows the high resolution images and the corresponding fast Fourier transform (FFT) of each image. The lattice parameter of the particle in Figure 3.9(a) is 0.58nm, corresponding to (10.0) plane. Bright spots in FFT image can be indexed to Fe_5Si_3 phase quite well. The particle is orientated in the direction of [0001]. Similarly, a particle oriented in [2110] direction is analyzed in Figure 3.9(c) and (d). The lattice parameter is 0.34nm, corresponding to (00.2) plane. Indexing of the bright spots in FFT reveals the same crystal structure. Their difference in aspect ratio arises from a view of different

orientation. To be noted, particles are not very uniform in terms of morphology, which can be a result of non-uniformity of the magnetic field across the erosion track of the sputtering target.

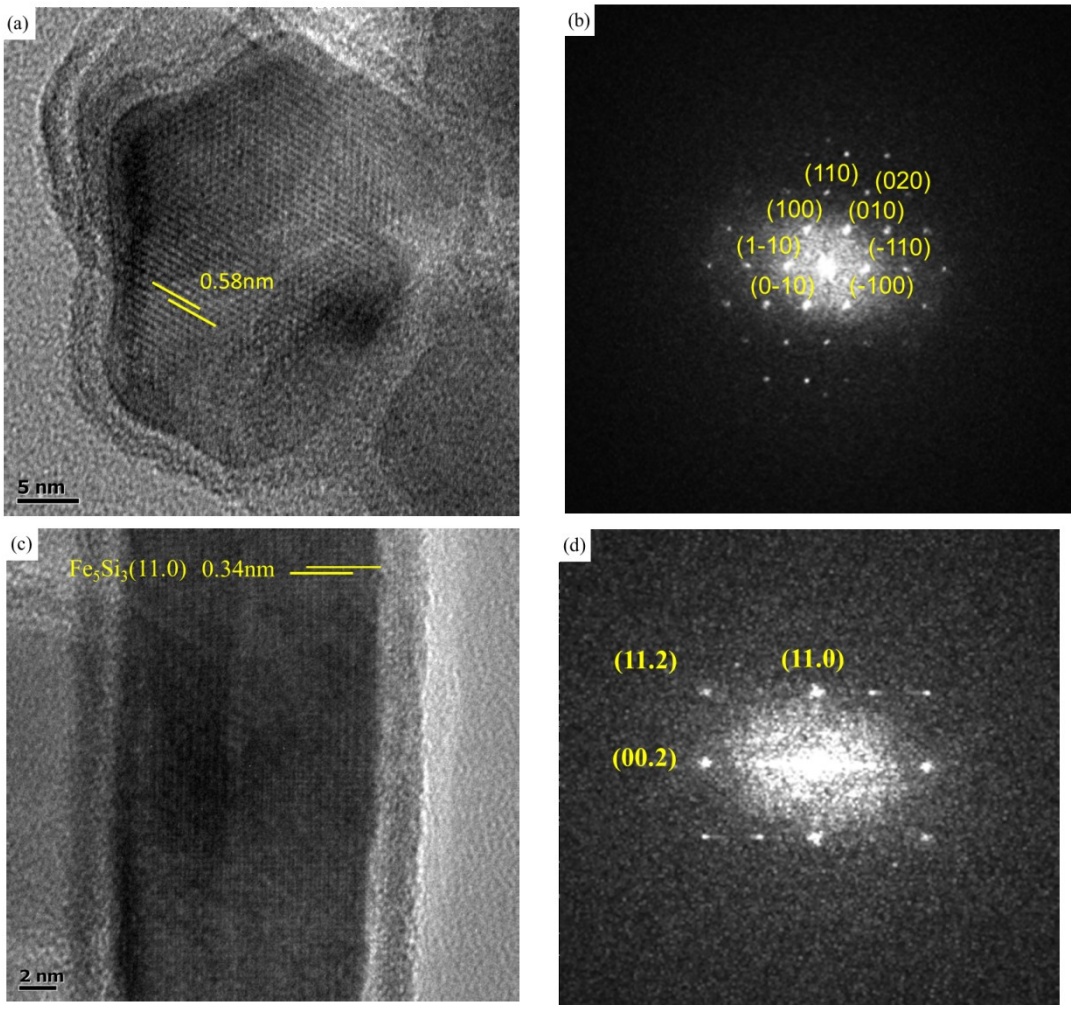

Figure 3.9 High resolution TEM image for a particle oriented in (a)[0001] direction and (c) [2110] direction; (b) and (d) are the corresponding FFT of (a) and (c), respectively

Composition of a single particle was examined by energy dispersive X-ray spectroscopy (EDX) equipped on TEM. The characterization was performed under STEM mode with

electron beam resolution of 2nm. Line scan across a particle was conducted to find out the distribution of Fe and Si within the particle. More than 10 particles were randomly selected and analyzed. They had different projection views. Figure 3.10(a) and (c) display the high-angle-dark-field (HAADF) images of two of them. The red line represents the path in which line scan was performed. The line scan result was plotted in Figure 3.10(b) and (d), respectively. It can be seen that the distribution of Fe and Si is quite uniform along the scanned direction. The ratio of Fe and Si keeps at a constant level close to 38at%. The surface of the particle is rich in Si due to the small surface energy of Si compared to Fe. All the examined particles have similar distribution profile of elements. The results prove that the elements of Fe and Si distribute uniformly on nanometer scale. The distribution of Fe and Si is important for the magnetic property of the material, because the exchange energy can be tuned only with effective incorporation of Si into Fe.

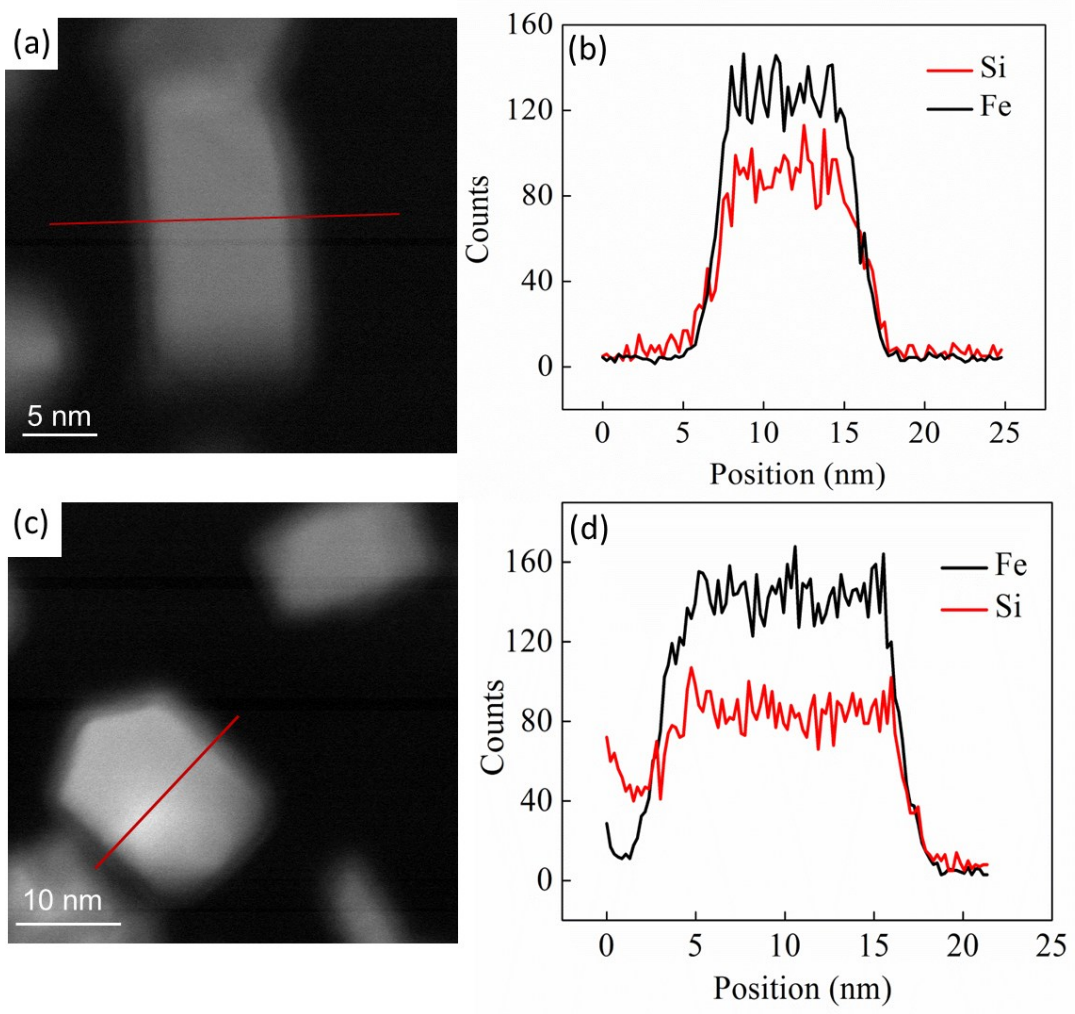

Figure 3.10(a) HAADF image of a Fe-Si nanoparticle; (b)EDX line scan of the particle in (a); (c) HAADF image of a Fe-Si nanoparticle with a different projection view; (d) EDX line scan of the particle in (c)

Magnetic properties of particles were characterized to exam the intrinsic temperature dependent property. A hysteresis loop of an ensemble of nanoparticles was measured by VSM at room temperature (Figure 3.11(a)). The value of saturation magnetization was calculated based on the magnetic moment and the mass of particles. Saturation magnetization was determined to be 80 emu/g, or 536 emu/cm^3 using density of 6.7g/cm^3. It is higher than the previously proposed ferrite materials with low T_c and is comparable

to the metallic alloy materials previously studied. The remanent magnetic moment of nanoparticles at the zero magnetic field is as low as 8.5% of saturation magnetic moment while a coercivity of 70 Oe is found for the sample. It is a reflection of possible dipolar interaction among nanoparticles due to the nature of collection process where particles pack together onto the substrate. In addition, some large particles in the sample may also contribute to the hysteresis. Temperature dependence of magnetization is depicted in Figure 3.11(b). A drop of magnetization takes place as the temperature increases and a transition at about 393K is seen. Such low T_c along with the promising magnetization value has not been observed in materials without using toxic metals and such limited amount of heavy metals. It is of great advantage to achieve simultaneously low T_c and high saturation magnetization in a biologically friendly material from a practical point of view.

It should be noticed that the anisotropy constant also changes with temperature, which can affect the self-regulation process profoundly. To probe that, initial magnetization curves were measured at different temperature after AC demagnetization of the sample. The anisotropy constant was extrapolated by fitting the magnetization curves to law of approach saturation for uniaxial materials[48]. Decrease of the anisotropy constant can be found as the temperature increases (Figure 3.11(c)). At room temperature, anisotropy constant is $3*10^5 erg/cm^3$. It is higher than the reported value of Fe-Si ribbons. One possible contributing factor is shape anisotropy due to the asymmetrical morphology of nanoparticles. In addition, surface anisotropy arising from surface atoms with missing neighbors could also contribute to the effective

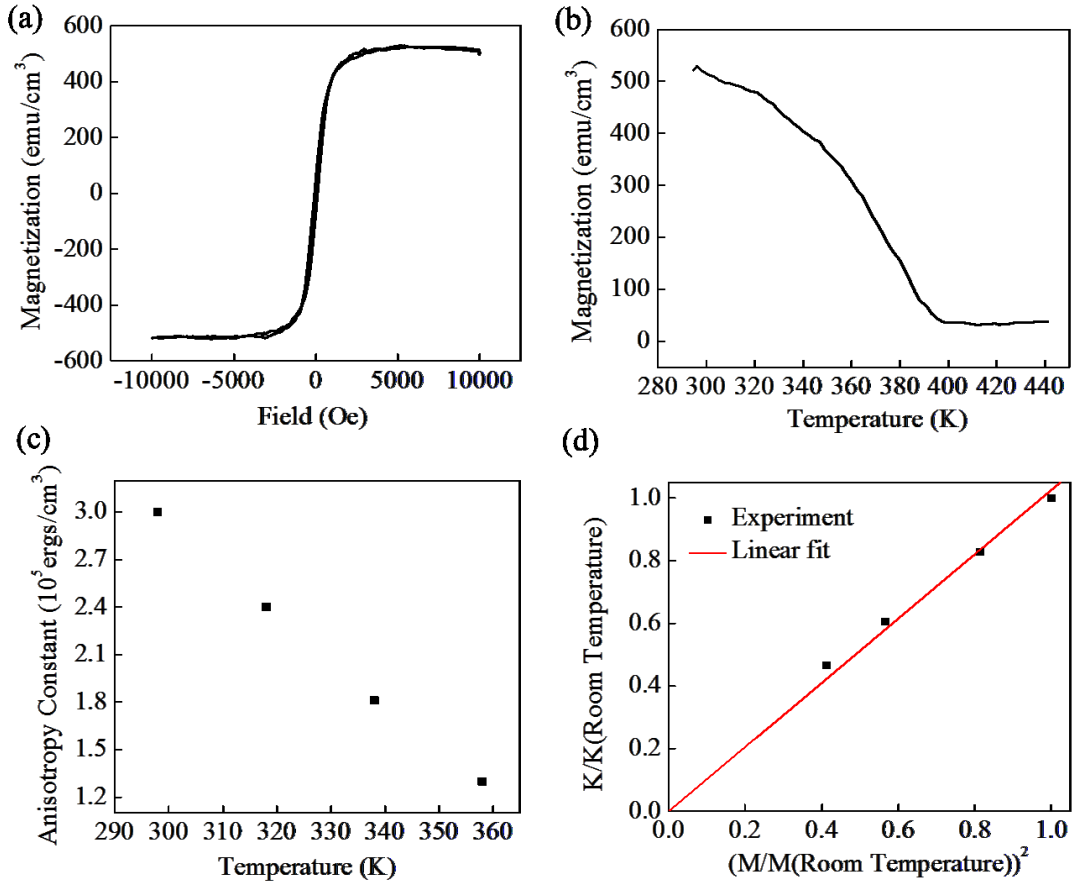

Figure 3.11(a) Hysteresis loop of Fe-Si nanoparticles (b) Temperature dependence of magnetization (c) Temperature dependence of anisotropy constant (d) Relationship between temperature dependence of magnetization and anisotropy constant

anisotropy constant determined in this way. A square power law relationship is deduced by comparing the temperature dependence of anisotropy and magnetization. Figure 3.11(d) shows how the experimental data follows a fitting of the square power law. Similar relationship between magnetization and anisotropy has been observed in other uniaxial materials[49-51]. In our case, because of the low T_c, Callen's law actually proposes a square instead of a cube power law at temperature range $T>0.6T_c$. In addition, shape anisotropy also follows a square power law which is possibly present in the sample. The

fast decline of anisotropy in principle can lead to temperature regulation effect more pronounced than expected from purely the decay of magnetization. Synthesis of this type of nanoparticles by physical method has never been reported so far based on our knowledge. It is promising to obtain such temperature sensitive magnetic properties at close to room temperature range. In the following, these Fe-Si nanoparticles are used for experiments of cytotoxicity and alternating magnetic field heating.

3.5.2 Influencing Conditions for the Formation of Low T_c Nanoparticles

It has been found that the formation of particles of low T_c is closely related with the structure. The finding is based on a comparison between diffraction patterns of samples with different percentage of Fe_5Si_3 phase. It is not easy to distinguish the difference because of the complicated diffraction pattern of iron silicides. However, there is a noticeable feature related with the strength of diffraction from reciprocal spacing 0.221nm and 0.235nm. The two diffraction line is formed by diffracted electrons from (00.2) crystal planes and (21.0) planes of Fe_5Si_3, which are essential planes in a hexagonal closed pack structure. Figure 3.12(a) and (c) shows the TEM image of samples with 33% and 56% low T_c Fe_5Si_3 phase, respectively. The percentage was determined from the percentage of change of magnetic moment in the temperature dependence curve of magnetization. Figure 3.12(b) and (d) are the corresponding diffraction pattern of particles in (a) and (d), respectively. Compared to the diffraction of previous sample with almost full percentage of low T_c Fe_5Si_3 particles, the strength of the diffraction from the (00.2) and (21.0) planes correlates with the percentage of Fe_5Si_3 phase in the sample.

Particularly, intense diffraction from (00.2) plane implies formation of hexagonal structure. It is different from the claim made in reference where 0.221nm (21.0) and 0.200nm (21.1) are considered as strong signature lines for Fe_5Si_3[6].

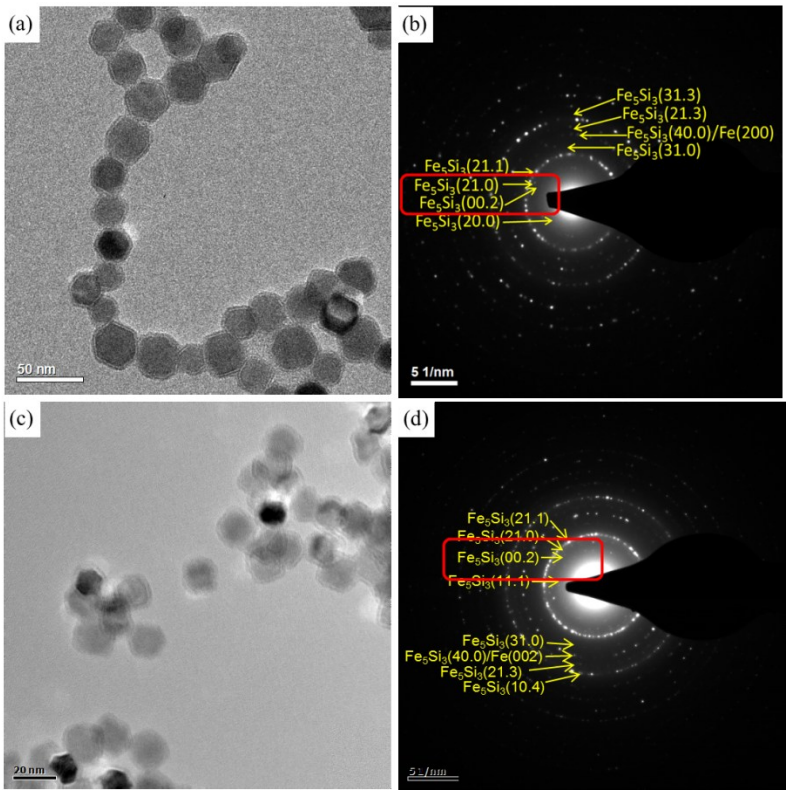

Figure 3.12 Bright field TEM images of (a) 33% Fe_5Si_3 (c) 56% Fe_5Si_3; Selected area diffraction for (b) 33% Fe_5Si_3 (d) 56% Fe_5Si_3;

In order to find out what governs the formation of Fe_5Si_3 phase, composition analysis on these samples was performed to investigate the ratio of Fe and Si elements. EDX equipped on the TEM was conducted on a collection of nanoparticles to probe the composition of three samples. During the collection of spectrum, the sample was tilted towards the X-ray detector at an angle of 20 degree to maximize the intensity. Integrated intensity of Fe Kα edge peak and of Si K edge peak was used to calculate the ratio of Fe

and Si. A reference sample was used to calibrate the result from EDX. The composition of the reference sample was measured by both Rutherford Backscattering Spectrometry (RBS) and EDX. There was about 8% difference in atomic ratio of Fe and Si between results from two methods. As RBS is a sensitive technique that probes impurity level down to sub-ppm range and accurate stoichimetry information without a standard, we would consider EDX provides results reasonably close to reality. Figure 3.14 shows the EDX spectrum for samples of 33% Fe_5Si_3, 56% Fe_5Si_3 and full percentage of Fe_5Si_3. Integrated intensity ratio of three samples doesn't show significant difference. Atomic ratio of Fe and Si is in the range of 1.8-1.5. Because the composition of the samples is really close to each other, the substantial difference of the percentage of low T_c phase is not due to the macroscopic level composition difference.

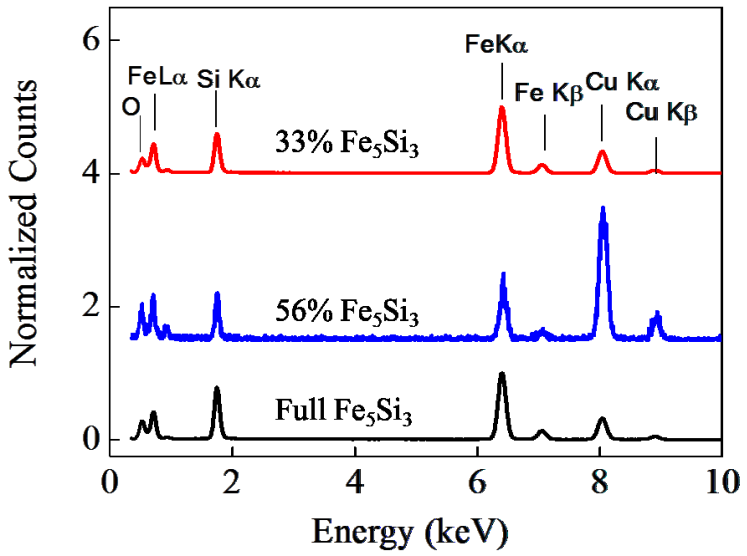

Figure 3.13 EDX spectra of samples with different percentage of Fe_5Si_3 phase

It has been found that the distribution profile of the magnetic field on the surface of the sputtering target has a great influence on the formation of low T_c phase. The distribution profile of the magnetic field was adjusted by changing the thickness of the target. It is possible to change how magnetic field distributes in this way because of the special composite target used here. The target was made of a piece of Si and a piece of Fe with spoke pattern. In practical experiments, the maximum magnetic field on the surface of the target was kept the same all the time. The geometry difference between targets brought subtle difference of the distribution profile of the magnetic field. In order to show how magnetic field distributes differently, a simulation was done by using finite element software Comsol Multiphysics. The model was built up based on the practical parameters in experiments. An iron cone piece of 5mm height was located at the center position above Fe-Si composite target. An iron ring piece of 3mm height was located around the edge of the target. Figure 3.14(a)-(c) shows the cross section view of the targets and the simulation results of the strength of the magnetic field over the surface of the target. A line was drawn in the vertical direction as indicated in Figure 3.14(a)-(c) to read out the strength of the magnetic field along that path. The strength was normalized to the maximum magnetic field, which varies from 1168Oe to 1120Oe for the three cases. The normalized magnetic field was plotted in Figure 3.14(d) as a function of distance from the surface of the target. As suggested by the plot, the magnetic field decreases faster for the case with high percentage of Fe_5Si_3 than that for the case with low percentage of Fe_5Si_3. For example, at 1mm distance away from the surface of the target, the strength of magnetic field decreases to 81%, 76%, 72% of the initial strength for samples with low to

high percentage of Fe_5Si_3, respectively. Therefore, the large decay rate of the field strength in close proximity of the target surface promotes the formation of Fe_5Si_3 phase.

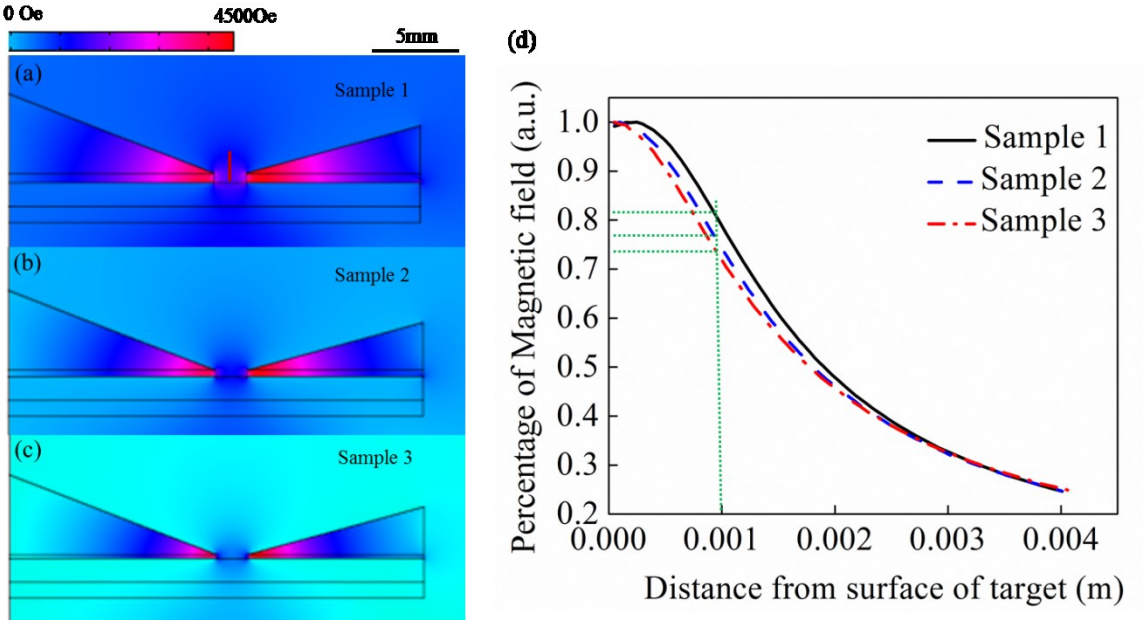

Figure 3.14 Simulated magnetic field distribution on the surface of target for (a) Sample 1 (b) Sample 2 (c) Sample 3 and (d) strength of magnetic field versus distance for Sample 1- Sample 3

It can be interpreted from the aspect of thermal environment for why the distribution of the magnetic field influences the formation of Fe_5Si_3 particles. The path of nanoparticle growth in our synthesis method starts from direct intermixing of Fe and Si atoms. Because the presence of magnetic field confines the movement of secondary electrons, different field distribution over the surface of the target leads to different distribution profile of secondary electrons. A decay of field strength indicates that the density of secondary electrons decreases in the direction perpendicular to the target surface. The energetic Ar ions which act as the energy supply are ionized by the interaction of secondary electrons and Ar molecules. Therefore, they will follow the distribution of secondary electrons. The magnetic field thus regulates the energy supply over a certain

distance above the target. A quick decay of magnetic field leads to a fast drop of supply of energetic Ar in the range close to the surface of the target. The thermal environment is therefore in a controlled manner. Small clusters nucleate and continue to grow in a controlled thermal energy supply. The growth stops when particles are out of the plasma region. Hexagonal Fe_5Si_3 forms in the temperature range 1100°C - 825°C based on the equilibrium phase diagram. It won't be obtained if the environment temperature for growth is above and below that range[52]. Considering the relatively short time that particles reside in plasma region, the equilibrium phase diagram is not followed exactly in our synthesis method. However, it still tells the importance of having a balanced energy supply for the phase formation. There should be neither deficient nor overwhelmed energy supply to obtain the phase. The condition with fast decay of magnetic field enables particles to go through a suitable thermal environment without exceeding amount of energy supply. The phase formation is benefited from the balanced condition employed here.

3.6 Cytotoxicity

To examine the cell response to Fe-Si nanoparticles, cytotoxicity of particles of low T_c was tested on NIH 3T3 cell line using standard MTT (3-(4,5-dimethylthiazol-2-yl)-2,5-diphenyltetrazolium bromide) array. Fe-Si nanoparticles with PEG surface wrapping were used for the experiment. 20 μL of Fe-Si nanoparticle in PBS buffer solutions were added to a 96-well plate containing NIH 3T3 cells seeded at 5000 cells/well in 180 μL cell culture media and was incubated at 37 °C in 5% CO_2 for 24 h before performing the

MTT assay to determine cell viability, triplicate. The in-vitro data in Figure 3.15 shows that high percentage of cell viability can be maintained up to 6.25ug/ml. When the concentration of Fe-Si nanoparticle is 12.5ug/ml, viability of cells dropped to below 80%. Compared to other metallic nanoparticles[53] [54], Fe-Si nanoparticles possess low toxicity due to the inherent material characteristic.

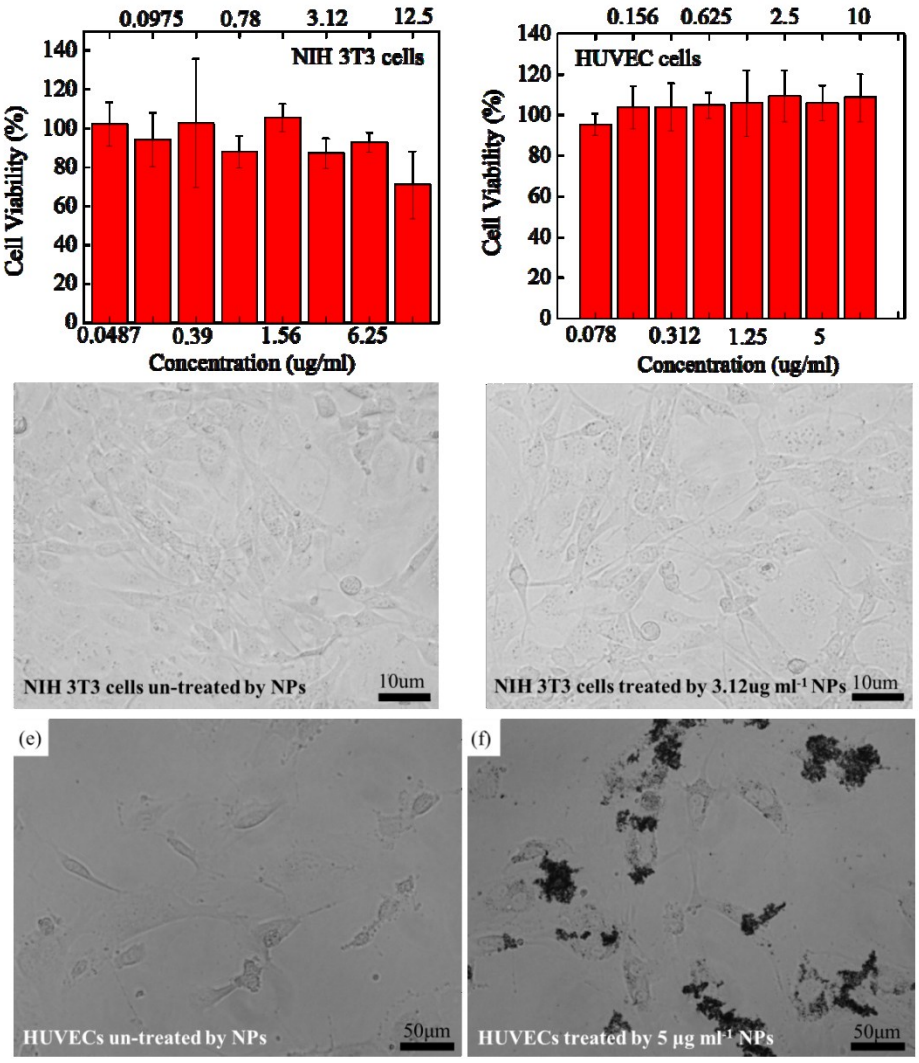

Figure 3.15 Cytotoxicity results of (a) Fe-Si particles on NIH T3T cells (b) Fe-Si particles on HUVECs. Optical images of NIH T3T cells (c) un-treated by Fe-Si particles (d) treated by 3.12ug/ml Fe-Si particles. Optical images of HUVECs (e) un-treated by Fe-Si particles (f) treated by 5ug/ml Fe-Si particles

Optical images of cells are presented in Figure 3.15 with different amount of nanoparticles loaded. A reference sample of cells without any treatment by nanoparticles was also imaged as shown in Figure 3.15(c). When the concentration of particles is within the safe range, the morphology of cells doesn't show any difference from the reference sample (Figure 3.15(d)). When the concentration of particles increases to 12.5ug/ml, morphology of cells changes to spherical. It is in consistence with the decrease of cell viability. The gradual change of morphology indicates a possible apoptosis mechanism for cell death. It is another evidence of the benign nature of the material Fe and Si. They haven't caused acute effects on cells such as cell death due to necrosis. Similar results were observed for HUVECs.

To further confirm that these particles can be potentially used in-vivo, hemolysis was done at different concentration. Blood was collected from an eight-month male mouse from the heart and centrifuged at 1500 rpm for 5 min at 4°C. The plasma supernatant was removed, and the erythrocytes were resuspended in 2ml ice cold PBS. The cells were again centrifuged at 1500 rpm for 5 min at 4°C. This procedure was repeated more than two times to ensure the removal of any released hemoglobin. After the supernatant was removed, the cells were resuspended in PBS solution and diluted to get a red blood cell (RBC) solution with Abs=0.6 at 650nm. Nanoparticles were also diluted in PBS to reach different concentrations. 0.1mL of the particles were added to 0.1mL of the RBC solution in a 96-well plate and incubated for 1 h at 37°C with mild shaking. Complete hemolysis was attained using a 2% v/v Triton-X yielding the 100% control value. PBS was used as negative control. After incubation, the 96-well plates were centrifuged at 1500 rpm for

5min, and 100μL of the supernatants were transferred to another 96 well plate. The release of hemoglobin was determined by UV at 414nm. Each sample was done triplicate. The percentage of relative hemoglobin release was calculated using % lysis = $100*(A_{NP} - A_{blank})/(A_{triton} - A_{blank})$.

As shown in Figure 3.16, particles didn't cause any damage to red blood cells without any leakage of hemoglobin. Aggregation of blood cells was not observed under the testing conditions. These results indicate that Fe-Si nanoparticles may be highly biocompatible, which is a major advantage for using these nanoparticles in-vivo for medical applications.

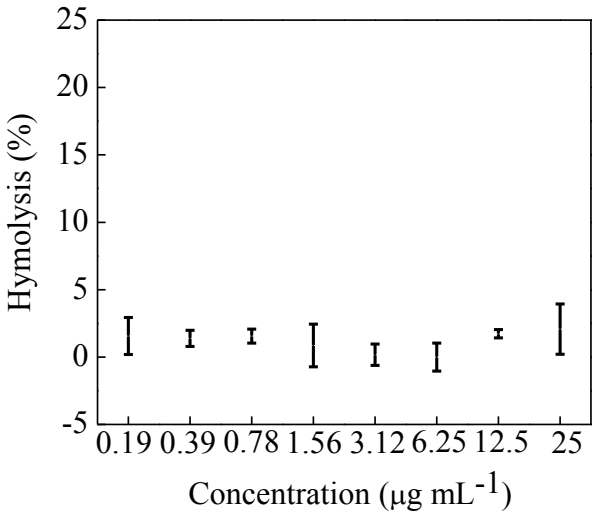

Figure 3.16 Hemolysis results of Fe-Si nanoparticles

3.7 Magnetic Field Heating

The capability to use Fe-Si particles to generate heat was demonstrated by performing heating experiments under an alternating magnetic field. Nanoparticles dispersed in distill water was subjected to an alternating magnetic field of 385kHz and 40Oe generated by an

induction coil system (Hyperthermia Inc.). The temperature change of the water was monitored by a fluoroptic thermometry system (Luxtron 3100, Lumasense Technologies) and recorded by a computer. A typical temperature rise with respect to time duration is plotted in Figure 3.17. Specific loss power (SLP) can be calculated based on Equation 2.11. The concentration of the particle solution was 2.1 mg/ml.

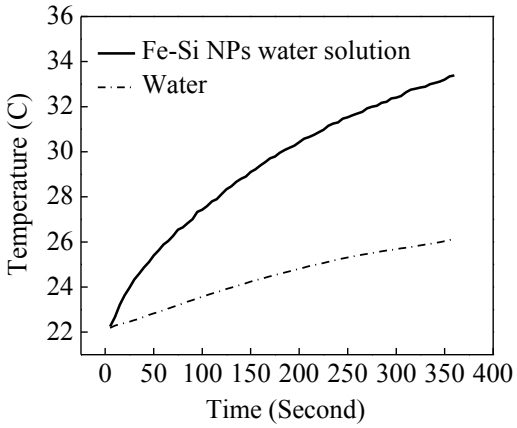

Figure 3.17 Temperature rise versus time of Fe-Si nanoparticles

In the following, magnetic field heating was performed under simulated human body conditions. Fe-Si nanoparticles were suspended in the mixture of distilled water and PBS PH=7.4 buffer. A 37°C water bath was applied to make particles start heating from the human body temperature. The same alternating magnetic field was used as in the previous experiment. Figure 3.18 displays the temperature rise as a function of time. SLP was also calculated and was found to be 209W/g.

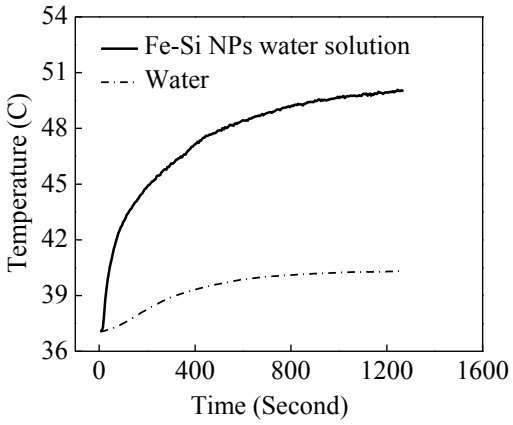

Figure 3.18 Temperature rise versus time of Fe-Si nanoparticles

The thermal energy has been proposed to enable targeted drug delivery , which has the potential to enable “on” and “off“ state, only activating the release mechanism of drugs locally at the affected area thus reducing the drug dose and unwanted side-effects. To test the possibility of using these particles for thermally assisted delivery of drug, heating experiment was also performed in combination with thermosensitive block copolymer. Poly(ortho ester amides) (POEA) block copolymer was synthesized according to the method published previously[36]. The block copolymer was specifically designed to have a gel-sol transition temperature at about 45°C. At low temperature, the POEA block copolymer is in the form of solid gel. It can act as a carrier of drug and magnetic NPs. As the temperature reaches the phase transition temperature, the POEA block copolymer changes to liquid sol and becomes soluable in water. A composite sample was prepared with POEA gel loaded with Fe-Si nanoparticles and fluorecent Rhodamine B dyes. 0.015 g POEA block copolymer was heated above the transition temperature to form the sol. Concentrated Fe-Si NPs and 0.001 g Rhodamine B dyes in PBS were mixed with the sol. A control sample was made with only POEA and dyes in a similar manner. The sample

was cooled down under shaking to form a gel. The concentration of NP was 0.5 wt% measured by ICP. 30μL PBS buffer was added afterwards. A control sample of POEA gel loaded with only dyes was also made. Both samples were subjected to the alternating magnetic field. Figure 3.19(a) shows the photo of the sample with nanoparticles before the magnetic field was turned on. A clear difference of color can be seen between PBS buffer and the composite gel, which suggests that the dye molecules are mostly entrapped in the gel. The temperature change of the composite during magnetic field heating was recorded and displayed in Figure 3.19(c). The composite gradually heats to the transition temperature of the block copolymer. As a result, the gel dissolves into the PBS buffer and the dye was completely released into the solution. The final solution has a uniformly dark red color from the released dye as shown in Figure 3.19(b). In comparison, the control sample without nanoparticles had an increase of temperature of about 3°C in total (Figure 3.19(e)). Before and after magnetic field heating, a clear difference of color exists between the PBS buffer and the composite (Figure 3.19(c) and (d)), which means that the gel couldn't dissolve without the heat generated by nanoparticles. Slight change of the color of PBS buffer before and after heating was possibly due to passive diffusion of dye molecules from the surface of the composite. Overall, this experiment provides evidence of the capability of Fe-Si nanoparticles for thermally assisted drug delivery. In conclusion, the heating experiments above established the feasibility of a potential drug release platform which consists of biocompatible Fe-Si nanoparticles and thermal sensitive block copolymer with intrinsic temperature regulation and drug release controlled by alternate magnetic field.

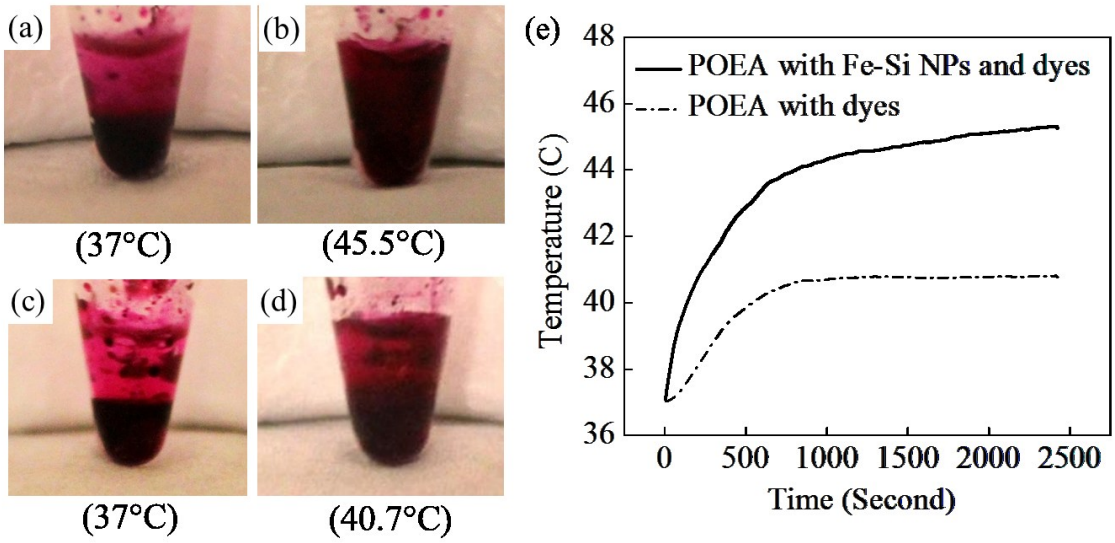

Figure 3.19 (a) POEA block copolymer in gel form (b) POEA block copolymer in sol form (c) Temperature rise versus time for POEA block copolymer gel loaded with low T_c Fe-Si nanoparticles

3.8 Conclusions

To summarize, we presented a route towards "smart" magnetic nanoparticles for self-regulated therapeutic applications. Analytical calculation was performed to show that temperature dependence of magnetization and magnetic anisotropy together lead to self-regulated heating performance. Fe-Si system was used to demonstrate the reduction of T_c through the tuning of exchange interaction. The decrease of T_c correlates with the weakening of exchange as the percentage of Si increases. Particles of Fe_5Si_3 phase show very low T_c which is potential for self-regulated therapy. The magnetic moment of particles can still be kept at a promising value. Meanwhile, with the choice of low toxic elements, Fe-Si nanoparticles provide low cytotoxicity compared to other metallic NPs. The capability to generate heat was proved using low T_c Fe-Si nanoparticles. And they can be combined with thermal sensitive block copolymer for drug release. This work

provides insights on a new type of biocompatible magnetic nanoparticles with intrinsic temperature regulation.

References

[1] J.-H. Lee, J.-t. Jang, J.-s. Choi, S. H. Moon, S.-h. Noh, J.-w. Kim, J.-G. Kim, I.-S. Kim, K. I. Park, and J. Cheon, Nat Nano **6,** 418 (2011).

[2] P. Guardia, R. Di Corato, L. Lartigue, C. Wilhelm, A. Espinosa, M. Garcia-Hernandez, F. Gazeau, L. Manna, and T. Pellegrino, ACS Nano **6,** 3080 (2012).

[3] C. Sun, J. S. H. Lee, and M. Zhang, Advanced Drug Delivery Reviews **60,** 1252 (2008).

[4] C. Martinez-Boubeta, K. Simeonidis, D. Serantes, I. Conde-Leborán, I. Kazakis, G. Stefanou, L. Peña, R. Galceran, L. Balcells, C. Monty, D. Baldomir, M. Mitrakas, and M. Angelakeris, Advanced Functional Materials**,** n/a (2012).

[5] H. Huang, S. Delikanli, H. Zeng, D. M. Ferkey, and A. Pralle, Nat Nano **5,** 602 (2010).

[6] Y. V. Kudryavtsev, Y. P. Lee, J. Dubowik, B. Szymański, and J. Y. Rhee, Physical Review B **65,** 104417 (2002).

[7] O'Handley, *Modern Magnetic Materials: Principles and Applications* (Wiley-Interscience, 1999).

[8] R. Hergt, S. Dutz, and M. Zeisberger, Nanotechnology **21,** 015706 (2010).

[9] G. Bertotti, *Hysteresis in Magnetism* (Academic Press Limited, 1998).

[10] J. Carrey, B. Mehdaoui, and M. Respaud, Journal of Applied Physics **109,** 083921 (2011).

[11] E. Pollert, K. Knížek, M. Maryško, P. Kašpar, S. Vasseur, and E. Duguet, Journal of Magnetism and Magnetic Materials **316,** 122 (2007).

[12] N. K. Prasad, K. Rathinasamy, D. Panda, and D. Bahadur, Journal of Biomedical Materials Research Part B: Applied Biomaterials **85B,** 409 (2008).

[13] O. Kaman, P. Veverka, Z. Jirák, M. Maryško, K. Knížek, M. Veverka, P. Kašpar, M. Burian, V. Šepelák, and E. Pollert, Journal of Nanoparticle Research **13,** 1237 (2011).

[14] T. N. Brusentsova, N. A. Brusentsov, V. D. Kuznetsov, and V. N. Nikiforov, Journal of Magnetism and Magnetic Materials **293,** 298 (2005).

[15] T. N. Brusentsova and V. D. Kuznetsov, Journal of Magnetism and Magnetic Materials **311,** 22 (2007).

[16] *Nanoparticle Technology Handbook* (Elsevier Science, 2007).

[17] M. Bettge, J. Chatterjee, and Y. Haik, Biomagnetic research and technology **2,** 4 (2004).

[18] J. Chatterjee, M. Bettge, Y. Haik, and C. Jen Chen, Journal of Magnetism and Magnetic Materials **293,** 303 (2005).

[19] K. L. McNerny, Y. Kim, D. E. Laughlin, and M. E. McHenry, Journal of Applied Physics **107,** 09A312 (2010).

[20] J. J. Ipus, H. Ucar, and M. E. McHenry, Magnetics, IEEE Transactions on **47,** 2494 (2011).
[21] K. J. Miller, A. Colletti, P. J. Papi, and M. E. McHenry, Journal of Applied Physics **107,** 09A313 (2010).
[22] Y. Akin, I. M. Obaidat, B. Issa, and Y. Haik, Crystal Research and Technology **44,** 386 (2009).
[23] H. C. S. J. Stohr, *Magnetism: From Fundamentals to Nanoscale Dynamics* (Springer, 2006).
[24] E. P. E. a. G. N. K. a. V. A. B. a. E. V. Voronina, Journal of Physics: Condensed Matter **4,** 7597 (1992).
[25] B. Mehdaoui, A. Meffre, J. Carrey, S. Lachaize, L.-M. Lacroix, M. Gougeon, B. Chaudret, and M. Respaud, Advanced Functional Materials **21,** 4573 (2011).
[26] C. G. Hadjipanayis, M. J. Bonder, S. Balakrishnan, X. Wang, H. Mao, and G. C. Hadjipanayis, Small **4,** 1925 (2008).
[27] C. Martinez-Boubeta, L. Balcells, R. Cristòfol, C. Sanfeliu, E. Rodríguez, R. Weissleder, S. Lope-Piedrafita, K. Simeonidis, M. Angelakeris, F. Sandiumenge, A. Calleja, L. Casas, C. Monty, and B. Martínez, Nanomedicine: Nanotechnology, Biology and Medicine **6,** 362 (2010).
[28] M. Moravej, F. Prima, M. Fiset, and D. Mantovani, Acta Biomaterialia **6,** 1726 (2010).
[29] H. Hermawan, D. Dubé, and D. Mantovani, Acta Biomaterialia **6,** 1693 (2010).
[30] D. T. a. Y. M. a. K. H. a. Kouki Fujioka and Masaki Hiruoka and Keisuke Sato and Noriyoshi Manabe and Ryosuke Miyasaka and Sanshiro Hanada and Akiyoshi Hoshino and Richard, Nanotechnology **19,** 415102 (2008).
[31] L. Wang, V. Reipa, and J. Blasic, Bioconjugate Chemistry **15,** 409 (2004).
[32] F. Erogbogbo, K.-T. Yong, I. Roy, G. Xu, P. N. Prasad, and M. T. Swihart, ACS Nano **2,** 873 (2008).
[33] E. Tasciotti, X. Liu, R. Bhavane, K. Plant, A. D. Leonard, B. K. Price, M. M.-C. Cheng, P. Decuzzi, J. M. Tour, F. Robertson, and M. Ferrari, Nat Nano **3,** 151 (2008).
[34] L. T. Canham, Advanced Materials **7,** 1033 (1995).
[35] F. Erogbogbo, K.-T. Yong, R. Hu, W.-C. Law, H. Ding, C.-W. Chang, P. N. Prasad, and M. T. Swihart, ACS Nano **4,** 5131 (2010).
[36] S. C. Bayliss, R. Heald, D. I. Fletcher, and L. D. Buckberry, Advanced Materials **11,** 318 (1999).
[37] V. Chin, B. E. Collins, M. J. Sailor, and S. N. Bhatia, Advanced Materials **13,** 1877 (2001).
[38] J. M. Qiu and J. P. Wang, Advanced Materials **19,** 1703 (2007).
[39] Y. H. Xu and J. P. Wang, Advanced Materials **20,** 994 (2008).
[40] M. K. Kolel-Veetil, S. B. Qadri, M. Osofsky, R. Goswami, and T. M. Keller, The Journal of Physical Chemistry C **113,** 14663 (2009).
[41] N. Dahal and V. Chikan, Chemistry of Materials **22,** 2892 (2010).
[42] S. Vitta, Journal of Applied Physics **101,** 063901 (2007).
[43] S. N. Kaul, Physical Review B **24,** 6550 (1981).

[44] R. d. B. a. Z. L. a. G. W. Ming Zhang and Ekkes Brück and Frank, Journal of Physics D: Applied Physics **37,** 2049 (2004).
[45] L. Ritchie, G. Xiao, Y. Ji, T. Y. Chen, C. L. Chien, M. Zhang, J. Chen, Z. Liu, G. Wu, and X. X. Zhang, Physical Review B **68,** 104430 (2003).
[46] V. Johnson, J. F. Weiher, C. G. Frederick, and D. B. Rogers, Journal of Solid State Chemistry **4,** 311 (1972).
[47] E. P. Elsukov, G. N. Konygin, V. A. Barinov, and E. V. Voronina, Journal of Physics: Condensed Matter **4,** 7597 (1992).
[48] R. W. McCallum, Journal of Magnetism and Magnetic Materials **292,** 135 (2005).
[49] S. Okamoto, N. Kikuchi, O. Kitakami, T. Miyazaki, Y. Shimada, and K. Fukamichi, Physical Review B **66,** 024413 (2002).
[50] O. Margeat, M. Tran, M. Spasova, and M. Farle, Physical Review B **75,** 134410 (2007).
[51] J. U. Thiele, K. R. Coffey, M. F. Toney, J. A. Hedstrom, and A. J. Kellock, Journal of Applied Physics **91,** 6595 (2002).
[52] T. Novet and D. C. Johnson, Journal of the American Chemical Society **113,** 3398 (1991).
[53] C. Xu, Z. Yuan, N. Kohler, J. Kim, M. A. Chung, and S. Sun, Journal of the American Chemical Society **131,** 15346 (2009).
[54] M.-J. Hu, Y. Lu, S. Zhang, S.-R. Guo, B. Lin, M. Zhang, and S.-H. Yu, Journal of the American Chemical Society **130,** 11606 (2008).
[55] R. Tang, R. N. Palumbo, W. Ji, and C. Wang, Biomacromolecules **10,** 722 (2009).

Chapter 4 High-Magnetic-Moment Fe_xCo_{1-x} Nanoparticles for Biomolecule Detection and Magnetic Coloring

4.1 Introduction

The use of magnetic nanoparticles or magnetic beads for bio-sensing is one of the important topics[1]. Detection of magnetic signal from the particles is realized by different types of sensors, such as magnetoresistive (MR) sensors, search coils, and superconducting quantum interface device (SQUID). Compared to optical detection by using quantum dots, a magnetic way has the advantages to reach high sensitivity, to have low interference from the biological background and to be able to be implemented into a portable device platform. Therefore, bio-molecule detection based on magnetic particles and sensors is emerging as a highly potential diagnosis tool.

In this chapter, we present a sensitive detection system based on GMR sensor and FeCo nanoparticles. We propose to have the ability to label and differentiate bio-molecules based on different magnetic nanoparticles — enabling "magnetic colors". It is in analogy to quantum dots that have emissions at different wavelength and provide distinct luminescent signal. Magnetic nanoparticles can produce different magnetic signal when they are carefully engineered. A possible way to build "magnetic colors" is using Fe-Co material system. Fe-Co nanoparticles of different composition (0.7:0.3, 0.40:0.6, 0.1:0.9) were made by a physical gas condensation method. Nanoparticles are well-crystallized and have small size distribution. Phase of nanoparticles evolve from body-centered-cubic

(BCC) to face-centered-cubic (FCC) as composition of Co increases in the particles. Magnetic characterization revealed composition dependent properties, which is also evidence of a successful control of phase and composition. The different magnetic properties as a function of composition provide the base of magnetic coloring for bio-sensing. Further investigations were carried out to assist understanding of the inherent property of the nanoparticles. We will discuss the influence of the metal-oxide core-shell structure and interparticle interactions on magnetic properties.

4.2 Biomolecule detection

GMR sensor and magnetic nanoparticles can make up a diagnosis system for biomolecule detection. When magnetic nanoparticles are on in close proximity of a GMR sensor, the magnetic dipolar field will be sensed by the sensor, and leads to a change of magnetoresistance of the sensor, as introduced in 1.4.4. We established a highly sensitive GMR sensor-magnetic nanoparticle detection system[2]. Specifically designed GMR sensor chips were fabricated with a proper coercivity to increase the sensitivity. In addition, we employed high-magnetic-moment $Fe_{70}Co_{30}$ particles which provide more advantages in terms of signal. The particles are uniform in size and have cubic shape as shown in Figure 4.1. The mean size ranges from 12.5nm-13.5nm with 10%-18% standard deviation. To demonstrate the capability of such a system, we adopted biotin-streptavidin as a model study. Magnetic nanoparticles surface was introduced amino group by ATPES modification. Afterwards, nanoparticles were labeled with streptavidin-AF488. It was estimated that one nanoparticle corresponded to 1.3 streptavidin molecule. After applying

these nanoparticles onto biotin modified sensor surface, the streptavidin-biotin interaction leads to chemical conjugation and generates a magnetic signal. Our quantification showed that as few as 600 copies of streptavidin can be detected.

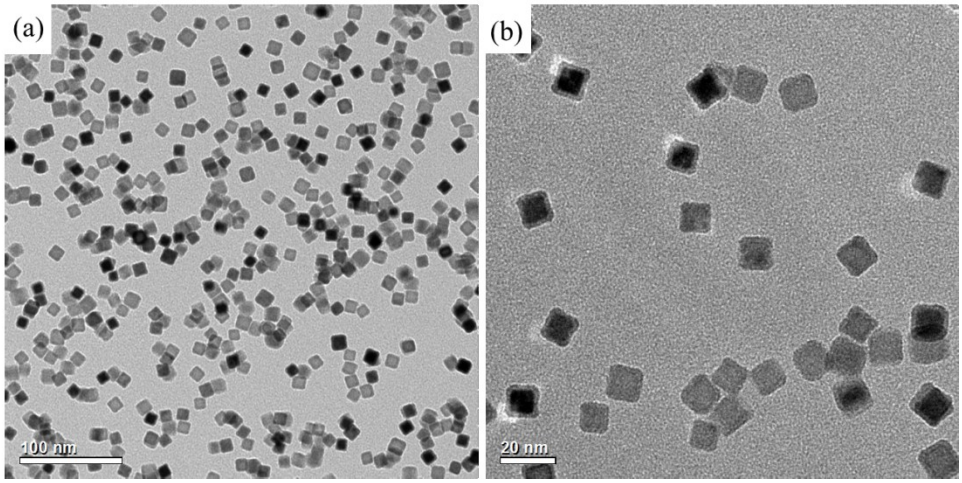

Figure 4.1 (a) TEM image of FeCo particles at low magnification (b) TEM image of FeCo particles at high magnification

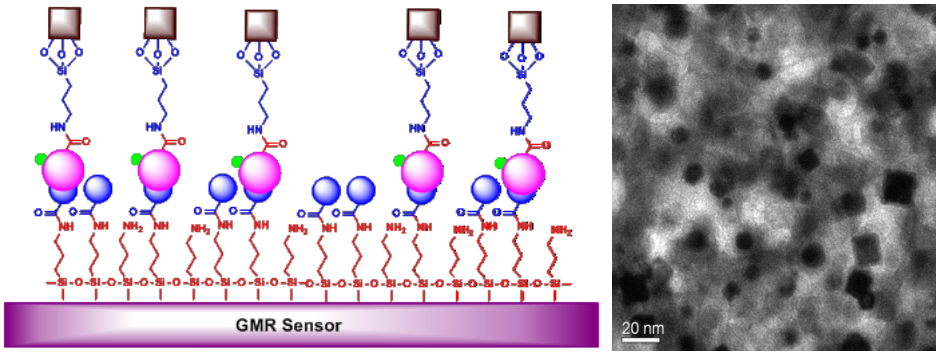

Figure 4.2 (a) FeCo nanoparticle labeled streptavidin-AF488 was allowed to bind with biotin on the sensor surface (b) TEM image of FeCo particles modified with strepavidin-AF488

The feasibility for such a system to detect real biological molecules, human interleukin-6 (IL-6), a biomarker of lung cancer was studied. Here a sandwiched approach was employed. Nanoparticles labeled by detection antibody (polyclonal anti-human IL-6) can

bind to IL-6, then bind to the surface of GMR sensor which was labeled with capture antibody (monoclonal anti-human IL-6). It has been found that a signal from as low as $2.08*10^6$ IL-6 molecules can be detected. The success proves that usage of proper magnetic particles benefits biosensing system. It is 13 times more sensitive than IL-6 ELISA assay. Later, by adopting a competition-based detection scheme e, we demonstrated that the GMR sensor and FeCo nanoparticle detection system can quantify unprocessed IL-6 human serum sample in 5 minutes[3]. Such a system may eventually become the ground of a low-cost and hand-held medical device for early detection of diseases.

4.3 Magnetic Coloring

A scheme is shown in Figure 4.3 to illustrate the concept of a magnetic coloring system we proposed based on MR sensors and different magnetic nanoparticles. In principle, "magnetic colors" can be realized by employing specially designed particles and a non-linear detection scheme[4]. Small magnetic nanoparticles usually used are superparamagnetic at room temperature. How their magnetic moment response to a

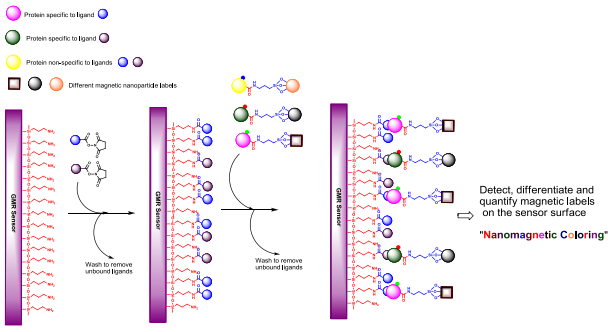

Figure 4.3 Scheme of a magnetic coloring system based on GMR sensor and different magnetic nanoparticles

magnetic field, namely the M-H loop, can be described or approximated by Langevin function.

$$M = M_s \times L(\frac{m_0\mu_0 H}{k_B T}) = M_s \times \left(c\tanh(\frac{m_0\mu_0 H}{k_B T}) - \frac{k_B T}{m_0\mu_0 H} \right) \quad \text{(Equation 4.1)}$$

where Ms is the saturation magnetization, m_0 is the magnetic moment of a single particle, μ_0 is the permeability of free space, H is the applied field, k_B is Boltzmann constant, T is temperature. Apply two sinusoidal fields to the particles, one with low frequency and high amplitude in the form of $A_1 \cos(2\pi f_1 t + \theta_1)$, and one with high frequency and low amplitude in the form of $A_2 \cos(2\pi f_2 t + \theta_2)$. The high amplitude field drives magnetization of particles to non-linear region. The low amplitude field modulates the magnetic signal of particles and contributes to the detected magnetic induction. A second order mixing component and a third order mixing component can be obtained by substituting the fields into Equation 4.1 and making Talor expansion at zero field. The magnetic response of nanoparticles in frequency domain is represented by linear terms f_1, f_2 and mixing terms mf_1+nf_2 (m, n are integers). A simulated spectrum is shown in Figure 4.4(a) and (b), which presents the spectrum in time domain and frequency domain of an M-H loop, respectively. Different magnetic response or M-H loops will lead to different spectra composed of f_1, f_2, mf_1+nf_2. Such spectra serve as an identity to recognize the corresponding magnetic particle. If we code the spectra into different colors, "magnetic coloring" is then going to be realized.

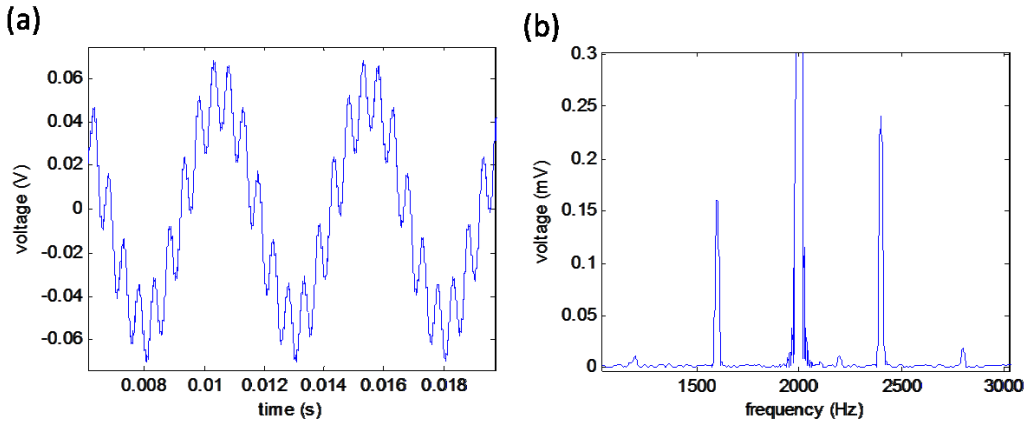

Figure 4.4 (a) Time domain spectrum of magnetic response of nanoparticles under an sinusoidal field (b) Frequency domain spectrum of magnetic response of nanoparticles under an sinusoidal field

From the above discussions, we can see that to create "magnetic colors" needs an archive of magnetic nanoparticles that can respond to magnetic field differently. There are different approaches to make such particles. For example, by tuning the size, by applying heterostructures, or by changing the shape can possibly lead to magnetic particles with different M-H loops.

In addition to achieving the distinct magnetic behavior, it is also critical to have individual nanoparticle possess as large as possible magnetic signal. Because all the detections rely on the magnetic signal from nanoparticles, nanoparticles that can provide high signal should improve overall performance in principle. Good signal to noise ratio can be kept in this way while total dose of nanoparticles is low. Although by increasing the size of nanoparticles can possibly increase the magnetic signal carried by a single particles, this method inevitably face physical limits for certain applications where particle size cannot be too large. For instance, in antibody detection it is sometimes

required a comparable size of particles with respect to that of proteins (15nm-20nm)[2]. It also puts limitation on using size as the knob to tune "color". Therefore, a practical way to achieve high magnetic moment nanoparticles is through choosing materials with intrinsic high saturation magnetization. An analytical calculation was made to compare the magnetic signal from nanoparticles made of materials with high and low saturation magnetization. $Fe_{0.6}Co_{0.4}$ nanoparticle, Fe_3O_4 and γFe_2O_3 nanoparticles of the same size are used as example materials. Their M-H loops were plotted in Figure 4.5 using the ideal Langevin function and bulk saturation magnetization. At an external field of 20 Oe, the moment of an isotropic $Fe_{0.6}Co_{0.4}$ nanoparticle is $2.4*10^{-15}$emu, which is 17 times larger than that of a Fe_3O_4 nanoparticle and 28 times than that of a γFe_2O_3 nanoparticle. It means that a single $Fe_{0.6}Co_{0.4}$ nanoparticle responses to the applied field much faster in the small field region, leading to a quick rise in magnetic moment value. This is even more critical than the absolute saturation magnetization for bio-sensing since in many cases, the working field is relatively small. Because oxidation usually takes place for unprotected Fe-Co nanoparticles, a comparison is also made between oxidized Fe-Co nanoparticles and iron oxide nanoparticles. In consideration of the natural oxidation layer (approximately 1.5nm thick), the calculated hysteresis loop of one oxidized Fe-Co nanoparticle is also shown in Figure 4.5 (dashed line). Its moment is still 6 and 10 times larger than that of the same size Fe_3O_4 and γFe_2O_3 nanoparticle. The analysis reveals significant advantages of high-magnetic-moment particles for bio-sensing. Some real applications already demonstrate the benefits by using such nanoparticles [2 5 6].

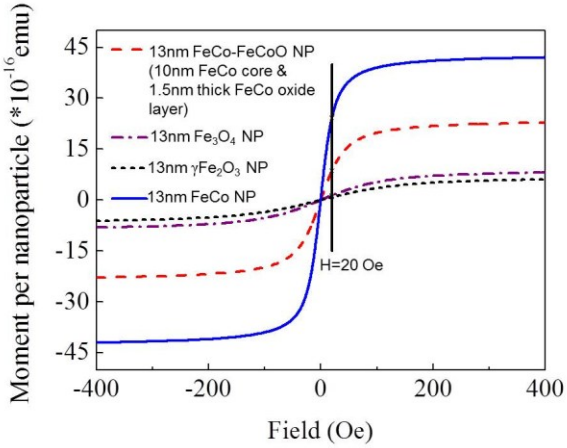

Figure 4.5 Calculated M-H loops of a single particle of unoxidized $Fe_{0.7}Co_{0.3}$, Fe_3O_4, γFe_2O_3 and $Fe_{0.7}Co_{0.3}$-FeCoO

TABLE 4.1 Calculated Magnetization Values

Nanoparticle type	Saturation magnetic moment of a single nanoparticle	Magnetic moment of a single nanoparticle at H=20Oe
Unoxidized FeCo (13nm)	$4.3*10^{-15}$ emu	$2.4*10^{-15}$ emu
Fe_3O_4 (13nm)	$9.1*10^{-16}$ emu	$1.36*10^{-16}$ emu
γFe_2O_3 (13nm)	$7.1*10^{-16}$ emu	$0.83*10^{-16}$ emu
FeCo-FeCoO (10nm FeCo core &1.5 nm FeCoO shell)	$2.38*10^{-15}$ emu	$8.65*10^{-16}$ emu

We took an approach to obtain nanoparticles with different “magnetic colors” as well as high magnetic moment by varying the composition of Fe-Co alloy. As the composition

varies, change of magnetization and magnetocrystalline anisotropy can lead to a change of magnetic behavior or the shape of M-H loops. Fe_xCo_{1-x} alloys occupy the top level of magnetization among transition metal and alloys. The highest saturation magnetization occurs when Fe is about 65at%. The material system is valuable in terms of technological potential. Many efforts have been devoted to synthesis of high magnetic moment nanoparticles such as elemental Fe, Co, Ni and their alloys. However, challenges still exist to get well-controlled properties. Arch plasma and laser pulsed deposition are physical methods previously investigated where particles show irregular morphology and poor crystallinity[7] [8]. Accessible chemical protocols lead to a popularity of various chemical synthesis which gives controllable growth of particles. Although elemental transition metal particles can be well synthesized with the advance of wet chemistry[9] [10], Fe-based bimetallic particles still face issues in phase and crystallinity control due to formation of intermediate complexes and segregation of elements[11]. There remains room for development of phase and composition controlled particles with non-depleted magnetic properties and small size distribution[12].

4.4 Fabrication and Characterization of Fe_XCo_{1-X} Nanoparticles

Fe_xCo_{1-x} nanoparticles were fabricated in gas phase using a magnetron-sputtering-based system. A piece of alloy target of specific composition was used as the source material. Ar gas was both sputtering gas and carrier gas. The strength of magnetic field on target surface was 650Oe-700Oe. Base pressure was around $1*10^{-7}$ torr. Sputtering current was

0.5A and sputtering voltage was about 250V. Controllable crystal growth in our method arises from the thermal environment control through manipulation of magnetic field[13]. The strength of magnetic field was set to medium range. When the strength was below or above this range much, Fe-Co particles can have poor crystallinity or sintering. Uniformity was kept by adjusting sputtering pressure with magnetic field maintained at the suitable range. A high pressure indicates a fast cooling rate in the process of crystal growth. In our experiments, relatively low sputtering pressure was applied to promote a gradual cooling.

Morphology and crystal structure of Fe_xCo_{1-x} nanoparticles was characterized by a transmission electron microscope. Bright field images were shown in Figure 4.6(a)(c)(e) of $Fe_{0.7}Co_{0.3}$, $Fe_{0.4}Co_{0.6}$ and $Fe_{0.1}Co_{0.9}$, respectively. When nanoparticles are rich in Fe, they exhibit cubic shape. For the sample with lowest Fe composition (x=0.1), an icosahedron shape can be deduced from the projection views of nanoparticles in the image. The difference in shape can actually be explained by minimization of surface energy in the frame of the corresponding crystal structure. Based on the selected area diffraction pattern of an ensemble of particles in Figure 4.6(b)(d)(f), the crystal structure of particles are determined. As labeled in the figure, Fe rich Fe-Co alloy particles possess BCC structure. The cubic shape of the particles suggests surface terminated with (200) planes. Although (110) plane of a BCC crystal has the lowest surface energy, minimal total surface energy doesn't correspond to (110) terminated surface. Because clusters with (110) planes terminated surface will have many corners and ridges, total energy is actually enhanced compared to the surface terminated with (200) planes. Therefore, given

enough time and energy to crystalize, particles form cubic shape driven by the minimization of total energy. $Fe_{0.1}Co_{0.9}$ particles were found to have FCC structure of which (111) plane is the lowest energy surface. Similarly, icosahedron shape is mainly present for $Fe_{0.1}Co_{0.9}$ which lower the surface energy by comprising many (111) planes on the surface[14]. Three samples of different composition all have similar size range around 12nm and good uniformity. The results demonstrate that by using gas phase synthesis method, well-crystalized Fe-Co alloy nanoparticles are able to be obtained.

Magnetic properties of Fe_xCo_{1-x} nanoparticles were explored by SQUID. Figure 4.7 displays hysteresis loops at room temperature of Fe-Co nanoparticles. The particles are not fully in superparamagnetic regime although they show small remanence and coercivity. Specific magnetization value was determined by measuring the total moment of nanoparticles and the mass of nanoparticles in the sample. The saturation magnetization is close to bulk value, which indicates great potential of the high magnetic moment nanoparticles. Change of magnetization along with composition is in consistence with the trend described by Slater-Pauling curve. The magnetization value proves that Fe-Co alloy nanoparticles fabricated by this method possess high magnetic moment and great potential in applications. If we look closely at the hysteresis loops when particles approach to saturation, the three loops show largely different curvature at around 1500 Oe. This difference means that the three types of nanoparticles can provide distinct magnetic signals when using the non-linear sensing scheme. It is possible to take advantage of such difference to establish a library of magnetic labels for magnetic coloring.

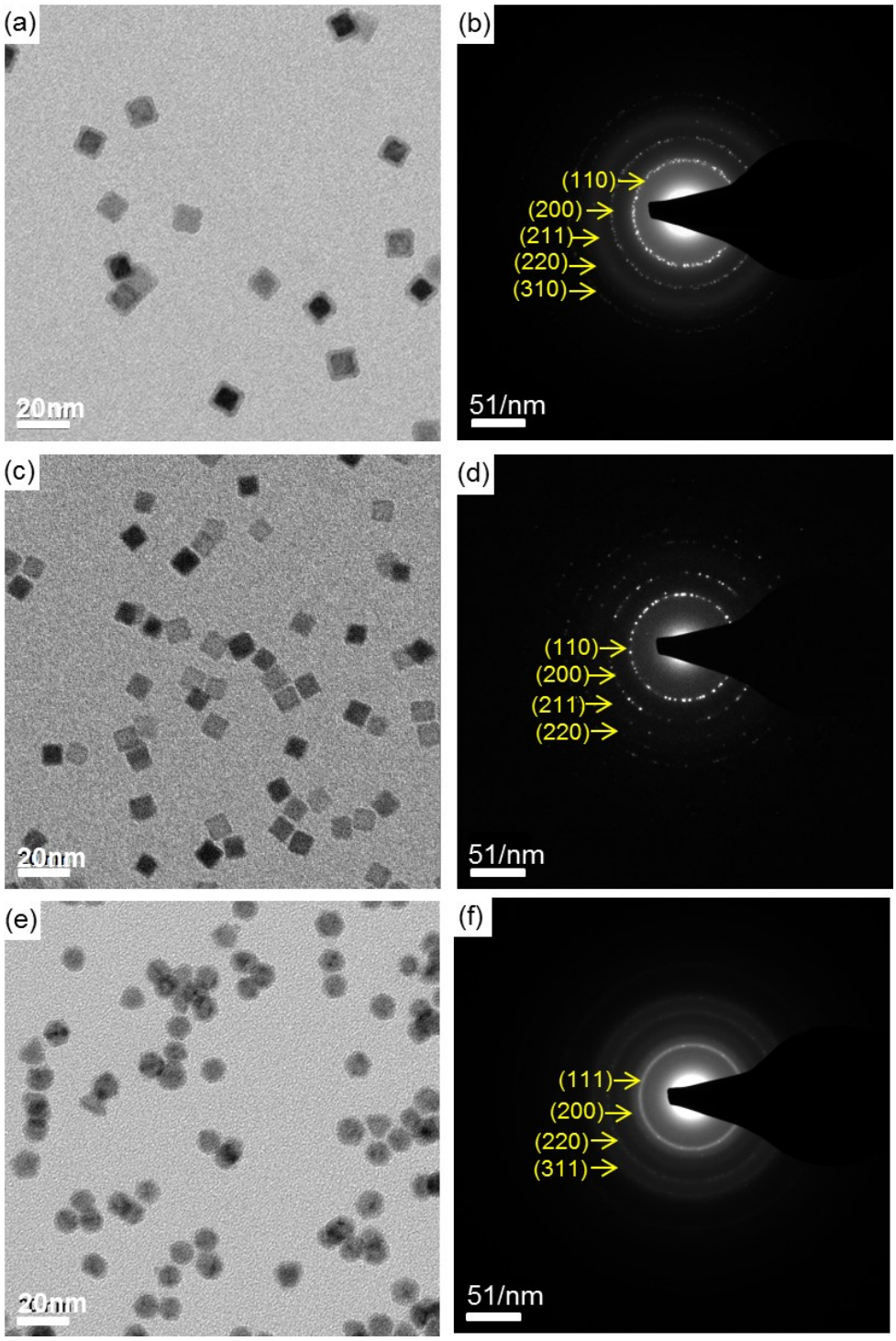
(a)
20nm
(b)
(110)
(200)
(211)
(220)
(310)
51/nm
(c)
20nm
(d)
(110)
(200)
(211)
(220)
51/nm
(e)
20nm
(f)
(111)
(200)
(220)
(311)
51/nm

Figure 4.6TEM bright field images and selected area diffraction pattern of (a) (b)$Fe_{0.7}Co_{0.3}$ (c)(d)$Fe_{0.4}Co_{0.6}$ (e)(f)$Fe_{0.1}Co_{0.9}$

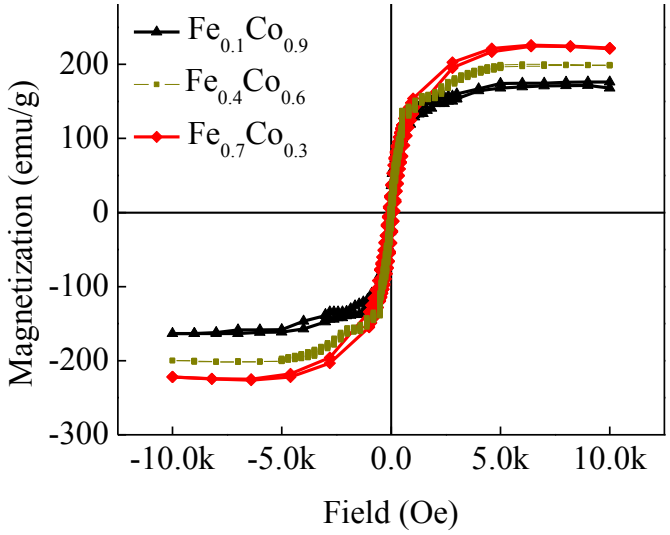

Figure4. 7 Hysteresis loops of $Fe_{0.7}Co_{0.3}$, $Fe_{0.4}Co_{0.6}$,$Fe_{0.1}Co_{0.9}$ Nanoparticles

4.5 Exchange biased core-shell Nanostructure

4.5.1 Exchange bias

Exchange bias was investigated in as synthesized Fe_xCo_{1-x} nanoparticles for further understanding of the nanostructure. Exchange bias was first studied in fine particles historically. Meiklejohn et. al found that field cooled, partially oxidized, Co particles exhibited hysteresis loops displaced along the magnetic field axis[15]. Thin film exchange biased system was then investigated extensively and was more popular than fine particle system due to the ease of interface control[16]. The underlying principle for the phenomena is the exchange interaction between ferromagnetic part and antiferromagnetic part in a sample. When the ferromagnetic part is aligned with a magnetic field, its interface spins couple with the antiferromagnetic part as shown in the right top corner of Figure 4.8.

When the magnetic field sweeps to the other direction, ferromagnetic part tends to follow the direction of the field. Spins at the interface need to overcome the coupling and eventual switching of ferromagnetic part takes place at a larger magnetic field compared to the case without exchange bias. Similarly, when the applied field sweeps back to the original direction, switching of ferromagnetic part is easier because spins at the interface favor parallel alignment with the antiferromagnetic part. Above all, exchange bias can be viewed as an effective field that is present along with the external applied field. This effective field is defined as exchange bias field H_{ex} and has a magnitude of relative shift of the loop along the magnetic field axis.

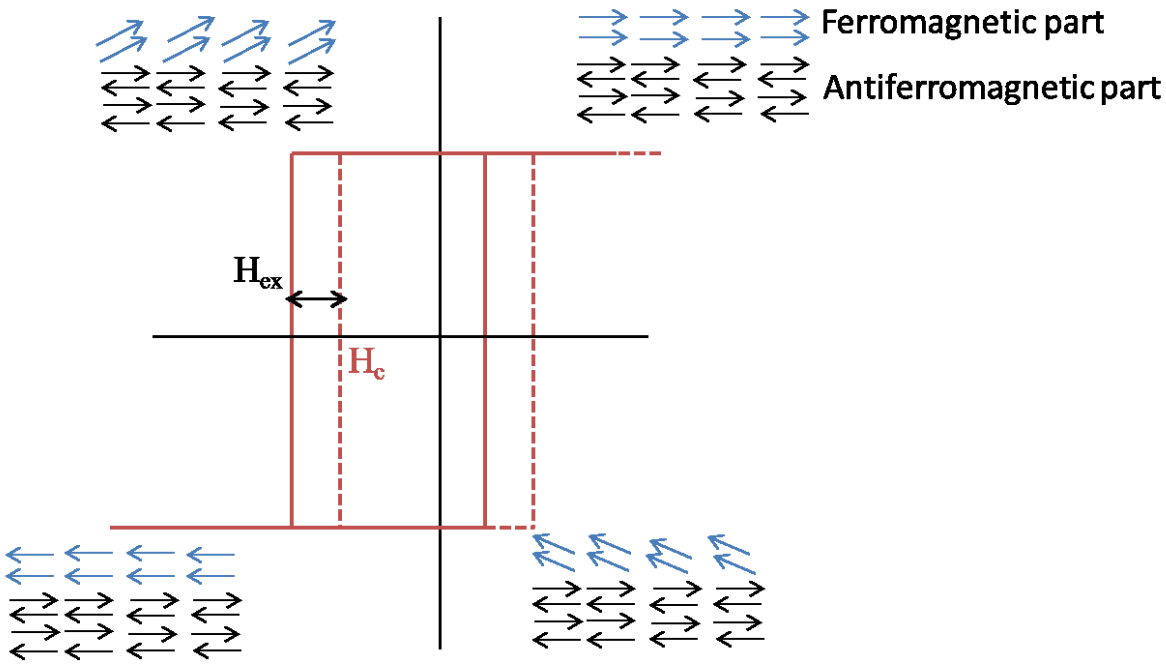

Figure4. 8 Illustration of exchange bias induced loop shift

In order to observe above loop shift effect of exchange bias, a few conditions have to be met. Antiferromagnetic material has phase transition temperature, called Néel temperature, at which the material changes from antiferromagneic to paramagnetic. Therefore, the temperature has to be kept below Néel temperature when measuring the hysteresis loop. In addition, the ferromagnetic part has to be aligned with the antiferromagnetic part. Usually, it is achieved by doing field cool process in experiments using a magnetometer. The sample was subjected to a large constant magnetic field when temperature is decreased from room temperature to below Néel temperature. The interface property can also influence how well exchange bias is developed.[16]

Exchange bias was proposed as one scheme to stabilize nanoparticles for magnetic recording and information storage[17]. Although the idea is not compatible with today's recording technology, investigation of exchange bias in nanostructures is extensively carried out since it can provide in-depth understanding of the magnetic structure[18 19].

4.5.2 Exchange bias in Fe_xCo_{1-x} based core-shell nanoparticles

In our synthesis method, Fe_xCo_{1-x} nanoparticles form an oxide shell after they are taken out of vacuum chamber and exposed to air. The oxide shell is mostly amorphous like. The metal core-oxide shell type nanoparticles were used for exchange bias study. Zero-field-cooling (ZFC) and field-cooling (FC) was carried out by SQUID. ZFC hysteresis loops were measured firstly at 5K when temperature was decreased from 300K with no magnetic field applied. FC hysteresis loops were measured at 5K afterwards when

temperature was decreased from 300K with 1.5T magnetic field applied. Figure 4.9 shows ZFC and FC hysteresis loops of Fe-Co nanoparticles in different composition. Covercity of hysteresis loops was also displayed in the figure. Coercivity of ZFC loops increases as a function of composition. It is due to an increase of crystalline anisotropy caused by increasing concentration of Co in the material. Intrinsically Co gives large spin-orbital interaction and magnetically hard property. Such variation of coercivity with composition is another evidence of successful phase control.

Enhancement of coercivity was observed for all three samples after nanoparticles went through FC compared to the coercivity after ZFC. The enhancement of coercivity is due to the exchange bias between antiferromagnetic part and ferromagnetic part of a nanoparticle. However, there wasn't a distinguishable loop shift after FC. When anisotropy of anitiferromagnetic part is small, exchange bias will not induce a shift of FC loop. Instead increase of coercivity is the resulting effect due to a small exchange bias field[16]. It is concluded for our particles that exchange bias arises from the coupling between the oxide layer and the metal core of a particle. The amorphous oxide is antiferromagnetic in nature and the core is ferromagnetic.

The property of the oxide layer varies with composition and gives rise to a change of exchange bias field. The exchange bias field increases in companion with the increase of Co in the particle, which indicates an increase of anisotropy of the oxide layer dependent on the amount of Co. Therefore surface oxide layer acts as the antiferromagnetic part and also has increasing cyrtalline anisotropy with the increase of Co. Presumably the oxide layer contains CoO and FeO in different percentage. Both oxides can be

antiferromagnetic at low temperature. The anisotropy change along with the composition of Co suggests that CoO is the majority of the oxide part with large crystalline anisotropy, which plays an important role in the exchange bias in Fe-Co alloy core-shell nanoparticles. The observed exchange bias in our nanoparticles is weak compared to that reported in Co-CoO nanostructures[17]. It can be a consequence of noncrystalline oxide structure and a mixture of two kinds of oxides on the surface.

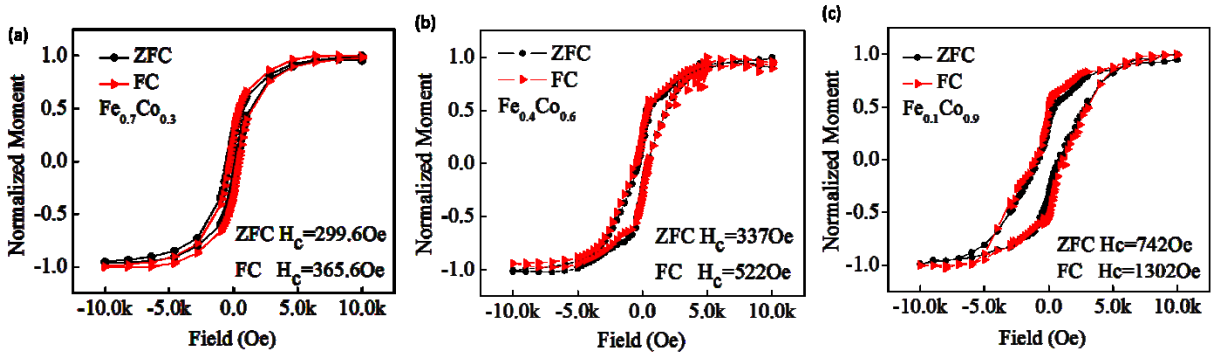

Figure 4.9 ZFC and FC loops of (a)$Fe_{0.7}Co_{0.3}$, (b)$Fe_{0.4}Co_{0.6}$ and (c)$Fe_{0.1}Co_{0.9}$ nanoparticles

In spite of the exchange bias effect, the oxide shell also changes the soft magnetic property of the Fe-Co nanoparticle. To examine the magnetic behavior of Fe-Co nanoparticles without oxide shell, $Fe_{0.7}Co_{0.3}$ particles were deposited onto a Si substrate and were capped by an additional layer of Cu in-situ. Hysteresis loops of Cu capped $Fe_{0.7}Co_{0.3}$ particles were displayed in Figure 4.10. At 300K, nearly zero hysteresis can be observed. More importantly, at 5K the coercivity is only 77Oe, which is much smaller than that of $Fe_{0.7}Co_{0.3}$ particles without capping (Figure 4.10(a)). It suggests that oxidation deteriorates the softness of particles. The deterioration is not a result of exchange bias because reduced softness was seen even when the exchange bias doesn't

take effect. This is evidenced by the fact that the coercivity of capped particles is smaller than that of ZFC loop of uncapped particles. In this case exchange bias is not present without aligning the ferromagnetic part and antiferromagnetic part by field cooling. We argue that the reduced softness is possibly due to geometrical effect. Particles are not uniformly oxidized over entire surface because the interface between particles and the substrate can be less exposed to air. The metal core may become asymmetric, which leads to increased effective anisotropy. Magnetization curve was measured at 5K to estimate the anisotropy constant for oxidized Fe-Co alloy particles. Nanoparticles were first demagnetized by a dc magnetic field with continuously varying magnitude. Then magnetization curve was measured up to 1T by SQUID. By applying law of approach to saturation, the anisotropy constant was deduced for the nanoparticles of three compositions (Figure 4.11). The value is higher than usual anisotropy constant of soft Fe-Co alloy, especially for $Fe_{0.7}Co_{0.3}$ nanoparticles. If we refer back to the hysteresis loop of $Fe_{0.7}Co_{0.3}$ at room temperature (Figure 4.7), the small hysteresis could have contribution from enhanced effective anisotropy.

In summary, the oxide shell of Fe-Co alloy particles is antiferromagnetic. Both crystalline anisotropy of the alloy core and the oxide shell are a function of the percentage of Co. The increasing percentage of Co correlates with the increase of anisotropy and thus the increase of coercivity field as well as exchange bias field. The asymmetrical oxidation causes an increase of effective anisotropy, which changes the magnetic soft property of Fe rich Fe-Co alloy.

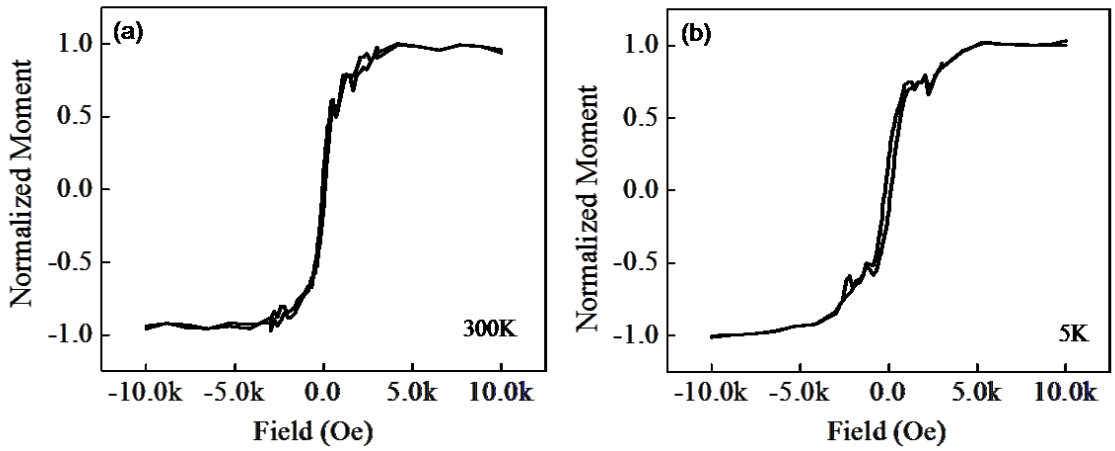

Figure 4. 10 Hysteresis loops of $Fe_{0.7}Co_{0.3}$ nanoparticles with Cu capping at (a)300K and (b)5K

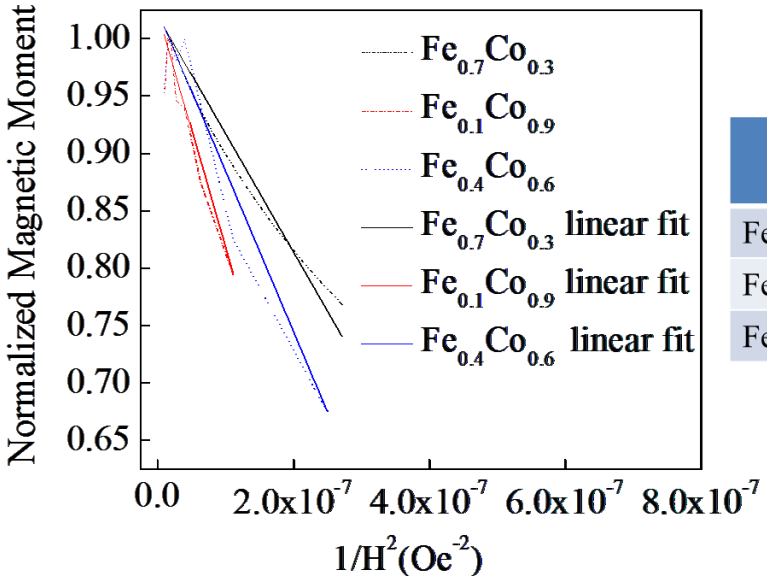

	Anisotropy constant ($ergs/cm^3$)
$Fe_{0.7}Co_{0.3}$	0.9×10^5
$Fe_{0.4}Co_{0.6}$	3.3×10^6
$Fe_{0.1}Co_{0.9}$	5×10^6

Figure 4. 11 Plots of normalized magnetic moment versus inverse of square of magnetic field for $Fe_{0.7}Co_{0.3}$, $Fe_{0.4}Co_{0.6}$, $Fe_{0.1}Co_{0.9}$ nanoparticles (left) and calculated anisotropy constants (right)

4.6 Interparticle Interactions of Fe-Co Nanoparticles

Interparticle interaction is usually present in nanoparticulate samples, which can affect the magnetic behavior of nanoparticles. Two categories of interparticle interactions are mostly studied: exchange interaction and dipolar interaction. Exchange interaction is the interaction between nanoparticles through atomic scale contact. Exchange coupling of spins on the contacting interface can change the magnetization reversal process, magnetic ordering temperature and so on. Such interaction is also possible in an indirect way. For example, indirect exchange coupling was observed among Fe dots through Cu substrate as the coupling media[20]. Dipolar coupling is the other category of interparticle interactions. Dipole field from a nanoparticle can apply on adjacent particles and dipole-dipole interaction can eventually cause a collective magnetic behavior[21]. Above all, interparticle interaction is a practical aspect to be considered when dealing with nanoparticulate system.

Interparticle interaction was examined for nanoparticles synthesized in gas phase. $Fe_{0.7}Co_{0.3}$ nanoparticles were used as a study example. Deposition time was varied to prepare samples with different deposition density on the Si substrates. In our synthesis system, because particles land onto a substrate randomly, there are chances that they are close to each other. The longer the deposition time, the higher probability to have nanoparticles closely packed together. The long deposition time leads to many local areas with several particles in close proximity. The particles are close enough to interconnect with each other for some regions. Hysteresis loops at 300K are shown in Figure 4.12 (b) and (d) corresponding to the different packing density, respectively. Enlarged hysteresis can be observed for the sample with high deposition density and a relatively large

coercivity of 83 Oe is associated with it. It reveals that geographical arrangement of nanoparticles can give strong interparticle interaction and cause apparent difference in hysteresis behavior. Hence the interaction is most possibly dipolar type and gives rise to an enhancement of effective magnetic energy barrier [22,23]. Overall, interparticle interaction is present and typical in our synthesis method. Magnetic characterization of nanoparticles probes collective magnetic property including the interaction in reality.

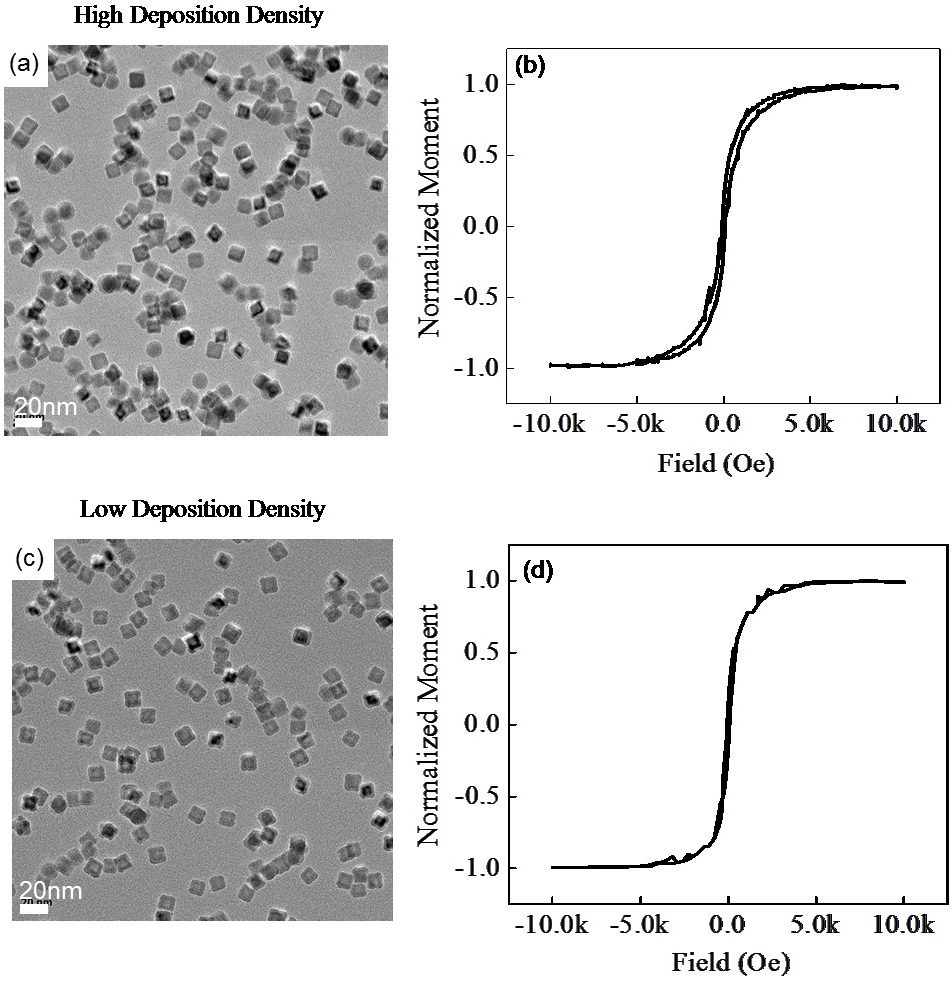

Figure 4.12 (a)TEM bright field images of $Fe_{0.7}Co_{0.3}$ nanoparticles at high deposition density and (b)the corresponding hysteresis loop at 300K; (c)TEM bright field image of $Fe_{0.7}Co_{0.3}$ nanoparticles and (d) the corresponding hysteresis loop at 300K

4.7 Conclusions

In conclusion, Fe_xCo_{1-x} nanoparticles of different compositions were synthesized with well crystallized structure and uniform size. The physical synthesis method is demonstrated here to be suitable for making high-magnetic-moment metallic particles in a controlled manner. Magnetic properties were found in agreement with the corresponding composition and structure. The integration of GMR sensor and FeCo nanoparticles were proven to be a capable system for bio-molecule detection. The tunability of magnetic behavior by changing composition offers an approach to build "magnetic colors". Different shape of loops of Fe_xCo_{1-x} nanoparticles suggests a possible magnetic coloring system with high-magnetic-moment. Detailed magnetic characterization provides additional understanding of the Fe_xCo_{1-x} nanoparticles. It has to be noticed that multiple effects are involved in magnetic measurements and embedded in the results, which includes surface oxide, interface coupling and interparticle interactions.

References

1 R. S. Gaster, D. A. Hall, and S. X. Wang, Nano Letters **11,** 2579 (2010).

2 B. Srinivasan, Y. Li, Y. Jing, Y. Xu, X. Yao, C. Xing, and J.-P. Wang, Angewandte Chemie International Edition **48,** 2764 (2009).

3 Y. Li, B. Srinivasan, Y. Jing, X. Yao, M. A. Hugger, J.-P. Wang, and C. Xing, Journal of the American Chemical Society **132,** 4388 (2010).

4 J. P. Wang.

5 C. G. Hadjipanayis, M. J. Bonder, S. Balakrishnan, X. Wang, H. Mao, and G. C. Hadjipanayis, Small **4,** 1925 (2008).

6 W. S. Seo, J. H. Lee, X. Sun, Y. Suzuki, D. Mann, Z. Liu, M. Terashima, P. C. Yang, M. V. McConnell, D. G. Nishimura, and H. Dai, Nat Mater **5,** 971 (2006).

7 P. L. Ong, S. Mahmood, T. Zhang, J. J. Lin, R. V. Ramanujan, P. Lee, and R. S. Rawat, Applied Surface Science **254,** 1909 (2008).

[8] F. Bulut, W. Rosellen, and M. Getzlaff, Applied Physics A: Materials Science & Processing **97,** 185 (2009).
[9] L.-M. Lacroix, N. Frey Huls, D. Ho, X. Sun, K. Cheng, and S. Sun, Nano Letters **11,** 1641 (2011).
[10] F. Dumestre, B. Chaudret, C. Amiens, P. Renaud, and P. Fejes, Science **303,** 821 (2004).
[11] X.-W. Wei, G.-X. Zhu, Y.-J. Liu, Y.-H. Ni, Y. Song, and Z. Xu, Chemistry of Materials **20,** 6248 (2008).
[12] D. Kodama, K. Shinoda, K. Sato, Y. Konno, R. J. Joseyphus, K. Motomiya, H. Takahashi, T. Matsumoto, Y. Sato, K. Tohji, and B. Jeyadevan, Advanced Materials **18,** 3154 (2006).
[13] J.-M. Qiu and J.-P. Wang, Applied Physics Letters **88,** 192505 (2006).
[14] N. Semagina and L. Kiwi-Minsker, Catalysis Reviews **51,** 147 (2009).
[15] W. H. Meiklejohn and C. P. Bean, Physical Review **105,** 904 (1957).
[16] J. Nogués, J. Sort, V. Langlais, V. Skumryev, S. Suriñach, J. S. Muñoz, and M. D. Baró, Physics Reports **422,** 65 (2005).
[17] V. Skumryev, S. Stoyanov, Y. Zhang, G. Hadjipanayis, D. Givord, and J. Nogues, Nature **423,** 850 (2003).
[18] V. Baltz, J. Sort, S. Landis, B. Rodmacq, and B. Dieny, Physical Review Letters **94,** 117201 (2005).
[19] K. Liu, S. M. Baker, M. Tuominen, T. P. Russell, and I. K. Schuller, Physical Review B **63,** 060403 (2001).
[20] L. Yin, D. Xiao, Z. Gai, T. Z. Ward, N. Widjaja, G. M. Stocks, Z.-h. Cheng, E. W. Plummer, Z. Zhang, and J. Shen, Physical Review Letters **104,** 167202 (2010).
[21] C. Djurberg, P. Svedlindh, P. Nordblad, M. F. Hansen, F. Bødker, and S. Mørup, Physical Review Letters **79,** 5154 (1997).
[22] J. M. Vargas, W. C. Nunes, L. M. Socolovsky, M. Knobel, and D. Zanchet, Physical Review B **72,** 184428 (2005).
[23] G. C. Papaefthymiou, E. Devlin, A. Simopoulos, D. K. Yi, S. N. Riduan, S. S. Lee, and J. Y. Ying, Physical Review B **80,** 024406 (2009).

Chapter 5 Optically Active Magnetic Nanoparticles of Core-Shell Structure

5.1 Introduction

The challenges of sustainable energy and environment are becoming the main concerns of the world economy and societal development. Catalysis is one strategic field of research that can address these challenges because it offers solutions to the sustainability of energy and environment. Green catalysis has been investigated, which can enable chemical reactions and minimize the use of toxic or hazardous substances [1,2]. Among various catalysis techniques, the photochemical process or photocatalysis provides an environmentally friendly direction which harnesses solar energy by using light-absorptive materials. Electron-hole pairs generated through the absorption of light can participate in and catalyze oxidation or degradation in chemical reactions.

Fe^{3+} oxides gained large interests for photocatalytic applications in organic pollutant destruction, synthesis of carbon nanotubes, and water splitting due to its active absorptivity, wide availability and low cost [3,4,5,6,7]. Commonly used iron oxide (αFe_2O_3 or γFe_2O_3) absorbs light in a large wavelength range where photon energy exceeds the band gap energy 2.2eV. However, iron oxide usually doesn't give a high photocurrent quantum efficiency or photodegradation rate so their application as efficient photocatalysts is limited. Many attempts have been made to change the structure or physical properties of

the material. Nanoparticulate structure is preferable in photocatalysis applications due to the large surface area to volume ratio. Apte et. al. synthesized αFe_2O_3 and γFe_2O_3 nanoparticles with a "ginger root" morphology and found a good photocatlytic activity because of the increased surface area[5]. Nevertheless, the average size of their nanoparticles is still relatively large in the 45nm-55nm range. The reported absorption spectrum indicates a large portion of holes generated in valence band made up of 3d crystal field orbitals of Fe^{3+}, which could affect photocatalytic performance due to the limited hole transfer [8,9]. Cherepty et. al tested doped γ-Fe_2O_3 nanoparticles with 10 at% Zn, Cu, Cr, Co and found no influence of these dopants on the optical properties[8]. Turner et. al[10] and Glasscock et. al[11] reported an enhanced photocurrent in Si doped αFe_2O_3 bulk (10 at%) and thin film (~5 at%) photoelectrode, respectively. Their results can be consulted for the choice of doping element in nanoparticulate structures. Feng et. al demonstrated degradation of organic pollutant catalyzed by an iron oxide pillared-layered clay composite composed of γ-Fe_2O_3 and iron silicate crystallites as a low cost catalyst system[12]. Unfortunately, this type of composite structure can have a large fluctuation of surface area and it is not easy to control preparative steps to achieve reproducibility[13]. One of the key challenges, which has not been addressed in previous attempts, is how to isolate and separate the photocatalysts from the final production. This is very critical for environmental and cost consideration[1,14]. Strongly magnetic nanocatalysts can bridge green catalysis and recycling by using a magnetic field for re-collection, and they are highly desirable in real-life applications. Performance of nanocatalysts can even be enhanced by controlling their motion using an alternating magnetic field[15].

In this chapter, we present a magnetic core-shell nanostructure with iron dominant as the core and Si doped iron oxide as the shell potentially for the recyclable photocatalysis application. Nanoparticles were fabricated by a physical method with a mean size of about 16nm and good crystallinity. Strong absorption observed in 310nm-450nm wavelength range could offer photocatalytic property of improved hole transfer[8,16,17]. The promising magnetic property from the core offers straightforward recycling of the nanoparticles.

5.2 Development of Optically Active Fe-FeSiO Nanoparticles

5.2.1 Si doped Iron-iron oxide Nanoparticles

Si doped iron-iron oxide (Fe-FeSiO) nanoparticles were fabricated directly by the physical gas condensation method. A piece of Fe-Si composite target was used in this work. The base pressure of the vacuum system was 10^{-7} Torr. Ar gas was used as both sputtering gas and carrier gas. Deposition pressure was controlled from 200mTorr to 500mTorr and sputtering voltage was about 250V. Oxidation passivation of the nanoparticles was performed by exposing them to ambient air.

The morphology and crystal structure of Fe-FeSiO nanoparticles were characterized by a transmission electron microscope (TEM). Figure 5.1(a)(b) displays the characterization results. The mean size, defined by the diameter of these nanoparticles, is 15.9 nm with 19% standard deviation. The selected area diffraction pattern suggests good crystallinity based on the discrete diffraction spots. Lattice spacing was measured in reciprocal space

and the determined value was then compared with standard powder diffraction file. The diffraction pattern confirms the existence of Fe and γ-Fe_2O_3.

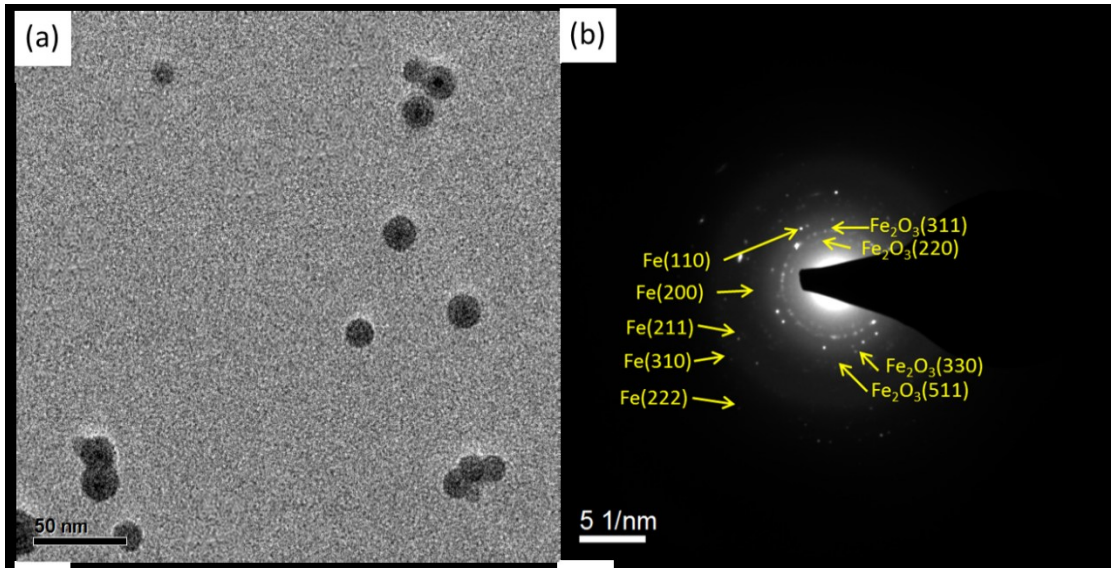

Figure 5.1 (a) Bright field image of Fe-FeSiO nanoparticles (b) Selected area diffraction pattern of Fe-FeSiO nanoparticles by TEM

Analysis of the composition of nanoparticles was carried out on a large scale as well as an individual particle level. The average composition of Fe-FeSiO nanoparticles was analyzed by a ThermoElemental PQ ExCell quadrupole ICP-MS. Nanoparticles suspended in solution were used for measurements. The readings reported 17 wt% of Si in the total mass of Fe and Si. The composition of silicon lies in the relatively low end of the Fe-Si system. The distribution of Si in Fe-FeSiO nanoparticles was explored by energy dispersive X-ray (EDX) equipped on TEM under STEM mode. The size of electron beam is around 1nm in diameter in STEM mode. The high-angle-diffraction-dark field image in Figure 5.2(a) reveals a core-shell structure which can be seen from the contrast between the core and the shell. Electron beam was placed in the core and shell region of a nanoparticle as shown in Figure 5.3(a), and the corresponding EDX spectrum

was taken. The spectrum gives composition ratio of Fe:Si:O=56.77wt%:13.13wt%:30.10wt% for the shell and Fe:Si:O=76.50wt%:5.00wt%:18.50wt% for the core. Considering the consistent contribution to the signal of Si and O from the surface, the result indicates a core-shell structure where the core consists of mainly Fe. Although there isn't complete exclusion of Si in the core, the shell is where most Si presents.

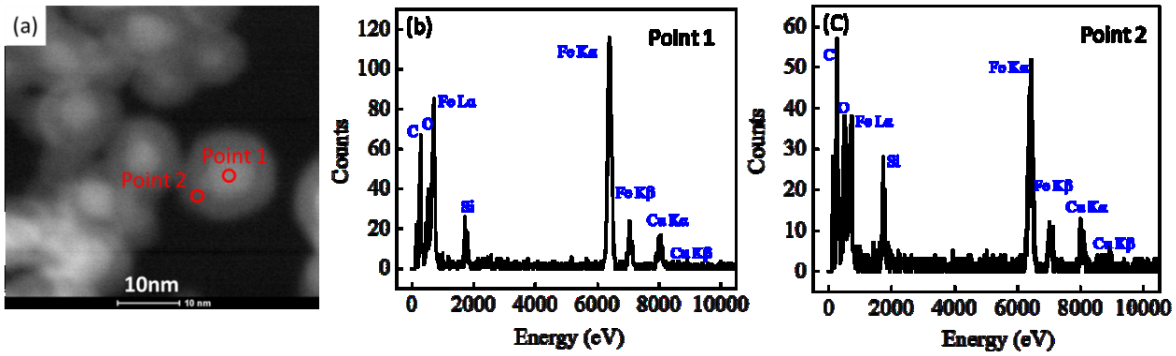

Figure 5.2 (a) HAADF image under STEM mode (b) EDX spectrum of point 1 (c) EDX spectrum of point 2

5.2.2 Iron-iron oxide and amorphous Si Nanoparticles

Iron-iron oxide (Fe-FeO) nanoparticles and amorphous Si nanoparticles were also prepared in a similar way as reference samples for the following absorption test. A piece of pure Fe target (99.9%) and a piece of pure Si target (99.99%) were used for the synthesis, respectively. The synthesis conditions were varied to optimize the final formation of particles. Figure 5.3 (a) and (b) show the morphology and crystallinity of Fe-FeO nanoparticles without any Si doping. They have a similar shape and size with that of Fe-FeSiO nanoparticles. Diffraction pattern of Fe-FeO nanoparticles also shows the crystalline form of Fe and γFe_2O_3. Si nanoparticles have a relatively larger size than that

of Fe-FeO. The mean size is about 23nm. The diffraction pattern of Si nanoparticles shows only blur shades, which is a sign of the amorphous structure of the particles.

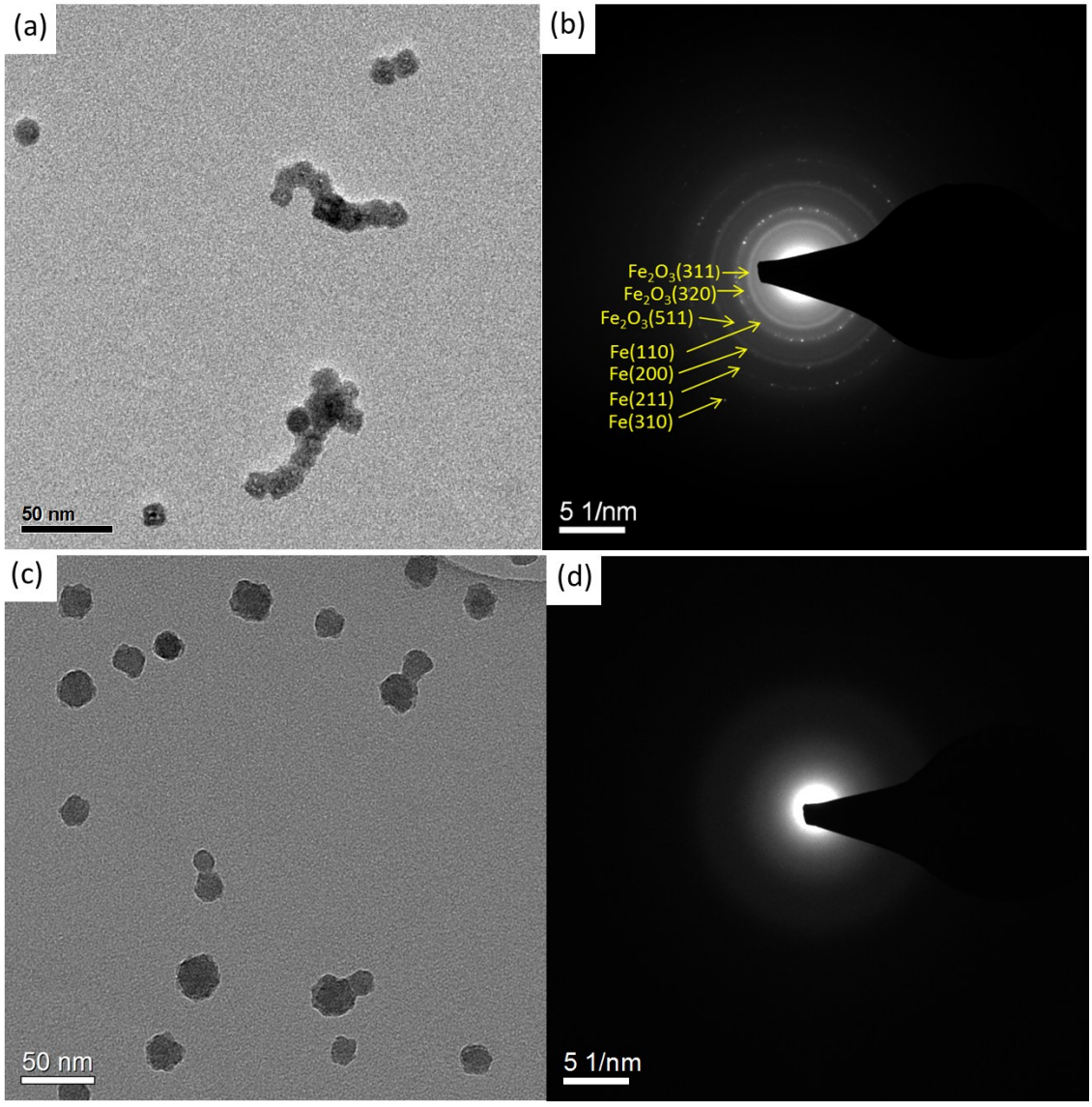

Figure 5.3 Bright field image of (a)Fe-FeO nanoparticles and (c)Si-SiO nanoparticles ; Selected area diffraction of (b)Fe-FeO nanoparticles and (d)Si-SiO nanoparticles

5.3 Optical Properties of Fe-FeSiO Nanoparticles

5.3.1 Mechanism of Optical Absorption

The capability of iron oxides to strongly absorb light arises from the transitions between different electronic configurations. Electronic transitions can originate from ligand field of Fe^{3+}, ligand to metal charge transfer or pair excitation. Usually, the three origins co-exist and contribute to the absorption in different wavelengths.

Ligand field transitions are electronic transitions taking place between electronic states of d electrons of Fe^{3+}. In oxidized iron, coordination sites of Fe^{3+} can adopt octahedral or tetrahedral arrangement depending on the particular crystal structure [19]. For octahedral coordination, Fe^{3+} is surrounded by six oxygen atoms and forms polyhedron $(FeO_6)^{9-}$ as illustrated in Figure 5.4(a). For tetrahedral coordination

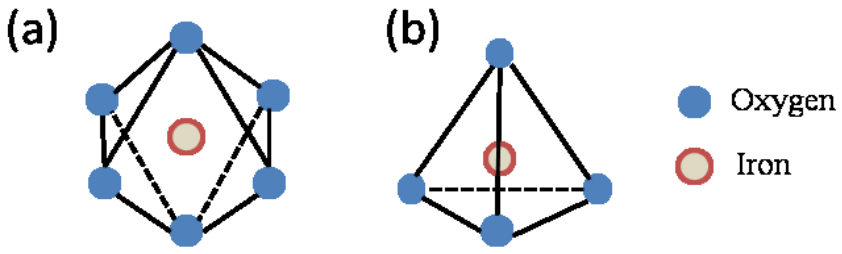

Figure 5.4 Octahedral and tetrahedral coordination of Fe^{3+}

$(FeO_4)^{5-}$, Fe^{3+} is surrounded by four oxygen atoms as illustrated in Figure 5.4(b). Ratio of Fe^{3+} octahedral sites to tetrahedral sites is 1:5 for example in γFe_2O_3. In such polyhedral coordination, Fe^{3+} atomic orbitals are split into two sets of orbitals, namely t_{2g} and e_g. The energy separation of these two orbitals is crystal field splitting. Within the orbitals, they each split due to exchange energy giving two sets of t_{2g} and two sets of e_g orbitals for

spin-up (α spin) and spin-down (β spin) electrons. The exchange energy is usually larger than crystal field energy. Therefore, state of spin-up will be first taken up by electrons. The arrangement of electrons in orbitals and their spin state make up the different possible electronic states of t_{2g} and e_g orbitals. Ligand field transitions happen between the electronic states. Figure 5.5 presents possible electronic states of octahedral or tetrahedral high spin Fe^{3+} called Tanabe-Sugano diagram. The ground state $^6A_1$ of Fe^{3+} is where spin-up electrons occupy t_{2g} and e_g orbitals in the configuration of $(t_{2g\alpha})^3(e_{g\alpha})^2$. The first possible excited configuration is $(t_{2g\alpha})^3(e_{g\alpha})^1(t_{2g\beta})^1$, which gives $^4T_1$ and $^4T_2$ in the diagram. The remaining states in the diagram come from $(t_{2g\alpha})^2(e_{g\alpha})^2(t_{2g\beta})^1$ and $(t_{2g\alpha})^3(e_{g\alpha})^1(e_{g\beta})^1$.

From the point of view of quantum mechanics, all of the transitions from ground state $^6A_1$ to excited states are both spin and parity forbidden. However, in the presence of

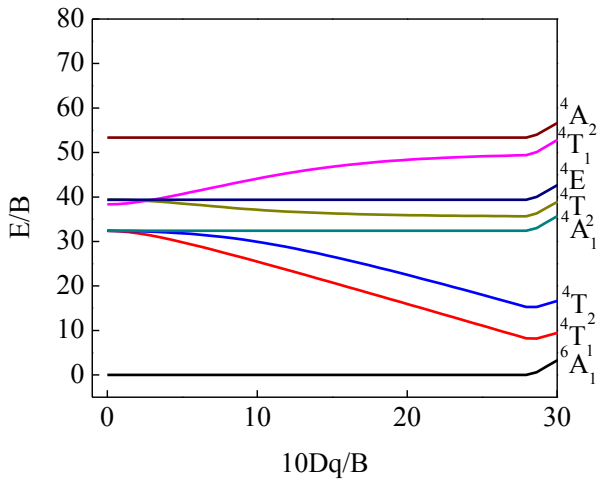

Figure 5.5 Octahedral and tetrahedral coordination of Fe^{3+}

magnetic coupling between neighboring Fe^{3+}, transitions become allowed considering spectroscopic selection rules for Fe^{3+}-Fe^{3+} pair. When the integral of transition moment within two transition states is not zero ($\int_{-\infty}^{+\infty}\Psi_1^{*}\mu\Psi_2 d\tau$), the transition is allowed [20]. A qualitative way to understand the electronic state associated with Fe-Fe pair is by assuming a coupling between two Fe through Heisenberg Hamiltonian: $H = JS_a \cdot S_b$ where S_a and S_b are electronic spins of two Fe^{3+}, and J is Heisenberg exchange integral. This Hamiltonian acts as small perturbation to the ligand field of uncoupled Fe. Energy state for the pair based on quantum mechanics is [21]:

$$E = (\frac{J}{2})[S(S+1) - S_a(S_a+1) - S_b(S_b+1)]$$

$S=S_a+S_b$, S_a+S_b-1, ····· S_a-S_b, representing the spin states of Fe^{3+} pair. When both Fe^{3+} are in ground state, $S_a=S_b=5/2$, states of the Fe^{3+} pair will be S=5, 4, 3, 2, 1, 0. When one of the Fe^{3+} is excited to a higher state such as $^4T_1$ ($S_a=5/2$, $S_b=3/2$), states of the Fe^{3+} pair will be S=4, 3, 2, 1. Transitions from ground states S=4, 3, 2, 1 to excited states can thus be spin allowed ($\Delta S=0$). The underlying mechanism of the electronic transitions determines that they are closely related with the crystal field of the material, which depends on symmetry and bonding strength. In addition, strength of exchange coupling between Fe^{3+} pair also affects how much the forbidden transitions can be relaxed. For instance, in αFe_2O_3 face-sharing octahedral clusters leads to trigonal distortion of $(FeO_6)^{9-}$, giving rise to a stronger antiferromagnetic coupling between neighbor Fe ions than that in γFe_2O_3. The absorption therefore for αFe_2O_3 due to the excitation of single-ion is stronger than γFe_2O_3.

Optical absorption can also take place based on other principles. Ligand to metal charge transfer is one of them. It typically shows up in the absorption spectrum at shorter wavelength regime than Fe^{3+} ligand field transitions. The charge transfer happens between molecular orbitals localized on oxygen atoms and 3d orbitals of Fe. For polyhedron $(FeO_6)^{9+}$, the transitions with lowest energy are from non-bonding orbitals on oxygen atoms to the anti-bonding t_{2g} orbitals of Fe^{3+}. Usually transitions at wavelength below 270nm are assigned to ligand-to-metal charge-transfer transitions[21].

The third possible mechanism for absorption is pair excitation. It is also based on magnetically coupled neighboring Fe ions as in ligand field transitions of Fe^{3+}. But in pair excitation, simultaneous excitation of a pair of Fe^{3+} ions from ground state to excited state gives absorption features. The energy level of pair excitation is about the sum of the two ligand field transitions of a single Fe^{3+}. The transition is spin allowed as a result of the magnetic coupling of Fe ions. When two Fe^{3+} are in excited states, we have $S_a=S_b=3/2$. Excited state of the Fe^{3+} pair will be S=3, 2, 1, 0. Transitions from ground state S=3, 2, 1, 0 to excited states are possible[22].

The above principles govern the absorption of different minerals and oxides containing Fe^{2+} or Fe^{3+}. Four regions can usually be found in the absorption spectrum with each regime designated to the specific principle[22]. Absorption in region 1 from 250nm to 400nm is mostly due to metal-to-ligand charge-transfer and ligand field transitions ($^6A_1 \rightarrow {}^4T_1$ (^4P) at 290nm-310nm, $^6A_1 \rightarrow {}^4E$ (^4D), $^6A_1 \rightarrow {}^4T_2$ (^4D) at 360-380nm). Absorption in region 2 from 400nm to 600nm arises from pair excitation process ($^6A_1 + {}^6A_1 \rightarrow {}^4T_1$ (^4G) + $^4T_1$ (^4G)). There could be contribution from ligand field transitions ($^1A_1 \rightarrow {}^4E$) too.

Region 3 at 600nm-750nm and region 4 at 750nm-900nm are both assigned to ligand field transitions, $^6A_1 \rightarrow {}^4T_2$ (^4G) and $^6A_1 \rightarrow {}^4T_1$ (^4G). It is thus possible for us to deduce the possible origin of absorption by observing the details of absorption spectrum.

It is convenient to view the three principles in the frame of band structure. The optical property is actually a result of the intrinsic band structure for iron oxides as what happens for other semiconducting materials. The band is composed of 3d orbitals of Fe^{3+} and 2p orbitals of O^{2-}. A schematic description of the band structure is shown in Figure 5.6 on the basis of the proposed configuration by Z. Zhang et. al[9] and L. Fu et. al[23]. The conduction band is mainly made up of empty 3d and 4s orbitals of Fe^{3+}. The valence band consists of non-bonding O 2p orbitals as well as partially filled 3d orbitals of Fe^{3+} at different energy levels. Many intra bands exist in between conduction band and valence band. They cause trapping of electrons and have great influence on the optical property. In the frame of such a band structure, widely accepted 2.2eV band gap can be interpreted in a simple way for αFe_2O_3 and γFe_2O_3. It is just the difference of energy level between partially filled 3d orbitals of Fe^{3+} and empty orbitals of Fe^{3+}. The picture of band structure is consistent with three different types of electronic transitions. The electronic transitions are in terms of hopping of electrons between different energy level. Electronic states shown in Tanabe-Sugano diagram are part of conduction band and valence band, as well as trapping state. The band structure provides a concise view of the electronic transitions and their contribution to the optical property.

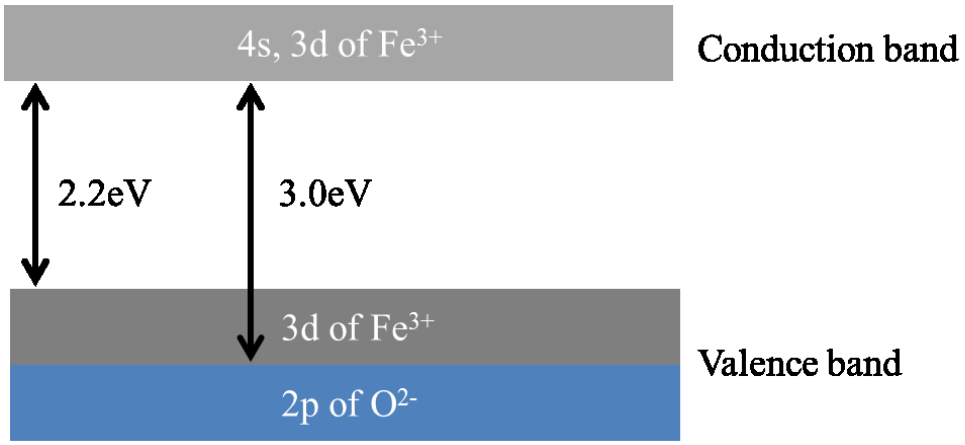

Figure 5.6 Schematic illustration of band structure of iron oxides

5.3.2 Absorption of Fe-FeSiO Nanoparticles

Because polyethylene glyol was used as the surface wrapping layer to suspend Fe-FeSiO nanoparticles into water, its absorption was first measured in comparison with Fe-FeSiO nanoparticle water solution. This was intended to give information of any influence on absorption due to the presence of polyethylene glyol (PEG). The absorption spectra were taken by UV-VIS spectra on a Hewlett-Packard series 8453 UV-VIS spectrophotometer equipped with an Agilent 89090A Peltier temperature controller. Figure 5.7 displays the absorption spectra of both PEG and Fe-FeSiO coated with PEG in water. Distilled water was used as blanking background. An absorption peak in ultra-violet range was seen in both samples, which is considered to come from PEG. In spite of that, unique absorption in 300nm-400nm wavelength range was found for Fe-FeSiO nanoparticle solution. The absorption was not observed for PEG, suggesting that it is characteristic of Fe-FeSiO particles. Existence of PEG doesn't affect the optical behavior of nanoparticles and

contribute only a background signal. In the following measurements, PEG solution was used as the background blanking so that their contribution is deducted.

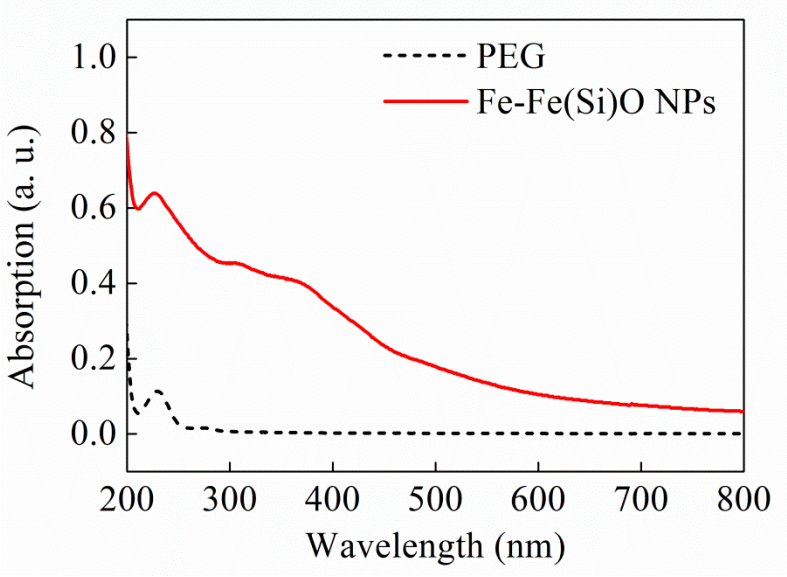

Figure 5.7 Absorption of PEG water solution and Fe-Fe(Si)O nanoparticle water solution

Optical absorption of Fe-FeSiO nanoparticles was then explored together with Fe-FeO and amorphous Si nanoparticles to test their absorptivity of light. Absorption spectra of the three kinds of nanoparticles are plotted in Figure 5.8. Absorption takes place in a wide wavelength range for both Fe-FeSiO and Fe-FeO nanoparticles. The spectrum of Si nanoparticles implies that Si or oxidized Si can only show a monotonic component. Stronger absorption in 310nm-450nm wavelength range was found for Fe-FeSiO nanoparticle than that of Fe-FeO nanoparticles. Appearance of strong absorption in this wavelength range is consistent with the observed orange/yellow color of nanoparticles. The peak in optical absorption near 310-450nm proves that Fe-FeSiO nanoparticles are optically active. As discussed, absorption arises from electronic transitions between different bands[21,22]. Absorption in the long wavelength range is mostly due to electronic

transitions between occupied 3d crystal field orbitals of Fe^{3+} and empty 3d crystal field orbitals of Fe^{3+}. d orbital-d orbital transitions are considered to be indirect and weakly absorptive due to the electronic selection rules [8]. Absorption in short wavelength range arise from electronic transitions between occupied 2p orbitals of O^{2-} and empty 3d crystal field orbitals of Fe^{3+} mainly. The absorption of Fe-FeSiO nanoparticles in 310nm-450nm range is due to the latter principle because it primarily locates at short wavelength regime and is the dominate part of the spectrum. The conclusion also agrees with the results of references[8,24]. Thus it can be seen that Si enhances the probability of transitions between O 2p orbitals and Fe 3d orbitals. Fe-FeSiO nanoparticles possess promising optical absorption for photocatalysis.

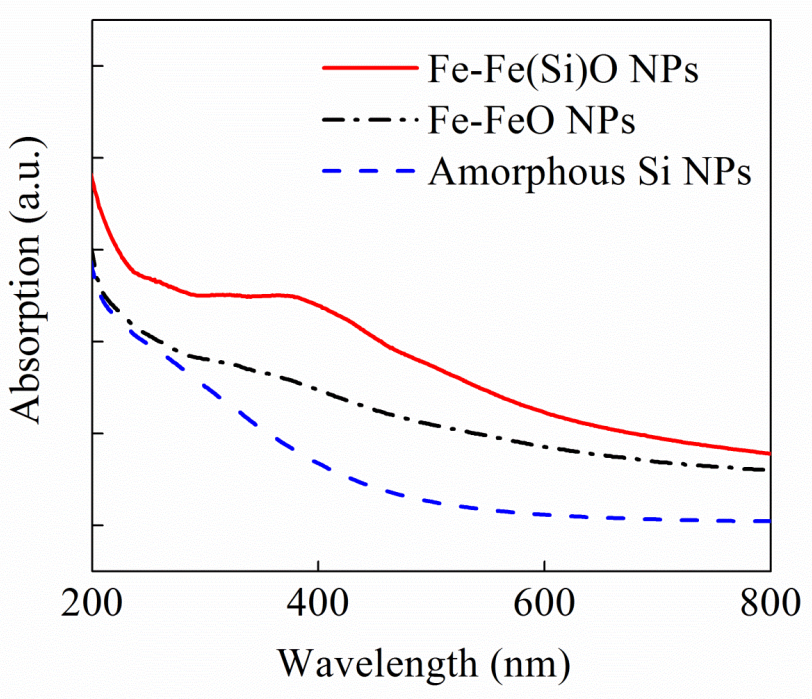

Figure 5.8 UV-VIS spectra of Fe-Fe(Si)O, Fe-FeO and Si nanoparticles

5.3.3 Luminescence of Fe-FeSiO Nanoparticles

Cathodoluminescence and photoluminescence were measured for Fe-FeSiO nanoparticles to examine emission of photons and their relationship with the absorption subsequently.

In cathodoluminescence technique, a high energy electron beam is generated and impinges onto the surface of the sample. The energy of electron beam can be transferred to electrons inside sample, promoting electrons to excited states. From the perspective of band structure, electrons could be excited from valence band to conduction band, generating a hole in valence band. The detected signal is the light emitted from recombination of electron and hole. Cathodoluminescence was measured by a scanning electron microscope (SEM) JEOL6500F. Fe-FeSiO nanoparticle solution was dropped on a polished Al stub, dried and examined by SEM. cathodoluminescence image and secondary electron image were both taken at electron beam energy of 20keV. Imaging was conducted on areas with and without nanoparticles at the same time. Figure 5.9 shows the corresponding images, where the left part of two images is the area with nanoparticles while the right part is pure Al surface. The bright spots in the cathodoluminescence image correspond to places where nanoparticles are in high density. Particles are probably in agglomerated state due to surface tension in drying. The brightness indicates that nanoparticles are luminescent. Cathodoluminescence spectrum was measured by setting electron beam energy at 30keV. In Figure 5.10, two peaks can be observed in the spectrum. A peak in the spectrum represents the highest probability of photon generation at the specific wavelength. The peak at 519nm is from Al stub while the peak at 405nm is from Fe-FeSiO nanoparticles. The emission peak caused by electron

beam excitation correlates with the characteristic optical absorption of Fe-FeSiO nanoparticles in the 310nm-450nm range. It reflects that electronic transitions responsible for the emission are the same conduction and valence band involved in the absorption.

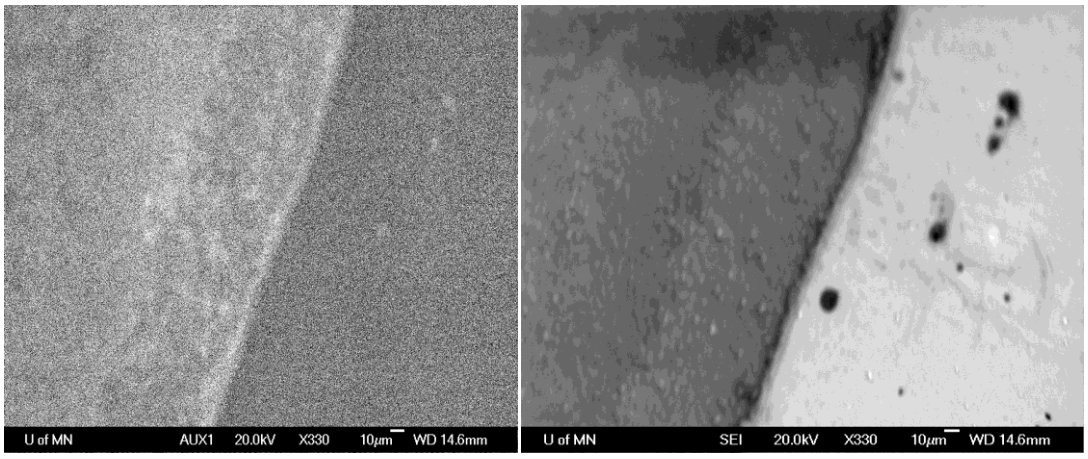

Figure 5.9 (a) Cathodoluminescence image and (b) secondary electron image of Fe-Fe(Si)O nanoparticles

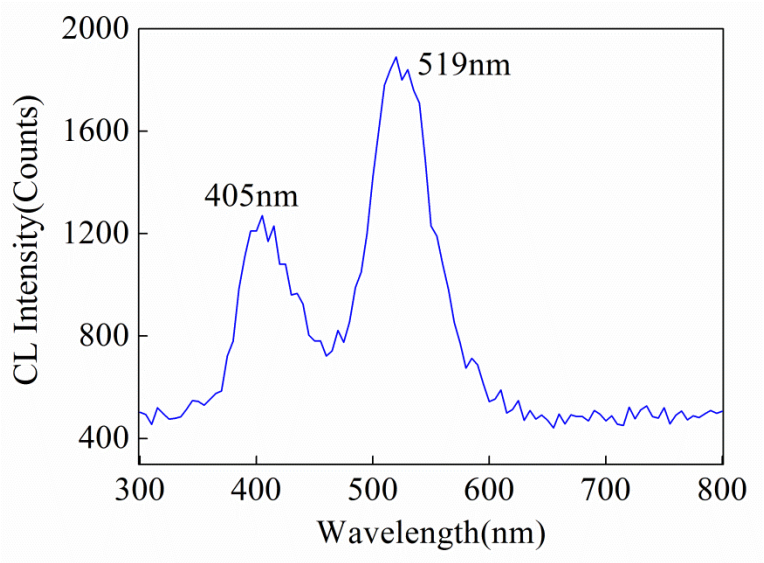

Figure 5.10 Cathodoluminescence spectrum of Fe-FeSiO nanoparticles

The photoluminescence study reveals a similar correlation between emission and absorption as what was found for cathodeluminescence. A photoluminescence spectrum was collected by a Spex Fluorolog-2 spectrofluorometer. An excitation wavelength of 315nm was used. Emission scan was performed on Fe-FeSiO nanoparticles suspended in distilled water in a quartz cuvette from 340nm to 600nm. The emission spectrum in Figure 5.11 shows a broad emission peak with the center at about 420nm. Emission of iron oxide particles can come from either d orbital-d orbital transitions or p orbital-d orbital transitions[4,8,25,26,27,24]. Here the photoluminescence echo the characteristic absorption peak of Fe-FeSiO, which suggests that luminescence of the nanoaprticles is a result of the intrinsic electronic transitions from O 2p orbitals to Fe 3d orbitals.

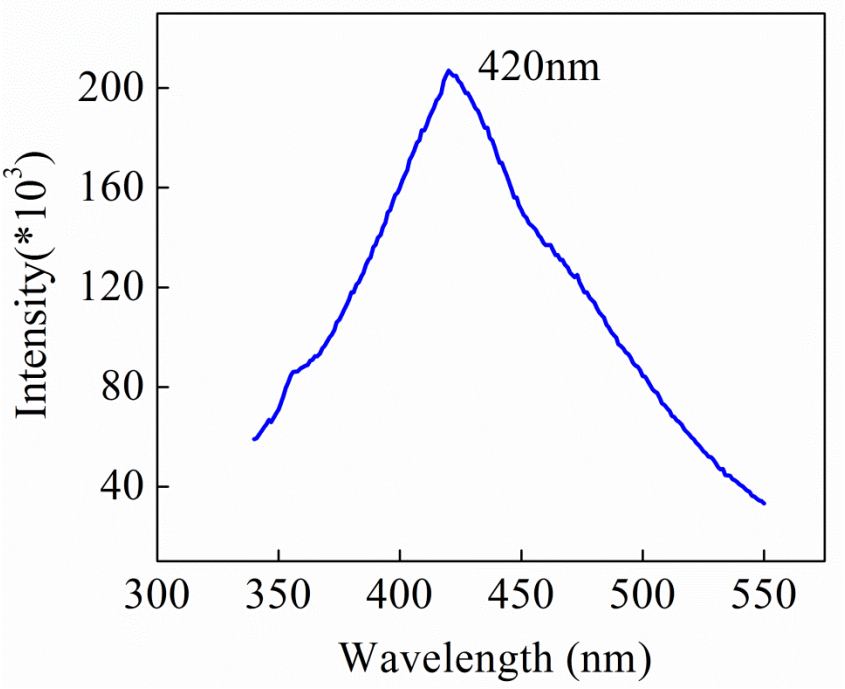

Figure 5.11 Photoluminescence spectrum of Fe-FeSiO nanoparticles

5.3.4 Photocatalysis of Fe-FeSiO Nanoparticles

Characterization of optical properties demonstrates that Fe-FeSiO nanoparticles have prominent optical activeness in the 310nm-450nm range and this is meaningful for photocatalysis performance. Holes generated from ligand field transitions are in d orbitals of Fe^{3+} which don't transfer efficiently to the hydroxyl group, a key surface group for catalysis process. Studies suggest that holes in d orbitals lie above the energy level of O 2p orbitals and are not facile to oxidation process due to energy mismatch[11]. It leads to poor photochemical performance of iron oxides[17]. For better photocatalysis and photocurrent generation, p orbital-d orbital transitions play a critical role. Holes are generated as a consequence of around 3eV absorption from the valence band in nature of O 2p, similar to the situation in TiO, and hole transfer is thus easy[9]. In Fe-FeSiO nanoparticles, where transition probability between p orbitals and d orbitals is promoted by Si doping, many holes in O 2p nature can be generated and participate in photochemical reactions. The enhancement brought by Si is probably related with the hybridization of d orbitals of Fe and p orbitals of Si. The increase of holes arriving in O 2p band could be one of the driven factors for the observed high quantum efficiency in a Si doped iron oxide electrode[11]. Si also increases the electron mobility which contributes to the photocatalytic process as well[10].

5.4 Magnetic Property of Fe-FeSiO Nanoparticles

Besides the promising optical property of Fe-FeSiO nanoparticles, their magnetic property is also showing advantages as characterized by a superconducting quantum interference device. Hysteresis loops of Fe-FeSiO were measured at room temperature

(300 K) and low temperature (5 K), with the maximum applied field of 3 Tesla, which are shown in Figure 5.12. The inset figure is the zoom-in of hysteresis loops. Hysteresis was clearly shown by the loops, which indicates that the Fe-FeSiO nanoparticles are ferromagnetic at room temperature. Coercivity at 300K and 5K are 96 Oe and 390 Oe, respectively. Ferromagnetism of the nanoparticles was also confirmed from zero field cooling and field cooling measurements. The sample was first cooled towards 5K without presence of any magnetic field. Magnetic moment of the sample was then measured during warming up till 345K with a small magnetic field 100Oe applied. The sample was then cooled towards 5K under 10kOe. Magnetic moment of the sample was again measured during warming up till 345K under a magnetic field of 100Oe. The two curves were plotted in Figure 4.12 as a function of temperature. In zero field cooling, an increase of magnetic moment along with the increase of temperature resulted from thermally activated switching of nanoparticles to align up with the small magnetic field. In field cooling, a decrease of magnetic moment is a result of rotation of magnetization away from initially aligned direction under thermal fluctuation. Convergence of the two curves will take place at the temperature when zero field cooling curve peaks. This is the temperature at which nanoparticles start to become superparamagnetic, which is called blocking temperature. Clearly, the blocking temperature of these nanoparticles is above 345K, proving their ferromagnetism at room temperature.

The appearance of ferromagnetism is an indirect support of the co-existence of Fe and γFe2O3 because anisotropy of γFe2O3 is generally small ($1.6*10^4$ J/m^3)[28] which doesn't give hysteresis in this size range. Interface coupling between Fe and γFe2O3 as well as

shape anisotropy of Fe are probably contributing factors to the hysteresis. The possession of advantageous magnetic property from the Fe core ensures that these nanoparticles are recyclable by magnetic field to achieve economic and sustainable photocatalysis.

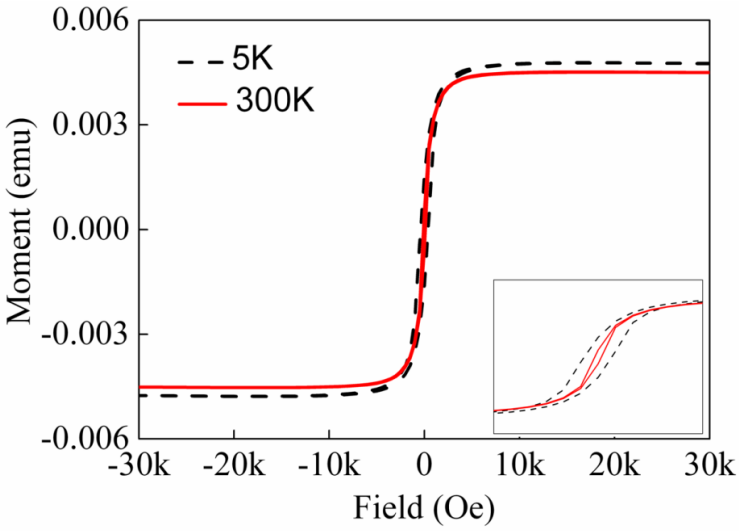

Figure 5.12 Hysteresis loops of Fe-FeSiO nanoparticles at 5K and 300K

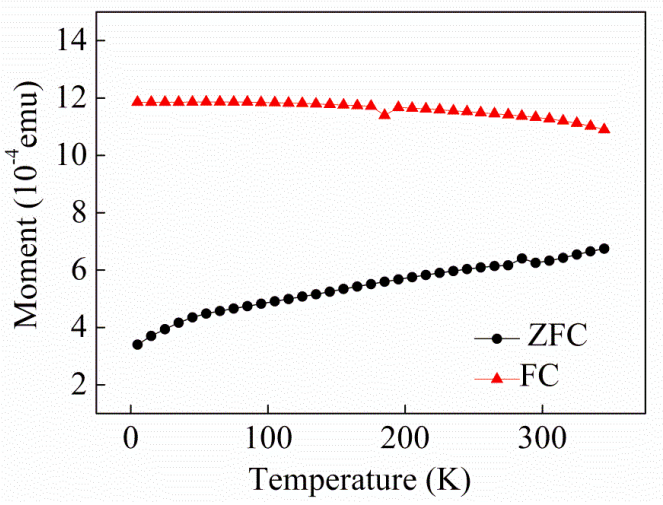

Figure 5.13 Zero field cooling and field cooling of Fe-FeSiO nanoparticles

5.5 Conclusions

Above all, this study presents a Si doped iron-iron oxide nanoparticle structure with promising optical absorption and magnetic property, which can be potentially applied for recycable photocatalysis. With the incorporation of Si in Fe-FeO nanoparticles, absorption was enhanced in the wavelength range 310nm-450nm compared to Fe-FeO nanoparticles without doping. Luminescence characterization indicates the same intrinsic electronic transitions from which strong absorption arises. The modified optical properties could assist hole transfer in the photocatalysis process. Active magnetic property of nanoparticles assures their recoverable capability. Additionally, the study presents an environmentally friendly production process by using only abundant, non-toxic materials. This work serves as a base towards further exploration of photocatalytic magnetic nano-materials.

References

1 V. Polshettiwar, R. Luque, A. Fihri, H. Zhu, M. Bouhrara, and J.-M. Basset, Chemical Reviews **111,** 3036 (2011).

2 V. Polshettiwar and R. S. Varma, Green Chemistry **12** (2010).

3 W. Du, Y. Xu, and Y. Wang, Langmuir **24,** 175 (2007).

4 Y. Zhang, W. Liu, C. Wu, T. Gong, J. Wei, M. Ma, K. Wang, M. Zhong, and D. Wu, Materials Research Bulletin **43,** 3490 (2008).

5 S. K. Apte, S. D. Naik, R. S. Sonawane, B. B. Kale, and J. O. Baeg, Journal of the American Ceramic Society **90,** 412 (2007).

6 B. C. Faust, M. R. Hoffmann, and D. W. Bahnemann, The Journal of Physical Chemistry **93,** 6371 (1989).

7 H. Liu and L. Gao, Journal of the American Ceramic Society **89,** 370 (2006).

8 N. J. Cherepy, D. B. Liston, J. A. Lovejoy, H. Deng, and J. Z. Zhang, The Journal of Physical Chemistry B **102,** 770 (1998).

9 Z. Zhang, C. Boxall, and G. H. Kelsall, Colloids and Surfaces A: Physicochemical and Engineering Aspects **73,** 145 (1993).

10 J. E. Turner, M. Hendewerk, J. Parmeter, D. Neiman, and G. A. Somorjai, Journal of The Electrochemical Society **131,** 1777 (1984).

[11] J. A. Glasscock, P. R. F. Barnes, I. C. Plumb, and N. Savvides, The Journal of Physical Chemistry C **111,** 16477 (2007).
[12] J. Feng, X. Hu, P. L. Yue, H. Y. Zhu, and G. Q. Lu, Industrial & Engineering Chemistry Research **42,** 2058 (2003).
[13] K. Ohtsuka, Chemistry of Materials **9,** 2039 (1997).
[14] S. Shylesh, V. Schünemann, and W. R. Thiel, Angewandte Chemie International Edition **49,** 3428 (2010).
[15] Kostedt, J. Drwiega, D. W. Mazyck, S.-W. Lee, W. Sigmund, C.-Y. Wu, and P. Chadik, Environmental Science & Technology **39,** 8052 (2005).
[16] J. W. B. Ingler and S. U. M. Khan, Electrochemical and Solid-State Letters **9,** G144 (2006).
[17] M. P. Dare-Edwards, J. B. Goodenough, A. Hamnett, and P. R. Trevellick, Journal of the Chemical Society, Faraday Transactions 1: Physical Chemistry in Condensed Phases **79** (1983).
[18] J. M. Qiu and J. P. Wang, Advanced Materials **19,** 1703 (2007).
[19] D. M. Sherman, Physics and Chemistry of Minerals **12,** 161 (1985).
[20] M. D. B. Daniel C. Harris, *Symmetry and spectroscopy* (Oxford University Press, 1978).
[21] T. D. W. David M. Sherman, American Mineralogist **70,** 1262 (1985).
[22] Y. P. He, Y. M. Miao, C. R. Li, S. Q. Wang, L. Cao, S. S. Xie, G. Z. Yang, B. S. Zou, and C. Burda, Physical Review B **71,** 125411 (2005).
[23] L. Fu, Z. Wu, X. Ai, J. Zhang, Y. Nie, S. Xie, G. Yang, and B. Zou, The Journal of Chemical Physics **120,** 3406 (2004).
[24] I. V. Chernyshova, S. Ponnurangam, and P. Somasundaran, Physical Chemistry Chemical Physics **12** (2010).
[25] B. Zou, W. Huang, M. Y. Han, S. F. Y. Li, W. Xiaochun, Y. Zhang, J. Zhang, W. Pengfei, and R. Wang, Journal of Physics and Chemistry of Solids **58,** 1315 (1997).
[26] S. S. Shinde and K. Y. Rajpure, Journal of Solid State Chemistry **183,** 2886 (2010).
[27] S. Chakrabarti, D. Ganguli, and S. Chaudhuri, Physica E: Low-dimensional Systems and Nanostructures **24,** 333 (2004).
[28] J.-P. Fortin, C. Wilhelm, J. Servais, C. Ménager, J.-C. Bacri, and F. Gazeau, Journal of the American Chemical Society **129,** 2628 (2007).

CHAPTER 6

Surface Modification of Gas Phase Synthesized Magnetic Nanoparticles

6.1 Introduction

Surface chemistry is a critical aspect for magnetic nanoparticles. Most of the biomedical applications need non-agglomerated particles. And some need particles to be compatible with biological environment, able to form specific bonding with proteins in addition to maintaining stability. Not only do biomedical applications require a modified surface, but many others also care about the surface property. For example, when magnetic nanoparticles are used as catalyst supports for recycle purpose, they should not aggregate in the chemical reactions. In high density information storage, it also relies on the surfactant on the surface of magnetic nanoparticles to assemble into periodical arrays with fixed spacing between each other. Therefore, surface modification is a crucial step before any real application of nanoparticles.

Surface modification is not trivial for gas phase synthesized nanoparticles. Nanoparticles experience mutual attraction due to Van-der-Waals force and magnetic dipolar force. General schemes to introduce forces against the attraction can be electrostatic repulsion, steric exclusion or a hydration layer. In order to do so, charges or

polymeric layers are developed on the surface of nanoparticles through chemisorption, electrostatic attraction or hydrophobic interaction[1]. It is quite mature in wet chemistry to synthesize, stabilize and functionalize nanoparticles. Surfactants were demonstrated to prevent particles from agglomeration when they were in presence of the synthesis of nanoparticles[2]. Organic surfactants such as oleic acid, trioctylphosphonic acid can bind to the surface of metals with natural oxide strongly. Polymer coatings are another method for stabilization of magnetic nanoparticles. Polymers can be chemisorbed onto the surface of particles[3]. Direct polymerization from the surface of particles is another approach that has been applied[4]. Unlike chemical synthesis, there is not any surfactant or ligand involved in gas phase synthesis generally and it is not clear how to attach them onto particle surface in an efficient way. Very little work has been done for stabilization and functionalization of magnetic nanoparticles synthesized in gas phase. In this chapter, we will present our attempts on surface modification of nanoparticles produced by our gas phase technique.

6.2 Indirect Approach

An indirect approach has been first applied to modify the surface of nanoparticles synthesized in gas phase. Fe-Co, Fe-Si alloy particles and FeCo-Au core-shell nanoparticles have been tried in this approach with various types of reagents. A schematic illustration of the indirect approach is shown in Figure 7.1. The basic idea of this approach is to first deposit nanoparticles onto a buffer polymer coated substrates, for which we choose to use polyethylene glycol (PEG) here (Section 2.2.3). After that

nanoparticles are taken out of deposition chamber and transferred into an aqueous solution. Chemicals with certain functional groups are added into the solution and allowed for reactions with particles. There are usually two steps involved in the reaction. The initial step establishes covalent bonds between the surface and hydrophobic molecules. The following step introduces a thick polymer layer to make nanoparticles hydrophilic. The hydrophilic polymer has chemical groups that can react with the hydrophobic surface of particles and form chemical bonds.

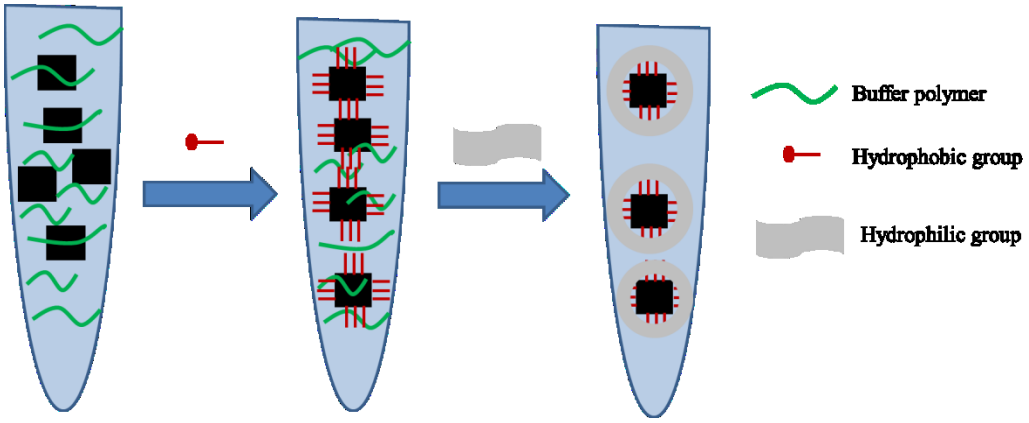

Figure 6.1 Schematic illustration of surface modification by the indirect approach

A standard procedure we've worked on includes salinization and mPEG reaction for alloy nanoparticles. Salinization is performed using (3-aminopropyl)-triethoxysilane (APTES) as the initial step. Alloy nanoparticles develop a native oxidization shell after exposure to air out of the vacuum chamber. The natural oxide surface contains hydroxyl groups which can displace the alkoxy groups on APTES. A covalent -Si-O-Si- bond is thus formed and an amino chemical group is left free on the surface of the particle. The

APTES modification process starts from an aliquot of nanoparticle water solution with PEG as a stabilizer. Here we use Fe-Si nanoparticles as an example. Multiple washings of particles using ethanol and distilled water (DI water) were done to get rid of extra PEG through centrifugation. Particles were re-suspended in a mixture of ethanol and DI water in 9:1 volume ratio after washing. APTES solution of 50 v% in ethanol was made and added into nanoparticle solution. The mixed solution was then put under sonication. In 20 minutes two drops of 29 wt% ammonium hydroxide was added into the solution under sonication. Continuous sonication was applied for 4 hours. Afterwards a permanent magnet was used to collect nanoparticles with APTES modified surface out of the solution. Nanoparticles were dispersed in ethanol after triple washings through magnetic collection.

A few types of functional PEG were used in the following step to make nanoparticles stable in water, for example, mPEG-glutaric acid (mPEG-COOH) and mPEG-succinimidyl carboxy methyl ester (mPEG-SCM). These functional PEGs have chemical groups that can react with the amino group on the particle surface after salinization. The modification process is similar for either type of functional PEG. 0.5mg/ml-3mg/ml functional PEG in dimethyl sulfoxide (DMSO) was prepared. The functional PEG was added into APTES modified nanoparticle solution and sonicated overnight. After extra functional PEG was washed off, particles were collected by the magnet and transferred to phosphate buffered saline (PBS) PH=7.4. Drops of Fe-Si nanoparticle solution were dried on the amorphous carbon coated Cu grids and imaged by a TEM (FEI T12). Figure 7.2 shows TEM images of Fe-Si particles before and after modification of functional PEG.

Although there appears to be slight improvement on dispersion, the result is still far from an optimal state. What's seen in the image also explains the fast sedimentation of particles out of the liquid.

The indirect approach has several drawbacks and affects the efficiency of surface modification. First, the surface of nanoparticles goes through gradual change after they are taken out of the vacuum chamber and are exposed to aqueous environment. As the physiochemical property of the surface varies, attachment of molecules could be interrupted. Second, nanoparticles are not sufficiently prevented from aggregation initially. The washing process leads to increasing chances for particles to bump into each other and form aggregates. Additionally, there is a significant loss of particles during the process which lowers the total yield.

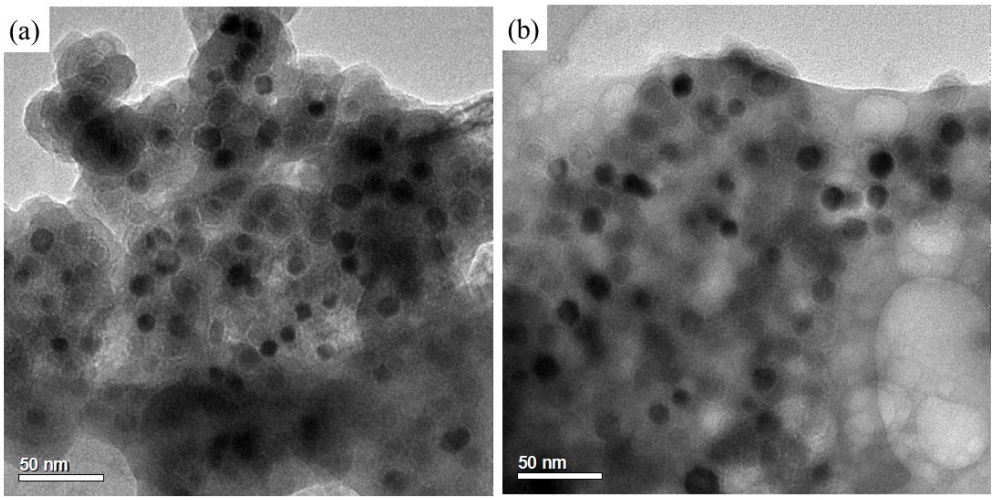

Figure 6.2 TEM images of Fe-Si nanoparticles (a) before surface modification (b) after surface modification

6.3 Direct Approach

A direct approach is proposed here for surface modification and functionalization in attempt to overcome the drawbacks of the indirect way. In the direct approach, functional groups are introduced to bind with the nanoparticle surface when nanoparticles are still in the vacuum chamber. In this circumstance, nanoparticles have pristine surface without oxide or any other contamination. The reaction can take place with a fixed surface condition. After in-situ modification, nanoparticles can be transferred into aqueous solvent. The presence of a layer of covalently bonded molecules prevents particles from aggregation and any further procedure can start from here. It is also possible to attach additional chemical groups on the surface for further functionalization procedure, which avoids intermediate process and possible loss of particles.

6.3.1 4-Arm- PEG-Acid

4-Arm-PEG terminated with carboxyl acid group (M.W. 10k Da) was used to test the concept of the direct approach. The polymer has a chemical structure shown in Figure 6.3. FeCo and Fe nanoparticles were used as the example materials. In principle, the carboxyl acid group can oxidize the metallic surface of nanoparticles and form metal-oxygen covalent bonds. Non-functional PEG water solution was prepared according to the procedure in Section 2.2.3. 4-Arm-PEG-COOH in viscous form was mixed with non-functional PEG solution in volume ratio of 2:3 and 4:1. The mixture was then spin coated onto glass substrates at 3500rpm in 30 seconds duration.

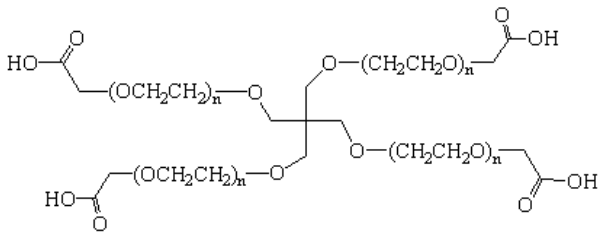

Figure 6.3 Chemical structure of 4-arm-PEG-acid

To experiment what reaction conditions are suitable to promote the binding, we performed in-situ heating after deposition of nanoparticles as a comparison to samples without in-situ heating. The heating was below 50°C for 20 minutes. After substrates were taken out of the chamber, they were treated with DI water and particles were transferred into solution. The dispersed solution was kept stationary and colloid stability was monitored. The sample with high polymer concentration prevented particles from agglomeration and sedimentation better than the low concentration one did. Generally, the solution stayed clear for about half an hour with high polymer concentration. In-situ heating promotes the reaction efficiency and leads to an improved colloid stability. Apparent agglomeration and sedimentation of particles happened in a few hours.

The study suggests that carboxyl acid group can react with the surface atoms of alloy nanoparticles, resulting in covalently bonded molecules on the surface. The armed structure with multiple carboxyl acid groups on one molecule provides possibility that multiple nanoparticles bind to a single molecule, which gives a tendency of aggregation. Therefore, linear structured functional PEG is more preferable than the armed ones in consideration of dispersion.

6.3.2 Oleic Acid

Oleic acid ($C_{18}H_{34}O_2$) is a fatty acid that has been used widely as a surfactant for iron oxide nanoparticles synthesized by chemical methods. It reacts with iron oxide particles as a carboxylate and the interaction between the carboxylate and metal atoms is characterized to be chelating bidentate[5]. Oleic acid helps stabilize iron oxide ferrofluid due to its good wettability in organic solvent such as hexadecane[6]. It has been proposed that oleic tails (C_{18}) can be solvated and fully wetted because the oleic tail with a cis-double-bond in the middle weakens the nematic attractions by forming a kink[7].

Because of the carboxylate nature of oleic acid in its reaction with metal atoms, we used oleic acid as a stabilizer to transfer FeCo nanoparticles into organic solvent. Solutions of oleic acid in isopropyl alcohol (IPA) were made with concentration of 0.1g/ml-0.8g/ml. The solution was coated onto transparency films by a meyer rod of 0.25mm wire size. FeCo particles were then deposited onto the transparency films with oleic acid coating in the vacuum chamber. The films were taken out of the chamber after deposition and treated with chloroform. In this way, FeCo particles were able to be transferred into organic solvent. Figure 6.4 shows pictures of chloroform solution of FeCo particles with oleic acid modification. Macroscopic stability of the suspension was monitored and recorded. It was found that the stability increased with an increase of initial concentration of oleic acid solution. However, a plateau was reached when the concentration was 0.4g/ml. Any further increase of concentration didn't bring in obvious improvement on colloid stability. It probably indicates the intrinsic limited binding efficiency through this method. In-situ heating was performed on samples with 0.5g/ml-

0.8g/ml oleic acid. The heating slightly improved the dispersion, but it had severe effect on the uniformity of the coating. The coating layer was partially destroyed due to the high mobility of the molecules.

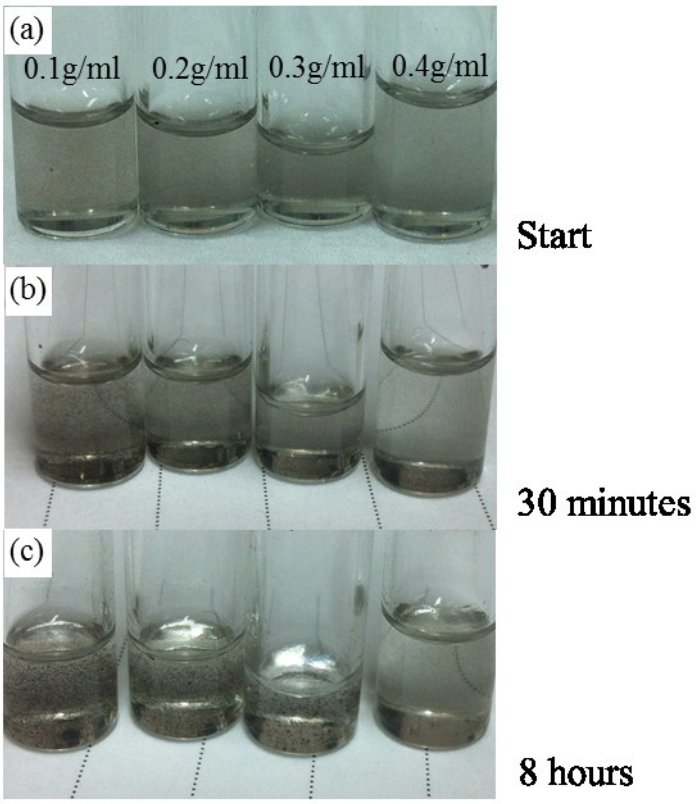

Figure 6.4 Photos of FeCo nanoparticle solution of 0.1g/ml-0.4g/ml oleic acid (a) freshly prepared (b) 30 minutes after prepared (c) 8 hours after prepared

To summarize, using oleic acid coated substrate, magnetic alloy particles can be directly modified in the chamber and transferred to organic solvent afterwards. High concentration of oleic acid is beneficial for dispersion, whereas a plateau is reached at 0.4g/ml. In-situ heating is not applicable for oleic acid coatings.

6.3.3 Polyvinyl Alcohol Film

Polyvinyl alcohol (PVA) is a water soluble synthetic polymer, which has a molecular formula $(C_2H_4O)_x$. This polymer dissolves into water quickly and is biocompatible and biodegradable. Its film has high tensile strength and flexibility. The hydroxyl group of the polymer can react with metallic surface by forming metal-oxygen bond.

The ability of PVA film was tested for transferring particles into water. A small piece of PVA film was used as the substrate. FeCo nanoparticles were deposited onto the film with and without post in-situ heating. After deposition, the film was put in a glass vial (Figure 6.5(a)). DI water was added to dissolve the film and make a solution of particles (Figure 6.5(b)). For comparison, a piece of PVA film without nanoparticles on was also dissolved in the same way. There wasn't any influence on dissolvability of the film by depositing particles on it. The colloid can stay stable for over 8 hours (Figure 6.5(c) and (d)) based on the observation. A permanent magnet was used to attract particles. Particles were collected out of the solution in 15 minutes (Figure 7.6(a)). After sonication, particles can be re-dispersed (Figure 7.6(b)).

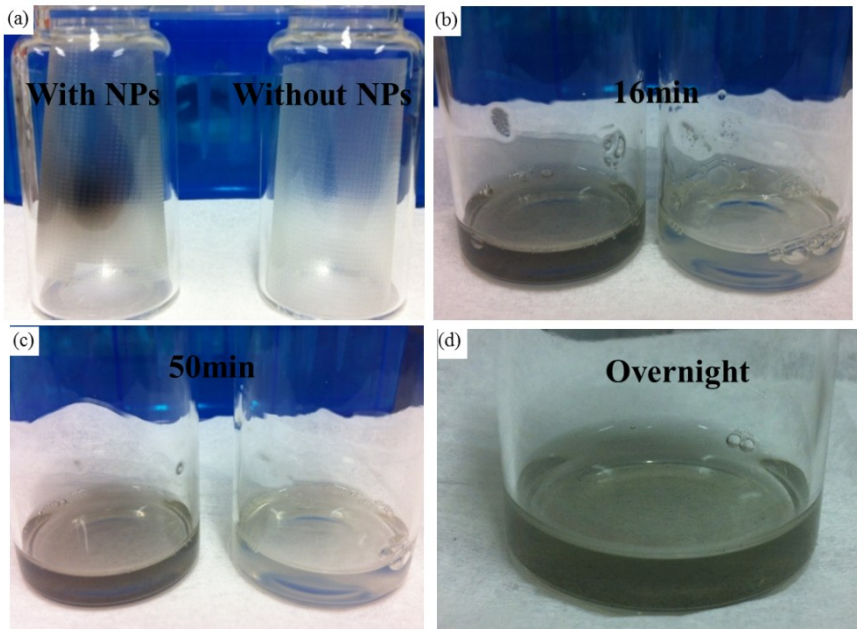

Figure 6.5 (a) Photo of PVA film with (left) and without (right) FeCo nanoparticle deposited on (b) Photo of water solution of FeCo nanoparticles and PVA film (left) and water solution of PVA film only (right) (c) Photo of solutions in 50 minutes since prepared (c) Photo of water solution of FeCo nanoparticle and PVA film overnight since prepared

The results demonstrate that PVA is a good media for making nanoparticle colloid. It stabilizes the colloid quite well due to its viscous nature at high concentration. The magnetic property of particles is not affected after interaction with PVA. And the colloid is able to stand disturbance such as magnetic attraction.

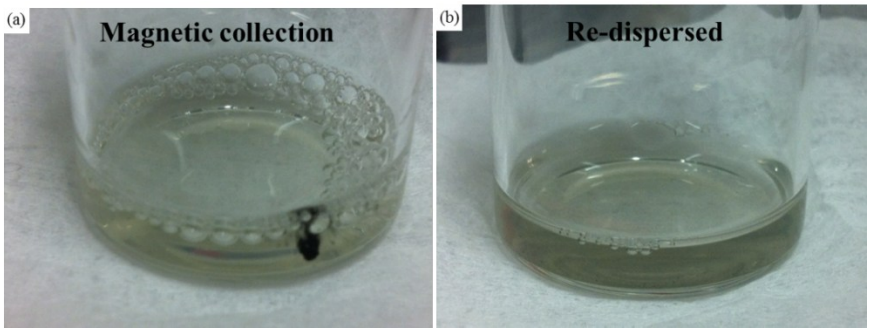

Figure 6.6 (a) Photo of FeCo nanoparticle solution under magnetic attraction (b) Photo of re-dispersed FeCo nanoparticle after magnetic attraction

6.3.4 NH_2-PEG-COOH

PVA can only help stabilize nanoparticles in water. It doesn't bring any functional groups onto the surface of particles. In order to use these particles for biomedical applications, sequential binding and labeling process are needed. Bi-functional PEG is an ideal candidate for surface functionalization. For NH_2-PEG-COOH, the -COOH group can react with metal atoms on the surface of nanoparticle while the -NH_2 will stick out of the surface as a functional group, which can be used for binding and labeling. PEG chain makes particle water soluble.

NH_2-PEG-COOH was experimented at different conditions to examine how well it can make particles water soluble. NH_2-PEG-COOH was mixed with normal PEG water solution and was made to solutions with concentration of 15wt%, 30wt%, 40wt% and 65wt%. Each solution was coated on transparency films using a meyer rod. After deposition of nanoparticles, the films were washed by DI water, PBS PH=7.4 or ethanol. It was found that the Bi-functional PEG was highly acidic. When a high concentration of it was dissolved in water, the solution showed so low PH that particles were degraded by the acid. To prevent particles from degradation and to remove extra acid, magnetic attraction was done immediately after particles were transferred into DI water or PBS. Particles were re-dispersed into fresh DI water and PBS. However, when using ethanol as the solvent, there didn't appear degradation of particles due to extra polymers below 65wt%. Figure 7.7 shows photos of ethanol solution of FeCo nanoparticles modified by different concentration of Bi-functional PEG. Washing was done only to the sample with

65wt% Bi-functional PEG after immediate transferring into ethanol through magnetic collection. The 40wt% of Bi-functional PEG was found to give the best colloid solubility among the conditions that were tested. In 1 hour, there hasn't been obvious change of the solution (Figure 6.7(d)). The solutions of lower concentration Bi-functional PEG could only maintain the colloid stable for 20mins-40mins (Figure 6.7(b) and (c)). The solution of high concentration Bi-functional PEG showed the worst stability which was probably due to the magnetic collection process.

The NH_2-PEG-COOH has been demonstrated to bring improved stability of FeCo nanoparticle solution. The direct binding between -COOH group and surface atom enables particles to disperse in aqueous solution. The surface of particles is terminated with -NH_2 which will facilitate further functionalization. This direct method for surface modification and functionalization by using Bi-functional PEG reduces intermediate steps and provides a direction for surface treatment in gas phase synthesis.

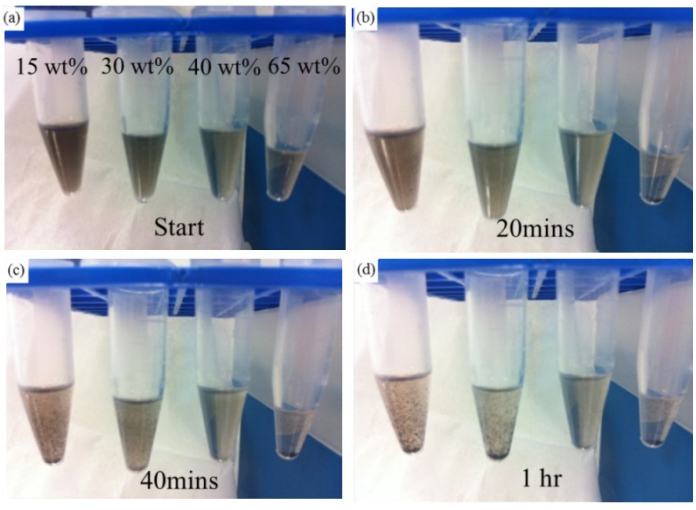

Figure 6.7 (a) Photo of FeCo nanoparticle ethanol solution modified by different concentration of Bi-functional PEG; Photo of FeCo nanoparticle ethanol solution taken in (b) 20 minutes (c) 50 minutes and (d) 1 hour since prepared

6.4 Collection of Nanoparticles

In our experiments, we have found that how particles distribute on the substrate has a significant impact on dispersion. The physical synthesis method generally produces particles that will randomly land on the substrate. Particles can quickly pack up to form multiple layers. It reduces particles' accessibility to chemical molecules for surface modification. Meanwhile, it increases the possibility for particles to touch each other and agglomerate or aggregate. Therefore, it is necessary to change the nature of this deposition method to enhance the efficiency of modification. We propose a few ways to collect and modify particles in attempt to overcome the hindrance.

6.4.1 Liquid Reactor

Nanoparticles experience limited access to molecules when they land on a sheet of substrate and start to form 2D structure. Even without multiple packing layers, a single nanoparticle which is 3D itself may not completely immerse in the polymer or surfactant coatings on the substrate. One way to increase the contact is to use a pool of liquid containing the polymer or surfactant as the substrate. Particles can directly fly into the liquid and be modified very similar to the wet chemistry method. The free of contact in any direction gives high binding efficiency. Particles will not pack together too because of the ability to move around. Figure 6.8 is a schematic illustration of using a well of liquid to collect particles.

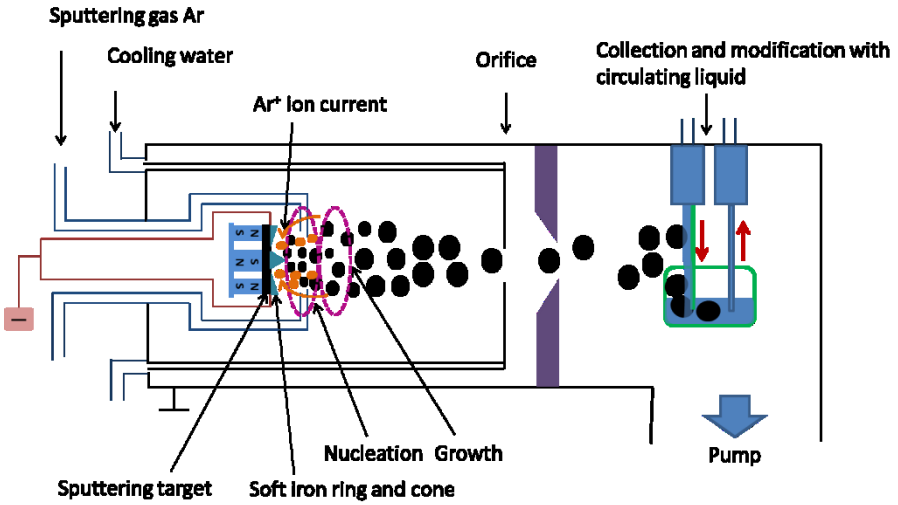

Figure 6.8 Schematic drawing of the nanocluster deposition system with collection and functionalization of nanoparticles using a pool of circulating liquid

6.4.2 In-situ Spray

Another possible strategy is to add a spray of functional molecules during the flight of particles to enhance the coverage of the modification layer. When nanoparticles are flying, their overall surface is free of occupation and is accessible easily. By incorporating a plasma of functional molecules on the way towards substrates, particles can form bonds with the molecules through collision. With the presence of a modification layer on the surface, agglomeration and aggregation of particles will be limited extensively on a substrate. To generate the chemical mist, a sprayer is integrated with the deposition system as shown in Figure 6.9. UV light or furnace can also be included to promote the binding reaction.

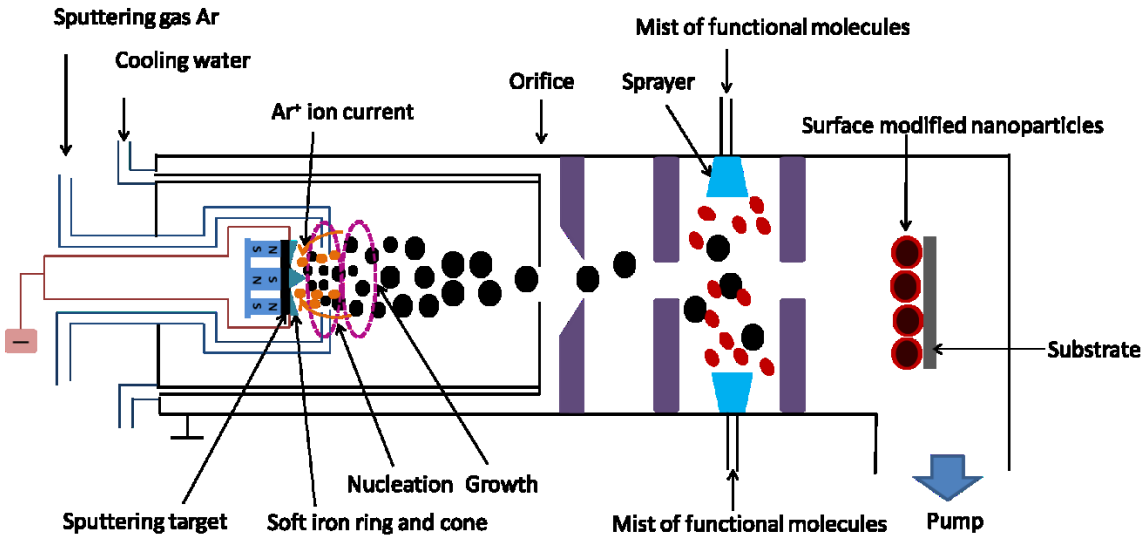

Figure 6.9 Schematic drawing of the nanocluster deposition system with an in-situ spray system for surface modification and functionalization

6.4.3 Rotating Tape Substrate

In order to prevent particles from forming a stack of multiple layers, a rotating tape type of substrate can enable deposition of a single layer of particles. With double side coated tape substrate, as the tape rolls up, both top and bottom surface of nanoparticles can have chances to be in contact with the functional molecules. In this way the strategy also ensures that every particle has a full amount of functional molecules to attach to. The tape substrate can be exchanged in a load lock chamber after complete use. The approach is compatible with the vacuum system and is easy to integrate with any present system. Figure 6.7(a) illustrates how nanoparticles can be deposited onto the tape and be rolled up. Figure 6.7(b) shows the front view of the vacuum chambers and the rotary design in detail. The design has been implemented on our present nanocluster deposition system to

prove the concept. The rotating substrate mechanism can also be combined with the in-situ spray to realize a manufacturing flow in future.

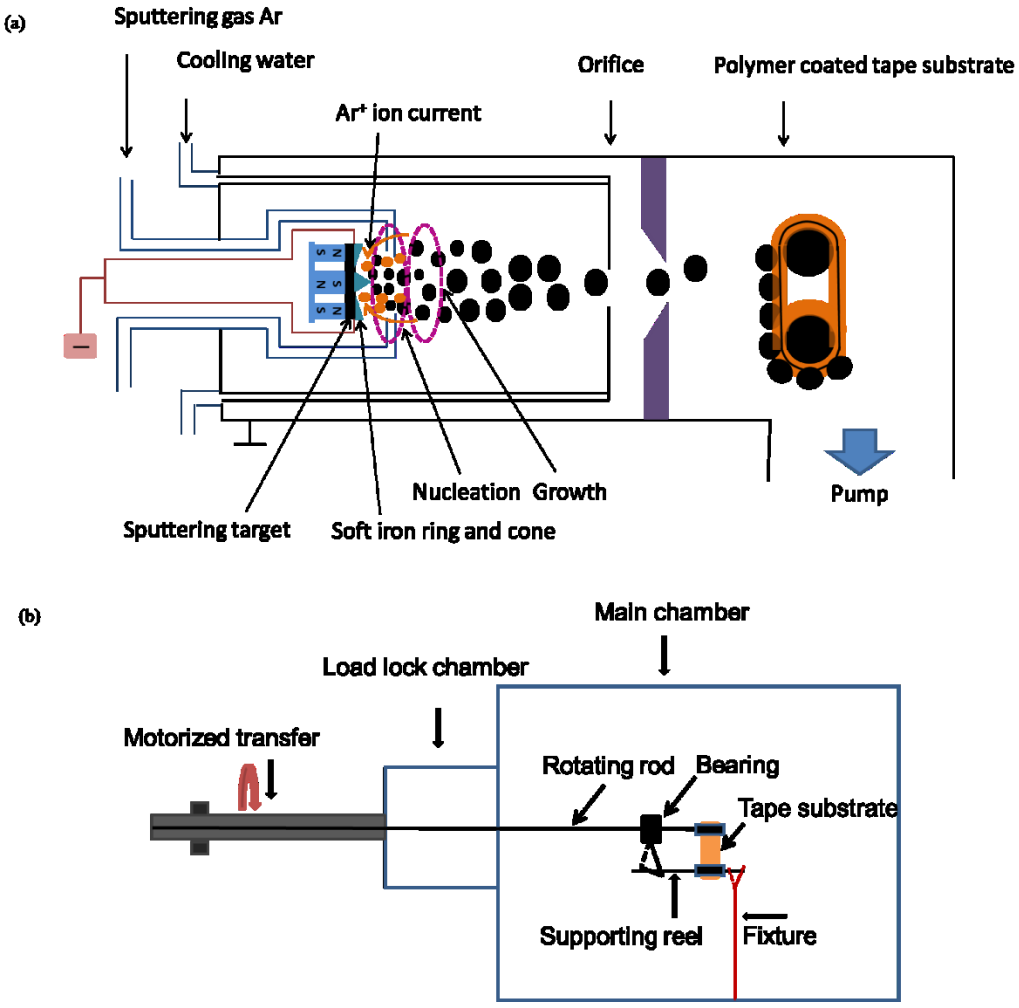

Figure 6.10 Schematic drawing of the nanocluster deposition system with an in-situ spray system for surface modification and functionalization

6.5 Summary

We have presented our attempts to transfer gas phase synthesized nanoparticles to solution and make a stable colloid. Both indirect and direct approaches were experimented. The direct approach was more preferable than the indirect approach

because it took advantage of the clean surface of nanoparticles in the vacuum and reduced time cost, labor cost and loss of yield. Based on trials with different materials, carboxyl acid group was found to be an active chemical group for modification of the surface of alloy particles. To address the typical agglomeration problem due to uncontrolled packing density of particles during collection, several designs have been proposed. A rotating tape type substrate was integrated with the current nanocluster deposition system.

References

1 R. A. Sperling and W. J. Parak, Philosophical Transactions of the Royal Society A: Mathematical Physical and Engineering Sciences 368, 1333 (2010).

2 S. Sun and C. B. Murray, Journal of Applied Physics 85, 4325 (1999).

3 Y. Zhang, N. Kohler, and M. Zhang, Biomaterials 23, 1553 (2002).

4 Y. Zhou, S. Wang, B. Ding, and Z. Yang, Chemical Engineering Journal 138, 578 (2008).

5 L. Zhang, R. He, and H.-C. Gu, Applied Surface Science 253, 2611 (2006).

6 A. K. Gupta and M. Gupta, Biomaterials 26, 3995 (2005).

7 R. Tadmor, R. E. Rosensweig, J. Frey, and J. Klein, Langmuir 16, 9117 (2000).

BIBLIOGRAPHY

[1] A. Hightower, B. Fultz, and R. C. Bowman Jr, Journal of Alloys and Compounds 252, 238 (1997).

[2] W. Hu, R. J. Wilson, A. Koh, A. Fu, A. Z. Faranesh, C. M. Earhart, S. J. Osterfeld, S.-J. Han, L. Xu, S. Guccione, R. Sinclair, and S. X. Wang, Advanced Materials 20, 1479 (2008).

[3] T. Hyeon, Chemical Communications, 927 (2003).

[4] N. A. Frey, S. Peng, K. Cheng, and S. Sun, Chemical Society Reviews 38, 2532 (2009).

[5] S. Sun and H. Zeng, Journal of the American Chemical Society 124, 8204 (2002).

[6] J. Rockenberger, E. C. Scher, and A. P. Alivisatos, Journal of the American Chemical Society 121, 11595 (1999).

[7] T. Hyeon, S. S. Lee, J. Park, Y. Chung, and H. B. Na, Journal of the American Chemical Society 123, 12798 (2001).

[8] H. Yu, M. Chen, P. M. Rice, S. X. Wang, R. L. White, and S. Sun, Nano Letters 5, 379 (2005).

[9] W. S. Seo, J. H. Lee, X. Sun, Y. Suzuki, D. Mann, Z. Liu, M. Terashima, P. C. Yang, M. V. McConnell, D. G. Nishimura, and H. Dai, Nat Mater 5, 971 (2006).

[10] W. Zhao, J. Gu, L. Zhang, H. Chen, and J. Shi, Journal of the American Chemical Society 127, 8916 (2005).

[11] K. Wegner, B. Walker, S. Tsantilis, and S. E. Pratsinis, Chemical Engineering Science 57, 1753 (2002).

[12] K. Nakaso, M. Shimada, K. Okuyama, and K. Deppert, Journal of Aerosol Science 33, 1061 (2002).

[13] M. T. Swihart, Current Opinion in Colloid & Interface Science 8, 127 (2003).

[14] M. L. Ostraat, J. W. De Blauwe, M. L. Green, L. D. Bell, H. A. Atwater, and R. C. Flagan, Journal of The Electrochemical Society 148, G265 (2001).

[15] S. Polarz, A. Roy, M. Merz, S. Halm, D. Schröder, L. Schneider, G. Bacher, F. E. Kruis, and M. Driess, Small 1, 540 (2005).

[16] R. Schmechel, M. Kennedy, H. von Seggern, H. Winkler, M. Kolbe, R. A. Fischer, L. Xaomao, A. Benker, M. Winterer, and H. Hahn, Journal of Applied Physics 89, 1679 (2001).

[17] H. K. Kammler, L. Mädler, and S. E. Pratsinis, Chemical Engineering & Technology 24, 583 (2001).

[18] H. K. Kammler, S. E. Pratsinis, P. W. Morrison Jr, and B. Hemmerling, Combustion and Flame 128, 369 (2002).

[19] J.-M. Qiu, Thesis, University of Minnesota.

[20] Y.-H. Xu, Thesis, University of Minnesota, 2007.

[21] X.-Q. Liu, Thesis, University of Minnesota, 2009.

[22] K. W. a. S. Hayakawa, *Handbook of Sputtering Deposition Technology: Princinples, Technology and Applications* (Noyes Publications).

[23] J. C. Q A Pankhurst, S K Jones and J Dobson, J. Phys. D: Appl. Phys. 36 (2003).
[24] J. A. Paulus, G. R. Parida, R. D. Tucker, and J. B. Park, Biomaterials 18, 1609 (1997).
[25] J.-C. Bolomey, *Thermoradiotherapy and Thermochemotherapy*, Vol. 2 (Springer, 1995).
[26] C. W. Song, Cancer Research 44, 4721s (1984).
[27] R. K. Jain and K. Ward-Hartley, Sonics and Ultrasonics, IEEE Transactions on 31, 504 (1984).
[28] D.-H. Kim, E. A. Rozhkova, I. V. Ulasov, S. D. Bader, T. Rajh, M. S. Lesniak, and V. Novosad, Nat Mater 9, 165 (2010).
[29] D. Cai, J. M. Mataraza, Z.-H. Qin, Z. Huang, J. Huang, T. C. Chiles, D. Carnahan, K. Kempa, and Z. Ren, Nat Meth 2, 449 (2005).
[30] M. Liong, J. Lu, M. Kovochich, T. Xia, S. G. Ruehm, A. E. Nel, F. Tamanoi, and J. I. Zink, ACS Nano 2, 889 (2008).
[31] N. Nasongkla, E. Bey, J. Ren, H. Ai, C. Khemtong, J. S. Guthi, S.-F. Chin, A. D. Sherry, D. A. Boothman, and J. Gao, Nano Letters 6, 2427 (2006).
[32] M. Arruebo, M. Galán, N. Navascués, C. Téllez, C. Marquina, M. R. Ibarra, and J. Santamaría, Chemistry of Materials 18, 1911 (2006).
[33] A. A. Kuznetsov, V. I. Filippov, O. A. Kuznetsov, V. G. Gerlivanov, E. K. Dobrinsky, and S. I. Malashin, Journal of Magnetism and Magnetic Materials 194, 22 (1999).
[34] J. L. Arlett, E. B. Myers, and M. L. Roukes, Nat Nano 6, 203 (2011).
[35] M. A. Cooper, Nat Rev Drug Discov 1, 515 (2002).
[36] P. I. Nikitin, P. M. Vetoshko, and T. I. Ksenevich, Journal of Magnetism and Magnetic Materials 311, 445 (2007).
[37] P. Knight, Nat Biotech 7, 175 (1989).
[38] D. R. Baselt, G. U. Lee, M. Natesan, S. W. Metzger, P. E. Sheehan, and R. J. Colton, Biosensors and Bioelectronics 13, 731 (1998).
[39] D. L. Graham, H. Ferreira, J. Bernardo, P. P. Freitas, and J. M. S. Cabral, Journal of Applied Physics 91, 7786 (2002).
[40] G. Li, V. Joshi, R. L. White, S. X. Wang, J. T. Kemp, C. Webb, R. W. Davis, and S. Sun, Journal of Applied Physics 93, 7557 (2003).
[41] J. Schotter, P. B. Kamp, A. Becker, A. Pühler, G. Reiss, and H. Brückl, Biosensors and Bioelectronics 19, 1149 (2004).
[42] B. Srinivasan, Y. Li, Y. Jing, Y. Xu, X. Yao, C. Xing, and J.-P. Wang, Angewandte Chemie International Edition 48, 2764 (2009).
[43] W. Shen, X. Liu, D. Mazumdar, and G. Xiao, Applied Physics Letters 86, 253901 (2005).
[44] C. Emmenegger, J. M. Bonard, P. Mauron, P. Sudan, A. Lepora, B. Grobety, A. Züttel, and L. Schlapbach, Carbon 41, 539 (2003).
[45] A. Schätz, O. Reiser, and W. J. Stark, Chemistry – A European Journal 16, 8950 (2010).

[46] A.-H. Lu, W. Schmidt, N. Matoussevitch, H. Bönnemann, B. Spliethoff, B. Tesche, E. Bill, W. Kiefer, and F. Schüth, Angewandte Chemie International Edition 43, 4303 (2004).
[47] Kostedt, J. Drwiega, D. W. Mazyck, S.-W. Lee, W. Sigmund, C.-Y. Wu, and P. Chadik, Environmental Science & Technology 39, 8052 (2005).
[48] C. Ross, Annual Review of Materials Research 31, 203 (2001).
[49] N. A. Frey and S. Sun, in *Inorganic Nanoparticles: Synthesis, Applications, and Perspectives* (CRC Press, 2010), p. 33.
[50] E. F. Kneller and R. Hawig, Magnetics, IEEE Transactions on 27, 3588 (1991).
[51] J.-H. Lee, J.-t. Jang, J.-s. Choi, S. H. Moon, S.-h. Noh, J.-w. Kim, J.-G. Kim, I.-S. Kim, K. I. Park, and J. Cheon, Nat Nano 6, 418 (2011).
[52] Y. Hou, S. Sun, C. Rong, and J. P. Liu, Applied Physics Letters 91, 153117 (2007).
[53] C. C. Corten and M. W. Urban, Advanced Materials 21, 5011 (2009).
[54] C. Sun, J. S. H. Lee, and M. Zhang, Advanced Drug Delivery Reviews 60, 1252 (2008).
[55] S.-H. Huang and R.-S. Juang, Journal of Nanoparticle Research 13, 4411 (2011).
[56] R. M. R. K. Gilchrist, W.D. Shorey, R.C. Hanselman, J.C. Parrot and C.B. Taylor, Ann Surg. 161, 890 (1957).
[57] R. Sharma and C. Chen, Journal of Nanoparticle Research 11, 671 (2009).
[58] R. Hergt, S. Dutz, R. Müller, and M. Zeisberger, Journal of Physics: Condensed Matter 18, S2919 (2006).
[59] W. A. a. H. Nowak, *Magnetism in Medicine* (Wiley-VCH, Weinheim, 2007).
[60] C. G. Hadjipanayis, M. J. Bonder, S. Balakrishnan, X. Wang, H. Mao, and G. C. Hadjipanayis, Small 4, 1925 (2008).
[61] B. Mehdaoui, A. Meffre, J. Carrey, S. Lachaize, L.-M. Lacroix, M. Gougeon, B. Chaudret, and M. Respaud, Advanced Functional Materials 21, 4573 (2011).
[62] T.-Y. Liu, S.-H. Hu, D.-M. Liu, S.-Y. Chen, and I. W. Chen, Nano Today 4, 52 (2009).
[63] P. Guardia, R. Di Corato, L. Lartigue, C. Wilhelm, A. Espinosa, M. Garcia-Hernandez, F. Gazeau, L. Manna, and T. Pellegrino, ACS Nano 6, 3080 (2012).
[64] J.-P. Fortin, C. Wilhelm, J. Servais, C. Ménager, J.-C. Bacri, and F. Gazeau, Journal of the American Chemical Society 129, 2628 (2007).
[65] M. S. S. a. V. S. a. P. D. a. S. N. a. Y. Y. C. a. C. L. C. a. S. W. C. a. C. C. Chen, Journal of Physics D: Applied Physics 43, 145002 (2010).
[66] S. Maenosono and S. Saita, Magnetics, IEEE Transactions on 42, 1638 (2006).
[67] C. Martinez-Boubeta, K. Simeonidis, D. Serantes, I. Conde-Leborán, I. Kazakis, G. Stefanou, L. Peña, R. Galceran, L. Balcells, C. Monty, D. Baldomir, M. Mitrakas, and M. Angelakeris, Advanced Functional Materials, n/a (2012).
[68] L. M. Lacroix, R. B. Malaki, J. Carrey, S. Lachaize, M. Respaud, G. F. Goya, and B. Chaudret, Journal of Applied Physics 105, 023911 (2009).
[69] T. L. Kline, Y.-H. Xu, Y. Jing, and J.-P. Wang, Journal of Magnetism and Magnetic Materials 321, 1525 (2009).

[70] J. Carrey, B. Mehdaoui, and M. Respaud, Journal of Applied Physics 109, 083921 (2011).
[71] R. Hergt, R. Hiergeist, M. Zeisberger, D. Schüler, U. Heyen, I. Hilger, and W. A. Kaiser, Journal of Magnetism and Magnetic Materials 293, 80 (2005).
[72] Y. Jing, H. Sohn, T. Kline, R. H. Victora, and J.-P. Wang, Journal of Applied Physics 105, 07B305 (2009).
[73] E. Kita, T. Oda, T. Kayano, S. Sato, M. Minagawa, H. Yanagihara, M. Kishimoto, C. Mitsumata, S. Hashimoto, K. Yamada, and N. Ohkohchi, Journal of Physics D: Applied Physics 43, 474011 (2010).
[74] O. Kubaschewski, ASM Handbooks Online (2004).
[75] J. H. a. D. Spišák, Phys. Rev. B 75 (2007).
[76] Y. P. L. Y. V. Kudryavtsey, J. Dubowik, J. Y. Rhee, Phys. Rev. B 68 (2003).
[77] M. R. A. Kawaharazuka, J. Herfort, H. –P. Schönherr, H. Kostial and K. H. Ploog, Appl. Phys. Lett. 85 (2004).
[78] D. N. T. Yoshitake, T. Ogawa, M. Itakura, N. Kuwano, Y. Tomokiyo, T. Kajiwara, K. Nagayama, Appl. Phys. Lett. 86 (2005).
[79] M. T. Ryosho Nakane, and Satoshi Sugahara, Appl. Phys. Lett. 89 (2006).
[80] F. Gazeau, M. Lévy, and C. Wilhelm, Nanomedicine 3, 831 (2008).
[81] D. F. N. I. Kulikov, J. Hugel and A. V. Postnikov, Phys. Rev. B 66 (2002).
[82] S. K. A. Bansil, P. E. Mijnarends and J. Tobola, Phys. Rev. B 60 (1999).
[83] B. Daniel Kmiec, Marcel Sladecek, Marcus Rennhofer, Svetoslav Stankov, Gero Vogl, Bart Laenens, Johan Meersschaut, Tomasz Ślęzak and Marcin Zając, Phys. Rev. B 75 (2007).
[84] T. Y. D. Nakagauchi, K. Nagayama, Vaccum 74, 653 (2004).
[85] S. K. Kensuke Akiyama, Teiko Kadowaki, Yasuo Hirabayashi and Hiroshi Funakubo, Jap. J. Appl. Phys 47 (2008).
[86] M. I. Masahiro Miyazaki, Takayuki Komatsu, and Kazumasa Matusita, J. Appl. Phys 71 (1992).
[87] P. K. M. J. Herfort, K. –J. Friedland, H. –P. Schönherr, K. H. Ploog, J. Magn. Magn. Mater. 310 (2007).
[88] J.-M. Qiu and J.-P. Wang, Applied Physics Letters 88, 192505 (2006).
[89] A. Ionescu, C. A. F. Vaz, T. Trypiniotis, C. M. Gürtler, H. García-Miquel, J. A. C. Bland, M. E. Vickers, R. M. Dalgliesh, S. Langridge, Y. Bugoslavsky, Y. Miyoshi, L. F. Cohen, and K. R. A. Ziebeck, Physical Review B 71, 094401 (2005).
[90] M. P. Sharrock, Journal of Applied Physics 76, 6413 (1994).
[91] R. C. O'Handley, *Modern Magnetic Materials - Principles and Applications* (JOHN WILEY AND SONS LTD 1999).
[92] K. Dong-Hyun, Y. T. Thai, D. E. Nikles, and C. S. Brazel, Magnetics, IEEE Transactions on 45, 64 (2009).
[93] M. Jeun, S. J. Moon, H. Kobayashi, H. Y. Shin, A. Tomitaka, Y. J. Kim, Y. Takemura, S. H. Paek, K. H. Park, K.-W. Chung, and S. Bae, Applied Physics Letters 96, 202511 (2010).
[94] N. A. Usov, Journal of Applied Physics 107, 123909 (2010).

[95] H. Huang, S. Delikanli, H. Zeng, D. M. Ferkey, and A. Pralle, Nat Nano 5, 602 (2010).
[96] Y. V. Kudryavtsev, Y. P. Lee, J. Dubowik, B. Szymański, and J. Y. Rhee, Physical Review B 65, 104417 (2002).
[97] O'Handley, *Modern Magnetic Materials: Principles and Applications* (Wiley-Interscience, 1999).
[98] R. Hergt, S. Dutz, and M. Zeisberger, Nanotechnology 21, 015706 (2010).
[99] G. Bertotti, *Hysteresis in Magnetism* (Academic Press Limited, 1998).
[100] E. Pollert, K. Knížek, M. Maryško, P. Kašpar, S. Vasseur, and E. Duguet, Journal of Magnetism and Magnetic Materials 316, 122 (2007).
[101] N. K. Prasad, K. Rathinasamy, D. Panda, and D. Bahadur, Journal of Biomedical Materials Research Part B: Applied Biomaterials 85B, 409 (2008).
[102] O. Kaman, P. Veverka, Z. Jirák, M. Maryško, K. Knížek, M. Veverka, P. Kašpar, M. Burian, V. Šepelák, and E. Pollert, Journal of Nanoparticle Research 13, 1237 (2011).
[103] T. N. Brusentsova, N. A. Brusentsov, V. D. Kuznetsov, and V. N. Nikiforov, Journal of Magnetism and Magnetic Materials 293, 298 (2005).
[104] T. N. Brusentsova and V. D. Kuznetsov, Journal of Magnetism and Magnetic Materials 311, 22 (2007).
[105] *Nanoparticle Technology Handbook* (Elsevier Science, 2007).
[106] M. Bettge, J. Chatterjee, and Y. Haik, Biomagnetic research and technology 2, 4 (2004).
[107] J. Chatterjee, M. Bettge, Y. Haik, and C. Jen Chen, Journal of Magnetism and Magnetic Materials 293, 303 (2005).
[108] K. L. McNerny, Y. Kim, D. E. Laughlin, and M. E. McHenry, Journal of Applied Physics 107, 09A312 (2010).
[109] J. J. Ipus, H. Ucar, and M. E. McHenry, Magnetics, IEEE Transactions on 47, 2494 (2011).
[110] K. J. Miller, A. Colletti, P. J. Papi, and M. E. McHenry, Journal of Applied Physics 107, 09A313 (2010).
[111] Y. Akin, I. M. Obaidat, B. Issa, and Y. Haik, Crystal Research and Technology 44, 386 (2009).
[112] H. C. S. J. Stohr, *Magnetism: From Fundamentals to Nanoscale Dynamics* (Springer, 2006).
[113] E. P. E. a. G. N. K. a. V. A. B. a. E. V. Voronina, Journal of Physics: Condensed Matter 4, 7597 (1992).
[114] C. Martinez-Boubeta, L. Balcells, R. Cristòfol, C. Sanfeliu, E. Rodríguez, R. Weissleder, S. Lope-Piedrafita, K. Simeonidis, M. Angelakeris, F. Sandiumenge, A. Calleja, L. Casas, C. Monty, and B. Martínez, Nanomedicine: Nanotechnology, Biology and Medicine 6, 362 (2010).
[115] M. Moravej, F. Prima, M. Fiset, and D. Mantovani, Acta Biomaterialia 6, 1726 (2010).
[116] H. Hermawan, D. Dubé, and D. Mantovani, Acta Biomaterialia 6, 1693 (2010).

[117] D. T. a. Y. M. a. K. H. a. Kouki Fujioka and Masaki Hiruoka and Keisuke Sato and Noriyoshi Manabe and Ryosuke Miyasaka and Sanshiro Hanada and Akiyoshi Hoshino and Richard, Nanotechnology 19, 415102 (2008).
[118] L. Wang, V. Reipa, and J. Blasic, Bioconjugate Chemistry 15, 409 (2004).
[119] F. Erogbogbo, K.-T. Yong, I. Roy, G. Xu, P. N. Prasad, and M. T. Swihart, ACS Nano 2, 873 (2008).
[120] E. Tasciotti, X. Liu, R. Bhavane, K. Plant, A. D. Leonard, B. K. Price, M. M.-C. Cheng, P. Decuzzi, J. M. Tour, F. Robertson, and M. Ferrari, Nat Nano 3, 151 (2008).
[121] L. T. Canham, Advanced Materials 7, 1033 (1995).
[122] F. Erogbogbo, K.-T. Yong, R. Hu, W.-C. Law, H. Ding, C.-W. Chang, P. N. Prasad, and M. T. Swihart, ACS Nano 4, 5131 (2010).
[123] S. C. Bayliss, R. Heald, D. I. Fletcher, and L. D. Buckberry, Advanced Materials 11, 318 (1999).
[124] V. Chin, B. E. Collins, M. J. Sailor, and S. N. Bhatia, Advanced Materials 13, 1877 (2001).
[125] J. M. Qiu and J. P. Wang, Advanced Materials 19, 1703 (2007).
[126] Y. H. Xu and J. P. Wang, Advanced Materials 20, 994 (2008).
[127] M. K. Kolel-Veetil, S. B. Qadri, M. Osofsky, R. Goswami, and T. M. Keller, The Journal of Physical Chemistry C 113, 14663 (2009).
[128] N. Dahal and V. Chikan, Chemistry of Materials 22, 2892 (2010).
[129] S. Vitta, Journal of Applied Physics 101, 063901 (2007).
[130] S. N. Kaul, Physical Review B 24, 6550 (1981).
[131] R. d. B. a. Z. L. a. G. W. Ming Zhang and Ekkes Brück and Frank, Journal of Physics D: Applied Physics 37, 2049 (2004).
[132] L. Ritchie, G. Xiao, Y. Ji, T. Y. Chen, C. L. Chien, M. Zhang, J. Chen, Z. Liu, G. Wu, and X. X. Zhang, Physical Review B 68, 104430 (2003).
[133] V. Johnson, J. F. Weiher, C. G. Frederick, and D. B. Rogers, Journal of Solid State Chemistry 4, 311 (1972).
[134] E. P. Elsukov, G. N. Konygin, V. A. Barinov, and E. V. Voronina, Journal of Physics: Condensed Matter 4, 7597 (1992).
[135] R. W. McCallum, Journal of Magnetism and Magnetic Materials 292, 135 (2005).
[136] S. Okamoto, N. Kikuchi, O. Kitakami, T. Miyazaki, Y. Shimada, and K. Fukamichi, Physical Review B 66, 024413 (2002).
[137] O. Margeat, M. Tran, M. Spasova, and M. Farle, Physical Review B 75, 134410 (2007).
[138] J. U. Thiele, K. R. Coffey, M. F. Toney, J. A. Hedstrom, and A. J. Kellock, Journal of Applied Physics 91, 6595 (2002).
[139] T. Novet and D. C. Johnson, Journal of the American Chemical Society 113, 3398 (1991).
[140] C. Xu, Z. Yuan, N. Kohler, J. Kim, M. A. Chung, and S. Sun, Journal of the American Chemical Society 131, 15346 (2009).
[141] M.-J. Hu, Y. Lu, S. Zhang, S.-R. Guo, B. Lin, M. Zhang, and S.-H. Yu, Journal of the American Chemical Society 130, 11606 (2008).

[142] R. Tang, R. N. Palumbo, W. Ji, and C. Wang, Biomacromolecules 10, 722 (2009).
[143] R. S. Gaster, D. A. Hall, and S. X. Wang, Nano Letters 11, 2579 (2010).
[144] Y. Li, B. Srinivasan, Y. Jing, X. Yao, M. A. Hugger, J.-P. Wang, and C. Xing, Journal of the American Chemical Society 132, 4388 (2010).
[145] J. P. Wang.
[146] P. L. Ong, S. Mahmood, T. Zhang, J. J. Lin, R. V. Ramanujan, P. Lee, and R. S. Rawat, Applied Surface Science 254, 1909 (2008).
[147] F. Bulut, W. Rosellen, and M. Getzlaff, Applied Physics A: Materials Science & Processing 97, 185 (2009).
[148] L.-M. Lacroix, N. Frey Huls, D. Ho, X. Sun, K. Cheng, and S. Sun, Nano Letters 11, 1641 (2011).
[149] F. Dumestre, B. Chaudret, C. Amiens, P. Renaud, and P. Fejes, Science 303, 821 (2004).
[150] X.-W. Wei, G.-X. Zhu, Y.-J. Liu, Y.-H. Ni, Y. Song, and Z. Xu, Chemistry of Materials 20, 6248 (2008).
[151] D. Kodama, K. Shinoda, K. Sato, Y. Konno, R. J. Joseyphus, K. Motomiya, H. Takahashi, T. Matsumoto, Y. Sato, K. Tohji, and B. Jeyadevan, Advanced Materials 18, 3154 (2006).
[152] N. Semagina and L. Kiwi-Minsker, Catalysis Reviews 51, 147 (2009).
[153] W. H. Meiklejohn and C. P. Bean, Physical Review 105, 904 (1957).
[154] J. Nogués, J. Sort, V. Langlais, V. Skumryev, S. Suriñach, J. S. Muñoz, and M. D. Baró, Physics Reports 422, 65 (2005).
[155] V. Skumryev, S. Stoyanov, Y. Zhang, G. Hadjipanayis, D. Givord, and J. Nogues, Nature 423, 850 (2003).
[156] V. Baltz, J. Sort, S. Landis, B. Rodmacq, and B. Dieny, Physical Review Letters 94, 117201 (2005).
[157] K. Liu, S. M. Baker, M. Tuominen, T. P. Russell, and I. K. Schuller, Physical Review B 63, 060403 (2001).
[158] L. Yin, D. Xiao, Z. Gai, T. Z. Ward, N. Widjaja, G. M. Stocks, Z.-h. Cheng, E. W. Plummer, Z. Zhang, and J. Shen, Physical Review Letters 104, 167202 (2010).
[159] C. Djurberg, P. Svedlindh, P. Nordblad, M. F. Hansen, F. Bødker, and S. Mørup, Physical Review Letters 79, 5154 (1997).
[160] J. M. Vargas, W. C. Nunes, L. M. Socolovsky, M. Knobel, and D. Zanchet, Physical Review B 72, 184428 (2005).
[161] G. C. Papaefthymiou, E. Devlin, A. Simopoulos, D. K. Yi, S. N. Riduan, S. S. Lee, and J. Y. Ying, Physical Review B 80, 024406 (2009).
[162] V. Polshettiwar, R. Luque, A. Fihri, H. Zhu, M. Bouhrara, and J.-M. Basset, Chemical Reviews 111, 3036 (2011).
[163] V. Polshettiwar and R. S. Varma, Green Chemistry 12 (2010).
[164] W. Du, Y. Xu, and Y. Wang, Langmuir 24, 175 (2007).
[165] Y. Zhang, W. Liu, C. Wu, T. Gong, J. Wei, M. Ma, K. Wang, M. Zhong, and D. Wu, Materials Research Bulletin 43, 3490 (2008).
[166] S. K. Apte, S. D. Naik, R. S. Sonawane, B. B. Kale, and J. O. Baeg, Journal of the American Ceramic Society 90, 412 (2007).

[167] B. C. Faust, M. R. Hoffmann, and D. W. Bahnemann, The Journal of Physical Chemistry 93, 6371 (1989).
[168] H. Liu and L. Gao, Journal of the American Ceramic Society 89, 370 (2006).
[169] N. J. Cherepy, D. B. Liston, J. A. Lovejoy, H. Deng, and J. Z. Zhang, The Journal of Physical Chemistry B 102, 770 (1998).
[170] Z. Zhang, C. Boxall, and G. H. Kelsall, Colloids and Surfaces A: Physicochemical and Engineering Aspects 73, 145 (1993).
[171] J. E. Turner, M. Hendewerk, J. Parmeter, D. Neiman, and G. A. Somorjai, Journal of The Electrochemical Society 131, 1777 (1984).
[172] J. A. Glasscock, P. R. F. Barnes, I. C. Plumb, and N. Savvides, The Journal of Physical Chemistry C 111, 16477 (2007).
[173] J. Feng, X. Hu, P. L. Yue, H. Y. Zhu, and G. Q. Lu, Industrial & Engineering Chemistry Research 42, 2058 (2003).
[174] K. Ohtsuka, Chemistry of Materials 9, 2039 (1997).
[175] S. Shylesh, V. Schünemann, and W. R. Thiel, Angewandte Chemie International Edition 49, 3428 (2010).
[176] J. W. B. Ingler and S. U. M. Khan, Electrochemical and Solid-State Letters 9, G144 (2006).
[177] M. P. Dare-Edwards, J. B. Goodenough, A. Hamnett, and P. R. Trevellick, Journal of the Chemical Society, Faraday Transactions 1: Physical Chemistry in Condensed Phases 79 (1983).
[178] D. M. Sherman, Physics and Chemistry of Minerals 12, 161 (1985).
[179] T. D. W. David M. Sherman, American Mineralogist 70, 1262 (1985).
[180] M. D. B. Daniel C. Harris, *Symmetry and spectroscopy* (Oxford University Press, 1978).
[181] Y. P. He, Y. M. Miao, C. R. Li, S. Q. Wang, L. Cao, S. S. Xie, G. Z. Yang, B. S. Zou, and C. Burda, Physical Review B 71, 125411 (2005).
[182] L. Fu, Z. Wu, X. Ai, J. Zhang, Y. Nie, S. Xie, G. Yang, and B. Zou, The Journal of Chemical Physics 120, 3406 (2004).
[183] I. V. Chernyshova, S. Ponnurangam, and P. Somasundaran, Physical Chemistry Chemical Physics 12 (2010).
[184] B. Zou, W. Huang, M. Y. Han, S. F. Y. Li, W. Xiaochun, Y. Zhang, J. Zhang, W. Pengfei, and R. Wang, Journal of Physics and Chemistry of Solids 58, 1315 (1997).
[185] S. S. Shinde and K. Y. Rajpure, Journal of Solid State Chemistry 183, 2886 (2010).
[186] S. Chakrabarti, D. Ganguli, and S. Chaudhuri, Physica E: Low-dimensional Systems and Nanostructures 24, 333 (2004).
[187] R. A. Sperling and W. J. Parak, Philosophical Transactions of the Royal Society A: Mathematical,Physical and Engineering Sciences 368, 1333 (2010).
[188] S. Sun and C. B. Murray, Journal of Applied Physics 85, 4325 (1999).
[189] Y. Zhang, N. Kohler, and M. Zhang, Biomaterials 23, 1553 (2002).
[190] Y. Zhou, S. Wang, B. Ding, and Z. Yang, Chemical Engineering Journal 138, 578 (2008).

[191] L. Zhang, R. He, and H.-C. Gu, Applied Surface Science 253, 2611 (2006).
[192] A. K. Gupta and M. Gupta, Biomaterials 26, 3995 (2005).
[193] R. Tadmor, R. E. Rosensweig, J. Frey, and J. Klein, Langmuir 16, 9117 (2000).

APPENDIX

Pt nanoparticles for Catalysts

1.1 Introduction

Nowadays people face an increasing demand for energy which poses challenges for the limited supply of available energy. Development of new source of energy is under extensive investigation. Fuel cells invented by Sir William Grove in the middle of 19th century have drawn great research interests in 20th century driven by this energy demand. A fuel cell is an electrochemical device that can convert chemical energy generated in reactions to electricity with low noise, low pollutant product generated[1]. The basic structure of a full cell device consists of an anode and a cathode. The electrical energy is generated through oxidation of the fuel which can be hydrogen, methanol, gasoline, etc. at the anode, and reduction of oxidant which is usually oxygen at the cathode. From a thermodynamics point of view, the change of Gibbs free energy relates with the voltage on the cell, a sign of electrical energy converted from chemical energy. The function to describe this process is written as $\Delta G = -nF\Delta E_0$ where n is the number of electrons involved in the process and F is Faraday constant[2].

In fuel cells, catalyst material is important for both reactions at the anode and the cathode. It is a popular direction to search for catalyst materials for fuel cells to gain high efficiency, low operation temperature and low environmental impact. Advancement of nanotechnology brings the opportunity for fuel cells towards these goals. Metallic

nanoparticles have been proved to offer exciting catalysis performance due to their large surface area, more detailed surface features and different band structures from their bulk counterparts[3]. Transition metals like Pt, Pd and bimetallic alloy have been synthesized through different methods, such as impregnation method, colloidal method and microemulsion method with size and shape control[2,4]. A general concern for these synthesis methods is that the presence of surface surfactant can cover available site on the surface of nanoparticles leading to low catalysis efficiency.

In this chapter, fabrication of Pt nanoparticles by the gas phase method is going to be introduced. Nanoparticles produced through this method are surfactant free which could address concern about contaminated surface. In addition, this method can also offer tunable size of Pt nanoparticles, which will be a good starting point for the study of electronic structure of nanoparticles. We will present how to control the size of nanoparticles and show the study of Pt nanoparticles of different sizes by ultraviolet photoemission.

1.2Catalytic Behavior of Transition Metals

1.2.1d Band Model

Catalytic behavior of metals has been applied in real life for a long time. It is important to understand the intrinsic properties of materials that give catalytic behavior in searching for new candidates with high efficiency. In catalysis, surface of the material plays the dominant role in determining its efficiency because catalytic reactions depend on

absorption/dissociation of gas molecules or radicals onto the surface. For example, in H_2-O_2 fuel cell, the cathode catalyst should be able to dissociate O_2 without binding to O too tightly. The anode catalyst should be able to dissociate H_2 without binding to H too tightly[5]. These processes all relate with the electronic structure of the surface of the material.

B. Hammer and J. K. Nϕrskov proposed the underlying principles that govern the reactivity of metal surfaces[6]. Their model has been found successful in explaining the catalytic behavior of many material systems[5,7]. In their model, the reactivity of metal surface depends on the entire d bands of the surface rather than merely density of states at the Fermi level. When an adsorbate for example H_2 interacts with the metal surface, the anti-bonding state and bonding-state of orbitals of H_2 will form bonds with d electrons of the metal. The molecule-d bonds also have orbitals in similar anti-bonding state and bonding state. The higher of the two states of the molecule is up-shifted and the lower of the two states of the molecule is down-shifted. This interaction is affected by the relative position of orbitals of the molecule to the Fermi level of d bands of metal, the coupling energy V of hydrogen and metal atoms, the filling f of the molecule-surface anti-bonding states given by the position of the Fermi level. Based on these arguments a parameter was proposed to represent the energy difference due to the coupling to the d bands, which acts as a direct measure of reactivity of the surface. The parameter has the following form

$$\delta E_{ts} = -2\frac{V^2}{\varepsilon_{\sigma^*_u} - \varepsilon_d} - 2(1-f)\frac{V^2}{\varepsilon_d - \varepsilon_{\sigma_g}} + \alpha V^2 \quad \text{(Equation 1.1)}$$

where $\varepsilon_{\sigma^*_u}$, ε_{σ_g}, ε_d are energy positions of anti-bonding, bonding state of H_2 molecule and the d band center of the metal surface, respectively. α is a constant. By computing various material systems, it was found that a large $\left|\varepsilon_{\sigma^*_u} - \varepsilon_d\right|$ would lead to cancellation of the first and the third term, giving little energy difference. When there is not any energy preference to form a bond, the metal has low reactivity. In gold for example, δE_{ts} is 0.1 compared to -1.51 of Pt. Because there is little change of $\varepsilon_{\sigma^*_u}$ from one material to another, the position of the d band center is thus one of the most critical electronic parameters for catalytic performance. The more negative of the d band center gives the weaker interaction strength between the adsorbates and the metal surface. Till this moment, we should be able to tell whether a metal can have active interaction with molecules by looking at its d band center.

1.2.2 Size Dependence of Electronic Structures of Metal Nanoparticles

There has been extensive research on electronic structures of transition metal nanoparticles (eg. Pt, Pd, Au) and their size dependence. However, the findings on electronic structures don't follow the same trend due to the complexity of nanostructures and photoemission processes. It is of crucial value for a study on transition metal nanoparticles synthesized in gas phase specifically.

Several studies are summarized here to show the complicated nature of electronic structures of nanomaterials. Toyoda et. al[8] found in simulation that d band center of Pt nanoclusters in a vacuum or deposited on graphene shifted close to Fermi level compared

to the bulk. There was a linear correlation between the size of Pt nanoclusters and the d band center, which was demonstrated by both the simulation and the experiments. Similarly, Bokhoven et. al[9] discovered that d band center of smaller Au clusters moved closer to the Fermi level than that of larger ones. In their findings, low coordination number of surface atoms was assigned as the reason for the difference of the d band center between nanostructures and bulk samples, as well as the size dependence of the d band center. A decrease of hybridizing wavefunctions leads to the narrow d-band and its shift close to Fermi level. However, Eberhardt et. al[10] and Murgai et. al[11] observed d band center shifted away from Fermi level as the size decreased for small Pt clusters sputtered on Si wafer and in Pt-SiO_2 granular films, respectively. It is probably because their Pt clusters are too small which contain only a few atoms to be analyzed in the context of a modified band structure of metals. Zhou et. al[12] discovered that the d band center of Pd nanoparticles downshifted from the bulk value and moved away from Fermi level as the size decreased. They explained this change in terms of compressive strain induced enhancement of d-hybridation[12,13,14]. Lee et. al[15] showed downshifted d band center of about 2nm Pt nanoparticles relative to the value of bulk Pt(111). This tendency was attributed to the coverage of O on the surface of Pt nanoparticles, which resulted in a broadening of the d-band.

Based on the different findings of the electronic structures of transition metal nanoparticles, it is thus concluded that the electronic properties are much dependent on the structure and surface chemistry of the nanoparticles. There isn't a universal rule that can be applied to the understanding of the surface electronic structures. Because there has

been rarely fabrication of free nanoparticles in gas phase without the use of precursors, our study provides in-depth investigation of the electronic properties of such nanoparticles and the implication of their potential for catalysis.

1.3 Fabrication of Pt Nanoparticles of Different Size in Gas Phase

Pt nanoparticles were fabricated by the physical condensation method introduced previously. To make Pt nanoparticles, a piece of pure Pt target was positioned in the vacuum chamber. The base pressure for the fabrication process was $2*10^{-7}$ torr. Magnetic field on the surface of the target was adjusted in the range of 2200Oe-1100Oe in order to optimize the crystallinity of Pt nanoparticles. It was found in the experiments that Pt usually requires a high magnetic field strength to crystalize well, which was not usually used for other materials. Magnetic field profile on the surface of the target was modified by a small soft iron cone with diameter of 1.27cm and height of 1mm, as well as a soft iron ring with width of 2.5mm and height of 1mm. Figure 1.1(a) shows typical morphology of Pt nanoparticles fabricated under 2200Oe magnetic field, 0.5A sputtering current and 350mTorr sputtering pressure. The corresponding selected area diffraction is shown in Figure 1.1(b) and is indexed to face-centered-cubic structure of Pt.

In order to obtain variable size of Pt nanoparticles, sputtering current and gas flow were varied to find out the suitable condition for size control. As what will be discussed in the following, sputtering current brings little effect on the size of Pt nanoparticles while gas flow influences it much more.

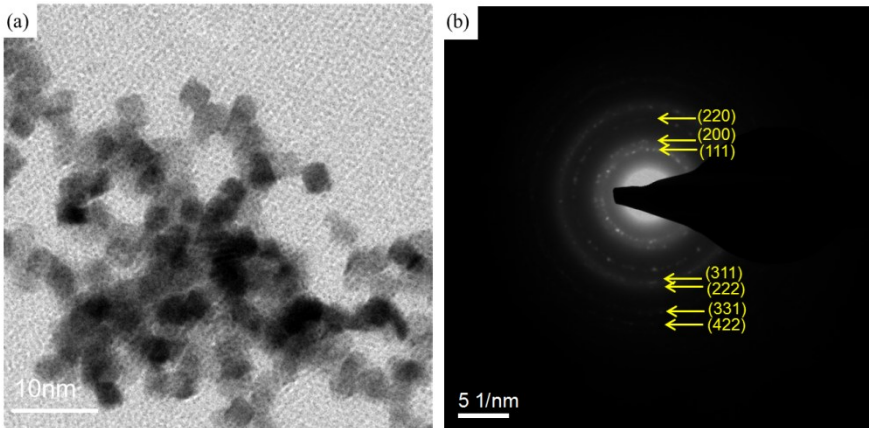

Figure 1.1 (a) TEM bright field image of Pt nanoparticles (b) Selected area diffraction pattern of Pt nanoparticles

1.3.1 Effect of Sputtering Current

In magnetron sputtering, sputtering current is associated with the charged species, such as Ar ions. Because the distribution of the current is confined in the erosion track region, increasing sputtering current will directly lead to an increase of the density of Ar ions

Density of the sputtered atoms will also increase because they are generated through bombardment of Ar ions onto the sputtering target. A high density of sputtered atoms increases the total amount of available source material and the probability of collisions among nucleated small particles and sputtered atoms. Under these arguments, there can be situation that increasing sputtering current will lead to an increase of nanoparticles' size because of the high density of sputtered species. However, particularly for Pt nanoparticles, we were not able to observe the effect of sputtering current on size control while the effect can be observed for FePt nanoparticles[16] and for certain cases of Fe-Si nanoparticles. Figure 1.2 displays TEM images of Pt nanoparticles fabricated under

different sputtering current and gas flow condition. At this moment, we focus on the sputtering current effect only. The gas flow effect will be explained in detail later. If we compare Figure 1.2(a) with (b) and Figure 1.2(c) with (d), there is hardly any size difference from one to the other. This suggests that size of Pt nanoparticles is not sensitive to the change of sputtering current. The current insensitivity could be due to enthalpy of vaporization for Pt is relatively high at 510kJ/mol, compared to for example 349.6kJ/mol of Fe. So it can result in a higher ratio of incident Ar ions to sputtered atoms for Pt than that for Fe. With limited increase of Ar ions by changing sputtering current, increase of sputtered Pt atoms may not be significant in reality.

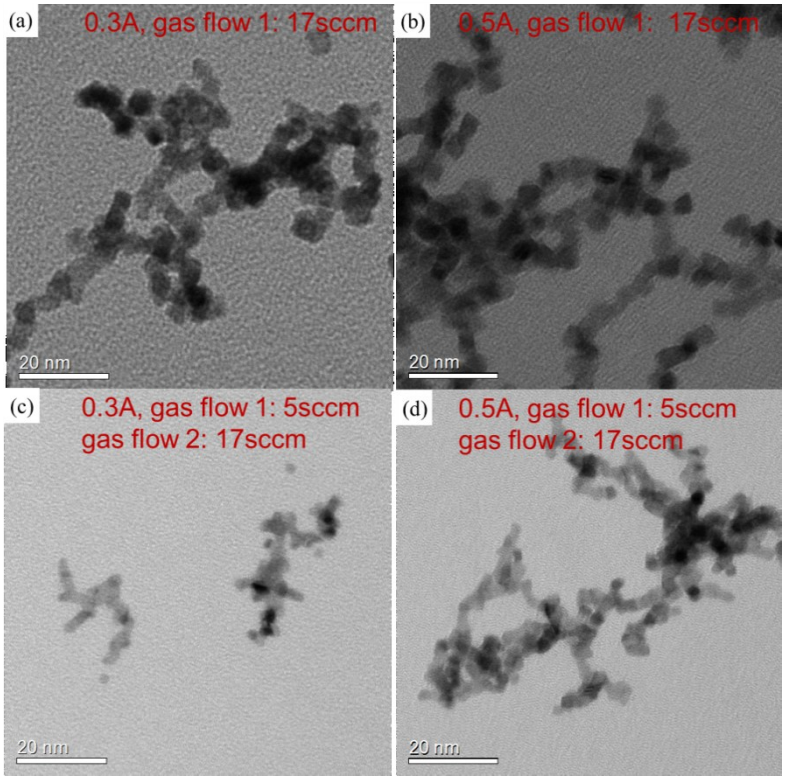

.

Figure 1.2 TEM bright field images of Pt nanoparticles fabricated under (a) 0.3A/gas flow 1 of 17sccm (b) 0.5A/gas flow 1 of 17sccm (c) 0.3A/gas flow 2 of 5sccm and gas flow 1 of 17sccm (d) 0.5A/gas flow 2 of 5sccm and gas flow 1 of 17sccm

1.3.2 Effect of Gas flow

The size of nanoparticle can also be affected by the time they spend in the nucleation and growth region, which is a region with high magnetic field strength and dense plasma. There are two gas inputs in our system. One is mainly for the input of sputtering gas (gas flow 1), which locates near the surface of the target. The other one is mainly for carrier gas input (gas flow2), which locates relatively far from the surface of the target. Ar gas has several functions in the fabrication process. It first serves as sputtering gas to provide ionized Ar^+. Second, it acts as carrier gas to bring sputtered species towards substrate. In the plasma region, Ar molecules are relatively "cool" with low kinetic energy compared to other species. They drain out the energy of kinetically active Ar ions and sputtered atoms. The presence of Ar molecules in the plasma as an energy drain influences the thermal environment for nucleation and growth in gas phase. On one hand, by manipulating the travel time of nanoparticles in the plasma region through carrier flow can adjust the total growth time. Nanoparticles could have small or large size when they are allowed for short or long time to grow. On the other hand, the thermal environment for a crystal to grow can be changed by manipulating the sputtering gas. It allows a change of how intense the energy drain effect takes place, which could also affect the final size of nanoparticles.

In Figure 1.3, TEM images of Pt nanoparticles fabricated under different pressure with different input gas flow set-up are displayed. 0.5A sputtering current and 2200Oe magnetic field condition were used for these samples. Figure 1.3(a) and (b) represents Pt nanoparticles fabricated under 256mTorr pressure without and with the addition of carrier

gas. Figure 1.3(c) and (d) represents Pt nanoparticles fabricated under 176mTorr without and with the addition of carrier gas. For both groups, when carrier gas was used, a reduction of the size of Pt nanoparticles can be observed. This reflects the fact that size can be affected by travel time in growth region as we previously discussed. The addition of the carrier gas accelerates the travel of Pt nanoparticles in the plasma region and leads to a reduction of time allowed for Pt nanoparticles to grow.

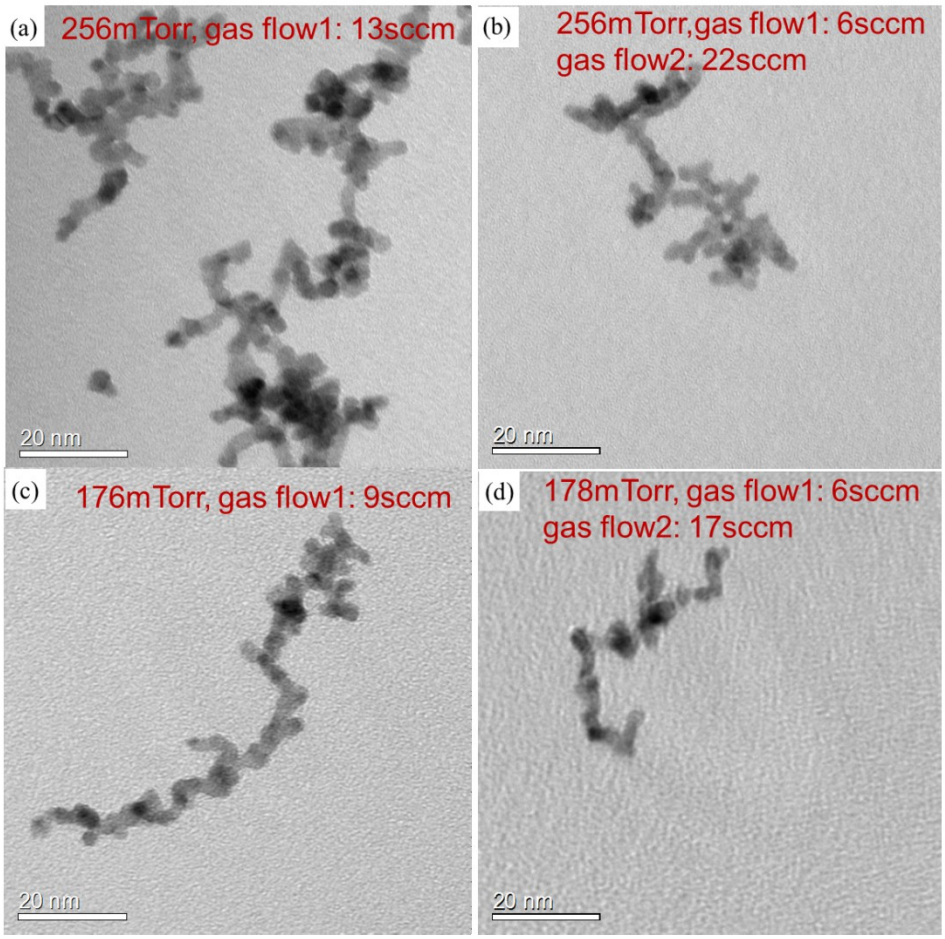

Figure 1.3 TEM bright field images of Pt nanoparticles fabricated under (a) 256mTorr/gas flow 1 of 13sccm (b) 256mTorr/gas flow 1 of 6sccm and gas flow 2 of 22sccm (c) 176mTorr/gas flow 1 of 9sccm (d) 178mTorr/gas flow 1 of 6sccm and gas flow 2 of 17sccm

However, if we compare between the groups, for example (a) versus (c) or (b) versus (d), the size of Pt nanoparticles seems to be related with the sputtering pressure. Nanoparticles fabricated under low pressure possess smaller size as in (c) and (d). This actually coincides with the energy drain effect of Ar gas on the size of nanoparticles mentioned earlier. Growth of nanoparticles starts with appreciable adsorption of atoms compared to desorption of atoms. When the pressure is low where energy drain effect is not intense, desorption of atoms may prevail at first due to the warm environment. After sufficient collisions in the plasma region, adsorption of atoms becomes dominant and continuous growth takes place. As the plasma region is mainly dependent on the modification of magnetic field and is almost fixed, low pressure condition modifies the actual time of growth in plasma region by postponing the point where growth starts to happen in plasma region. This is why pressure can also affect the size of nanoparticles. In Figure 1.2, if we compare Pt nanoparticles in (a) with (c), and (b) with (d), smaller size can be seen for Pt nanoparticles fabricated under conditions with two Ar gas input. This reflects a combination of the influence of carrier gas and pressure on the size of Pt nanoparticles.

Overall, we are able to manipulate the total input Ar gas and to adjust the exact flow configuration with the combined use of two gas inputs. Different size of Pt nanoparticles can be obtained by varying the synthesis conditions. One phenomenon that was constantly observed for these Pt nanoparticles is a strong tendency of small Pt nanoparticles to agglomerate into chain or network form. The strong tendency of forming agglomerated chain is driven by a minimization of total Gibbs free energy, where

reduction of surface energy is critical in nano-systems. With a certain density of Pt nanoparticles traveling in gas phase, there might still be appreciable chances for them to coalesce in the presence of high kinetic energy. This means that even after leaving the plasma region, nanoparticles are still "hot" and are active to coalesce, which facilitates the reduction of surface energy and is preferable. It has been found that the smaller the nanoparticles are the stronger tendency to form coalesced structure.

1.4 Electronic Structure of Pt Nanoparticles of Different Sizes

1.4.1 Experiments and Results

Pt nanoparticles of four different sizes were prepared by employing previously introduced size-control scheme. Fabrication conditions are listed in Table 1.1for each size. Gas input was manipulated as the main factor to introduce size control while sputtering current and magnetic field were adjusted to optimize the crystallinity. Figure 1.4 shows TEM images of the samples (left) and the corresponding histogram of the size of the nanoparticles (right). Pt nanoparticles with a mean size of 3.4nm, 2.7nm, 2.1nm and 1.6nm were used for the study of their electronic structure. The nanoparticles were deposited on highly ordered pyrolytic graphite (HOPG) substrates. During deposition, half of the HOPG substrate was covered by parafilm to leave a blank background for reference. After the samples were taken out of the vacuum chamber, they were purged with N_2 gas before being sealed into a small bottle. The electronic structure of these Pt nanoparticles was probed using surface sensitive ultraviolet photoemission spectroscopy (UPS) by Prof. Yang's group at Massachusetts Institute of Technology.

Table 1.1 Fabrication conditions of Pt nanoparticles of different size

sample	Magnetic field (Oe)	Current (A)	Pressure (mTorr)	Gas flow 1	Gas flow 2
3.4nm	2200	0.5	350	17	0
2.7nm	2200	0.5	353	6	28
2.1nm	2200	0.6	255	6	22
1.6nm	1130	0.3	159	5	17

The working principle of UPS is similar to X-ray photoelectron spectroscopy (XPS). They both utilize photo-ionization and the analysis of the kinetic energy of the emitted photoelectrons to study the composition and electronic state of the surface of the material. The basic principle of UPS is governed by Einstein's photoelectric law:

$E_K = h\nu - I$ (Equation 1.2)

in which h is the Plank's constant, ν is the frequency of electromagnetic wave, I is the ionization energy. When a material absorbs incident electromagnetic wave, the energy can excite electrons of the material. If one electron obtains the amount of energy from a photon more than its work function or say binding energy, the electron will be ejected which is then named as a photoelectron. Therefore, by measuring the kinetic energy of photoelectrons, we are able to trace out the binding energy of the electrons in the material. Due to the short travel range of photoelectrons, analysis based on them mainly reflects the surface property of the material.

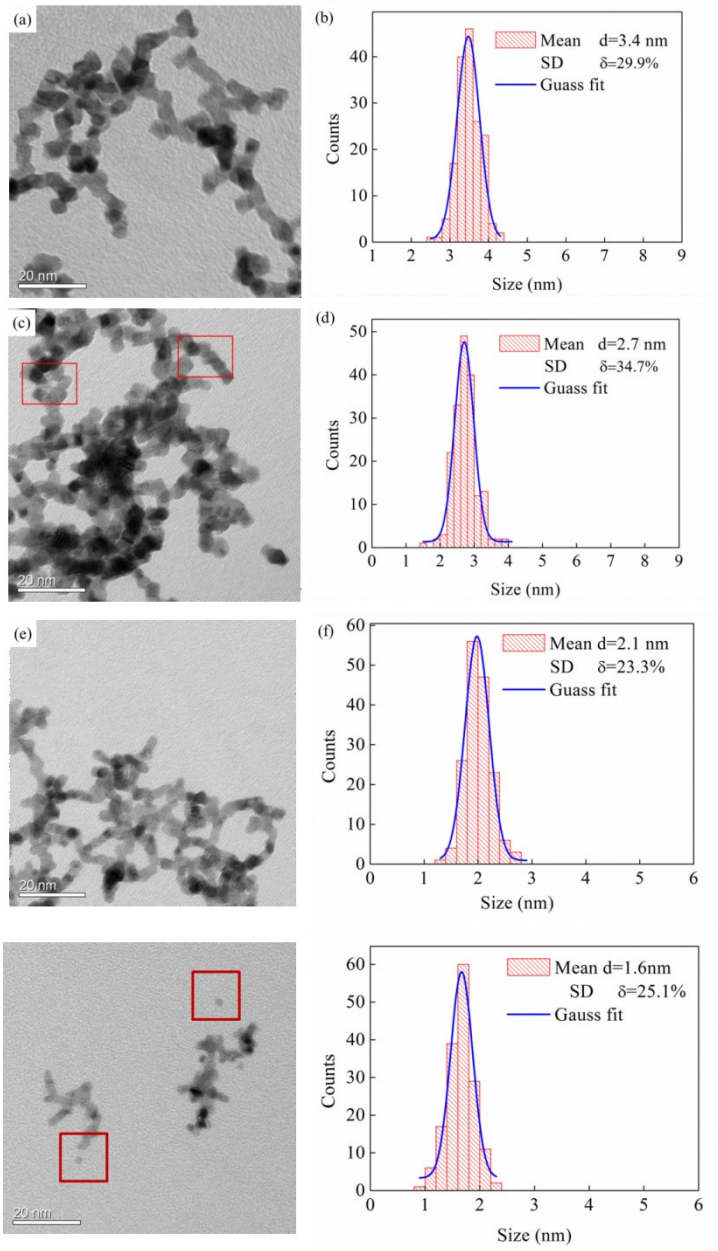

Figure 1.4 (a)(c)(e)(h) TEM bright field image of Pt nanoparticles (b)(d)(f)(h) size histogram of the corresponding Pt nanoparticles shown on the left

High photon energy of 129eV was used to explore the surface core level 4f electrons of the Pt nanoparticles. Figure 1.5 shows core level spectra of Pt nanoparticles. $4f_{\frac{5}{2}}$ and

$4f_{\frac{7}{2}}$ peaks of Pt can be observed from the spectra for four sizes. The sample which has the smallest size 1.6nm gives very week signal probably due to the low coverage on the substrate and thus the features of 4f peaks are vague. 4f peaks of the four samples with different mean size possess the same position in the spectra. Binding energy of $4f_{\frac{5}{2}}$ and $4f_{\frac{7}{2}}$ is about -74.8eV and -71.5eV, respectively. Reported binding energy of $4f_{\frac{5}{2}}$ varies among -74.2eV to -74.5eV and the binding energy of $4f_{\frac{7}{2}}$ varies among -70.83eV to -71.3eV[17]. The core level peak positions of our samples are very close to the reported values. Compared to $4f_{\frac{7}{2}}$ of bulk metal Pt 71.2eV, the core level of Pt nanoparticles has 0.3eV shift. There isn't any observable size dependence of the binding energy of 4f electrons.

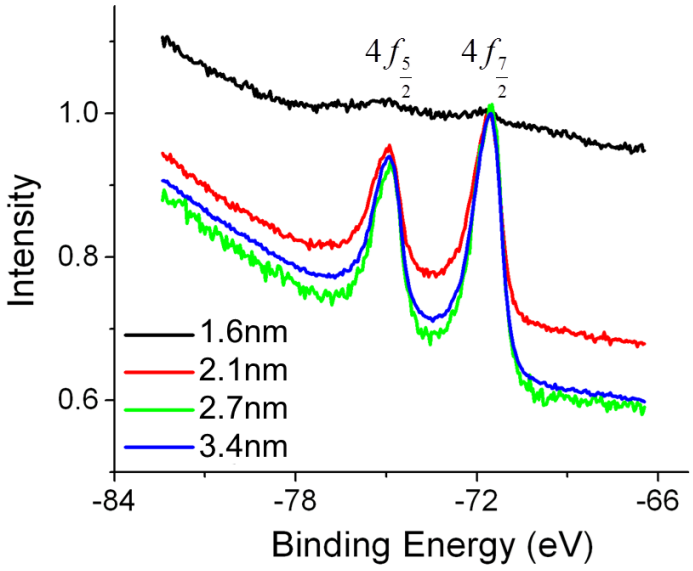

Figure 1.5 Core-level spectra of Pt nanoparticles

Valence band of Pt nanoparticles was also probed using low photon energy of 80eV by UPS. Before the measurements the empty halve of HOPG without Pt nanoparticles was partially peeled by adhesive tape in order to expose the fresh HOPG surface. Spectra were taken on unpeeled part of HOPG substrate, peeled part of HOPG substrate and the Pt nanoparticles on the same HOPG substrate. Figure 1.6(a) displays valence band spectra of Pt nanoparticles of four different sizes together with the background of unpeeled and unpeeled HOPG substrate. The two peaks with high intensity are from HOPG substrate and can be observed in all of the three curves for each size. A small bump arising from the Pt nanoparticles locates close to zero binding energy in the spectra of Pt/HOPG. This feature is present in the samples of size 3.4nm, 2.7nm and 2.1nm. There is hardly any similar feature observed for 1.6nm Pt nanoparticles due to the small quantity of particles on the substrate. The structure of valence band of Pt nanoparticles was analyzed except for the sample with size 1.6nm.

It can be noted that the signal from HOPG substrate is not the same for the four samples. This is because the photoemission angles were slightly changed during experiments. HOPG is highly oriented signal crystal whose photoemission is angle sensitive. All the spectra of a sample were taken at one angle whereas the angle was different from sample to sample. It was for the purpose to optimize the spectra of Pt/HOPG to reduce the effect from the random packing configuration of Pt on the substrate and the surface roughness. Figure 1.6(b) shows how spectra of HOPG vary along with the change of photoemission angle. Spectra of peeled HOPG were measured first at different angles and spectra of Pt/HOPG were measured later at these angles.

Change of signal of HOPG can be found by comparing the curves collected at different angles. At one fixed angle, HOPG peaks overlap quite well for the spectrum of substrate only and Pt/HOPG. But from one angle to another angle, peaks from HOPG no longer keep the same. There is slight deviation between the HOPG peaks of pure substrate and Pt/HOPG in the case of 142 degree and144 degree. It is probably due to beam hitting places off the sample after a large degree of rotation.

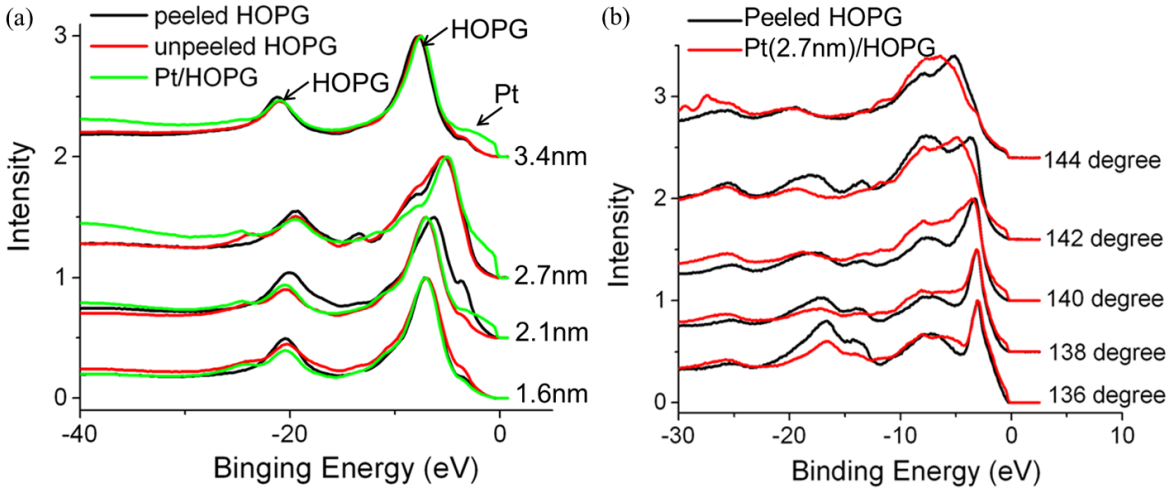

Figure 1.6 (a) Valence band spectra of Pt nanoparticles of different size (b) Valence band spectra of 2.7nm Pt nanoparticles taken at different angle of incident beam

Valence band spectra exclusively for Pt nanoparticles were obtained through subtraction of the spectra of unpeeled HOPG and Pt-HOPG. This method was employed previously by Eberhardt et al.[10] Figure 1.7(a) shows the subtraction results for Pt nanoparticles of 3.4nm, 2.7nm and 2.1nm. At 80eV, the photoemission cross-section of Pt is dominated by the d states because the s and p states have very small cross-section. Therefore, the valence band spectrum is a reflection of the features of d bands of Pt nanoparticles. In Figure 1.7(a), valence band spectra of Pt nanoparticles show somewhat

resolved $5d_{\frac{3}{2}}$ and $5d_{\frac{5}{2}}$ features. The width of the valence band for the three samples keeps almost the same. As introduced previously, a measure of the activity of the metal surface is the center of the d band. d band center energy was thus calculated relative to the Fermi level using Equation 6.3 in a similar way with what was done by Mun et. al[7]

$$d_{center} = \frac{\int N(\varepsilon)\varepsilon d\varepsilon}{\int N(\varepsilon)d\varepsilon} \quad \text{(Equation 1.3)}$$

where N(ε) is the density of states and in our case is the photoemission intensity after background subtraction. The d band center energy is shown in Figure 1.6(b) as solid blocks. It stays around -2.2eV for the three samples and doesn't show any clear size dependence. What is also included in the figure is the d-band center energy of Pt polycrystal, (110) and (100) planes of Pt single crystal. An up-shift trend can be found for our Pt nanoparticles compared to the listed bulk values of d band center energy. The d band center moves towards Fermi level and away from the bulk value.

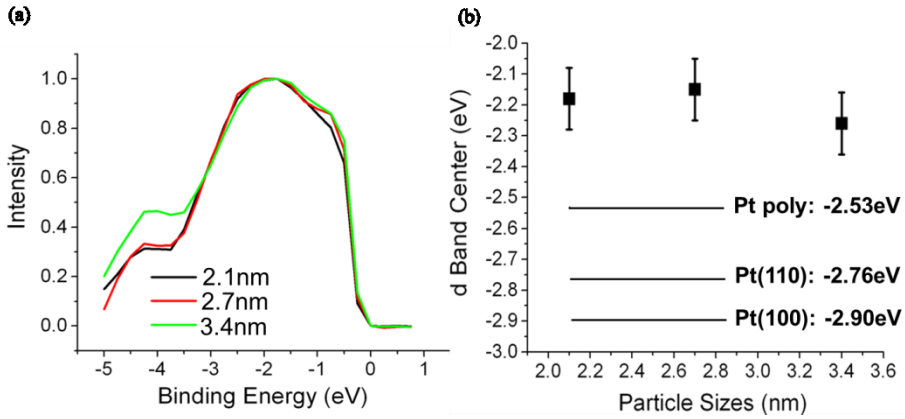

Figure 1.7 (a)Valence band spectra of Pt nanoparticles with the subtraction of background (b) d-band center energy of Pt nanoparticles calculated from the spectra on the left (dots) and d-band center energy of Pt bulk (line)

1.4.2 Discussions

The lack of size dependence of core level 4f energy and valence 5d energy is probably due to the agglomerated state of our Pt nanoparticles. As a lot of studies reveal the size dependence of electronic structures of nanoparticles, it was expected to observe variation of electronic structures of the Pt nanoparticles of three sizes. Nevertheless, both 4f and 5d peaks of Pt nanoparticles didn't show traceable change with respect to different sizes. Although difference of physical size was confirmed by TEM characterization based on the individual nanoparticles, there are a large percentage of nanoparticles that form agglomerated or densely packed state. This spatial arrangement blurs the difference of size and causes the outcome of none size dependent electronic structures.

The small shift of core level binding energy is attributed to photoemission process induced charge. 4f peaks of the Pt nanoparticles suggest 0.3eV higher binding energy than that of the bulk. It is suspected that the core-level shift is a result of a positive hole created after photoemission. The hole is not completely neutralized on the timescale of femtoseconds of the emission process and contributes to the core-level shift. The effect from coverage of oxygen on the surface can make another contribution. It's been reported that adsorption of oxygen on the surface could lead to an increase of binding energy and downshift of valence band away from Fermi level. Although the observed change of valence band is not consistent with the assumption of coverage of oxygen as the cause of core-level shift, this possibility cannot be ruled out completely considering that the observed change of electronic structures is a sum of multiple contributions.

The shift of d band center of Pt nanoparticles reflects a narrowing of their d band compared to bulks'. The size of the Pt nanoparticles is very small which gives a large surface to volume ratio. The surface property is thus dominated. The reduction of the width of the d band is a result of weakened hybridization between wave functions of d electrons, which has a major contribution from an increase of low coordinated atoms on the surface of Pt nanoparticles. It can be seen that most of the nanoparticles possess octahedron or dodecahedron geometry in previous TEM images. This indicates that a large number of atoms have few surrounding neighbors, especially for those on steps and kinks of the surface of nanoparticles. The band width becomes narrow due to the limited hybridizing wave functions in a local environment of low coordination number. Upshift of the d band center to Fermi level is concluded by applying the conservation of occupancy of valence band. It is also possible to have tensile strain in the Pt nanoparticles as another contribution of the narrow d band. When there is an expansion of lattice, overlapping of wave functions of d electrons is reduced between neighboring atoms. Therefore tensile strain leads to weak hybridization and thus decreased width of d band.

Based on the model proposed by Hammer, the Pt nanoparticles will appear very active to foreign molecules because of the position of their d band center. In a simplified point of view, the weak hybridization among Pt atoms can lead to active interaction between Pt atoms and other molecules. Strong bonding is expected to form between Pt nanoparticles and the adsorbates. However, it should be pointed out that high reactivity doesn't necessarily give optimal catalytic performance. As previously mentioned a good catalyst should react actively without bonding to adatoms too tightly[5,18]. It is because of the more

negative d band center of Pt alloys than pure Pt that better catalytic performance are found in some bimetallic or core-shell material systems such as Pt-Ni, Pt-Ru[18,19,20]. The negative d band center leads to reduced reactivity but it also gives reduction of the binding energy of atomic O and CO, which can leave many surface sites for the reaction. In short, the overall catalysis performance in a real system cannot be judged by the absolute number of the d band center only. The d band center is nevertheless one of the most important parameters to measure how active the catalyst is and can be referenced to understand the catalytic behavior of the nanocatalysts. The work here reveals the strong chemisorption and intrinsic reactivity of gas phase synthesized Pt nanoparticles with relatively clean surface.

1.5 Conclusions

Pt nanoparticles were synthesized in gas phase with relatively clean surface as a unique study subject for catalysis in fuel cells. Pt nanoparticles of different sizes were obtained by tuning different fabrication parameters. It was found that gas flow condition had great influence on the size of Pt nanoparticles. Electronic structure of Pt nanoparticles of different sizes was explored by UPS. Both 4f core-level energy and 5d valence band energy didn't show observable size dependence possibly due to the agglomerated spatial arrangement of Pt nanoparticles on the substrates. The d band center position of Pt nanoparticles shifted close to Fermi level compared to the bulk. It reflects strong chemisorption and reactivity of Pt nanoparticles synthesized by this method.

References

[1] V. Mazumder, Y. Lee, and S. Sun, Advanced Functional Materials **20,** 1224 (2010).

[2] S. B. Yoon, B. Fang, M. Kim, J. H. Kim, and J.-S. Yu, in *Frontiers of Nanoscience*; *Vol. Volume 1*, edited by W. Gerhard (Elsevier, 2009), p. 173.

[3] A. Z. Moshfegh, Journal of Physics D: Applied Physics **42,** 233001 (2009).

[4] H. Liu, C. Song, L. Zhang, J. Zhang, H. Wang, and D. P. Wilkinson, Journal of Power Sources **155,** 95 (2006).

[5] J. R. Kitchin, J. K. Norskov, M. A. Barteau, and J. G. Chen, The Journal of Chemical Physics **120,** 10240 (2004).

[6] B. Hammer and J. K. Nørskov, Surface Science **343,** 211 (1995).

[7] B. S. Mun, M. Watanabe, M. Rossi, V. Stamenkovic, N. M. Markovic, and J. P. N. Ross, The Journal of Chemical Physics **123,** 204717 (2005).

[8] E. Toyoda, R. Jinnouchi, T. Hatanaka, Y. Morimoto, K. Mitsuhara, A. Visikovskiy, and Y. Kido, The Journal of Physical Chemistry C **115,** 21236 (2011).

[9] J. A. van Bokhoven and J. T. Miller, The Journal of Physical Chemistry C **111,** 9245 (2007).

[10] W. Eberhardt, P. Fayet, D. M. Cox, Z. Fu, A. Kaldor, R. Sherwood, and D. Sondericker, Physical Review Letters **64,** 780 (1990).

[11] V. Murgai, S. Raaen, M. Strongin, and R. F. Garrett, Physical Review B **33,** 4345 (1986).

[12] W. P. Zhou, A. Lewera, R. Larsen, R. I. Masel, P. S. Bagus, and A. Wieckowski, The Journal of Physical Chemistry B **110,** 13393 (2006).

[13] M. Mavrikakis, B. Hammer, and J. K. Nørskov, Physical Review Letters **81,** 2819 (1998).

[14] B. Richter, H. Kuhlenbeck, H. J. Freund, and P. S. Bagus, Physical Review Letters **93,** 026805 (2004).

[15] S. W. Lee, S. Chen, W. Sheng, N. Yabuuchi, Y.-T. Kim, T. Mitani, E. Vescovo, and Y. Shao-Horn, Journal of the American Chemical Society **131,** 15669 (2009).

[16] X. Liu, Thesis, University of Minnesota, 2009.

[17] NIST.

[18] S. Alayoglu, A. U. Nilekar, M. Mavrikakis, and B. Eichhorn, Nat Mater **7,** 333 (2008).

[19] M. Wakisaka, S. Mitsui, Y. Hirose, K. Kawashima, H. Uchida, and M. Watanabe, The Journal of Physical Chemistry B **110,** 23489 (2006).

[20] K.-W. Park, J.-H. Choi, B.-K. Kwon, S.-A. Lee, Y.-E. Sung, H.-Y. Ha, S.-A. Hong, H. Kim, and A. Wieckowski, The Journal of Physical Chemistry B **106,** 1869 (2002).